Title	Optimisation of high-efficiency UV and visible light sources utilising lateral localisation in InAlN and InGaN based nano-structure devices
Author(s)	Norouzian Alam, Shahab
Publication date	2018
Original citation	Norouzian Alam, S. 2018. Optimisation of high-efficiency UV and visible light sources utilising lateral localisation in InAlN and InGaN based nano-structure devices. PhD Thesis, University College Cork.
Type of publication	Doctoral thesis
Rights	© 2018, Shahab Norouzian Alam. http://creativecommons.org/licenses/by-nc-nd/3.0/
Embargo information	Not applicable
Item downloaded from	http://hdl.handle.net/10468/7639

University College Cork, Ireland
Coláiste na hOllscoile Corcaigh

Optimisation of High Efficiency UV and Visible Light Sources Utilising Lateral Localisation in InAlN and InGaN Based Nano-Structure Devices

BY

Shahab Norouzian Alam

Nitride Materials Group, Tyndall National Institute
Department of Electrical and Electronic Engineering
University College Cork, Ireland

A Thesis Submitted To
The National University Of Ireland, Cork

For The Degree Of
Doctor Of Philosophy (Ph.D.)

January 2018

Research Supervisor: Prof. Peter James Parbrook
Mentor: Dr. Stefan Schulz

Head Of School Of Engineering: Prof. William Marnane

TABLE OF CONTENTS

Declaration

I hereby declare that all of the work undertaken in this thesis is original in content and was carried out by the author. Any contribution made to the research by others, with whom I have worked directly at Tyndall National Institute and University College Cork or elsewhere, is explicitly acknowledged in the thesis. The work presented has not been accepted in any previous application for a degree in any other University or Institution.

Author's Name   . . . .

Signature:

Date: . . . .

بِسْمِ اللّٰهِ الرَّحْمٰنِ الرَّحِيْمِ

Dedicated to:

My dearest family, my beautiful kids and especially to my lovely wife, Maryam, who has been there for me through all the time, and I don't think I would have survived without her support, patience and kindness.

Acknowledgments:

First and foremost I want to thank my supervisor Professor Peter James Parbrook. It has been an honour to be his PhD student. He has taught me, both consciously and unconsciously, how good experimental physics is done. I appreciate all his contributions of time, ideas, and funding to make my PhD experience productive. Especial thanks to Dr Vitaly Zubialevich for his guidance, support and encouragements during my PhD studentship. He is the excellent example of a great scientist with an outstanding morality.

Many thanks to all group members who I have been working with for their help and supports to undertake this work. Especial thanks to Dr Van Duc Dinh, Pietro Pampili, Brian Corbett, Pleun Maaskant, Dr Mahbub Akhter and Dr Michele Conroy.

I would like to thanks our colleagues in Strathclyde University (Prof. Robert Martin, Dr Gunnar Kusch and Christopher Bryce) for their contribution and collaborations particularly to do the Cathodoluminescence spectroscopy of my samples.

The TEM analysis, electron beam lithography and ICP dry etching were performed at Tyndall by Dr Michael Schmidt, Brendan McCarthy and Alan Hydes respectively.

I would like to also thanks to our colleagues in the theory group Prof. Eoin O'Reilly and Dr Stefan Schulz for their contributions to the research and advises. Especial thanks to Stefan who is also kindly and supporting mentoring my PhD program.

Abstract

III-nitride semiconductor materials (including GaN, InN and AlN and their alloys), have the capability to emit light at wavelengths spanning from the near IR to the deep UV. However, understanding these materials is challenging due to the presence of strong polarisation fields and large difference in optimum growth temperature between binary compounds are two such examples. InAlN is perhaps the least well understood III-N alloy. It has potential be applied for optoelectronic devices operating in the UV spectral range. However, the variation of band-gap with alloy composition, particularly in the low In content regime, is not understood. In this work, a strongly composition dependent bowing parameter has been observed for ~100 nm thick $In_xAl_{1-x}N$ epitaxial layers with $0 \leq x \leq 0.224$, grown by metalorganic vapour phase epitaxy (MOVPE), prepared on AlN/Al_2O_3-templates. Also a double absorption edge was observed for InAlN with $x < 0.01$, attributed to crystal-field splitting of the highest valence band states. These results indicate that the ordering of the valence bands is changed at much lower In contents than linear interpolation of the valence band parameters would predict. Coupling our results with the published literature data the band-gap and bowing parameter of InAlN across the full composition range were determined. Additionally, applying the InAlN band-gap data with those for other alloys the refractive index of III-N alloys is predicted using an Adachi model resulting in a very good agreement with previous experimental data where available.

For InAlN/AlGaN multi-quantum-wells (MQWs) excited by photoluminescence (PL) and emitting between 300-350 nm, high apparent internal quantum efficiencies (IQE) ($I_{PL(300\ K)}/I_{PL(T)max}$) of up to 70% were obtained. This is attributed to the exceptionally strong carrier localisation in this material, which is also manifested by a high Stokes shift (0.52 eV) of the luminescence. A non-monotonic dependence of luminescence efficiency on indium content with a maximum at about 18% In was explained as a trade-off between a strain relaxation for higher indium contents and a type I to type II band line-up conversion for low In content alloys.

Nanoscale materials have attracted a lot of attention due to their ability to decrease dislocations as well as build-in field reduction. In the second part of this thesis, GaN nanostructures, were used as templates for InGaN MQW growth targeting nano-LED structures. Two nano-structuring methods were examined; using GaN nano-columns (NCs) following an etch regrowth methodology, and selective area aperture growth (SAG). In the former case we determined the optimal etch conditions for the GaN columns and conditions for overgrowth InGaN QWS. The rod tops formed semipolar facets. InGaN QWs grown on these pyramids were found to be extremely thin leading to difficulties in obtaining PL in our case. Using the SAG approach, nano-pyramids were formed in nano-apertures, with good uniformity. InGaN QWs exhibited blue PL, which cathodoluminescence (CL) showed to be made up of two spectral features, attributed to the pyramid nano-facets and pyramid apex tips, respectively.

List of Publications:

Journal Papers:

o <u>Shahab N. Alam</u>, Vitaly Z. Zubialevich, Duc V. Dinh, Stefan Schulz, Eion O'Reilly, and Peter J. Parbrook. "*Optical properties of InAlN and AlGaN Across Full Composition Range.*" (**Under preparation**).

o <u>Shahab. N. Alam</u>, Duc V. Dinh, V. Z. Zubialevich, Michael Schmidt, Christopher Bryce, Robert W. Martin and P. J. Parbrook. "*Growth and Characterisation of InGaN/GaN QWs on Defect-Free and Uniformly Formed GaN Nanopyramids for Visible LED Applications.*" (**Under preparation**).

o <u>Shahab N. Alam</u>, Vitaly Z. Zubialevich, Duc V. Dinh, and Peter J. Parbrook. "Temperature and *Excitation Power Dependent Photoluminescence Spectroscopy of InAlN/AlGaN Quantum Wells on Sapphire Substrate.*" (**Under preparation**).

o Vitaly Z. Zubialevich, Mikalai V. Rzheutski, Haoning Li, <u>Shahab N. Alam</u>, Evgenii V. Lutsenko, Gennadii P. Yablonskii, Peter J. Parbrook. "*$In_xAl_{1-x}N/Al_{0.53}Ga_{0.47}N$ multiple quantum wells on $Al_{0.5}Ga_{0.5}N$ buffer with variable in-plane lattice parameter.*" **Journal of Luminescence**, 23 September (**2017**).

o Vitaly Z. Zubialevich, <u>Shahab N. Alam</u>, Haoning Li, Peter J. Parbrook. "*Composition dependence of photoluminescence properties of InAlN/AlGaN quantum wells.*" **Journal of Physics D: Applied Physics** 49, No. 38 (**2016**), 385105.

o Duc V. Dinh, <u>Shahab N. Alam</u>, Peter J. Parbrook. "*Effect of V/III ratio on the growth of* $(11\overline{2}2)$ *AlGaN by metalorganic vapour phase Epitaxy.*" **Journal of Crystal Growth** 435 (**2016**): 12-18.

o Vitaly Z. Zubialevich, Duc V. Dinh, <u>Shahab N. Alam</u>, Stefan Schulz, Eion O'Reilly, and Peter J. Parbrook. "*Strongly nonparabolic variation of the band gap in $In_xAl_{1-x}N$ with low indium content.*" **Semiconductor Science and Technology**, 31.2 (**2015**): 025006.

o Vitaly Z. Zubialevich, Thomas C. Sadler, Duc V. Dinh, <u>Shahab N. Alam</u>, Haoning Li, Pietro Pampili, and Peter J. Parbrook. "*Enhanced UV luminescence from InAlN quantum well structures using two temperature growth.*" **Journal of Luminescence** 155 (**2014**): 108-111.

o Duc V. Dinh, F. Oehler, Vitaly. Z. Zubialevich, M. J. Kappers, <u>Shahab. N. Alam,</u> M. Caliebe, F. Scholtz, C. J. Humphreys, and P. J. Parbrook. "*Comparative study of polar and semi-polar* $(11\overline{2}2)$ *InGaN layers grown by metalorganic vapour phase epitaxy.*" **Journal of Applied Physics** 116, No. 15 (**2014**): 153505-153505.

Presentations (Oral and Poster):

o <u>Shahab. N. Alam</u>, V. Z. Zubialevich, Michael Schmidt, Christopher Bryce, Robert W. Martin and P. J. Parbrook. "*Blue luminescence from InGaN/GaN nano-pyramids prepared by selective area epitaxy technique*" **UK Semiconductors**, Sheffield, UK, July **2017**.

o <u>Shahab. N. Alam</u>, Duc V. Dinh, V. Z. Zubialevich, Michael Schmidt, Christopher Bryce, Robert W. Martin and P. J. Parbrook. "*Growth and Characterisation of InGaN/GaN QWs on Defect-Free and Uniformly Formed GaN Nanopyramids for Visible LED Applications.*" **International Workshop on Nitride Semiconductors (IWN)**, Orlando, USA, October **2016** (Poster)

o <u>Shahab. N. Alam</u>, V. Z. Zubialevich, Duc V. Dinh and P. J. Parbrook. "*Temperature Dependent Bandgap and Bowing Parameter of Indium Aluminum Nitride.*" **UKNC conference**, Cambridge, UK, January **2016** (Oral)

o <u>Shahab. N. Alam</u>, Duc V. Dinh, V. Z. Zubialevich, and P. J. Parbrook. "*Growth and Optical Characterization of InGaN/GaN Multiple Quantum Wells on GaN Nano-Pyramids*". **Intel Ireland Research Conference,** Dublin, Ireland, October **2015** (Poster).

o Shahab. N. Alam, V. Z. Zubialevich, Duc V. Dinh, and P. J. Parbrook. "*Composition dependent band-gap and bowing parameter of Indium Aluminum Nitride*". **Photonics Ireland 2015,** Cork, Ireland, September **2015** (Oral).

o Duc V. Dinh, Shahab. N. Alam, H. N. Li, Peter J. Parbrook. "*Growth and characterization of polar and semipolar* $(11\bar{2}2)$ *Al(In,Ga)N layers using MOVPE.*" **11th ICNS,** Beijing, China, August **2015** (Oral).

o Pietro Pampili, Vitaly Z. Zubialevich, Shahab N. Alam, Haoning Li, Sergey V. Ivanov, Valentin N. Jmerik, Dmitrii V. Nechaev, Mahbub Akhter, Pleun P. Maaskant, Brian Corbett, and Peter J. Parbrook, "*Realization of UVLEDs Using InAlN Based Quantum Wells.*" **11th International Conference on Nitride Semiconductors,** Beijing, China, August **2015** (Oral).

o Shahab. N. Alam, V. Z. Zubialevich, , Duc V. Dinh, E. O'Reilly, S. Schulz, and P. J. Parbrook. "*Determination of Bandgap and Bowing Parameter of Al Rich InAlN.*" **UKNC conference**, Nottingham, UK, January **2015** (Oral).

o Shahab. N. Alam, V. Z. Zubialevich, P. Pampili, P. J. Parbrook, "*Excitation Power Dependent Photoluminescence Spectroscopy of InAlN/AlGaN Quantum Wells on Sapphire Substrate.*" **7th Wide Band Gap Semiconductor and Components Workshop**, ESA-ESRIN, Frascati (Rome), Italy, September **2014** (Poster).

o V. Zubialevich, T. Sadler, Duc V. Dinh, H. Li, Shahab. N. Alam, P. Pampili, P. Parbrook. "I*nAlN: An alternative quantum well material for UV emitters*." **UKNC conference,** Bristol, UK, January **2014** (Oral).

o P. Pampili, V. Zubialevich, Shahab. N. Alam, M. CaroBayo, S. Schulz, E. O'Reilly, P. J. Parbrook. "*Quantum Confined Stark Effect reduction by polarization matching of a near-UV LED active region.*" **UKNC conference,** Bristol, UK, January **2014** (Oral).

o H. Li, V. Zubialevich, Shahab. N. Alam, P. J. Parbrook. "*Effect of Growth Temperature on Composition and Photoluminescent Properties of InxAl1-xN/ AI0.59Ga0.41N Multiple Quantum Wells,* **10th International Conference on Nitride Semiconductors**, Washington – DC, USA, August **2013** (Oral).

o V. Z. Zubialevich, H. Li, Shahab. N. Alam, P. J. Parbrook, G*rowth Optimization and Photoluminescence Properties of In0.18Al0.82N/Al0.53Ga0.47N Multiple Quantum Wells*, **10th International Conference on Nitride Semiconductors**, Washington – DC, USA, August **2013** (Oral).

o Duc V. Dinh, Fabrice Oehler, Menno J. Kappers, Shahab N. Alam, Silvino Presa, Colin J. Humphreys, Peter J. Parbrook. "*Growth and characterization of semipolar (11-22) InGaN by MOVPE.*" **15th European Workshop on Metalorganic Vapour Phase Epitaxy (EWMOVPE 2013)**, Aachen, Germany, June **2013** (Oral).

o Vitaly Z. Zubialevich, Haoning Li, Thomas C. Sadler, Michele Conroy, Shahab. N. Alam, Peter J. Parbrook. "*Photoluminescence of InAlN/AlGaN multiple quantum wells grown on AlGaN buffer relaxed from AlN-template with thin GaN layer.*" **15th EWMOVPE 2013**, Aachen, Germany, June **2013** (Oral).

o Haoning N. Li, Thomas C. Sadler, Vitaly Z. Zubialevich, Michele Conroy, Shahab N. Alam, Peter J. Parbrook, *Effect of thin GaN layer between AlN-template and AlGaN buffer on optical properties of 340 nm InAlN/AlGaN multiple quantum wells*, **UKNC conference**, Cardiff, UK, January **2013** (Oral)

.

INTRODUCTION:

Background and motivation:

InN, GaN and AlN and their alloys are so-called III-nitride semiconductors which are very interesting and vital materials regarding science and technology. III-nitride alloys can emit photons in the wavelengths that span from the near infrared to the deep ultraviolet. They potentially could be used in a wide range of optical and optoelectronic applications, including light-emitting diodes (LEDs), detectors, sterilization, medical diagnostics, optical storage, with other electronic applications such as power electronics [1, 2].

There was no efficient blue LED available prior to the first demonstration of III-nitride blue LED by the Japanese scientist Shuji Nakamura and colleagues in 1994 [3] which Nakamura, Amano and Akasaki were awarded the Physics Nobel Prize for in 2014. Thereupon, interest in the research of these materials has continuously expanded over the past two decades since this invention raised.

Although III-nitride semiconductors are technically very important materials, understanding of their properties is challenging. The presence of strong polarisation fields due to the wurtzite crystallography and strain complicates their analysis, particularly for quantum well (QW) structures, where the potential wells are modified due to induced electric fields. These fields can be mitigated for semipolar and nonpolar planes, accessible through growth on nanostructured arrays [4, 5] [6, 7] [8-10].

The large carrier effective mass and changes in band-gap with alloy composition also lead to carrier localisation and broad emission linewidths, resulting in further challenges for the characterisation and understanding of these materials [11, 12].

For many semiconductor alloys, to predict their physical properties one can simply apply a linear function using the parameters of the semiconductor components at the endpoints. This is known as Vegard's law [13]. However, the band gap variation of III-nitride alloys does not follow the linear Vegard's law with composition, and some degree of deviation is observed which is called "bowing". The bowing parameter measurement is a key matter of interest for researchers for all three systems: AlGaN, InGaN and InAlN [14]. This "bowing parameter" is usually found to be constant across the alloy range, but in extreme cases, this empirical rule is not valid. This is the case for InAlN, for example.

Nanoscale materials have attracted a lot of attention due to their ability to decrease dislocations as well as build-in field reduction. Another noticeable properties of using nanostructured materials, especially III-nitrides, is to provide possible growth on foreign as well as native materials [15-17]. GaN nanostructures (especially, nano-rods and nano-pyramids), have been used as the template for InGaN MQW growth. These nanostructures can provide templates free of dislocations and that are strain relieved, due to the large surface-to-volume ratio [18-21], accordingly, increasing the quantum efficiency [22, 23]. Despite many successful advances, there are still challenges and limitations regarding to growth and fabrication of these nanostructures.

In this thesis, two techniques were used to prepare nanostructured GaN template for InGaN/GaN MQW heterostructures, selective area growth (SAG) and a combination of top-down/bottom-up techniques by selective area dry etch followed by MOVPE growth. Combination of top-down and bottom-up techniques by selective dry etch of GaN template followed by MOVPE growth, allows us to use benefits of both top-down (ability to growth planar material with low impurity and controlled doping) and bottom-up (strain free and low density of dislocation) methods. Also, using this technique allows us to growth nano-rods separately without coalescence [24]. In SAG technique, areas are intentionally selected using a mask and exposed for desired material growth. This technique has been studied intensively by scientists, owing to the several advantages for the light emitting devices, including; adjustable diameter and spacing of the grown nano/micro-structures [25, 26], and the capability of growing LEDs with a variety of colours on the same substrate [25, 27]. Another most noticeable advantage of using SAG is to increase the efficiency by lowering of the defects by trap and bending the threading dislocations [28-30] and reduction of piezoelectric field on semipolar/nonpolar facets [31-35].

The aim of this work is to grow and characterise high-efficiency indium content material as an active region for higher efficiency visible and UV light sources utilising lateral localisation in InAlN and also InGaN based nanostructure devices.

Thesis outline and overview:

Chapter 1, describes the principal properties of III-nitride materials (InN, GaN, AlN and their alloys). This includes discussion of crystal structure, band structure, polarisation and the effects of the composition.

The optical processes that occur in III-N materials are also described. This includes an introduction to light absorption and mechanism of light emission and how these vary with temperature and excitation power.

In chapter 2; the experimental techniques, used in this thesis (including growth, fabrication and characterisation) are described. The MOVPE growth technique has been exclusively used in this work and is explained in detail, with a brief summary of other deposition methods.

III-nitride technology has become a commercial reality by applying hetero-epitaxy techniques and employing foreign substrates such as sapphire, silicon carbide, and silicon. Hence, some of the inherent properties of these foreign substrates (especially about sapphire as the most common substrate) such as lattice constants and thermal expansion, will be summarised concisely.

Structural, optical and electronic characterisation of materials and devices are explained. These include electron microscopy, X-ray diffraction, photoluminescence, cathodoluminescence and electroluminescence. The final part of this chapter is dedicated to the fabrication process of LEDs. This chapter will include short introductions about photo-lithography, electron beam lithography, etching and metallisation.

Chapter 3, is about growth and characterisation of InAlN alloys. Thick layers of InAlN with different composition (In content) were grown by varying the growth temperature. The optical and electronic behaviours of these layers will be discussed in detail. The band-gap of the InAlN alloys is determined using photoluminescence excitation, in particular, focusing on low In contents. By using our low In content data in combination with data reported by other scientists, the band-gap and bowing parameter of the InAlN alloy at the full composition range were derived. Using the 'best-estimated' band-gap data, the band-offset relationships and the refractive index of the alloys are estimated.

In chapter 4, InAlN is considered as a material for use in the active region of a light-emitting diode. The InAlN alloy potentially can be a good candidate for light emitting applications, especially in the blue and UV range. This study includes optimisation of the InAlN QWs growth from luminescence point of view which includes: QW thickness, composition and growth temperature. The effects of

temperature and excitation power density on the luminescence properties of the InAlN were also investigated.

Chapter 5, deals with the growth and characterisation of InGaN QWs on nano-structured GaN. Two main techniques were used in this thesis to prepare nanostructured GaN templates for InGaN/GaN MQW heterostructures. These two techniques are: selective area growth (SAG) as a bottom-up technique; and a combination of top-down/bottom-up methods by selective area dry etch followed by MOVPE growth.

Experimental details of preparing nano-columns using the top-down/bottom-up technique will be reported. This will contain; scooping transfer nano-lithography, dry etch and MOVPE growth of GaN and InGaN materials. Effects of growth parameters like temperature, duration as well as dimensions of nanospheres on optical properties of InGaN/GaN nanostructures will be studied in detail.

The second part of this chapter will be about the preparation of nano-structured InGaN/GaN in the forms of nano-pyramids using the SAG technique. Optical characterisation of nano-pyramids was carried out using photoluminescence and cathodoluminescence techniques along with structural analysis by TEM and SEM. This chapter will finish with reports about the fabrication of a full LED, followed by optical analysis of nanostructures.

In Chapter 6, summary and conclusions of this thesis will be presented and will include suggestions for future works in these areas.

Chapter 1

Principal Properties

of

III-Nitride Materials

1 PRINCIPAL PROPERTIES OF III-NITRIDE MATERIALS

Group III nitrides including binary (GaN, InN and AlN), ternary ($In_xGa_{1-x}N$, $Al_yGa_{1-y}N$ and $In_zAl_{1-z}N$) and quaternary ($In_xAl_yGa_{1-x-y}N$), are considered as one of the most important semiconductor material families. Nowadays, with a high level of certainty, everyone can find these materials in many kinds of applications including; lighting, lasers, high-power amplifiers, detectors and displays. This is because of exceptional optical and electrical properties of III-nitride materials. In this chapter, the principal properties of nitride semiconductors will be primarily reviewed; this will include structural, optical, electrical and thermal properties.

1.1 Basic Properties of Binary Nitrides

1.1.1 Crystal Structure

Binary nitride semiconductors (GaN, InN and AlN), can be in the crystalline structures of wurtzite (WZ) and zinc blende whereby wurtzite is the most thermodynamically stable phase under ambient condition [14]. In the case of WZ hexagonal crystal structures, instead of three index Miller notation (*hkl*), four indices (*hkil*) or Miller-Bravais is normally used, where h, k and l are identical to the Miller indices. The additional index i is equivalent to $-(h+k)$. This four-indices layout is very useful in hexagonal lattice to represent the nature of reticular planes. For instance, similar properties of a-planes ($11\bar{2}0$) and ($1\bar{2}10$) can be explained better using this scheme than in the format of (110) and ($1\bar{2}0$). Figure *1-1* shows a schematic view of a hexagonal crystal system indication for two identical a-planes.

Wurtzite crystal structure of III-nitride materials is shown in Figure 1-2. The unit cell of the hexagonal lattice, can be described by the two lattice parameters of *a* and *c*, as shown in Figure 1-2 and summarised in Table 1-1.
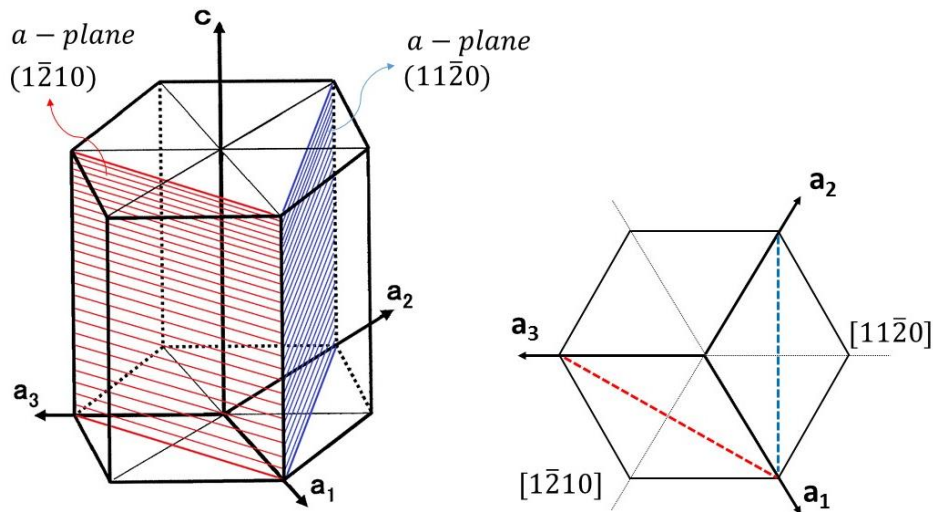
Figure 1-1 *Schematic illustration of a hexagonal crystal system indication two identical a-planes (112$\bar{0}$) and (12$\bar{1}$0).*

Table 1-1 Lattice constants of wurtzite GaN, AlN and InN at ambient condition [36] .

	a (Å)	c (Å)	c/a
GaN	3.189	5.185	1.626
AlN	3.112	4.982	1.601
InN	3.545	5.703	1.609
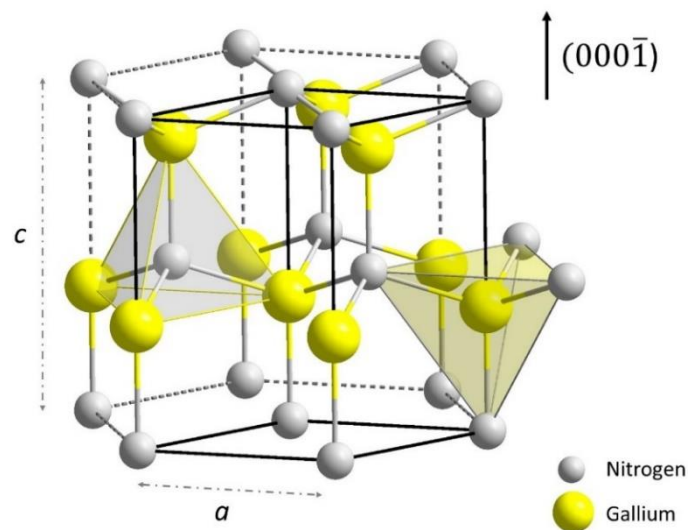
Figure 1-2 *Wurtzite crystal structure of III nitrides. Grey spheres depict the nitrogen atoms while yellow spheres represent the metallic Ga, Al or In atoms. Picture is taken and modified from Ref.* [37].

Nitrogen and group-III atoms in wurtzite structure form two embedded hexagonal atom stacks, named as A and B, respectively. They assemble in the form of ABABAB... sequences along the [0001]

direction. This structure is also named hexagonal close packed (HCP) structure. In this thesis, wurtzite III-nitride crystals are studied.

As depicted in Figure 1-3 (in the form of stick-and-ball diagram), polarisation depends on which atom (nitrogen or group III (Al, Ga or In) atoms) appears on the bare top surface of the crystal, it will be called N-polarity (the $[000\bar{1}]$ direction) or Ga-polarity (the $[0001]$ direction), respectively [14]. Understanding of this polarity is important in nitride semiconductors, as it defines the direction of the polarisation charge inside that is responsible for the quantum confined Stark effect (QCSE) phenomenon in III-nitride based quantum well heterostructures (see below for more details on this).
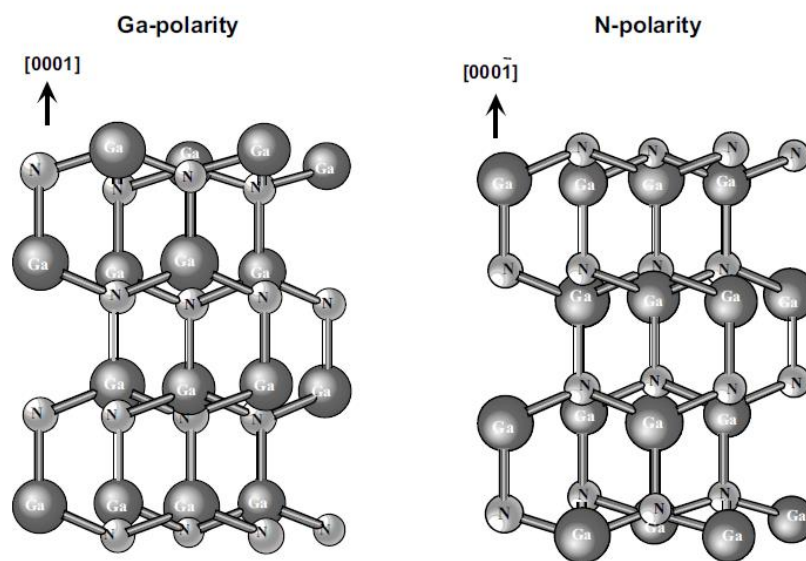
Figure 1-3 Stick-and ball diagram of GaN showing Ga-polarity and N-polarity [14].

The (0001) c-plane of III-nitrides is a so-called "polar" plane, indicating the polarisation field, that can align along the $[0001]$ or $[000\bar{1}]$ directions. More details about the polarisation field will be discussed in section 1.1.3. Apart from the polar plane, there are other crystal planes named non- and semi-polar planes. Figure 1-4 shows schematic views of polar, semi-polar and non-polar planes of wurtzite nitride crystal. The nonpolar planes are inclined 90° to the c-plane. The nonpolar $(11\bar{2}0)$ and $(1\bar{1}00)$ planes are called a-plane, and m-plane, respectively. Planes, that are inclined between 0-90° to the c-plane and non-polar planes are called semi-polar planes such as $(10\bar{1}1)$, $(11\bar{2}2)$ and $(10\bar{1}3)$ [38].
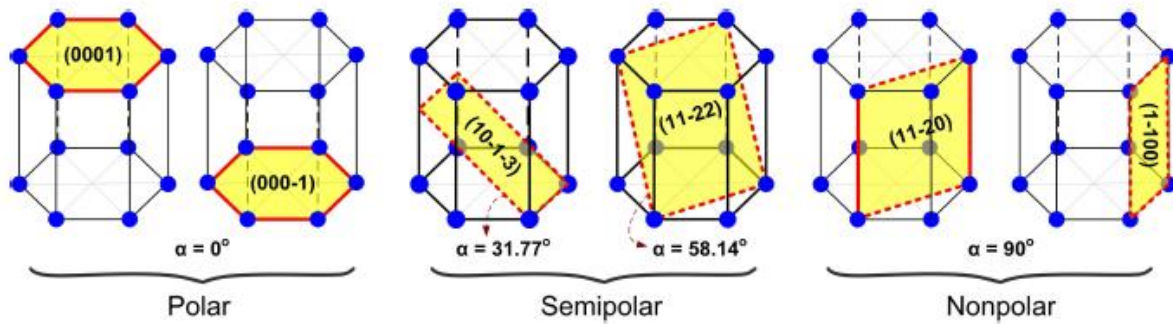
Figure 1-4 Schematic view of polar (0001) *plane, nonpolar* $(11\bar{2}0)$ *and* $(1\bar{1}00)$ *planes, and semipolar* $(10\bar{1}\bar{3})$ *and* $(11\bar{2}2)$ *planes in the wurtzite crystal. The* α *angles are given for the InN crystal [39] .*

1.1.2   Band Structure

Knowing about band structure of semiconductor materials is essential in order to determine their potential applications. Direct band-gap and the size of their band-gaps makes III-nitrides a point of interest in a variety of photonic and electronic device applications: including: laser diodes (LDs) [40, 41], light-emitting diodes (LEDs) [3, 42] and field effect transistors (FETs) [43, 44]. III-nitride semiconductors can be classified into two main groups. One is pure nitrides (GaN, AlN and InN) in the crystal forms of wurtzite and zinc blende. Dilute nitrides is another class of material, wherein very small amounts of nitrogen added to the lattice causing very large negative bowing of the band-gap which makes these dilute nitrides useful for longer wavelength applications. For example, by adding a small quantity of nitrogen to GaAs, the emission wavelength can be extended up to 1.3 μm [45].

1.1.2.1   *Gallium Nitride*

The band-gap of wurtzite GaN is known to be direct and around 3.42 eV at room temperature [46-48]. The energy band-gap of GaN is normally measured using photoluminescence (PL) spectroscopy by determination of the wavelength of the exciton lines, and accounting for the exciton binding energies [49, 50]. There are three main free exciton lines attributed to the A exciton $FX(A)$, B exciton $FX(B)$, and C exciton $FX(C)$, where FX stands for free exciton. The observation of the peak associated with $FX(A)$ can be regarded as an indicate of high quality GaN [51]. Early measurement of the free A exciton led to the value of $E_A = 3.475\ eV$ in association with the binding energy of around 28 meV, at temperatures close to $T = 0\ K$ [47, 49, 50]. From then a lot of other studies have reported A exciton transition energy values between 3.474 to 3.496 eV where these variations are dependent on strain conditions [36, 52] and other properties like impurity level, quality, etc. Experimental studies and theoretical calculation of the binding energy of free exciton A show values between

23 meV to 28 meV [52-54]. The energy band-gap can be calculated accurately by adding up the exciton transition energy (E_A) and the binding energy of free exciton A (E_A^b):

$$E_g = E_A + E_A^b \cong 3.510 \text{ eV } (0K) \qquad \text{Equation 1-1.}$$

The GaN conduction band (CB) minimum is at the Γ point where located at the centre of the Brillouin zone with $k = 0$. For the WZ semiconductor, an interaction of crystal-field splitting and spin–orbit coupling (Δ_{SO}) leads to three sub bands at the top of the valence band, as shown in Figure 1-5 for GaN. The spin–orbit and crystal-field VB splittings in GaN can be derived from the A, B, and C free exciton lines..

The band structure of the wurtzite crystal structures of GaN is shown in Figure 1-5. The spin orbit interaction causes the Γ_{15}^v valence band of the GaN crystal to split into two Γ_8^v and Γ_7^v bands with higher and lower energies, respectively (as shown in the right hand side of the figure) This would be the valence band splitting expected for zinc blend GaN. For Wurtzite materials there is a crystal fild splitting which, as shown on the left hand side of Figure 1-5 splits the Γ_{15} band into Γ_1 and Γ_5 (or Γ_6) states. The Γ_1 and Γ_6 states are then further split into Γ_9^v, Γ_{7-}^v (lower) and Γ_{7+}^v (upper) bands by spin-orbit coupling [55, 56]. The positive crystal-field splitting energy in GaN leads to the optical transition between the conduction and Γ_9^v band. Thus, the light polarisation dominantly becomes perpendicular to the c-axis (E⊥c) [57].

An initial study found values of $\Delta_{SO} = 11 \ meV$ and $\Delta_{CF} = 22 \ meV$ [47]. In 2003 Vurgaftman et al. in a review paper recommended the values of: $\Delta_{SO} = 17 \ meV$ and $\Delta_{CF} = 10 \ meV$ [36].
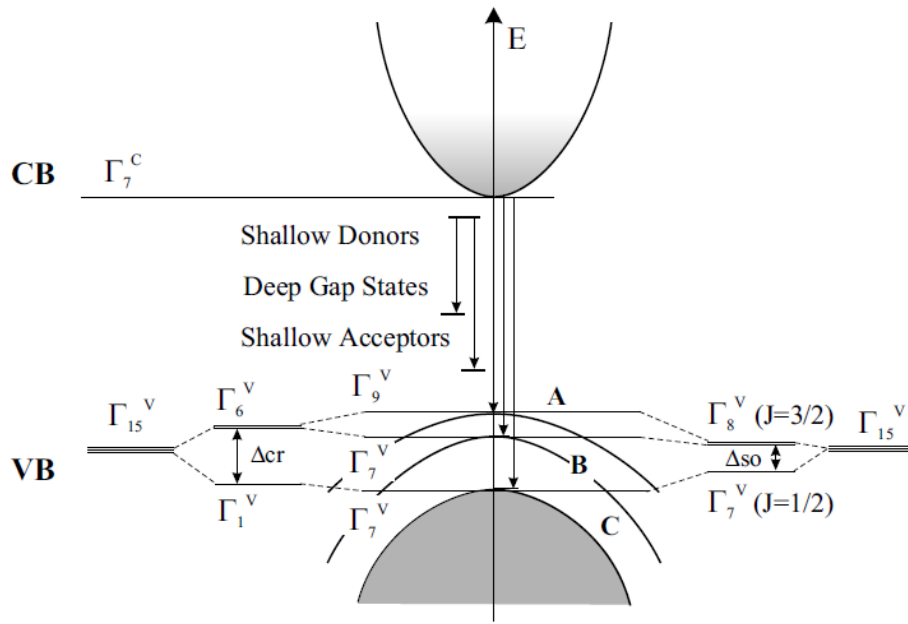
Figure 1-5 Schematic illustration of the electronic band structure of wurtzite GaN at the Γ point of the first Brillouin zone ($k = 0$) [58].

The positive crystal-field splitting energy in GaN leads to the orders of $\Gamma_9^v(6)$ (heavy hole; HH), $\Gamma_7^v(6)$ (light hole; LH), and $\Gamma_7^v(1)$ (crystal-field split-off hole; CH) bands on the top valence band, which causes the fundamental optical transition between the conduction and HH bands. Therefore, the light polarisation becomes dominantly perpendicular to the c-axis (E⊥c) [57].

Assuming no localisation, temperature dependence variation of the band-gap in semiconductors is normally characterised by an empirical expression introduced by Varshni [59]:

$$E_g(T) = E_g(0) - \frac{\alpha T^2}{\beta + T}$$

Equation 1-2.

where $E_g(0)$ and $E_g(T)$ are the band-gap energy at temperature $T = 0 \, K$ and T, respectively. α and β are Varshni (fitted) parameters which depend on material properties.

The Varshni parameters for wurtzite GaN have also been extensively studied. Teisseyre et al. [60] obtained the values of $\alpha = 0.939$– $1.08 \, \text{meVK}^{-1}$ and $\beta = 745$– $772 \, K$ from optical absorption of epitaxial GaN layers grown on sapphire and bulk single crystals. Petalas et al. [61] reported $\beta = 700 \, K$ and found $\alpha = 0.858 \, \text{meVK}^{-1}$ by means of spectroscopic ellipsometry, whereas Shan et al. reported $\alpha = 0.832 \, \text{meVK}^{-1}$ and $\beta = 836 \, K$ [62] for the temperature variation of the A exciton resonance. Salvador et al. [63] got the values of $\alpha = 0.732 \, \text{meVK}^{-1}$ and $\beta = 700 \, K$ using

the PL spectroscopy. Eventually based on the more reliable reported values Vurgaftman et al. [36] recommended Varshni parameters of $\alpha = 0.914$ meVK^{-1} and $\beta = 825$ K. The experimental data for GaN used in this work were taken from Nepal et. al. [64] ($\alpha=0.94$ meV/K and $\beta=791$ K). Taking into account that the variation of the band-gap energy ($72\ meV$ between 0 and $300\ K$) is relatively small, a GaN device could be considered comparatively insensitive to temperature variations [52]. There are still discrepancies about temperature dependent band-gap variation of GaN in published data, confirming the importance of the material quality and growth conditions of a particular epitaxial layer.

1.1.2.2   Aluminium Nitride

Like GaN, AlN also has both wurtzite and zinc blende phases, where the former is more stable and technologically interesting. Wurtzite AlN is a compound with direct and largest energy gap among all conventional semiconductors [52]. This characteristic of wurtzite AlN has made this material gain attention, because of the increasing interest in UV emitters, UV detectors and solar blind devices.

Wurtzite AlN has a direct band-gap near 6.1 eV at low temperature (LT). Despite its large band-gap it is still considered as a semiconductor material because of its ability to be doped [55]. Early experiments on wurtzite AlN using absorption measurements, showed a large energy gap of about 6.2 eV at room temperature (RT) and 6.28 eV at 5 K [65-67]. Guo et al. [68] and Vispute et al. [69], found the similar room temperature band-gap of 6.13 eV. At low temperature different researchers found different values, such as Jiang et al. [70] (6.280 eV), Onuma et al. [71] ($E_g = 6.211$ eV) and a value of 6.18 eV from the transition ascribed to the free A exciton by Chen et al.[72].

The valence band structure of Al-rich InAlN is similar to AlN and its polarisation, which are different from what we have for GaN [73, 74], and affects light extraction efficiency. Because of the smaller c/a ratio in comparison with GaN, AlN has a negative crystal-field splitting (Δ_{CF}) [74]. Therefore, the three levels of the valence band in AlN in the decreasing order of energy would be Γ_{7vbm} (CH) where *vbm* stands for valence band maximum, Γ_{9v} heavy hole (HH) and Γ_{7v} light hole (LH) [57]. The values reported from theoretical calculations for Δ_{CF} ranging from $-58\ meV$ to $-244\ meV$ [36, 48, 75-77]. Again from experimental studies listed in Ref [36], especially those from Chen et al. [72] and Silveria et al. [78] the value of $-220\ meV$ to $-230\ meV$ are recommended. Values for spin-orbit splitting have been reported in literature ranging from 11 to $20\ meV$ [76, 77, 79-81]. Due to the relatively large negative Δ_{cr} in AlN, at the Γ point, the fundamental optical transition is to the top Γ_{7vbm} band and the light polarisation is parallel to the crystal c-axis (E∥c). It is also in a case for Al

rich AlGaN when Al content higher than the cross-point between the HH and CH bands, therefore TM polarisation is dominant [82].

Calculated band structures of AlN with the experimentally measured energy band-gap and exciton binding energies are shown schematically in Figure 1-6.
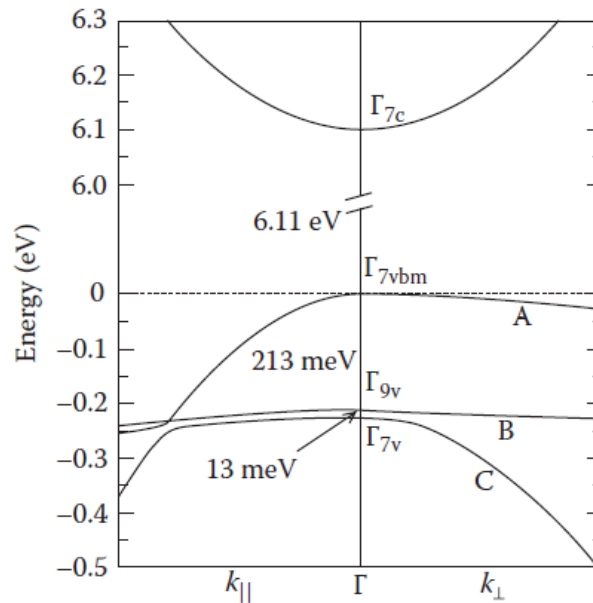
Figure 1-6 Calculated band structures of AlN with the experimentally measured energy Band-gap and exciton binding energies [74].

We have recently determined the effective band-gap of AlN ($E_{g,eff}^{AlN}$ = 6.155 eV) at room temperature (RT) from the AlN absorption edge, which matches well the classical ~6.2 eV AlN band-gap corresponding to $\Gamma_7^c \rightarrow \Gamma_9^v$ transition after deduction of the exciton binding energy [83]. Therefore the RT apparent energy band-gap of AlN can be calculated by exciton transition energy (E_A) plus binding energy of free exciton A (E_A^b):

$$E_{g,app} = E_A + E_A^b \cong 6.2 \ (300K) \qquad \text{Equation 1-3.}$$

The Varshni constants for wurtzite AlN have also been investigated by several researchers. From early researches Guo and Yoshida [68] the reported values of α = 1.799 meVK^{-1} and β = 1462 K from optical absorption and Jiang et al. [70] obtained α = 1.7 meVK^{-1} and found β = 1480 K by theoritical procedure of reflection spectra. Eventually, based on our knowledge from literature [36, 52, 64, 84, 85] the following values are recommended for Varshni parameters of wurtzite AlN: α = 2.63 meVK^{-1} and β = 2082 K.

1.1.2.3   Indium Nitride

One of the historically most contentious issues in III-nitride materials is associated to determination of the InN band gap. Despite relatively accurate values that have been accepted by scientists for energy band-gap of the GaN and AlN so far, considerable discrepancies existed for the energy band-gap of InN. For a long time it had been considered that the InN band-gap was around 1.9 eV [86, 87], but since 2002, a value in the range of about $0.6\ eV$ to $0.9\ eV$ have been proposed and then commonly accepted by scientists based on theoretical calculation and experimental data. The changes is related to production of high quality pure samples using modern crystal synthesis methods using [87-91]. Today a narrow band-gap of around 0.7 eV, has been confirmed theoretically and experimentally [81, 92, 93]. The previous observations of a wide gap are now believed to be attributed to $InN - In_2O_3$ alloying [94] and the Moss-Burstein effect where band-gap value depends on carrier concentration [95, 96]. The small value for InN gap energy was surprising, because this value is much smaller than the InP band-gap (1.35 eV), whereas the band-gap of a compound semiconductor is believed to increase with decreasing of the atomic number of the anion [97]. This finding showed the possibility of covering a wide range of spectrum from near-IR to near-UV using alloys of InN and GaN.

Guo and Yoshida [68] reported the Varshni parameters of $\alpha\ =\ 0.245\ \text{meVK}^{-1}$ and $\beta\ =\ 624$ K, (for energy band gaps of 1.994 and 1.970 eV at low- and room temperature, respectively), however Walukiewicz et al. [98] reported high quality InN grown using MBE with the Varshni parameters of $\alpha\ =\ 0.414\ \text{meVK}^{-1}$ and $\beta\ =\ 454$ K for an energy gap of 0.69 eV at low temperature. Data taken from Holtz et. al [99] ($\alpha=0.31$ meV/K and $\beta=650$ K) are used in this thesis as the reliable parameters.

For the crystal-field splitting in wurtzite InN, measurements gives values ranging from 17 to 301 meV [76, 80, 100], where a value of 40 meV is recommended in a review paper by Vurgaftman et al. [36]. Spin-orbit splitting value varying from 1 to 13 meV [76, 80] based on calculations have been proposed, but $\Delta_{SO}= 55$ meV is recommended [52].

1.1.3   Polarisation Fields

If the difference between electronegativity of two bonding elements is $\Delta\chi$, then a bond would be considered ionic if $\Delta\chi>1.7$. If $0.5<\Delta\chi<1.7$, then bond can be considered as "polar covalent". Therefore, AlN ($\Delta\chi\_AlN\cong1.5$), GaN ($\Delta\chi\_GaN\cong1.4$) and InN ($\Delta\chi\_InN\cong1.3$) are polar covalent

compounds. Polarisation fields can be considered as an intrinsic material property of wurtzite III-nitride materials, one which affects intensively LED performance. .

The polarisation fields affects the band structure of heterostructure quantum wells in III-N LEDs. This is known as the quantum confined Stark effect (QCSE). The QCSE and its impacts on the spectral stability of and efficiency of LEDs have been studied for years. Here we will give introductory information about these fields and ways to decrease these fields, like growth on semipolar facets used in this thesis and which will be discussed later.

1.1.3.1   *Spontaneous Polarisation Fields*

The wurtzite crystal form of the III-Nitride materials show spontaneous polarisation (P_{sp}) in the absence of any external electric field [101]. The orientation of the spontaneous polarisation is along the $[000\bar{1}]$ direction. The polarity of the crystal can change the orientation of the polarisation, as discussed earlier in section 1.1.1 (Ga/N polarity for GaN as an example). For the III-nitride wurtzite crystals, this spontaneous polarisation is originated from the deviation from an ideal tetrahedral coordination along the [0001] axis and the ionicity of the crystal due to the difference in electronegativity of the two elements, metal (Ga, Al, In) and nitrogen [5], therefore, each unit cell shows a non-zero dipole momentum along the $[000\bar{1}]$ orientation, as shown schematically in Figure 1-7. This polarisation field can be the values up to 0.1 *C/m²* in nitride semiconductors [102].
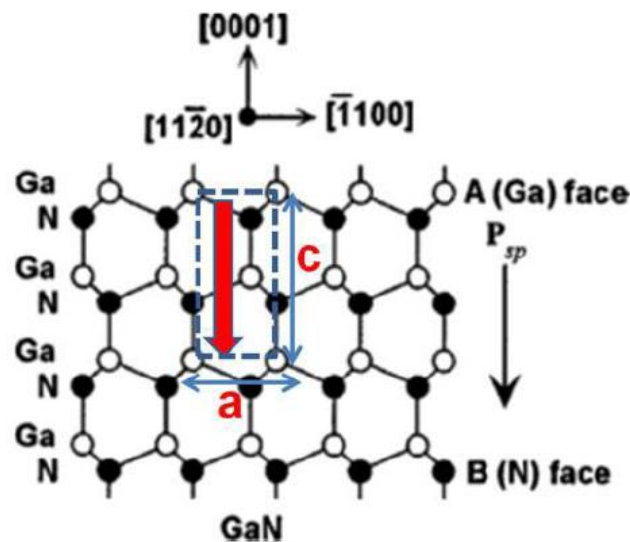
Figure 1-7 Crystal structure for GaN, with unit cell (blue dashed line), dipole moment (red arrow) and lattice parameters a and c denoted in red [7].

The ideal ratio of the lattice constants c_0 and a_0 for a hexagonal closed packed crystal(hcp) crystal with zero spontaneous polarisation can be calculated by considering identical hard spheres packed together in the hcp crystal structure, given by [7]:

$$\frac{c_0}{a_0} = (8/3)^{1/2} \cong 1.63299)$$

Equation 1-4.

For non-ideal structures the c/a ratio deviates from the ideal value, leading to spontaneous polarisation. The *c/a* ratio for the binary III-nitride compounds is shown in Table 1-1.

These lattice polarisations are electrostatically equivalent to two dimensional lattice charge densities (σ) located at the two sides of the specimen with values between 10^{13} and 10^{14} *e/cm²* [102]. Due to this macroscopic polarisation and the associated surface charges an internal electric field is induced:

$$E_{sp} = P_{sp}/\varepsilon_0(\varepsilon - 1)$$

Equation 1-5.

where ε is the dielectric constant of the material. In the case of AlN with a polarisation field of $P_{sp} = 0.09\ C/cm^2$, electric build in field would be up to 10^7 *V/cm*, equivalent to 1 *V/nm*. Spontaneous polarisation, P_{sp}, for InN and GaN are 0.042 and 0.034 *C/cm²*, respectively [102].

In the particular case of GaN, for a Ga-polar specimen (see section 1.1.1), the polarisation direction is from the surface down to the substrate, whereas the internal electric field has the opposite direction. In this case, the polarisation-induced lattice charges are positive at the substrate interface and negative at the surface. For an N-polar specimen, all directions and charges are opposite.

N-polar and Ga-polar domains can be grown simultaneously by epitaxy on the same substrate, causing a more complicated situation, called inversion domain boundaries [102], where shown schematically in Figure 1-8.
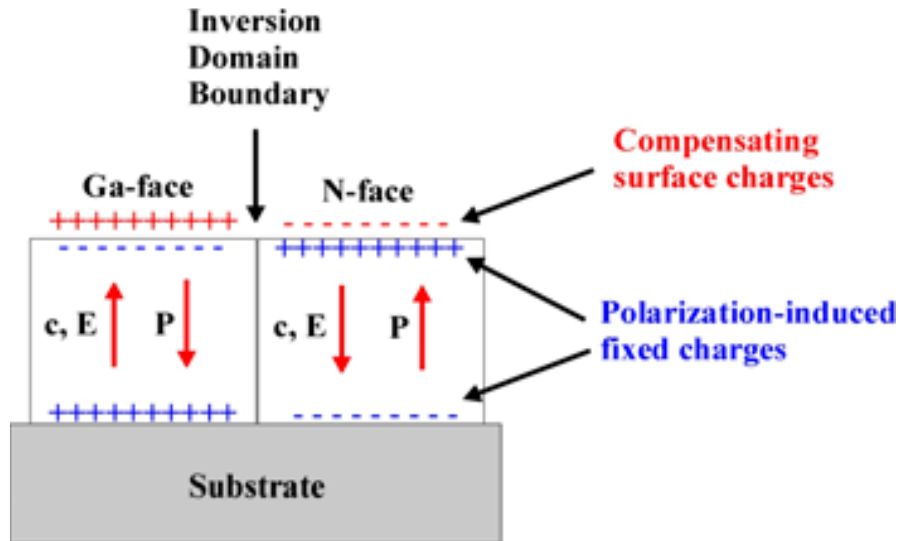
Figure 1-8 Macroscopic spontaneous polarization P_{sp} and corresponding electric field E_{sp} for Ga-polar and N-Polar GaN [102].

It has been shown that the larger the aberration from the ideal wurtzite structure, the larger the spontaneous polarisation [6]. This is more obvious for AlN which has the highest ionic character in comparison with other III-nitride binary compounds.

In addition to binary compounds, it is worth to understand the values of the spontaneous polarisation of ternary and quaternary alloys as well. For the random ternary nitride alloys, the spontaneous polarisation with respect to the composition (*x*) can be expressed by [4]:

$$P^{sp}_{Al_xGa_{1-x}N}(x) = -0.090x - 0.034(1-x) + 0.019x(1-x)$$

$$P^{sp}_{In_xGa_{1-x}N}(x) = -0.042x - 0.034(1-x) + 0.038x(1-x) \qquad \text{Equation 1-6.}$$

$$P^{sp}_{Al_xIn_{1-x}N}(x) = -0.090x - 0.042(1-x) + 0.071x(1-x)$$

The variation of spontaneous polarisation *versus* lattice constant for the III-nitrides is depicted in Figure 1-9.
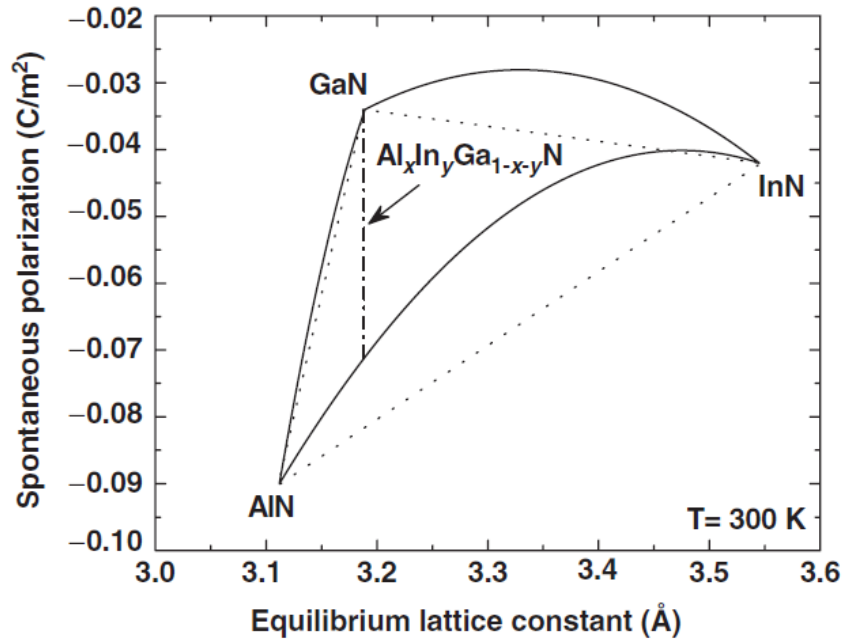
Figure 1-9 Room temperature variation of spontaneous polarization versus lattice constant for the Al$_x$In$_y$Ga$_{1-x-y}$N compounds [6].

1.1.3.2 Piezoelectric Polarisation Field

In addition to spontaneous polarisation effects, piezoelectric effects will also come across when the crystal lattice will be deformed, corresponding to the crystal anisotropy variation.

Polar crystalline materials like III-N semiconductors, exhibit a *piezoelectric* polarisation, P_{pz}, as well [101]. The piezoelectric polarisation is become critical during evaluation of III-nitride materials, as most of the III-nitride devices are hetero-epitaxially grown with a typical heterostructure, where layers are under compressive or tensile stress due to lattice mismatch [7]. Biaxial compressive stress will reduce the lattice parameter *a* and enlarge the lattice parameter *c*. This change in lattice parameters from ideal values, therefore, induces the piezoelectric polarisation in the opposite direction of spontaneous polarisation [7], see Figure 1-10.

Beside, tensile stress is decreasing the *c/a* ratio, hence piezoelectric and spontaneous polarisation would be in the same direction and as a result, the overall polarisation will be increased [6].
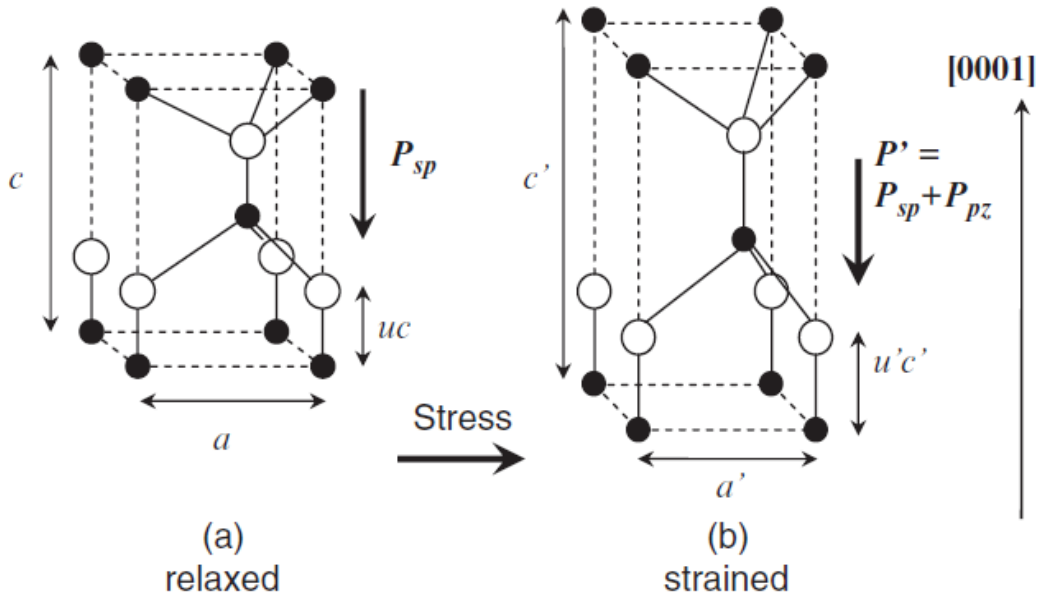
Figure 1-10 Crystal deformations due to strain induce a variation of the spontaneous polarization [6]

It has been shown that unlike the case of spontaneous polarisation, piezoelectric polarisation follows a linear function of Vegard's law for ternary III-nitride alloys [4]. As an example, the effect of the built-in electric field on electron-hole energy transition (E_{e1-hh1}) in a 5 nm thick quantum well (QW) GaN/Al$_{0.1}$Ga$_{0.9}$N heterostructure is shown schematically in Figure 1-11. In Figure 1-11a very large polarisation fields in the [0001] direction results in a quantum confined Stark effect and poor electron–hole overlap, whereas, in the non-polar [1$\bar{1}$00] direction (shown in Figure 1-11b) the polarisation field is zero, and hence a flat-band configuration is expected [103]. The fundamental transition energy in a typical heterostructure can be written as:

$$E_{e1-hh1} = E_g + e_1 + hh_1 - E_B - eF_W l_W \qquad \text{Equation 1-7.}$$

where E_g, is the band-gap of the QW, l_W is the QW thickness, e_1 and hh_1 are the confinement energies of electron and hole, respectively, e is the electronic charge, E_B is the exciton binding energy and F_W is the electric field in the QW [6]. The final term in Equation 1-7 is describing the so-called Quantum Confined Stark Effect (QCSE) which causes the transition energy E_{e1-hh1} redshift in QWs. The QCSE was initially reported for QWs by Miller et al. [104, 105].
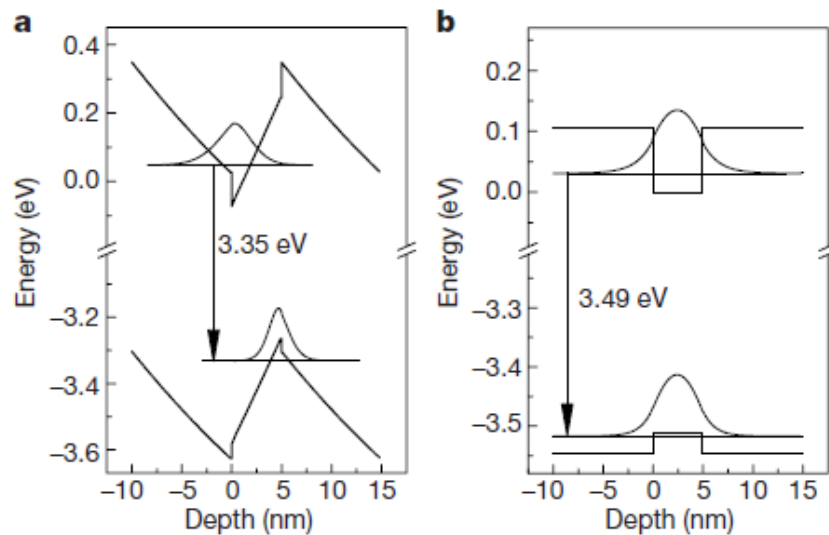
Figure 1-11 Schematic band structure of a 5nm GaN/Al$_{0.1}$Ga$_{0.9}$N QW, with (a) and without (b) built-in electric field [103].

1.1.3.3   Effects of Polarisation Fields on Optical Properties of Heterostructure III-Nitrides

In order to determine the optical transition in heterostructure semiconductors, especially in the case of simple planar QWs, several approaches have been conducted. In a special case, as described earlier in this chapter, one of the specifications of III-nitride semiconductors is the built-in electric field, oriented parallel to the c-axis originated from spontaneous and piezoelectric polarisation. This electric field can modify the electron and hole confinement potentials. If we can estimate this built-in electric field, it is possible to find the wave function and shape/position of energy levels by solving the Schrodinger equation [6, 106].

As shown in Figure 1-11, the built-in field bends the QW band diagram from a rectangular to a 'saw-tooth' shaped, causing the reduction of electron and hole wave functions overlap [7, 103].

In the case of visible InGaN/GaN LEDs, the polarisation field is dominated by contribution to the QCSE of the piezoelectric strain, due to the large lattice mismatch between GaN and InN [107, 108]. As an example polarisation charges and band structure of a 3 nm InGaN QW sandwiched between two 15 nm GaN barriers grown on both polar (0001) and nonpolar (11$\bar{2}$0) planes are depicted in Figure 1-12.

It has also been theoretically and experimentally found that in addition to nonpolar orientations, QCSE can be weakened or even eliminated by implementation of semipolar orientations [8, 9, 109-111]. It is believed that the best results can be obtained by angles between 45°–60° [110, 112]. The band-structure properties of different crystal planes can be assessed by the variation of the composition and the piezoelectric polarisation. In the case of InGaN QWs the variation of polarisation field with respect to the incline angle, θ, with reference to the c-plane at two different In compositions of 10% and 30% is depicted in Figure 1-13.
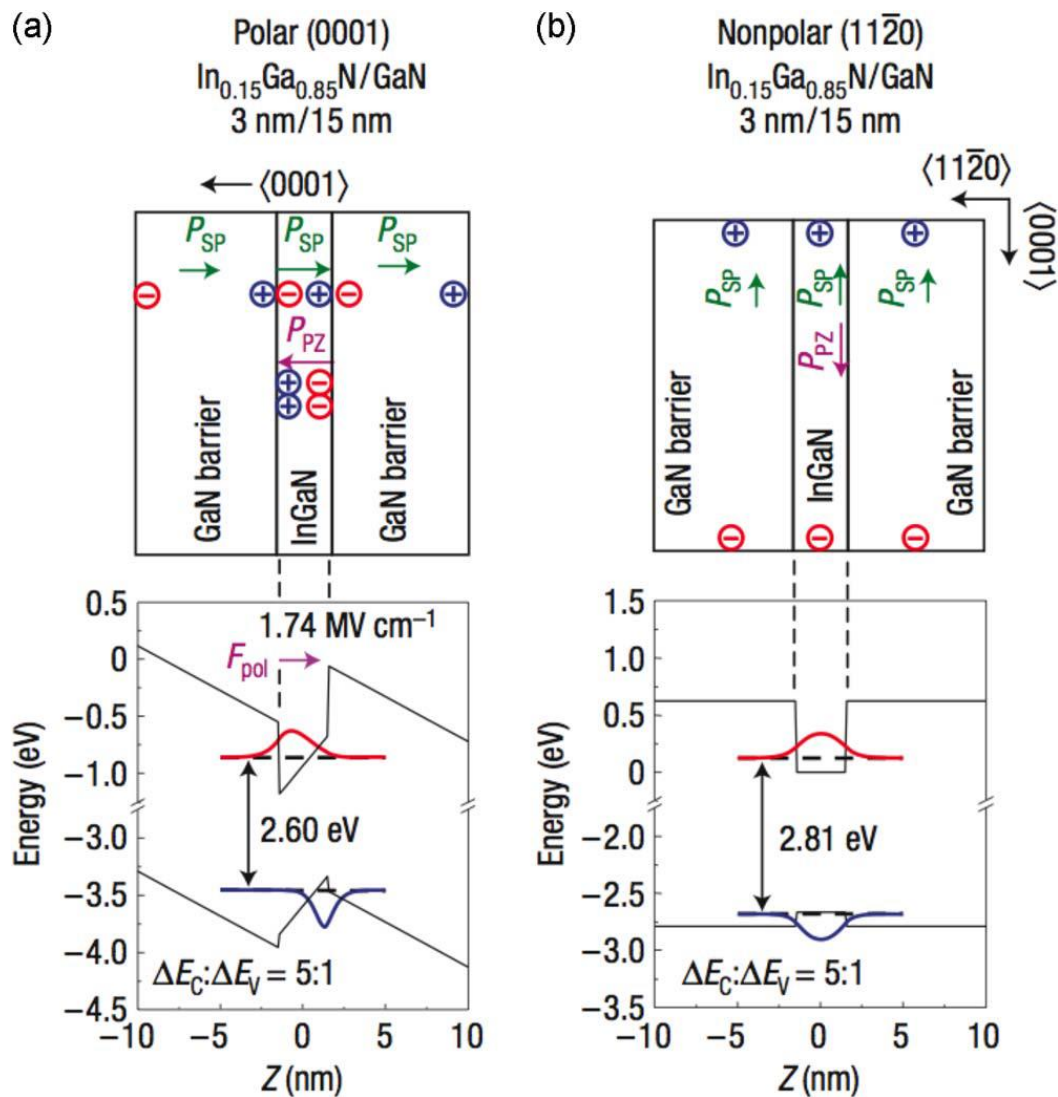
Figure 1-12 Illustration of polarisation fields and band band-structure of In$_{0.15}$Ga$_{0.85}$N/GaN QW; note the accumulation of charges at interfaces due to spontaneous polarisation (P$_{sp}$) and piezoelectric polarisation (P$_{pz}$)[7, 110].
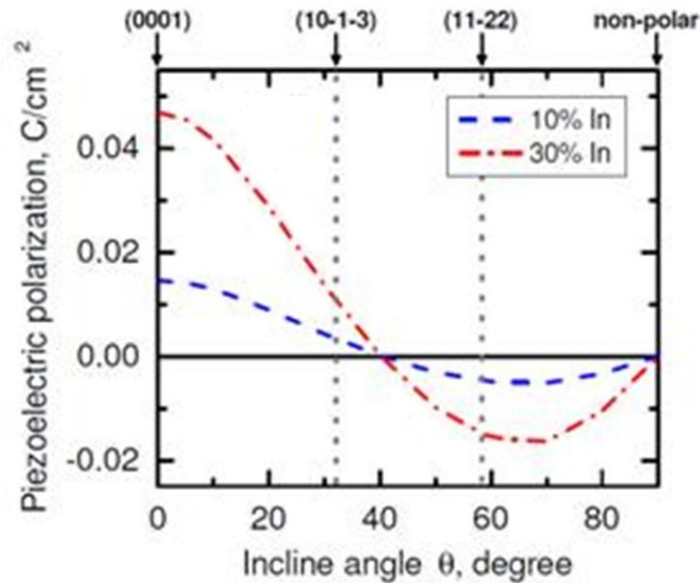
Figure 1-13 Calculated polarization charge density for In$_{0.1}$Ga$_{0.9}$N and In$_{0.3}$Ga$_{0.7}$N versus incline angle [8].

One of the techniques has been used for reduction for polarisation fields by engineering of the polarity is to grow QWs on either semipolar facets of pyramids or nonpolar facets of sidewalls of the nanostructures mostly in the shapes of nano-columns and nano-wires [113-118]. In this thesis, two different techniques are used to fabricate nano-structure materials (nano-columns and nano-pyramids) in order to reduce polarisation fields in QWs as well as reduction of defects.

1.2   III-Nitride Ternary Alloys

A simple possible prediction of the physical properties of a semiconductor alloy is to change linearly between the properties of the semiconductor at the endpoints. This is actually generally valid in the case for lattice constants with composition, to a high level of precision. This effect is expressed using the Vegard's law and has been applied to many semiconductor materials to measure alloy composition, as already discussed.

However, for long-time, it has been known that in most semiconductor materials, the band-gap of an alloy does not follow a linear Vegard's law with composition, and that some degree of deviation is observed, which is called "bowing".

1.2.1   Composition dependence of lattice parameters

Most of the basic approaches for predicting the effect of alloying on the lattice parameters of nitride semiconductors assume a linear change with composition. However, the applicability of this rule is sometimes disputed owing to the large difference in ionic sizes and iconicity of the nitride binaries. Some calculations offer small deviations from Vegard's law. For example, the values of 0.063 Å and −0.16 Å for the *a* and *c* lattice parameters were reported for wurtzite In$_x$Al$_{1-x}$N alloy [119]. Deviation parameters of 0.047 Å for the *a* and 0.117 Å for the *c* lattice constant of In$_x$Ga$_{1-x}$N are also reported [120, 121]. Also, the Vegard's law deviation parameters for Al$_x$Ga$_{1-x}$N are reported as 0.018 Å for the *a* and −0.036 Å for the *c* lattice constant, respectively [122]. Based on theoretical and experimental results, we are using the basic Vegard's law in this thesis, assuming the linear variation of lattice parameter of ternary alloys with composition:

$$a_i^{A_xB_{1-x}N}(x) = x . a_i^{AN} + (1-x) \cdot a_i^{BN} \qquad \text{Equation 1-8.}$$

where a_i is lattice parameter of crystal (*a*, *b* or *c*), A and B are indicating metals and *x* is composition.

1.2.2   Composition dependence band gap of III-nitrides

The relation between the band-gap value and alloy composition in nitrides deviates from Vegard's law (linear interpolation) and is commonly described by the so-called virtual crystal approximation (VCA):

$$E_g^{A_xB_{1-x}N}(x) = x . E_g^{AN} + (1-x) \cdot E_g^{BN} - \boldsymbol{b} \cdot x \cdot (1-x). \qquad \text{Equation 1-9.}$$

where E_g^{AN} and E_g^{BN} are representing the band-gap values for the two binary compounds with a *composition-independent* bowing parameter of $\boldsymbol{b}$. With regards to its great importance to the technology of semiconductors, the behaviour of band-gap bowing has been extensively studied. Determination of the bowing parameter $\boldsymbol{b}$ requires a detailed knowledge of sample quality, precise composition and strain condition. Since it is difficult to have all these parameters exactly, different values for bowing parameter of nitrides can be found in the literature.

For the band-gap bowing parameter of AlGaN different values have been reported in the literature. The value of 0.86 eV reported by Nam et al. [123] which covers the whole composition range, to 1.1 eV reported by Jmerik et al. [124]. There are other values of 0.91 eV, 1.0±0.3 eV and 0.9 eV

reported by Teofilove [125], Koide et al. [126], and Buchheim et al.[127], respectively. The values for bowing parameter of AlGaN are in reasonably similar range. The main difference is that Buchheim et al. took conduction/valence band crossing into account (at a value of 53% Al content). In 2011 Plea et al. using first-principles calculations based on the density functional theory reported the value of 0.8 eV [128]. A more recent experiment done by Neuschl et al. [129] took into account the sample strain and its effect on the composition dependence of the valence band crossing and crystal field bowing where the bowing parameters of 0.85 eV for the energy gap between the conduction and the valence band with Γ_9 symmetry as well as the value of -0.12 eV for crystal field bowing, were found. More recently Coughlan et al. recommended the value of $b = 0.94$ eV, using an atomistic tight-binding model and in good agreement with experimental data, in which the band edge bowing parameters of CB and VB are $b^{CB} = 0.78$eV and $b^{CB} = -0.16$ eV, respectively [130].

The diversity of the values reported for b for indium containing III-nitride ternary alloys ($In_xGa_{1-x}N$ and $In_xAl_{1-x}N$), are higher. This scattering is due to the low material quality for the long time as well as the wrong estimation of the InN band-gap, as described in 1.1.2.3.

Along with material quality and wrong value of the InN band-gap, these discrepancies are probably due to two further reasons; first due to strain in such layers (shown already by Parker et al. and Ponce et al. [131, 132]), and the second reason for this variation of values for bowing parameter could be related to techniques used to measure the band-gap energy. It is known that the band-gap energy determined from either photoluminescence (PL) or cathodoluminescence (CL) are the subject to the effect of Stokes shifting to the band-gap energy as compared to methods such as optical absorption, reflection or transmission. This shifting gives rise to an underestimation of the band-gap energy for a known composition [132-135].

Similar to AlGaN, the energy band-gap of $In_xGa_{1-x}N$ through $0 \leq x \leq 1$ can be expressed by the empirical expression of Equation 1-9, although, phase separation with clustering of In-rich regions makes the determination of InGaN alloy even potentially harder [36, 136].

Since the acceptance of new and small value for the gap of InN, the earlier band-gap data for $In_xGa_{1-x}N$ were no longer reliable, therefore re-evaluation of the other material parameters (e.g., the bowing parameter) was essential.

The recent growth of high-quality materials helped to determine reliably the bowing parameter over the whole compositional range, especially for large x. Wu et al. report a value of ~1.4 eV using PL emission from localised indium-rich regions, associated with absorption band edge [134].

However, since then large disparities were observed for **b** fluctuating in the range 1.4 eV–3.0 eV [128, 133, 134, 137-140]. The effect of strain on bowing parameter in InGaN layers were already shown by Parker et al. and Ponce et al. [131, 132] and also proved later by Orsal and colleagues which led to values of 2.87 eV and 1.32 eV for relaxed and compressively strained layers, respectively [141]. The effect of polarisation on bowing parameter of InGaN alloy was also evaluated by Gedam et. al [142]. Generally speaking, the bowing parameter depends on composition, but the experimental information is clearly not enough to address this for InGaN alloy [139]. In this thesis a fixed value of b=2.0 eV [139] is used for the bowing parameter, a based on a blend of the available experimental data.

Another special point of attention about InGaN band-gap is about temperature variation of band-gap which is expected to follow the well-known Varshni's equation (Equation 1-2.), but, due to indium compositional fluctuation and phase separation, an "S-shape" temperature dependence of the band-gap was reported for InGaN alloy for low indium contents [143-145].

A very wide variety of values has been reported in the literature so far for the bowing parameter of $In_xAl_{1-x}N$ alloy. Again the large diversity in the reported bowing parameters may be related to a number of factors, such as poor sample quality, a limited composition range and the techniques used to measure both the compositions and the band gaps of the alloys and for early studies mostly due to wrong estimation of InN [36, 83, 146].

Early studies from experimental investigation of sputtered InAlN film showing the strong band gap bowing which showed even smaller energy gap of InAlN for the lattice-matched alloy than for GaN [36, 147]. Guo et al. [148] reported the incorrect value for InN-rich AlInN, because of the wrong estimation of InN band-gap. Kim et al. [149] found a bowing parameter of above 2.5 eV. For Al-rich InAlN, on the other side, Peng et al. [150] suggested a cubic expression for the energy gap that fitted experimental values. A strong bowing parameter over the wide range of composition was also reported by Lukitsch et al. [151], but still using overestimated the energy gap for InN.

On the theoretical point of view, a calculation for zinc-blende InAlN by Wright et. al [136] gave a value of 2.53 eV for bowing parameter, assuming that is similar to the wurtzite alloy. A calculation

by Goano et. al [152] for wurtzite InAlN yielded a value of 2.38 eV, while other researchers reported the values in the range of 2.20–4.67 eV [153].

The reported experimental band-gap bowing parameter of InAlN values are scattered from 2.5 eV to 10 eV for high to low indium content [36, 149, 154, 155]. Therefore, concept of a composition independent b has been considered by several groups [156, 157]. It has actually been shown theoretically [153, 158], [146] and demonstrated experimentally [146, 157, 159] that it is a composition dependent parameter.

Vurgaftman et. al. [160] suggested the formula of $b = 16 - 9.1x$ for the bowing parameter of InAlN alloy, but with the incorrect value of 1.9 eV accepted as the InN band gap. Also, Iliopoulos et. al [159] suggested an empirical formula for composition dependent bowing parameter of InAlN by fitting the experimental data:

$$b^{In_xAl_{1-x}N}(x) = \frac{15.3}{1 + 4.8 * x} \qquad \text{Equation 1-10.}$$

Later, Sakalauskas et al. modified the Iliopoulos formula and proposed the new empirical equation for composition dependent InAlN alloy on GaN as below:

$$b^{In_xAl_{1-x}N}(x) = \frac{A}{1 + C * x^2} \qquad \text{Equation 1-11.}$$

where A and C are constants obtained by fitting with the values of 9.31 ± 0.48 eV and 1.71 ± 0.34 eV respectively [Sakalauskas 2010].

It is clear that challenges that still remaining are the exact value of the bowing parameter and also band-gap for the whole composition range, especially for low indium content, $x < 0.10$, and the most interesting region in terms of technology, which is $In_xAl_{1-x}N$ lattice matched to GaN, $x \approx 0.18$.

In order to find out the source of the composition dependent bowing in InGaN and InAlN, M. Ferhat and F. Bechstedt [153] have suggested the contributions of three elements: volume deformation (b_{vd}), different atomic electro-negativities and structural relaxation. They noticed that the b_{vd} of InGaN and especially for InAlN is large. This could be related to the large lattice mismatch of the corresponding

binary compounds (around 14 % between InN and AlN and around 10 % between InN and GaN). Therefore volume deformation affects the bond lengths, inducing disorder and controlling composition dependence band-gap bowing. Also, the different electro-negativities of InAlN atoms is high and scales up with the electronegativity mismatch between In and Al [161].

To design InAlN-based optoelectronic devices operating in the UV spectral range, a knowledge of the variation of the band gap with alloy composition, especially in the low In content regime, is critical. For example this spectral region, there is a potential for InAlN/Al(Ga)N Bragg reflectors to be used in the solar blind detectors [162]. Despite the interest in InAlN alloys the band-gap variation with composition has not yet been determined unambiguously across the entire composition range, with a fairly large spread in the reported experimental values even for the most studied and technologically important composition range close to lattice match to GaN [146, 159]. In addition to the predicted composition immiscibility [163], a further uncertainty relates to the recently reported role of Ga auto-incorporation [164, 165] which, depending on reactor design, can occur in InAlN grown by metalorganic vapour phase epitaxy if no special efforts are undertaken to suppress it. In spite of the scatter of experimental data, it is clear that the virtual crystal approximation [166] fails for $In_xAl_{1-x}N$ which, unlike AlGaN or InGaN, cannot be described with a single composition-independent band-gap bowing parameter. It was shown both experimentally [157, 159] and theoretically [146, 153, 158] that the bowing parameter is instead strongly composition-dependent, varying from around 3 eV for high indium contents ($x > 0.8$) to presumably more than 10 eV for $x < 0.1$.

In addition to the band gap variation, the light polarisation characteristic of InAlN-based devices is important, since light extraction efficiencies of the device are significantly affected by this property [167]. The light polarisation characteristic is related to the valence band ordering in the InAlN material; in Al-rich InAlN systems, a transverse magnetic (TM) optical emission is expected. In this case, the emitted light is polarised along the wurtzite c-axis. With increasing In content, due to changes in the valence band structure, the emission switches to be transverse electric (TE). For surface emitting light emitting diodes, TE polarisation is vital for high light extraction efficiency, and therefore for device design, the information on this crossover is important. Recently, it has been shown theoretically [146] that in InAlN it might appear at much lower In contents than expected from a linear interpolation of the valence band parameters. However, to analyse this experimentally, low In content InAlN has to be studied.

Nonetheless, research and understanding deeply of bowing parameter is still in an early stage with limited knowledge and needs more studies. Here in this thesis, I will show the results for low indium content $In_xAl_{1-x}N$ and combine them together with other reports in the literature.

The variation of room temperature band-gap energy of III–nitride semiconductors as a function of the lattice constant is plotted and shown in Figure 1-14.
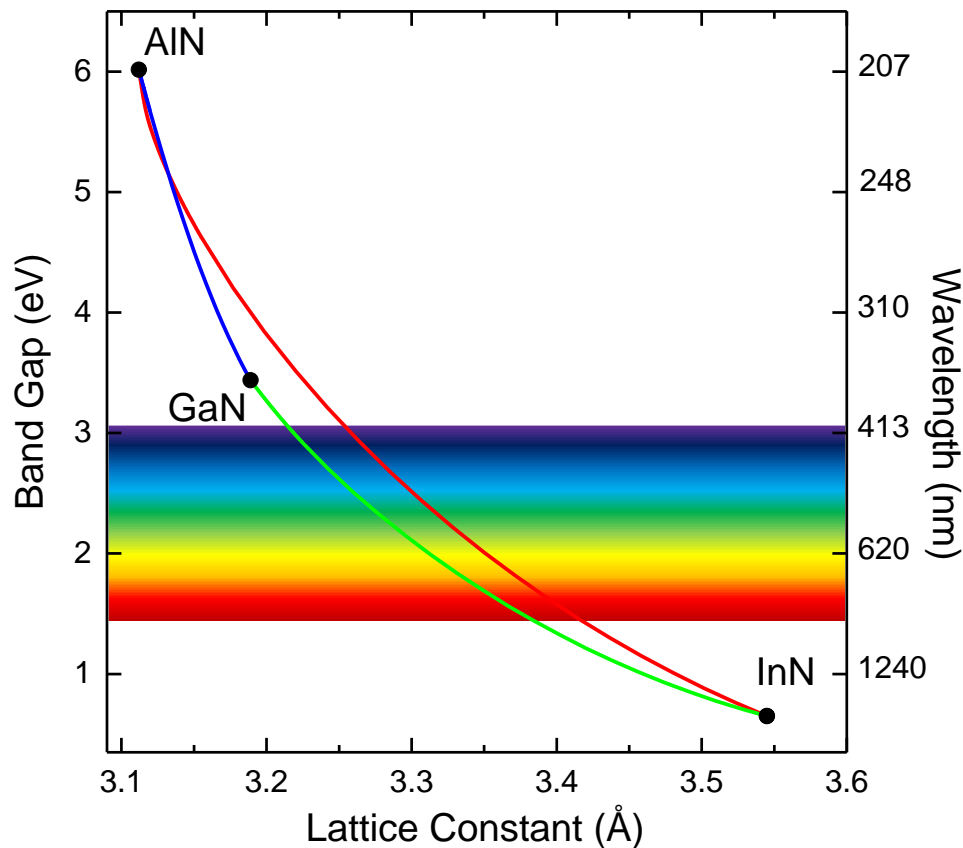
Figure 1-14 RT band-gap energy and lattice constant of III–nitride binary and ternary alloys

1.2.3 Band Anticrossing (BAC) Model

In highly mismatched alloys (HMAs), like InAlN, when the anion is replaced by an isoelectric and highly dissimilar impurity (in terms of size and electronegativity), this results a localised defect potential which is very spatially localised, but broad in k-space. Therefore, these localised states interact with different bands in Brillion zone directions, as a consequence changing the properties of the host material. The band structure of HMAs can be explained by a BAC model [168] which makes

it possible to explain composition dependence of band-gap. In the conduction band, interaction of the localised state with extended states leads to splitting of the matrix band into two high and low non-parabolic bands, E+ and E- respectively. This behaviour is shown by way of example for the conduction band splitting of $Ga_{0.995}AsN_{0.005}$ in Figure 1-15. In the InAlN alloy with low InN fractions, it is assumed that In atoms/clusters are acting as isoelectric resonant defects/impurities, which are randomly distributed and weakly coupled with the host material (AlN). Therefore the variation of the Conduction Band Energy (CBE) with composition x can be treated with the BAC model by solving the 2×2 Hamiltonian and get the lower eigenvalue of this determinant [35, 36]:

$$\begin{vmatrix} E_M(k,x) - E(k,x) & V_{MD} \\ V_{MD} & E_D(x) - E(k,x) \end{vmatrix} = 0 \qquad \text{Equation 1-12.}$$

where $E(k,x)$ is the dispersion relation of the perturbed system. $E_M(k,x)$ is the energy level associated with the unperturbed extended conduction band edge states of the (In)AlN matrix which varied with the composition based on virtual crystal approximation (VCA) and $E_D(x)$ is the dispersion energy associated with the localised defect states. These two states linked by a matrix element $V_{MD} = \langle k|V|D \rangle$ describing the interaction between the extended host material and the localised defect states.

Eventually, the solution to the Equation 1-12 can be written as below:

$$E_{\pm}(k,x) = \frac{E_M(k,x)+E_D}{2} \pm \sqrt{\left(\frac{E_M(k,x)-E_D}{2}\right)^2 + V_{MD}^2} \qquad \text{Equation 1-13.}$$

Based on the assumption that defect states are randomly distributed and their concentration is low enough not to have significant wave-function overlap, the V_{MD} matrix can be written as $\beta \cdot x^{1/2}$, where β is an empirically determined constant describing the coupling between localised states and the extended states of the matrix and x is the alloy composition.

Here we assume that $E_D(x) = E_{In}(0) - \gamma x$, to reflect the increasing In atoms/composition with x. Likewise, the CBE varies based on the VCA, $E_M(k,x) = E_{AlN}(0) - \alpha x$. Here $E_{AlN}(0)$ is the conduction band edge energy in AlN, and E_{In}

In this case, $E_-(k)$ becomes the position of the new, dispersion related, conduction band which defines the band-gap. This causes the gap to be smaller than otherwise expected in this low

composition situation, which can be seen in Figure 1-15. This leads large band-gap shrinkage observed for low InN content InAlN. To visualise and understand better the BAC model, as an example, the conduction band structure and splitting of $GaAs_{0.995}N_{0.005}$ is shown in Figure 1-15.
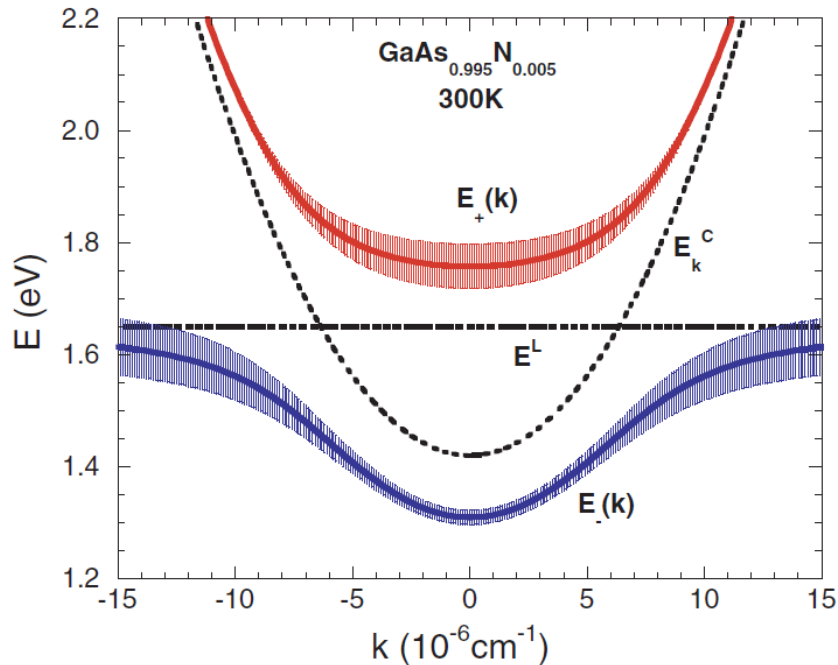
Figure 1-15 Conduction band restructuring for GaAs$_{0.995}$N$_{0.005}$. Solid lines show the CB dispersion). Dotted line: host matrix CB dispersion; dashed line: N resonant defect energy level[169].

1.3   Optical Processes in Nitride Semiconductors

Light emission is the one of the most interesting processes in semiconductors, especially in direct band-gap semiconductors, which was revolutionised optoelectronics in the last decades. Light emission can happen through electrical injection, when electrons and holes are injected into the active region of a device (e.g. quantum wells) by application of an external voltage to the p-n junction. This recombination of the carriers results in the emission of a photon with the energy equal to energy difference between states occupied by electrons and holes. In indirect band-gap semiconductors, phonons are predominantly generated, causing inefficient light emitters unless there is a high degree of carrier localisation, (which delocalise the carriers in k-space allowing momentum conservation). Another way to observe light emission is photoluminescence (PL). The incident photons, after being absorbed by media, excite electrons from the valence band to the conduction band. Before recombining across the band-gap, the electrons and holes, drop to the bottom of their corresponding

bands via thermalisation which results in phonon emission. Carriers at the band edges then can recombine either between bands or mediated through defects, to give luminescence. In fact, not all recombinations lead to photon emission. A recombination process leading to photon emission is called *radiative recombination*. Those recombination which do not generate photons are called *non-radiative recombination*, where the energy is transferred to the lattice via phonons and heat the material. Finally, light emission can also be happened by increasing the temperature of the semiconductor, which is known as thermo-luminescence.

1.3.1   Absorption and Emission

Spectroscopy can be applied to get useful information about a particular semiconductor, notably direct band-gap semiconductors, for their application in optoelectronics. The fact that most of the III-nitride light emitting materials are grown on sapphire substrates which is transparent for visible light, lets scientists perform absorption measurements without removing the substrate.

Let's consider the absorption coefficient. If $I(v)$ indicates the optical intensity of the incident light, the spatial intensity change of the incident light is proportional to the incident intensity, which is given by:

$$\frac{dI(v)}{dx} = -\alpha I(v)$$

Equation 1-14.

where α is the absorption coefficient. III-nitride semiconductors typically have large absorption coefficients at near band edge with values in of around $10^5 \; cm^{-1}$, hence a large fraction of the incident light is absorbed near the surface of the material, at the range of few hundred nanometres [170]. For a direct band-gap semiconductor, if a parabolic band structure is assumed (see Figure 1-5), the optical absorption near the band-gap is given by the square root law:

$$\alpha_0(E) = C\sqrt{E - E_g} \qquad \left(E \geq E_g\right)$$
$$\alpha_0(E) = 0 \qquad (E < E_g)$$

Equation 1-15.

where $E = \hbar\omega$ is the energy of incident photon, E_g is the energy band-gap and C is a constant depending on material properties [171, 172]. As discussed in section 1.1.2, considering the contribution of the light and heavy hole bands associated with the absorption, the near-band-edge optical absorption (assuming no band split)can be rewritten (to the first approximation) as below:

$$\alpha_0(E) = C_{hh}\sqrt{E - E_g} + C_{lh}\sqrt{E - E_g} \qquad \left(E \geq E_g\right)$$
$$\alpha_0(E) = 0 \qquad (E < E_g)$$

Equation 1-16.

where C_{hh} and C_{lh} are associated with heavy and light holes, respectively.

If semiconductor is excited with a light source (or other type of excitation source) filling of the bands happens. During filling of a band with carriers, there is a probability of CB occupation by an electron and/or a probability of VB being empty. If considering E_a as the energy in the valence band and E_b as the energy in the conduction band, the absorption coefficient of an excited semiconductor can be given by [172, 173]:

$$\alpha(N, P, E) = \alpha_0(E)[f_v(E_a) - f_c(E_b)]$$ Equation 1-17.

where N and P are the concentrations of free electrons and holes, respectively, α_0 indicates the absorption of the material, $f_v(E_a)$ is the probability of occupation of a valence band state with energy E_a and $f_c(E_b)$ is the probability of occupation of a conduction band state with energy E_b.

Excitons are very important in III-N materials, especially in GaN. InGaN excitons can have large binding energy, allowing them to be able to survive at RT. As aforementioned, the three valence bands in wurtzite crystal structure of III-Ns, allows three exciton transitions. Exciton peaks can be shifted or broadened by strain, impurities, phonon coupling, etc. They may also affect the optical coefficients near band-gap and shift/broaden the absorption band-edge. Because of phonon coupling the A and B exitons overlap at RT, while the C exciton appears as a change in absorption coefficient slope [148]. The absorption coefficient change with photon energy, is shown for a GaN layer grown on sapphire in Figure 1-16. Jayaprakash et. al showed that it is also varying with temperature [174].
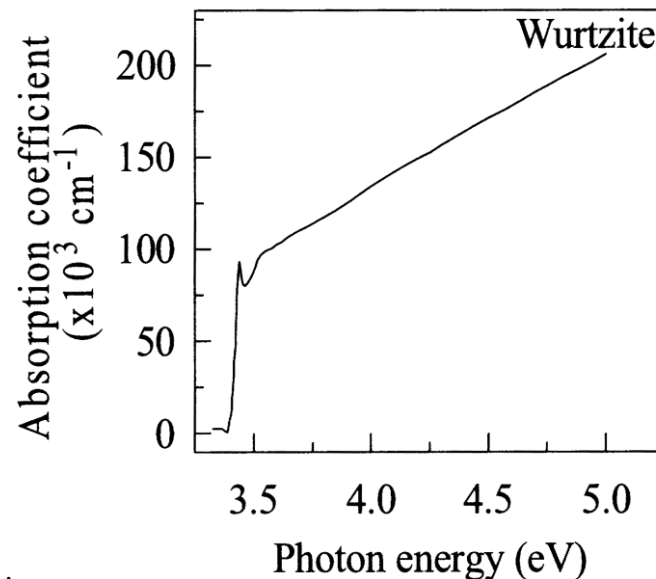

Figure 1-16 The room temperature absorption coefficient versus photon energy for wurtzite GaN grown on sapphire [170].

1.3.2 Band-to-Band Transitions

When the material is excited and excess carriers are introduced to a direct-band-gap semiconductor, as occurs in electroluminescent devices such as LEDs and lasers, the probability of direct recombination of electrons and holes is high. This is because at the top of the valence band and the bottom of the conduction band momentum is equal and no additional momentum is required for the transition across the band. The rate of the direct recombination R is proportional to the number of carriers available in the conduction and the valence band:

$$R = \beta n \cdot p$$

Equation 1-18.

where β is the probability of radiative recombination. The units of R and β are $cm^{-3}s^{-1}$ and $cm^{3}s^{-1}$ respectively. The average lifetime of carriers before radiative recombination is called the radiative lifetime (τ_t). In thermal equilibrium the recombination rate is balanced by the generation rate, in this case, the minority carrier radiative lifetime, τ_r, to depict the recombination process, this is actually the time that takes for an extra minority carrier to be recombined radiatively by the majority holes [173, 175].

In addition to the radiative recombination, there is the non-radiative process in semiconductors because of defects and imperfections which act as non-radiative centres. For a semiconductor containing non-radiative centres, which is normally the case, in time-resolved PL (TRPL), the decay rate can be expressed as [175]:

$$\frac{1}{\tau_t} = \frac{1}{\tau_r} + \frac{1}{\tau_{nr}}$$

Equation 1-19.

In a PL spectroscopy, the emission spectrum is determined by the density of states $\propto (h\nu - E_g)^{1/2}$ and the probability of occupying states being available for recombination, $\propto e^{-E/kT} = e^{-h\nu/kT}$, therefore the total lineshape for exciting energies bigger than band-gap would be in the form of [176]:

$$(h\nu - E_g)^{1/2} \cdot e^{-h\nu/kT}$$

Equation 1-20.

1.3.3   Indirect Recombination

For indirect-Band-gap semiconductors, like silicon, it is very unlikely to have direct recombination, because the momentum between the electrons at the bottom of the conduction band and the holes at the top of the valence band is nonzero. Therefore without lattice interaction, the direct transition which conserves energy and momentum together is not possible. Hence, indirect transition via localised energy states in the forbidden energy gap would be the dominant recombination process in such materials [173].

1.3.4   Excitonic Transitions

Wide-band-gap semiconductors such as GaN have large exciton binding energies of around 20 meV with an exciton Bohr radius of about 28 Å [38]. Also, in QWs the exciton binding energy increases which make excitons even more important in these structures [177]. Therefore, whether or not these excitons are involved in the radiative recombination process in these semiconductors is an interesting question.

Optical transitions in semiconductors, can be divided into two classes: *intrinsic transitions* and *extrinsic transitions.* Intrinsic transitions are associated with material free from impurities and defects. Free excitons and their phonon replicas, and free to free transitions are examples of such intrinsic transitions. Extrinsic transitions, on the other hand, originate from impurities and defects. The transitions such as free-to-bound and bound-to-bound associated with impurities and defects are representing extrinsic transitions. Schematic views of some intrinsic and extrinsic transitions are depicted in Figure 1-17.

Excitons are generally categorised into free and bound excitons. With regards to the band structure of III-nitride semiconductors, there are three free excitons. The bound excitons can be bound to structural defects shallow and deep donors, as shown schematically in Figure 1-18, as an example. When an exciton bound to a neutral acceptor (A^0), the associated PL emission line is labelled as A^0X transition. A free exciton can also be bounded to a neutral donor (D^0), and corresponding PL emission lines is named D^0X transitions. Also, an example of bound to-bound transition is donor–acceptor pair (DAP) transition.
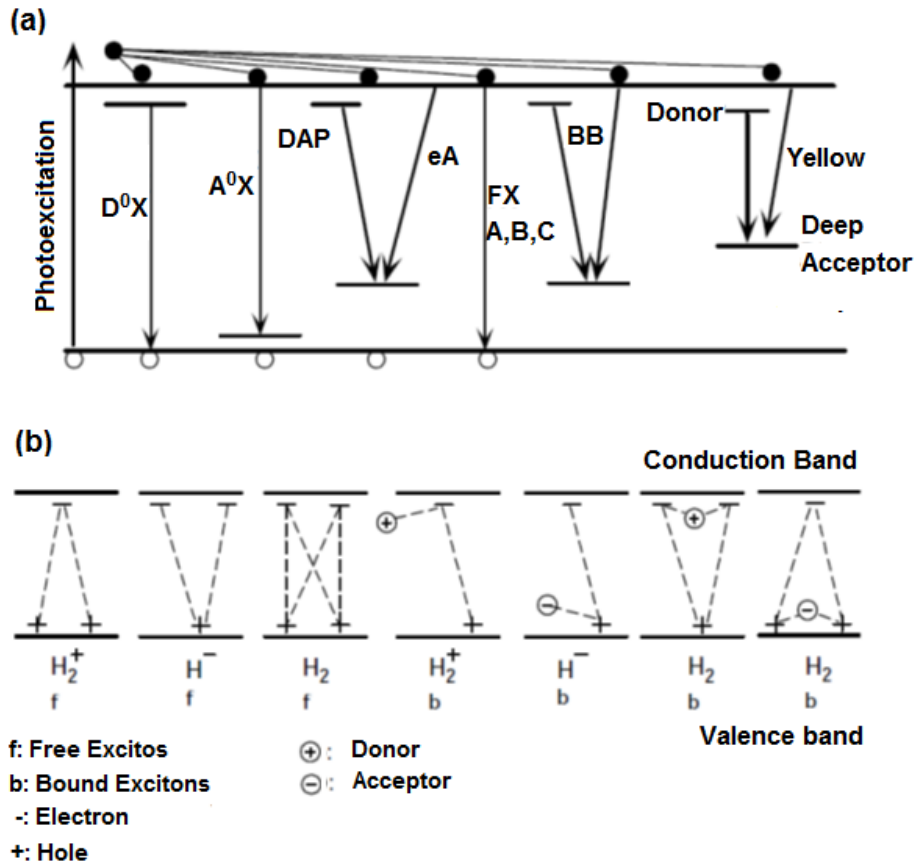
Figure 1-17 (a) Intrinsic and extrinsic optical transitions in GaN. (b) Different free and bound exciton complexes that can form in a semiconductor [175]

The band splitting related free exciton transitions from the CB to these three VBs are called A, B, and C excitons, where A is associated with $\Gamma_7^c \rightarrow \Gamma_9^v$ (heavy hole state) transition, B with $\Gamma_7^c \rightarrow \Gamma_{7+}^v$ (heavy hole state) and C with $\Gamma_7^c \rightarrow \Gamma_{7-}^c$ (light hole state), see Figure 1-5 for re valence band states. In ideal strain free Wurtzite crystals, in α polarisation which $\mathbf{E}\perp c$ and $\mathbf{k}\|c$, excitons related to all three bands are allowed. In the σ polarisation ($\mathbf{E}\perp c$ and $\mathbf{k}\perp c$), A and B excitons can be observed but the C exciton is very weak. In the π polarisation where $\mathbf{E}\|c$ and $\mathbf{k}\perp c$, A exciton is forbidden, B exciton is weak and C exciton is strong. Here $\mathbf{E}$ and $\mathbf{K}$ are the electric field and momentum vectors, respectively and c shows the c-axis of the crystal. These excitonic transitions are summarised in Table 1-2.
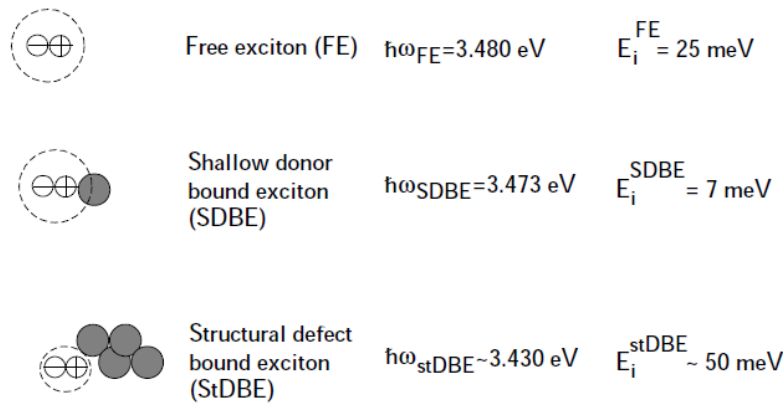
Figure 1-18 Free and bound excitons and their binding energies in GaN[175].

Table 1-2 Excitonic transitions in GaN [175].

Polarisation	A exciton	B exciton	C exciton
α polarisation (**E**⊥c and **k**∥c)	Allowed	Allowed	Allowed
σ polarisation (**E**⊥c and **k**⊥c)	Allowed	Allowed	Weak
π polarisation (**E**∥c and **k**⊥c)	Forbidden	Weak	Strong

It is accepted that the ordering of the valence bands in AlN is different from GaN due to its negative crystal field (Δ_{CF}). The valence bands transition energy in AlN would be $\Gamma_{7vbm}^{v} \rightarrow \Gamma_{9}^{v} \rightarrow \Gamma_{7}^{v}$ in the order of increasing emission energy, associated with A, B and C excitons, whereas in GaN, the order is $\Gamma_{9vbm}^{v} \rightarrow \Gamma_{7+}^{v} \rightarrow \Gamma_{7-}^{v}$, respectively as shown schematically in Figure 1-19 [73, 178, 179]. The difference in the ordering of the three valence bands would result in different optical properties for AlN, compared to those of GaN and InN, and leads to a difference in the polarisation properties of emitted light from AlN, GaN and InN [180], notably polarisation switch in their alloys with composition [130].
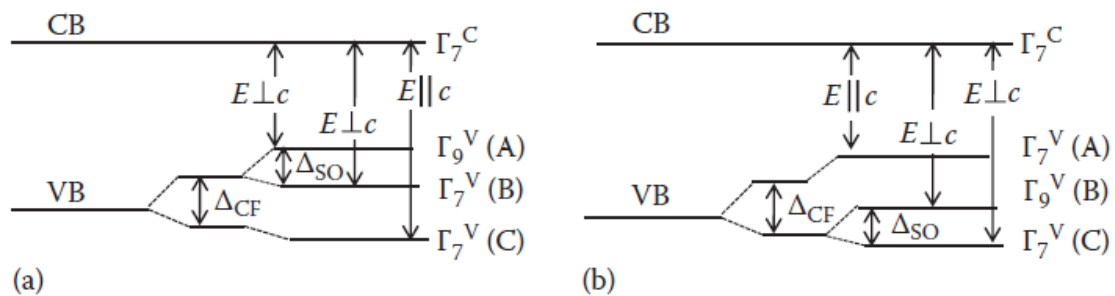
Figure 1-19 (a) Schematic diagram of the crystal-field and spin-orbit splitting of the valence bands of (a) GaN and (b) AlN [179].
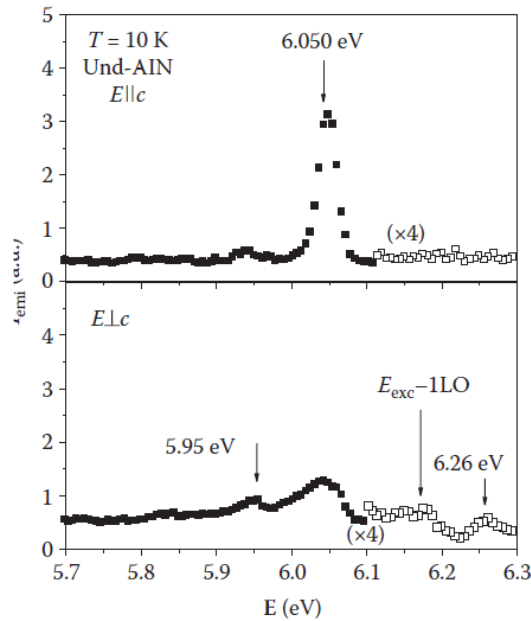
Figure 1-20 Low temperature polarization resolved PL spectra of AlN epilayer with E∥c and E⊥c

[178].

It has been shown that for **E**⊥c, the recombination between electrons in the conduction band and the A valence band (Γ^v_{7vbm}) is almost forbidden, whereas, for **E**∥c, the recombination between the electrons and holes in the B and C valence bands are prohibited [178]. As shown in Figure 1-20, polarisation-resolved PL spectra of AlN epilayers grown on c-plane sapphire measured by Sedhain et al. [181] two emission peaks at 6.05 eV associated with A-exciton and 6.26 eV observed, where the lower energy is polarised in **E**∥c and higher energy is polarised in E⊥c direction.Low-temperature transmission spectra, optical reflectivity and cathodoluminescence (CL) of bulk single crystal AlN in the near band edge emission areas are shown in Figure 1-21. All three different optical measurements are similarly showing the free A-excitonic (FX$_A$) at around 6.030 eV, consistence with the observed results from AlN homo-epilayer (see section 2.1) by PL spectroscopy [182]. A small difference between this values for FX$_A$ from what was shown previously in Figure 1-20 is due to the different layers grown on different substrates which causes the deviation in values of stresses. Assuming the bonding energy of FX$_A$ to be 50–70 meV [183], low temperature fundamental band-gap of strain-free AlN is given to be $\sim$6.09 $\pm$ 0.01 eV.

Due to the compressive strain in the AlN epilayer grown on sapphire substrate, the energy gap of AlN at 10 K is determined to be about 20 meV higher than that of strain-free AlN bulk, therefore the value of ~6.11 ($\pm$0.01) eV was given [178].
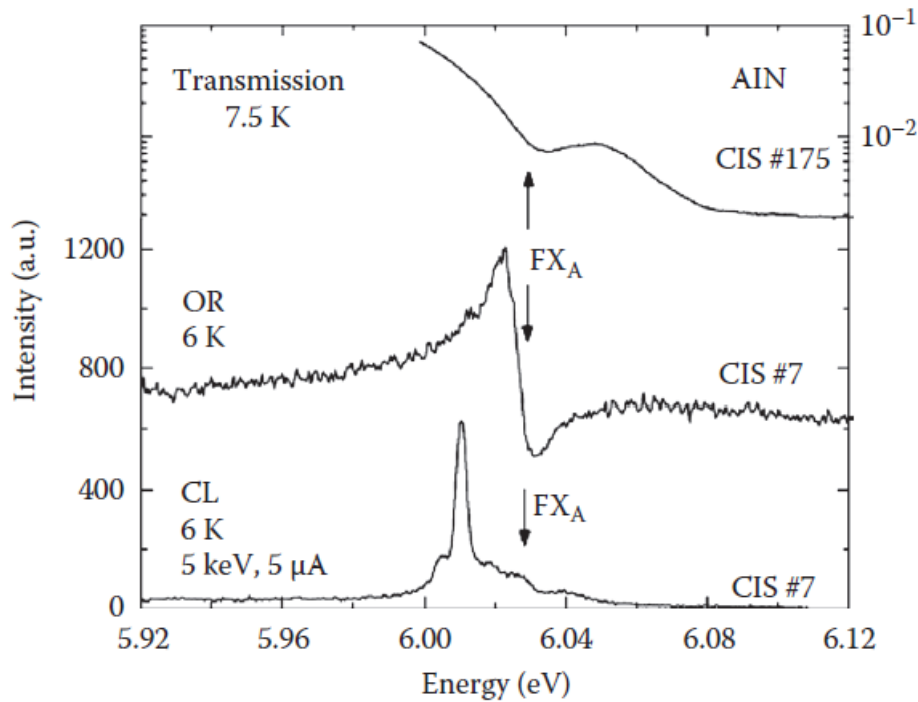
Figure 1-21 Low-temperature cathodoluminescence (CL), optical reflectivity (OR), and transmission spectra of AlN bulk crystals in the near band edge energy range [178].

1.3.5   Effect of Temperature

The variation of the band-gap of binary compounds with temperature is given by Equation 1-2, assuming no localisation. In the case of III-nitride ternary and quaternary alloys, in most cases localisation exists (also known as band-tail effects). This is particularly obvious in InGaN [184-186] and InAlN [108, 187, 188] alloys. As a result the variation of the emission energy of material would deviate from the Equation 1-2. Assuming the Gaussian-like distribution of the density of states for the valence and conduction bands and using the band-tail model, the temperature-dependent emission energy is expressed by the following equation [175]:

$$E_g(T) = E_g(0) - \frac{\alpha T^2}{\beta + T} - \frac{\sigma^2}{kT} \qquad \text{Equation 1-21.}$$

where the last term represents the localisation and σ indicating the band-tailing or the extent of localisation [175].

1.3.6   Quantum Efficiency

The fraction of electron–hole pairs recombining radiatively within the active region is defined as internal quantum efficiency. Some of the carriers recombine non-radiatively (i. e in defect states). When a defect and its associated trap is located nearly to the middle of the band-gap and energy of defects is about $\frac{E_g}{2}$, the corresponding recombination process is called the *Shockley–Read–Hall* (SRH) process [175]. *Auger* process is another form of non-radiative recombination. In the Auger process, the energy of released from band to band recombination, excites another carrier (electron) to higher energy, which then emits phonons to thermalise and return to the band-edge. Another process, is carrier escape from the active region where recombination occurs outside the active region, usually non-radiatively. This last process can be more dominant and is referred to as carrier leakage [175]. In Figure 1-22 three non-radiative recombination and radiative recombination mechanisms in an InGaN/GaN LED structure are shown schematically.
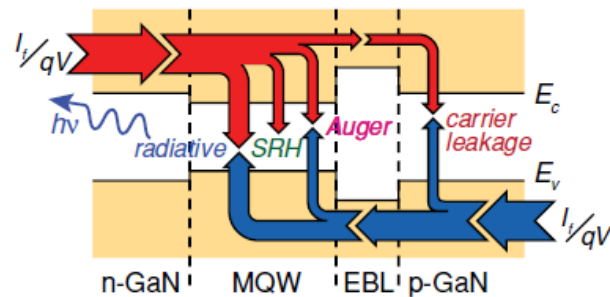
Figure 1-22 Schematic illustration of the three non-radiative recombination and the radiative recombination channels in an InGaN/GaN LED structure.[189].

At high injection levels where carrier leakage is neglected (assuming the excess carrier concentrations dominate), the total recombination rate can be expressed as:

$$R = An + Bn^2 + Cn^3$$
<div align="right">Equation 1-22.</div>

It is a simple, so-called ABC model with few assumptions; neglecting the carrier leakage from the active region and an equal concentration of electron (*n*) and holes (*p*). Here constant A corresponds to the SRH non-radiative recombination, B corresponds to the radiative recombination and C is related to the non-radiative Auger recombination [190]. Typical values for A and B would be $2 \times 10^7 s^{-1}$ and $10^{-11} cm^3 s^{-1}$, respectively [191] Using Equation 1-22, internal quantum efficiency (IQE) with the carrier concentration n can be expressed as follows:

$$\eta_i = \frac{V_{QW} \cdot Bn^2}{I_{int}/q} = \frac{Bn}{A + Bn + Cn^2}$$
<div align="right">Equation 1-23.</div>

where I_{int} is the current injected into the active region, q is the electron charge and V_{QW} is the total active region volume [191]. Also, the external quantum efficiency of the LED can be determined using the following expression:

$$\eta_e = \eta_{ext} \cdot \eta_i$$

Equation 1-24.

where η_{ext} is representing light extraction efficiency (LEE) of the LED, which is assumed to be independent from the carrier concentration, n [190].

At low current densities, one of the main mechanisms which affects the LED efficiency is carrier localisation in the active region [108, 187, 192]. Deep localisation states in indium-rich regions in the QWs can capture non-equilibrium carriers, preventing them from moving laterally to non-radiative centres.

At high current densities, on the other hand, there are a number of mechanisms which may affect the efficiency behaviour from that predicted by the ABC-model. One is the self-heating of LEDs. To avoid self-heating, measurements should be done under pulsed injection [190].

The effect of different values of A, for a constant value of B is shown in Figure 1-23, plotted on log-log scale. For low excitation densities the increase in emission rate is clearly dependent on the value of A. For higher values of A a slope of 2 is observed indication of a process dominated by non-radiative recombination, which falls to 1 (dominated by radiative recombination) for lower values of A. At higher excitation densities, the slope tends to one as the non-radiative processes sat weak and radiative recombination dominates. These results assume C=0. Optical measurement can be in principal be generalised to electrical excitation as well [175].
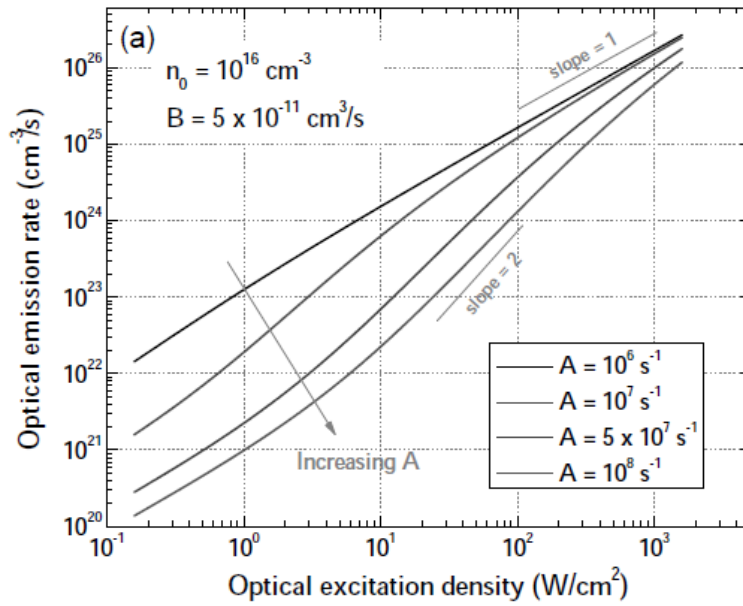
Figure 1-23 Optical emission rate versus the excitation power density for a B coefficient and different A coefficient [175].

1.3.7 Efficiency Droop in LEDs

One of the most important challenges for developing high-power nitride-based LEDs is the efficiency droop. When driving current in an LED increases, the external quantum efficiency (EQE) decreases. Typical polar GaN-based LEDs have a maximum peak output power at current densities less than $10 \ mA/cm^2$, at higher current densities the efficiency decreases gradually, as shown as an example in Figure 1-24 [189].

Referring back to Equation 1-23, in indium containing nitrides, it has also been suggested that another nonradiative channel can be derived, which is delocalisation of the carriers from states where carriers are assumed to be confined at low current densities. To be able to contribute to the droop, this mechanism rate has to be proportional to n^m, with $m \geq 2$ [191]. As mentioned earlier another mechanism for losses is leaking carriers from the active region which recombine non-radiatively in the n-, p- or buffer layers. Considering all these mechanisms, IQE can be expressed as:

$$IQE = \eta_i = \frac{Bn^2}{An + Bn^2 + Cn^3 + k(n-n_0)^m + \frac{I_{LK}}{qV_{QW}}} \qquad \text{Equation 1-25.}$$

Where the term $(n-n_0)^m$ is associated with carrier delocalisation, I_{LK} is leakage current, n_0 and k are carrier density triggering threshold of delocalisation and a constant, respectively [191]. Auger

recombination has been assumed to be at least the major cause for droop and depends on the value of the Auger coefficient C [189, 191, 193].

Figure 1-24 Efficiency versus driving current for GaN-based UV, blue and green LEDs [189]

Chapter 2

Experimental Techniques

2 EXPERIMENTAL TECHNIQUES

In this chapter, I will describe the material growth system used in this thesis and will give an overview of growth processes. Also other frequently used techniques for epitaxial growth of III-nitride semiconductors will be briefly introduced. This chapter also, involves the description 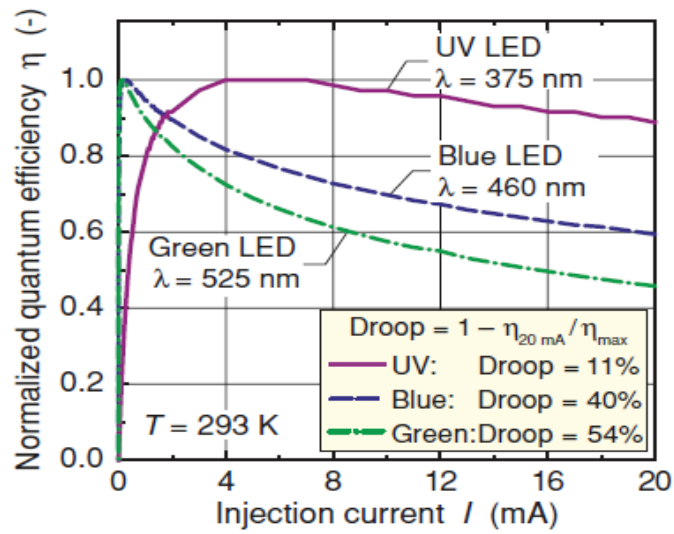of material characterisation tools, including structural, morphological, optical and electrical analysis. Furthermore, because GaN and AlN are normally grown on foreign substrates, commonly used substrates for nitride epitaxy will be discussed in short. It will include sapphire and silicon.

Techniques used for fabrication of LEDs, including; photolithography, electron beam lithography, etching and metallisation will also be described in this chapter.

2.1 Material Growth

Due to the high melting point and high nitrogen vapour pressure, the growth of a group III-nitrides (such as GaN, AlN, and InN) is relatively difficult. Some methods, such as high-pressure high-temperature synthesis, have been used to obtain bulk group III-nitride crystals. Gallium nitride (GaN) was initially synthesised by Jusa and Hahn in 1938 [194] using ammonia flow over hot gallium. Using this technique small needles and platelets of GaN were produced. In order to characterise the structural and optical properties of III-nitride thin layers, the first attempts started in the 1970s applying chemical vapour deposition or sputtering processes to grow InN, GaN and AlN [195, 196]. At that time, electronic grade purity metalorganic precursors containing In or Al and plasma sources compatible with molecular beam epitaxy (MBE) were not available. Also, there were no substrate available lattice matched to the nitride based materials. As a result, due to oxygen impurities and intrinsic defects, as grown InN and GaN layers were containing large concentrations of free electrons, also the structural quality of the AlN layers was poor and not suitable for electronic or optical applications. Development of the MOCVD and plasma-induced MBE (PIMBE) techniques has led to a lot of improvements and advances for growing III-nitrides, so far [197].

2.1.1 Widely Used Epitaxial Growth Techniques

Epitaxy is the process of growing layers of a crystalline material on a substrate with repetition of the crystal structure. If the grown and the substrate materials are the same it is called *homoepitaxy* and if different it is *heteroepitaxy*. Growing high-quality materials with eminent properties, such as

controllable composition and conductivity becomes possible by epitaxy. Epitaxial methods are perfectly suitable for growth of quite complicated heterostructures for specific semiconductor devices such as LEDs and laser diodes (LDs) (including vertical-cavity surface emitting lasers; VCSELs), etc.

There are techniques to prepare or grow such crystalline layers, it is including high vacuum techniques (e.g. MBE) where a "beams" of precursors (either atoms or molecules) are directed to a substrate which is normally heated, to grow the crystalline layer.

In *MBE*, a beam of high purity elements as the source materials are supplied and send to a heated substrate. Since the atoms must have a mean free path for collisions longer than the source to substrate distance, the MBE technique needs growth pressures of around 10^{-10} torr. Atoms react on the substrate surface and if the growth conditions are properly optimised, material grows layer by layer in two dimensions. A plasma is often used to supply atomic source of nitrogen as the ammonia cracking efficiency is quite low at the temperatures used in MBE. One major advantage of this method for nitride materials growth is the capability for growth at low temperatures because of the atomic nitrogen source. During substrate cooling in MBE, the lower the growth temperature the lower the thermal stress is. Hence the alloy segregation and interface diffusion are reduced [198]. This is especially important in growing the materials with large thermal expansion mismatch such as AlGaN alloys [198]. Using MBE technique to grow III-nitride materials do not need metal organic resources which contain carbon and hydrogen. Atomic hydrogen can passivate the Mg-doped GaN layers during growth, which needs a subsequent process to activate the acceptors. Therefore another advantage of MBE is that the as-grown p-GaN layer is not passivated [198]. The possibility to control the interface at the level of a single atomic layer is another great advantage of this growth technique [1].

However, in spite of these advantages, it is difficult to control substrate temperature especially at high growth temperatures where high thermal radiation losses happen. Another difficulty is to get uniform temperature across substrate wafer, this due to high radiation losses at the edge of the wafer and also due to the refractory metal coated on the back of the substrate [199]. A schematic cross-section view of a typical MBE system is depicted in Figure 2-1.
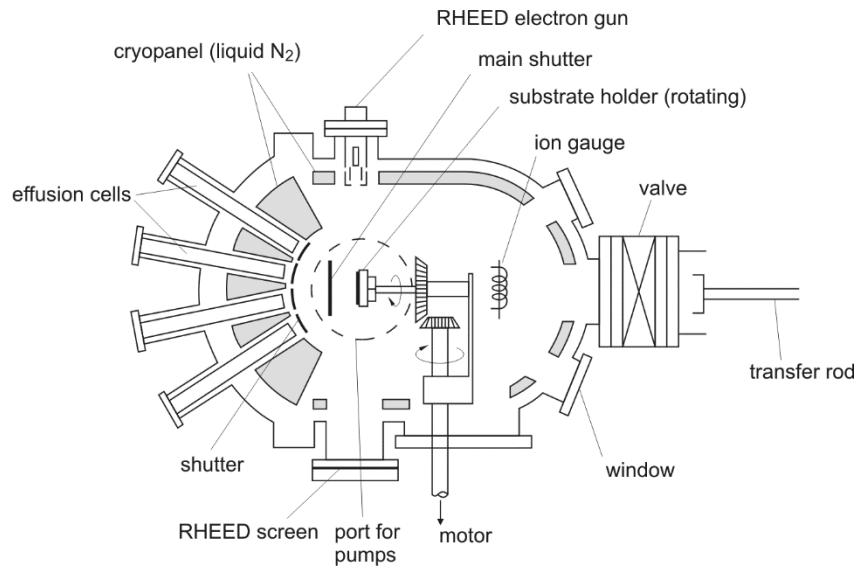
Figure 2-1 Schematic cross-section of a typical MBE growth chamber [200].

Another interesting technique which recently attracted more attention, owing to its low cost, versatility, and scalability is *sputtering*. In reactive sputtering growth technique, a Ga target bombarded with nitrogen or nitrogen-argon mixtures, transferring (both Ga and N) to the substrate to create GaN layer [201]. Also, some problems have been reported due to the low melting temperature of gallium which affects the reproducibility of growing GaN, for example [202]. However, during the last few years, GaN films have been deposited using both Ga and GaN targets [203]. The ability to deposit at low temperatures on different kinds of substrates opens opportunities for deposition of the semiconductors including III-nitrides, for potential applications in photonics, electronics, optoelectronics, and photovoltaics.

There are other epitaxy techniques based on chemical reactions on the surface where materials transported to the substrate in a gas phase (Vapour Phase Epitaxy) or liquid phase (Liquid Phase Epitaxy).

Liquid Phase Epitaxy (LPE) is the solidification from a liquid phase of a material onto a substrate so that the crystallinity of the substrate is retained in the grown layer. These kinds of crystal growth have received great attention since their first introduction. In 1836, Frankenhein for the first time managed to grow layers by LPE [204].

Large, single crystal GaN can be grown using Na flux method in LPE system [205]. In this technique, by applying the nitrogen gaseous pressure to the melted Ga–Na system, nitrogen will be dissociated and as a result, GaN single crystal grows at ~800 °C and ~50 atm [206].

Besides advantages, like the ability to grow on various substrates at high deposition rate, this method has some disadvantages. One is that liquid gallium does not uniformly wet sapphire, resulting in a poor thickness uniformity and a high surface roughness [207]. A schematic of typical LPE growth by Na flux method is shown in Figure 2-2.
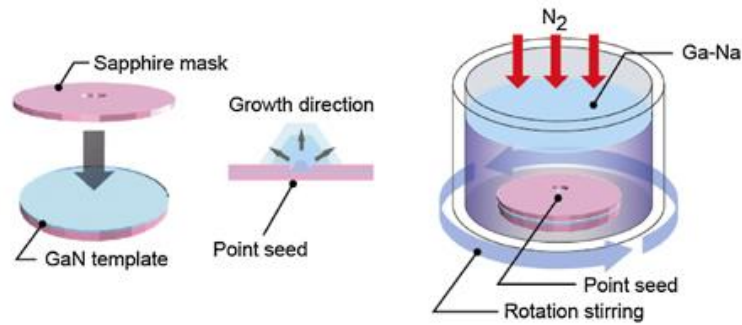
Figure 2-2 Schematic illustration of LPE growth of GaN using Na flux technique [208].

Hydride Vapour Phase Epitaxy (HVPE): the first single-crystal epitaxial GaN thin films was grown using vapour transport technique by Maruska and Tietjen [209]. In that technique, vaporised Hydrochloride (HCl) flowing over melted gallium causes the formation of GaCl. Then, the GaCl mixed with NH_3 at the substrate, leading to the chemical reaction below:

$$GaCl + NH_3 \rightarrow GaN + HCl + H_2$$ Equation 2-1.
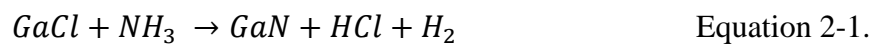
Although n-type carrier concentration in initially grown GaN by vapour transport was very high (around $10^{19} \ cm^{-3}$), due to technology advances, this level has dropped to values of about $10^{17} \ cm^{-3}$ with mobility approaching $900 \ cm^2/V.s$ at room temperature [175]. The schematic diagram of a horizontal HVPE reactor is shown Figure 2-3.
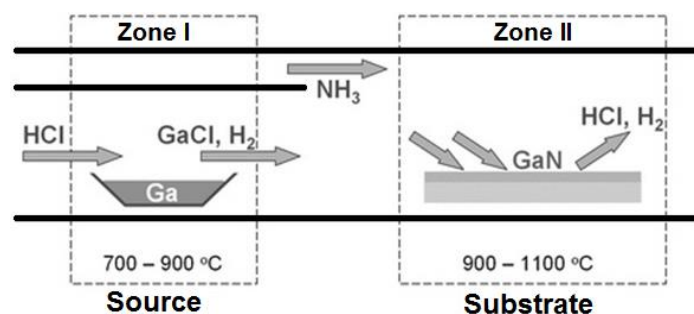
Figure 2-3 Schematic representation of GaN growth by HVPE [210].

Due to high melting and sublimation temperatures, it makes it difficult to design the reactor. However, relatively high vapour pressures of metalorganics allow them to be suitable as the metal sources for epitaxy because they can be transported to the reaction zone at RT through pipelines.

Among all epitaxial growth techniques, MOVPE is the most popular and claimed to the most suitable method for industrial mass-production of semiconductors growth [211-213]. Some strengths and weakness as of the most popular techniques are summarised in Table 2-1.

Table 2-1 Overview of some epitaxial techniques [214].

Technique	Strength	Weakness
LPE	Simple High purity	Scale economics Inflexible
HVPE	Well developed Large Scale	Complex process/ reactor Difficult to control Hazardous precursors
MBE	Simple process Uniform Abrupt interfacing In-situ monitoring	Difficult for nitride materials Low throughput "Oval" defect Expensive
MOVPE	Most flexible Abrupt interfaces High purity Robust process Large scale High growth rate In-situ monitoring	Low throughput Expensive (capital) Expensive reactants Difficult for nitride materials

A non-equilibrium growth technique, based on vapour transport of the precursors and reactions of group-V and group-III precursors in a heated zone is Metal Organic Vapour Phase Epitaxy (MOVPE)

or Metal Organic Chemical Vapour Deposition (MOCVD) which will be discussed in more detail in the next section.

2.1.2   Metal-Organic Vapour Phase Epitaxy (MOVPE) of III-Nitrides:

MOVPE stands for metal-organic vapour phase epitaxy, is often considered the most versatile material growth technique. High uniformity of grown layer, high growth rates, high flexibility of growing materials and capability for large-scale production, selective growth and in-situ monitoring makes this a strong and reliable technique for epitaxial growth. The research for MOVPE technique originated from the early research of Manasevit and his co-workers [215], who demonstrated the use of triethylgallium ($TEGa$) for deposition of single crystal GaAs pyrolytically in an open tube cold-wall reactor.

One of the main reasons that made MOVPE the preferred route for III-nitride growth was the invention of the nitride-based LEDs by the groups of Akasaki and Nakamura in the early 90s [11, 196, 216]. Since then, the technique has been widely used in the semiconductor industry. For this purpose, it is now used to create materials for a many different devices, including LEDs, LDs, field-effect transistors, photovoltaics, etc [213]. In this thesis, an MOVPE system was used for epitaxial growth of III-nitride structures, more details of which [42] will be described later.

2.1.2.1   *Reaction process in MOVPE growth:*

The MOVPE process is basically a CVD process where metalorganic compounds are used as the group-III sources. For growth of III-V semiconductor compounds, a mixture of the group-V element gases, like AsH_3 or NH_3, with group-III metalorganic sources is normally used. Generally, CVD can be defined as a vapour-to-solid process. All chemical reactions are controlled externally by means of heat, ion beam, plasma and photons for instance, as the sources of energy for pyrolysis of the precursors [217]. The growth in MOVPE can be simplified into few key steps as shown in Figure 2-4.
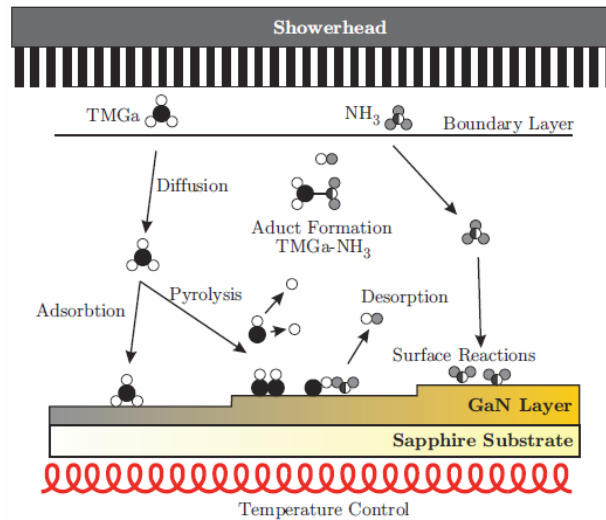
Figure 2-4 Illustration of CVD process in an MOVPE reactor [194].

There are many thermodynamic reactions during MOVPE growth of III-V compounds, but the basic reaction processes involved can be simplified as an equation below:

$$A^{III}R_3 + B^V X_3 \rightarrow A^{III}B^V + by\ products$$
Equation 2-2.
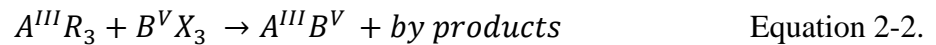
R is representing organic groups as a radical for example ethyl (CH_2CH_3) and methyl (CH_3) and X is typically hydrogen in nitride growth. A is representing cation and B is anions, which are metallic Ga/Al/In and N in the case of III-nitride growth, respectively. For GaN growth [1, 218]:

$$Ga(CH_3)_3(v) + NH_3(v) \rightarrow GaN(s) + 3CH_4(v)$$
Equation 2-3.
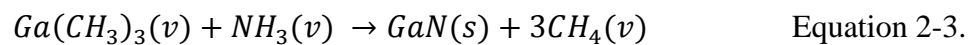
In our case, NH_3 as a nitrogen source and a metal-organic (MO) as a metallic source are injected into the reactor via a showerhead. Because of the high temperature, normally higher than 900°C, the MO source is decomposed and form pyrolysis products. The decomposed products in the form of pyrolysis and/or MO are adsorbed to the surface and contributing the epitaxy by diffusing into the growth sites on the surface as shown schematically in Figure 2-4 [194]. By-products also exhaust from the reactor chamber.

In MOVPE growth rate and composition of materials are varied by controlling parameters such as resources flow rate, dilution of the precursors, temperature and reactor pressure. The MO group III sources are either liquids, such as trimethylgallium ($TMGa$) and trimethylaluminum ($TMAl$), or solids such as trimethylindium ($TMIn$). The metal-organic sources are kept in bubblers where a carrier gas

(hydrogen or nitrogen) flowing through, picks up some amount of precursor as a vapour. The bubbler temperature is precisely controlled to give a desired vapour pressure and hence pick up.

The amount of MO supplied to the reactor can be calculated using the formula below:

$$f_{MO}\left(\frac{\mu mol}{min}\right) = \frac{f_{H2}}{22414(sccm/\mu mol)} \cdot \frac{P_{MO}}{P_{Bubler} - P_{MO}} \qquad \text{Equation 2-4}$$

where, f_{H2} is the hydrogen flow and $P_{Bubbler}$ is the back pressure on the bubbler set. Also, P_{MO} is the vapour pressure of the MO which depends on temperature and given by:

$$log[P_{MO}] = B - A/T \qquad \text{Equation 2-5}$$

where A and B are constants given for each MO source [194], see Table 2-2.

Table 2-2 Physical properties of commercially available metal organic sources [194], [219].

Symbol	Chemical	Formula	A	B	Melting (°C)	Use
TMGa	Trimethyl Gallium	$(CH_3)_3Ga$	1703	8.07	-15.8	Primary gallium source
TEGa	Triethyl Gallium	$(C_2H_5)Ga$	2162	8.083	-82.3	High purity and low growth rates
TMAl	Trimethyl Aluminium	$(CH_3)_3Al$	2134.8	8.224	15.4	Most common Al source, high carbon incorporation
TEAl	Triethyl Aluminium	$(C_2H_5)Al$	3625	10.78	-52.5	Low vapour pressure, Low C
TMIn	Trimethyl Indium	$(CH_3)_3In$	3014	10.52	88	Most common In source, high carbon incorporation
TEIn	Triethyl Indium	$(C_2H_5)In$	2815	8.93	-32	Liquid indium source, pre-reaction
Cp2Mg	Cyclopentadienyl Magesium (Bis)	$(C_5H_5)_2Mg$	3556	10.56	175	p-doping material
DEZn	Diethyl Zinc	$(C_2H_5)_2Zn$	2109	8.28	-28	p-doping material
DMZn	Dimethyl Zinc	$(CH_3)_2Zn$	1560	7.802	-42	p-doping material

The most common group V sources are gaseous hydrides, for example, ammonia NH_3. For *p*-type doping, the III-nitrides, metal organic precursors such as cyclopentadienyl-magnesium, Cp_2Mg, can be used and hydrides such as silane or disilane Si_2H_6, can be used for *n*-type doping. The substrate is usually placed on a heated graphite holder called a susceptor. One of the important features of the MOVPE process is that the walls are kept radically colder than the substrate to prevent the interference from depleted reactants with the growth by reducing the chemical reactions on the walls (like thermal decomposition) and minimise the deposition of the material on the walls [1].

There are still no lattice matched commercially viable substrates available for GaN growth. Hence, for compensating the crystal lattice mismatch between the substrate and the GaN, a low-temperature nucleation layer was proposed [220]. Also, an in-situ reflectance measurement is utilised to control the growth, therefore, in MOVPE reactors, it is very critical to have optical access to the surface of the wafer.

2.1.2.2   *Overview of the Close Coupled Showerhead Aixtron MOVPE system*

Currently, different kinds of MOCVD reactors are being developed for the mass production of GaN-based materials and devices. They are mostly produced in atmospheric pressure and low-pressure configuration. Three types of geometrie designs of a reactor are illustrated in Figure 2-5.
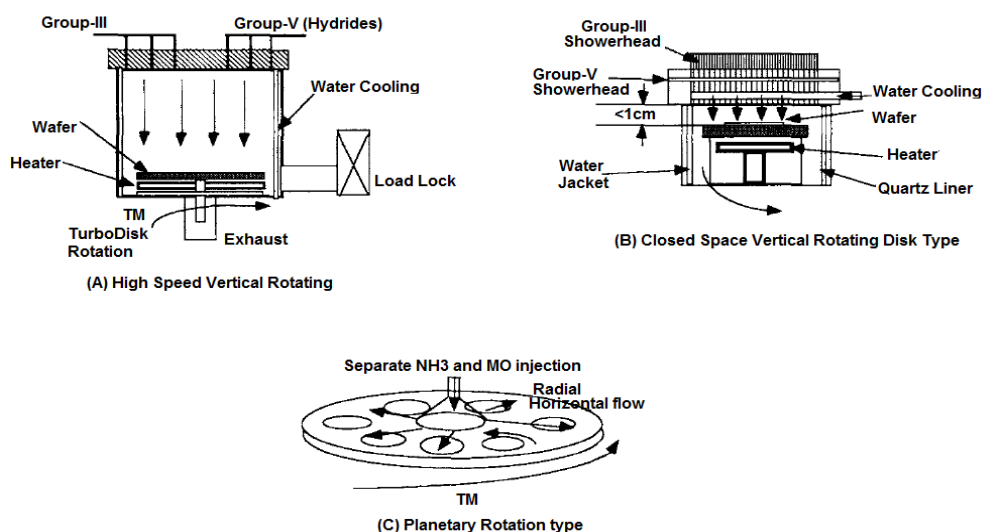
Figure 2-5 Three types of MOCVD production reactors for GaN [1].

For the high-speed vertical reactors, the main advantage is the availability of the large reactors as well as the layer uniformity due to the high rotation speed. The two-flow horizontal planetary rotation reactor can operate at near atmospheric pressure which makes it suitable for mass production. The

advantage of closed space RDR is the ability to operate it at near atmospheric pressure. Material quality, reproducibility, easy maintenance, high throughput and the types of material sources are the key factors for selection of the reactor type [1].

One of the most important issues regarding to MOCVD is to produce uniform layers. This is a particular problem in III-Ns as AlN, GaN and InN all need very different growth conditions (temperature, pressure, flows, carrier gas used, etc.). In a classical horizontal tube reactor, precursor concentration falls along its length, which is addressed in reactors design to increase the diffusion of the precursors to the surface to compensate the concentrate drop. This is hard to control of the growth temperature and gas flows are changing. The showerhead design has precursors injected uniformly across the surface of the wafer and so is by design more robust in allowing uniform growth over a range of reactor conditions. Another advantage is that the short distance between the showerhead and wafers reduces the risk of precursors reacting in the gas phase (so-called pre-reaction), this is a particularly well known problem for AlN growth, for example [199].

For this work, the Close Coupled Showerhead MOVPE system has been set up to epitaxial growth of III-nitride materials and it is shown in Figure 2-6, and its schematic is illustrated in Figure 2-7.

Figure 2-6 3×2" Close Coupled Showerhead Aixtron MOVPE system used in this work.
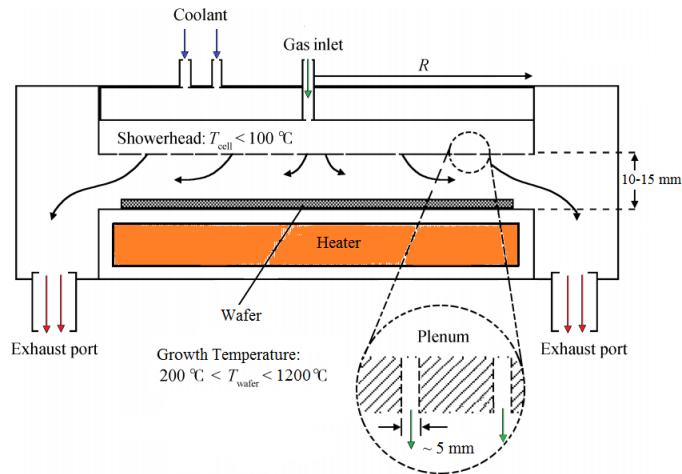
Figure 2-7 Schematic view of Close Coupled Showerhead MOCVD reactor [221](modified).

2.2 Epitaxial growth of III-nitride materials

2.2.1 Lattice matching

One of the important factors which affect the growth of an epitaxial film is lattice matching between the epitaxial layer and the substrate. The lattice mismatch, f, of the film with respect to the substrate lattice is defined by:

$$f = \frac{a_{epi} - a_{sub}}{a_{sub}}$$

Equation 2-6

where a_{epi} is lattice constant of unstrained grown material (epilayer) and a_{sub} is the lattice constant of the substrate [222].

There are at least two possible ways for an epilayer to be grown on the foreign substrates. For small mismatch atoms of the epilayer, at the initial stage of the growth, stick on top of the corresponding atoms of the substrate. This is in the case during the early stages of film formation and gives a so-called *pseudo-morphically* grown layer. However, as the epilayer thickness increases, the elastic strain energy increases until the point which misfit dislocations start to activate and plastic relaxation occurs. The critical thickness at which misfit dislocations are generated varies approximately inversely with the above mentioned mismatch parameter, f [223]. The second possibility is that the atoms of the epilayer retain their bulk lattice constant and therefore to minimise the mismatch and then release the interface strain, dislocation defects will be formed leading to *relaxed* epitaxy [224].

If the mismatch is higher than around 15%, the growth can result in polycrystalline material. Exceptions to this criterion can be explained by a rule called *coincidence site lattice* (CSL), which is explained below.

Correct coincidence lattice matching between the epilayer and substrate lattices would occur if $\frac{d_{epi}}{d_{sub}} = m/n$, where m and n are integers, and d_{epi} and d_{sub} are relatively atomic distances of the epilayer and substrate. This simple lattice matching model is schematically shown in Figure 2-8. If for instance $m = n + 1$, there would be one excess lattice plane. For example, an edge dislocation (misfit dislocation) in each unit cell of the coincidence lattice [225].
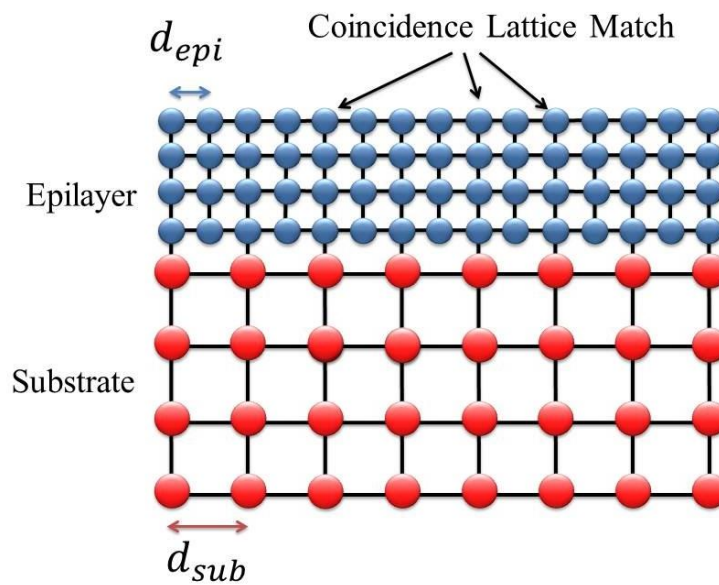
Figure 2-8 Schematic view of Coincidence Lattice Matching.

The coincidence lattice mismatch δ, which shows the deviation from correct coincidence, is defined by:

$$\delta = \frac{md_{sub} - nd_{epi}}{md_{sub}} \qquad \text{Equation 2-7}$$

2.2.2   Substrates for III-N epitaxy

To reach the full potential of applying III-nitride based semiconductor devices, there are two main limitations and challenges researchers face (in spite of rapid growing in mass production and commercialization): i) high biaxial strain and defect density due to the heteroepitaxial growth on foreign substrates,   and ii) strong built-in electric field due to spontaneous and piezoelectric

polarisation in the wurtzite structures along [0001] growth direction [226]. Despite of availability of free standing 2-inch GaN with the TD dislocation density below 10^7 cm^{-2} in the market, its price is still very high, between €1,000 and €5,000 [227], therefore using foreign substrate is unavoidable.

In spite of these difficulties, the III-nitride technology has become a commercial reality by applying hetero-epitaxy techniques and employing foreign substrates such as sapphire, silicon carbide, and silicon [228-232]. Some materials properties of the common substrates are shown in Table 2-3.

Table 2-3 Lattice parameters and thermal characteristics of some prospective substrate materials for nitride growth [14].

Crystal	Lattice Parameters			Thermal Conductivity	Thermal Expansion	
	a (Å)	b (Å)	c (Å)	κ, (W cm^{-1} K)	$\Delta a/a$, (10^{-6} K^{-1})	$\Delta c/c$ (10^{-6} K^{-1})
GaN (Wurtzite)	3.189	---	5.185	~2	5.59	3.17
AlN (Wurtzite)	3.112	---	4.982	~3	4.2	5.3
Al$_2$O$_3$ (Sapphire)	4.758	---	12.991	0.3-0.5	7.5	8.5
6H-SiC	3.0817	---	15.112	4.9	4.2	4.68
Si (Cubic)	5.43	---	---	1.5	3.59	
GaAs (Cubic)	5.653	---	---	0.5	6	
ZnO (Wurtzite)	3.25	---	5.206	0.3-0.4	4.75	2.9
MgO	4.216	---	---	45-60	10.5	

Silicon is a potential substrate for growing III-nitrides and its family due to its availability of large sizes, low price and the possibility of integration with current and mature Si technology as well as integrating of the optical with electronic devices. Despite its cubic lattice, it is possible to grow wurtzite nitrides on silicon cut perpendicular to [111] direction, because of the same surface symmetry. Most of the scientists have focused their research on Si(111) so far [233]. Although (100) is potentially the preferred orientation for III-nitride growth, because Si(100) is the standard substrate for silicon processing technology, the growth of GaN on this orientation is not very straightforward due to different crystallographic surface symmetry and the reported blue light emitting diodes on Si(100) had lower quality than those on Si(111) [233].

6H-SiC, as a substrate for III-nitride materials technology, has the advantages of the almost similar lattice constant and the thermal expansion to those of AlN. The lattice mismatch between 6H-SiC and GaN on c-plane, on the other hand, is about 3.5 %, which is still much better than Si. Also, the thermal conductivity of SiC (~5 *W/cmK*) is better than of which for GaN (~1.3 *W/cmK*) and Si (~1.5 W/cmK) [234] therefore theoretically allowing devices on SiC to operate at higher power densities. These properties may bring us to the conclusion that growth on this substrate should be better.

However, the development of the III-nitride materials technology on SiC is limited by a relatively high price of this substrate.

Other crystalline materials such as MgO [235], ZnO [236], [237] etc., also have been used as substrate for nitride semiconductors, but further developments are needed to employ these in technology. The majority of GaN devices are prepared on sapphire.

2.2.3   Sapphire for III-nitride epitaxy

Although there are significant differences in lattice constant and thermal expansion coefficient between sapphire (Al_2O_3) and gallium nitride, it is still the most commonly used substrate for *GaN* growth because of its relatively low price, hexagonal symmetry and availability. Sapphire is also stable at high temperature (1000°C), which is required for growth of III-nitride materials using metalorganic vapour phase epitaxy (MOVPE) [14]. Furthermore, sapphire has a very wide band-gap of about 9.9 eV [238], meaning that it is optically transparent from UV to near IR; this transparency allows light to be extracted through the substrate across this very wide wavelength range.

To date, several sapphire substrate surface orientations have been used for growing III-nitride materials, such as a-plane $(11\bar{2}0)$ [239], c-plane (0001) [240], m-plane $(10\bar{1}0)$ [241], and r-plane $(1\bar{1}02)$ [242] sapphire.

Sapphire for AlN epitaxy. AlN is one of t he most commonly used buffer layers for gallium nitride growth on the sapphire substrate. Using Equation 2-6 and the data in Table 2-3, the in-plane lattice mismatch between c-plane AlN (0001) and sapphire (0001) would be around 0.346 which is a very large value, so at first glance, epitaxy cannot be expected.

Fortunately, when the AlN (0001) is grown on sapphire (0001), epi-crystal is twisted by 30 ° around c-axis with respect to that of sapphire [69]. In this particular case, AlN (0001) plane would be parallel

to Al_2O_3 (0001) and AlN $[2\bar{1}\bar{1}0]$ parallel to Al_2O_3 $[1\bar{1}00]$ which is schematically shown in Figure 2-9.
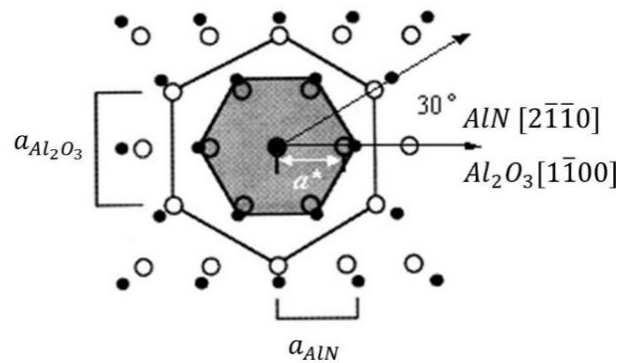
Figure 2-9 Schematic top view of the epitaxial relationship between AlN (0001) and Al₂O₃ (0001) [225].

In this case, the atomic distance between the O atoms in sapphire (a*) is 2.747 Å, and Al-Al distance in aluminium nitride is 3.112 Å, therefore the lattice mismatch in this orientation is significantly reduced to ~13%, which still not low for epitaxial growth. However, back to section 2.2.1, this epitaxial relationship, shown in Figure 2-9, leads simultaneously to a coincidence site lattice which $\frac{d_{AlN}}{d_{Al_2O_3}} = \frac{m}{n} = \frac{9}{8}$, means that eight Al-A1 interatomic distances in AlN is equal to nine O-O interatomic distances in sapphire (m=9, n=8) with the CSL lattice mismatch of only δ= 0.70%, using Equation 2-7 (see Figure 2-10). This low δ mismatch might be the primarily responsible for the epitaxial growth of AlN on sapphire. Here AlN epilayer would be under tensile strain [243].
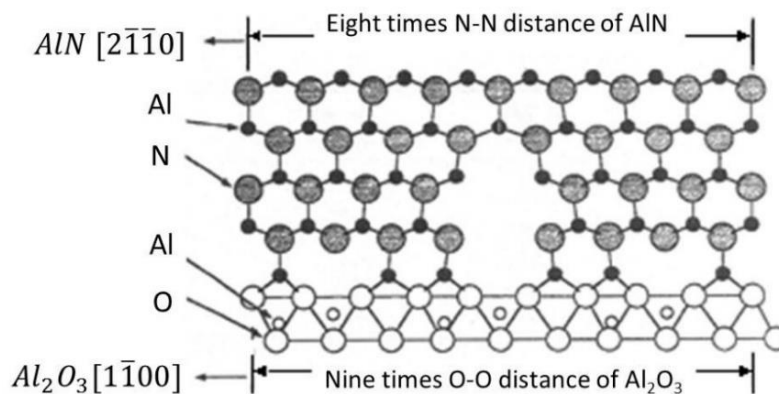
Figure 2-10 A crystallographic model of AlN (00̄01) epitaxial growth on Al₂O₃ (0001) substrate [243].

Sapphire for GaN Epitaxy. By far, growing the GaN on sapphire is very common especially on c-plane sapphire, which has been reported to be reasonably good in quality and having the smooth and flat surface which is very crucial in many applications, such as growing nanostructures, as it is done in this thesis and will be discussed later. The schematic top view of the epitaxial c-plane GaN on c-plane sapphire is illustrated in Figure 2-11.
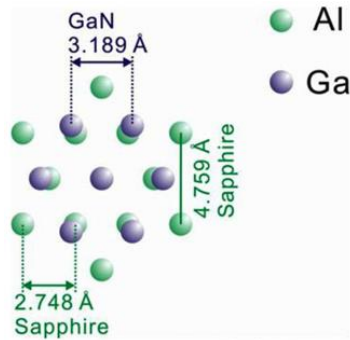
Figure 2-11 Schematic top view of the epitaxial relationship between GaN (0001) and Al₂O₃ (0001) [233].

Using the data in Table 2-3 and applying Equation 2-6, the in-plane lattice mismatch between c-plane GaN (0001) and Al$_2$O$_3$ (0001) would be around 0.33 which is very high for epitaxial growth.

The epitaxial GaN on c-plane sapphire is forced to twist by 30° around the c axis during growth, which makes the [$\bar{1}2\bar{1}0$] GaN and [$\bar{1}100$] sapphire orientations parallel [244], see Figure 2-12. In this orientation, the lattice mismatch between sapphire and rotated GaN would be around 16% instead of 33%. Due to this lattice mismatch, which still high and depends on different parameters such as growth temperature, layers are found to be under biaxial compressive stress [245], [246]. Here we could have another type of CSL lattice matching [247], although it is more complicated than the situation in the case of AlN/Al$_2$O$_3$.
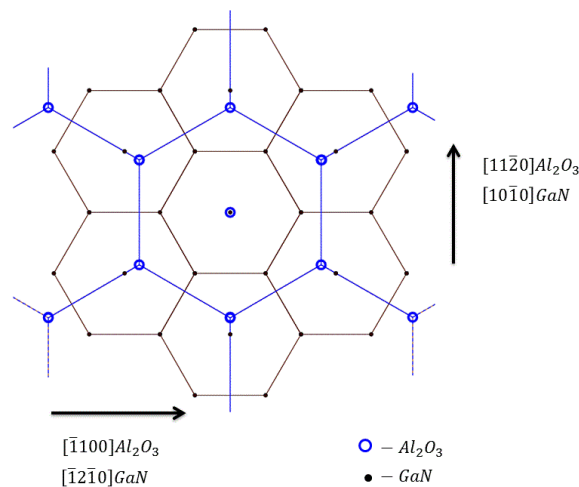
Figure 2-12 Schematic view of crystal orientation of GaN (0001) on Al₂O₃ (0001) after 30° rotation.

2.3   Structure/morphology characterisation techniques

2.3.1   Electron Microscopy (SEM & TEM)

An electron microscope is a type of microscope which create the image by illumination of the specimen with electrons. Incident electrons are absorbed (with the emission of secondary electrons), reflected, or transmitted and can, in turn, cause light or X-ray emission [248]. Electrons can be focused, and accelerated, detected and their energy and angular distribution can be measured by appropriate tools. Electrons, on the other hand, may cause sample charging leading to image distortion [248].

The resolution and magnifications of typical electron microscopes are much higher than those for optical microscopes. Some electron microscopes can magnify samples up to 2 million times, in comparison, the magnification of the best optical microscopes is limited to about 2,000 [249]. Both electron and optical microscopes are limited with resolution, caused by their wavelength. The use of electrons instead of photons in microscopy has two main advantages: larger magnifications, due to much smaller wavelengths of electrons (De Broglie wavelength: $\lambda_e = \frac{h}{p}$) than photons and much higher depth of field:

$$\lambda_e = \frac{h}{mv} = \frac{h}{\sqrt{2gmV}} = \frac{1.22}{\sqrt{V}} \ (nm)$$

Equation 2-8

As an example; for acceleration voltage of V = 10 kV; wavelength is λ_e = 0.012 nm, which is much lower than the 400 to 700 nm wavelengths of visible light, making the resolution of an electron microscope much higher than that of an optical microscope. Two most commonly used electron microscopes are *Scanning Electron Microscope (SEM)* and *Transmission Electron Microscope (TEM)*.

2.3.2   X-ray Diffraction

X-ray diffraction (XRD) is a rapid analytical technique primarily used for identifying the atomic and molecular structure of a crystal. In XRD, an X-ray radiation with a wavelength (λ), which is in the same order of magnitude of the lattice constant, probes a crystal and causes diffraction in specific directions, Figure 2-13 (a). In some directions, constructive interference occurs between the diffracted

X-rays, when the path length difference between X-rays scattered from different hkl-planes is an integer number of the wavelength, λ. This is the fundamental of Bragg's law [250]:

$$n\lambda = 2d_{hkl}\sin\theta$$

Equation 2-9

where d_{hkl} is the 'interplanar' spacing, θ is the diffraction angle at which the incident beam probes the plane (*hkl*) to give constructive interference, see Figure 2-13. Any parameter which changes the interplanar spacing, would change the diffraction angle, therefore the position of the diffraction spots. As mentioned earlier in a Wurtzite crystal structure, which is in case for III-N family, four indices (*hkil*) or Miller-Bravais is often used. In cubic crystals the interplanar spacing (d_{hkl}) can be determined using formula below:

$$d_{hkl}^{cubic} = \frac{a}{\sqrt{h^2 + k^2 + l^2}}$$

Equation 2-10

while in an ideal hexagonal crystal, the parameter d_{hkil} can be calculated using the following equation [251]:

$$d_{hkl}^{hexagonal} = \frac{a}{\sqrt{\frac{4}{3}\left(h^2 + k^2 + hk\right) + \left(\frac{a}{c}\right)^2 l^2}}$$

Equation 2-11

The lattice parameter of an alloy is affected by material composition and strain. XRD can get data about the crystal lattice, and as a result, determination of alloy composition and residual strain, along with thickness, crystallite size, wafer bowing etc. can all be made. In XRD, the crystal behaves as a diffraction grating, and the sample and/or the detector are moved with respect to the incident beam, (Figure 2-13). Hence, with rotation of the sample or detector a 3D pattern of diffraction spots can be determined, due to constructive interference. The position and shape of each spot are related to each set of planes. The diffraction spots are correlated with the reciprocal lattice [251]. Reciprocal lattice measurement is actually very useful for realisation of a crystal structure. It can provide both interplanar spacings and angles from single spot, because any parameter that changes the interplanar spacing and/or plane angle will vary the position/shape of the diffraction spot.
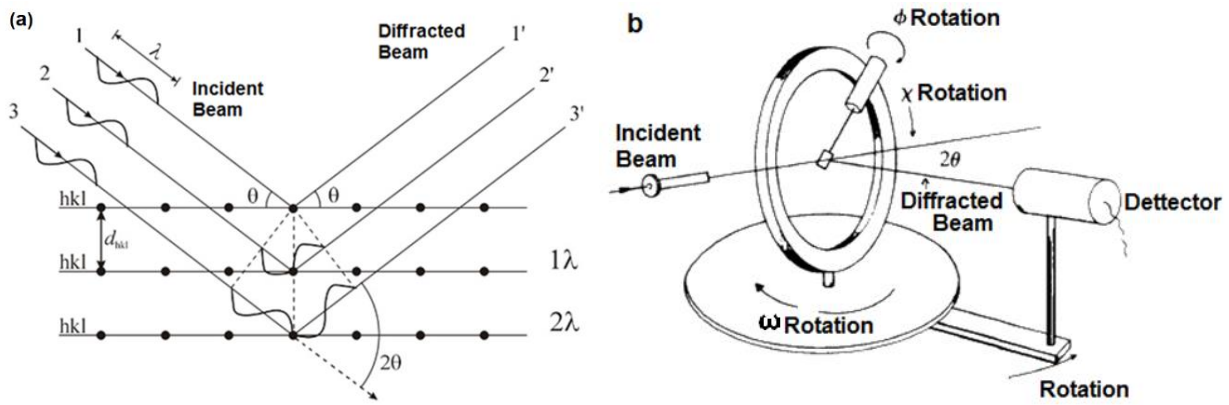
Figure 2-13. Schematic view of X-Ray diffraction process (a) and a diffractometer (b).
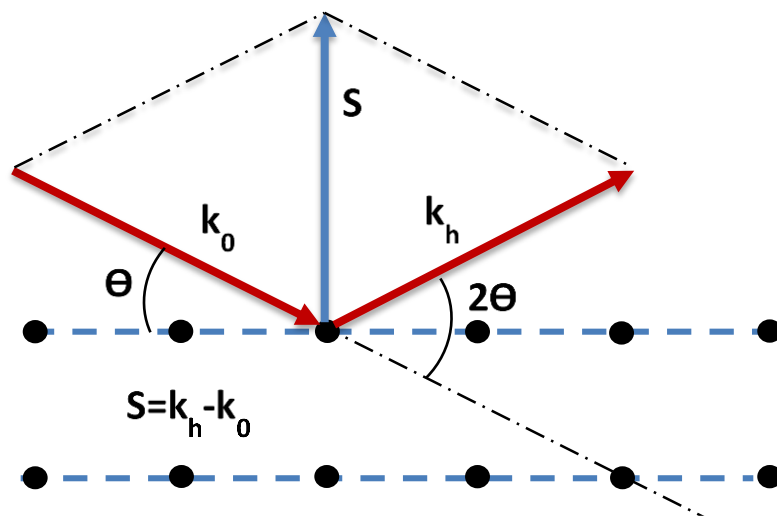
Figure 2-14. Schematic illustration of relationship between the incident (k_0), diffracted (k_h) and scattering (S) vectors with respect to the crystal.

As shown in Figure 2-14, a so called *scattering vector*, **S**, which is equal to **S**=k_h-k_0, is used to onstruct the reciprocal lattice. k_0 and k_h are the incident and the diffracted beam vectors, respectively. The scattering vector, **S**, will end at a reciprocal lattice point and its length can be changed by changing the angle 2θ. As a result, various areas of reciprocal space can be probed by means of varying crystal direction and altering the length of **S.** The length of the scattering vector can be changed by the angles ω and 2θ. Here, ω is the incident angle with respect to the surface of the sample, which may be different from θ.

The quality of a wafer can be determined using ω-scans. It is carried out by measuring the broadening associated with dislocations and wafer bowing. This scan is often called a rocking curve as the sample is rocked.

To measure the lattice parameter, ω–2θ scans are typically used. To do this accurately using Equation 2-11, at least two measurement needed, because of two unknown parameters (*a* and *c*). Additionally, in symmetric scan, compositional and strain changes can yield the same peak shift. Therefore, in order to determine both composition and strain in layer, a combination of both symmetric and asymmetric scans needed, see Figure 2-15 for clarification.
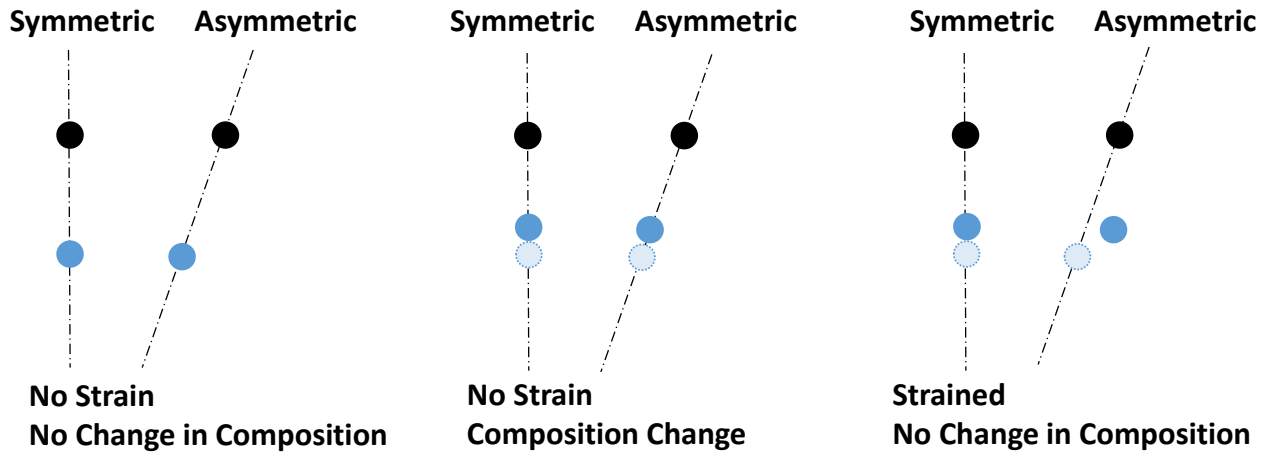
Figure 2-15. Schematic view of composition and strain variation in symmetric and asymmetric scan systems.

Technically, one or two symmetric reflections are measured to determine parameter c. Two typical high angle symmetric reflections are 0004 and 0006 with (0001) direction in GaN crystallographic measurement. After determination of parameter c, another two asymmetric reflections are evaluated. Two typical high angle asymmetric reflections are $10\bar{1}5$ and $20\bar{2}4$.

As mentioned earlier, having the lattice parameter can lead to determination of composition. If an alloy (e. g. InAlN) is unstrained, then the simple Vegard's law can be used, as discussed in section 2.2.1 and using Equation 1-8.

 In a fully strained layer which lattice constant changes to match the substrate value, Equation 1-8 is needed to be modified to take the out of the plane lattice parameter and calculate a relaxed value, to get the composition of an ABN film (where A and B are group III metals) on BN substrate (e. g. GaN) can be driven using following equation [251]:

$$x = \frac{(1-\nu)(c_{meas}^{ABN} - c_0^{BN})}{(1+\nu)(c_0^{AN} - c_0^{BN})} \qquad \text{Equation 2-12}$$

where ν is Poison's ratio, estimated by linearly interpolating between the values of AN and BN. If, the epitaxial layer is partially strained to the substrate, effects of both the in-plane and out-of-plane

lattice parameters have to be taking into consideration. As an example reciprocal space maps (RSMs) of a fully strained and a fully relaxed AlGaN layer on a thick GaN bulk material is shown in Figure 2-16.
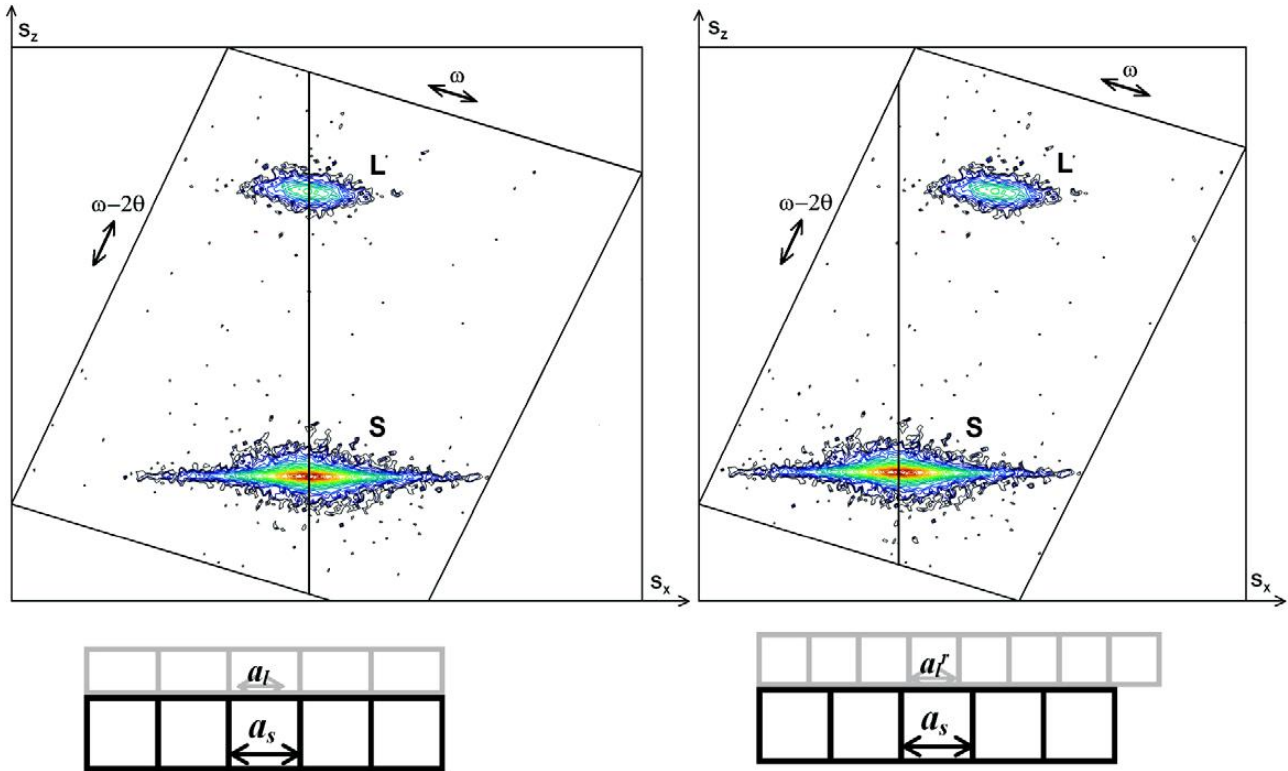
Figure 2-16. RSM of (a) a strained and (b) a relaxed AlGaN layer (L) on a thick GaN buffer layer (S) [250].

An image of the XRD system used in this thesis is shown in Figure 2-17.
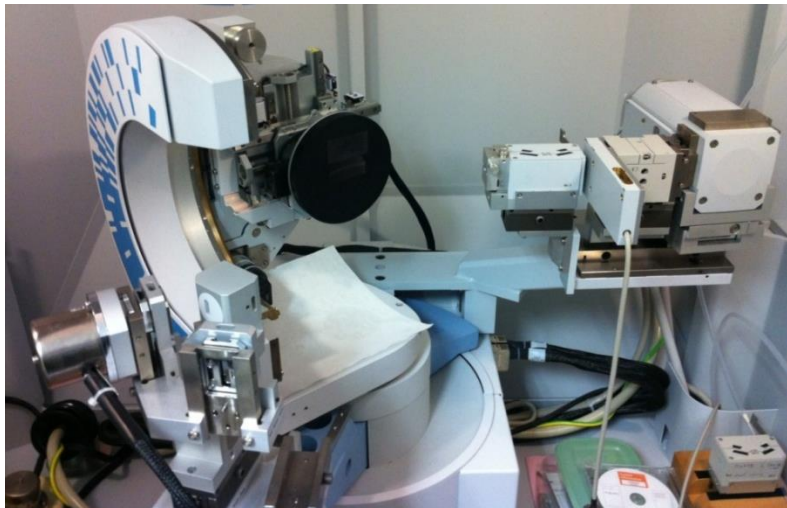
Figure 2-17. Image of the XRD system used in this thesis.

2.3.3   Nomarski Interference Optical Microscope

Differential interference contrast (DIC) microscopy, also known as *Nomarski* microscopy, is basically optical microscope developed by Georges Nomarski in 1953 [252]. Nomarski microscopy principally works on light refraction by different positions of a specimen.

Generally, the optical microscope is one of the most useful instruments in a material research laboratory because it is non-destructive and almost no need for sample preparation. However, when feature sizes are down to sub-micron regime, it becomes almost useless. Normally optical microscopy is useful for feature sizes at around 0.5 *μm* and bigger. For smaller sizes, another kinds of microscopes such as electron microscopes have to be used.

A typical Nomarski microscope configuration is shown in Figure 2-18*a*. An analyser and polarizer are inserted into the optical pathway after the objective and before the condenser, respectively [253].
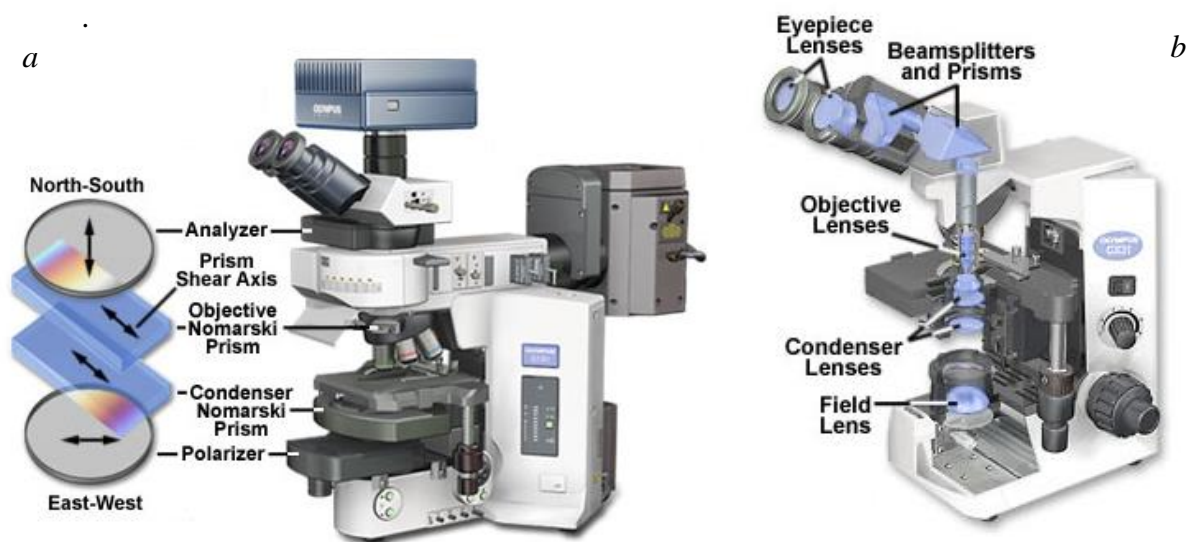
Figure 2-18. Typical Nomarski microscope configuration (a) and locations of the lenses and optical paths [253]

2.3.3.1   Geometrical Optics

The principle of an optical microscope is based on forming an image of a sample on the stage, by an incident light which pass through series of lenses and focus on an optical detector or an eyepiece. Schematic image of a typical microscope with location of lenses and light beam path is shown in Figure 2-18*b* [253]. The main components of the optical microscopes include light sources, microscope objectives, numerical aperture and resolution will be discussed in brief.

2.3.3.2   Light Sources

Modern microscopes today are normally using an incandescent tungsten-halogen lamp as illuminator. Typical tungsten-halogen lamp for optical microscopy is shown in Figure 2-19*a*. The technology of these lamps are based on thermal radiation, able to emit light from about 300 nm up to around 1400 nm. The luminescence spectrum and colour temperature of these light sources are controlled by voltage [253], see Figure 2-19*b*.
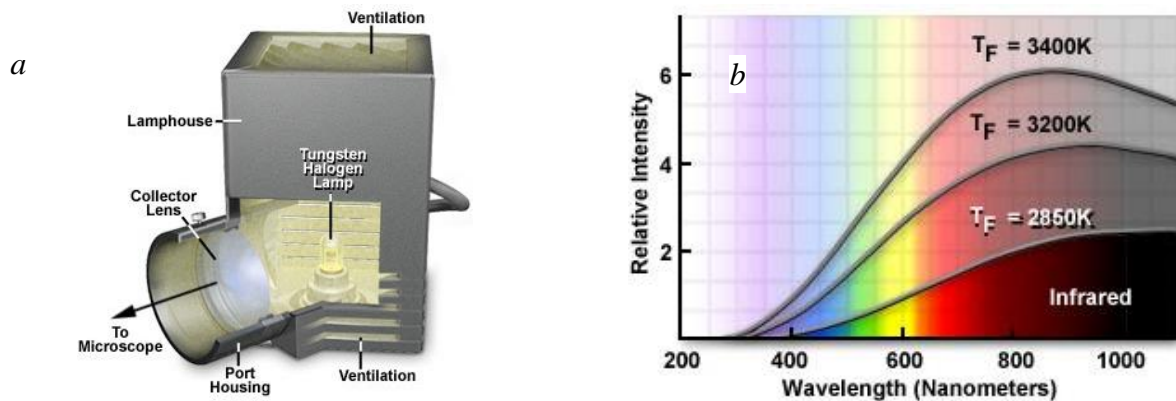
Figure 2-19. A typical tungsten-halogen lamp (a) and thermal radiation spectrum [253]

2.3.3.3   Microscope Objectives:

One of the most important element of an optical microscope is microscope objective. Basically objectives are responsible for formation and controlling the quality of the specimen image. Controlling the magnification and resolution of a sample are other functions of the microscope objectives.

The ultimate resolution of an optical microscope is technically limited by wavelength of illuminating light, the angular aperture of the light trapped by objective and the refractive index of the material between objective lens and the specimen [253]:

Resolution for a diffraction-limited optical microscope can be defined as the minimum distance between two closely spaced specimen points that is detectable [253]:

$$R = \lambda / 2n(sin(\alpha))$$ Equation 2-13

where R is the distance between points, λ is the incident light wavelength, n is the refractive index of the separation material and α is one-half of the objective angular aperture, see Figure 2-20.
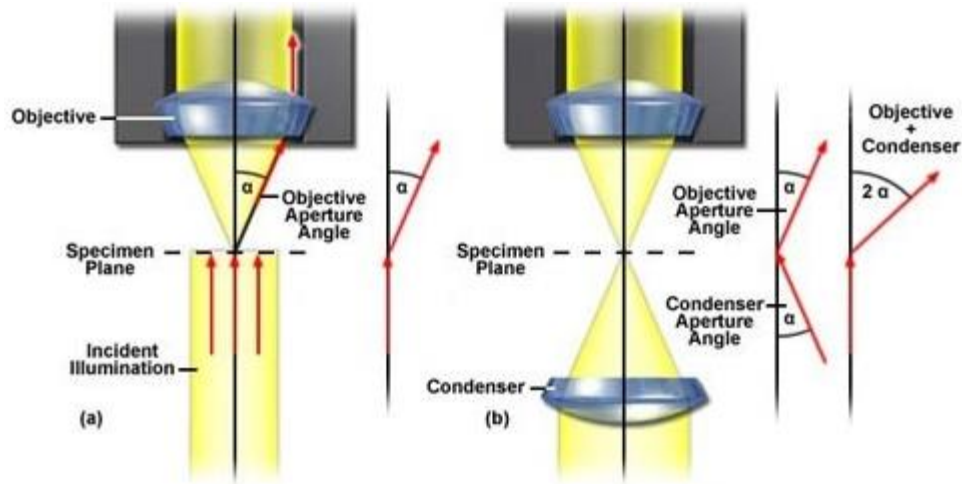
Figure 2-20. Schematic image of a microscope system with an objective and sample illuminated by a light beam without (a) and with (b) condenser [253]

2.3.3.4   Basics and Concept of the DIC Microscopy

Differential interference contrast (DIC) microscopy, also known as Nomarski, is an optical microscopy technique normally used to obtain the better contrast in material science and semiconductor devices characterisation. It is in principle, based on interferometry to get information from the features that are sightless in normal microscopy.

In the DIC microscopy, the interference of two polarised beams separated due to different optical paths is detected. Contrast is generated by different physical path length or different refractive index of different neighbouring areas of a specimen. A light beam which is already polarised by passing through a polariser, passes through a Nomarski prism which spatially splits the light beam. The two beams travelled to the sample, separated by a small amount (typically much less than 1 µm). The beams then are reflected back (in our case) and are recombined again by the second Nomarski prism. Areas of different height lead to the path difference which is hence visualise by interferometry of the recombined beam at the analyser [253, 254], see Figure 2-18.

The advantages of using the DIC microscopy in comparison with another phase microscopies are including the ability to produce high contrast and excellent resolution with optical colour striking 3D images. Furthermore, in principle, Nomarski microscopy can be used in combination with fluorescence microscopy to get brighter images. In biology, it is also possible to obtain image from living cells simultaneously as it is non-invasive [253, 254].

In this thesis Nomarski Optical microscopy was used for initial characterisation of samples, especially for the nanostructured GaN based LED processing. In nanostructured LED processing the surface

patterning and formation of GaN nano-pyramids are points of concern which need to be examine before growing full structure LED. Optical microscope image of nanostructured GaN material grown on patterned substrate using SAG technique is shown in Figure 2-21 for indication.
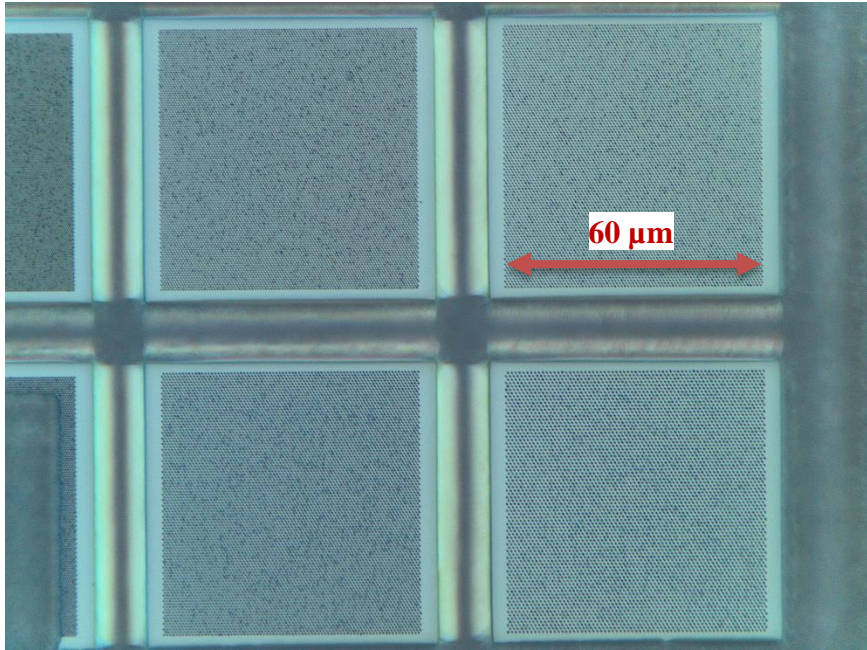
Figure 2-21. Optical microscope image of nanostructure GaN on patterned substrate.

2.4 Optical Characterisation

The study and characterisation of materials is a bold scientific area which relies of variety of experimental techniques. Among these, using electromagnetic radiation is very fruitful. From the X-rays with the very short wavelengths which enable examine the atomic lattice and crystallography of solids (as discussed previously), to wavelength from ultraviolet (UV) through visible and infrared (IR) have huge capabilities to examine many kinds of material properties especially semiconductors, including; band-gap measurement, crystal lattice, impurity and defect level, localisation of carriers, etc. Another advantage of optical characterisation of materials is that generally they are not destructive. These properties make it very useful, particularly for day-to-day analysis to determine material's intrinsic and extrinsic characteristics.

In the following section, these optical characterisation techniques which have been used in this thesis will be briefly discussed.

2.4.1   Photoluminescence Spectroscopy

Luminescence is the defined as spontaneous emission of the light when electronic states of a physical system is excited (excess over Planck's radiation). The emission is happening when the material is excited by an excitation source. If excitation proceed by absorption of the light it is called *photoluminescence (PL)*, by an electric current *electroluminescence (EL)*, by a chemical reaction *chemiluminescence*, and so on [255].

2.4.1.1   PL Process

Photoluminescence (PL), is a non-destructive spectroscopy technique which can be used to examine the electronic and photonic properties of materials. Light from either laser source or a lamp, is focused on sample and excite materials inducing non-equilibrium electron and holes. This process is called "photo-excitation". During this process, the excess energy resulting from photo-excitation will affect electrons to jump from a lower state to higher and permissible state (from valance band to conduction band in semiconductors). When these excited electrons fall back to their equilibrium states, the electron energy is released (through different possible paths), including emission of light with the specific energy equal to energy difference between two levels. The emitted light then collected and focused by optical components, directed to a photo detector (PD) via spectrometer. Sample can be mounted in a cryostat sample holder and cooled down or heated up to the desired temperatures. Particulary low temperature measurements are interesting because it can provide more detailed spectroscopic information by reducing thermally activated non-radiative recombination process and thermal broadening of the studied bands. Detailed information about PL and recombination processes were given in section 1.3.

2.4.1.2   Excitation sources:

Depending on particular tasks and materials, different kinds of light source can be used as excitation sources, coherent; continuous wave (CW) lasers, pulsed lasers and broadband; various lamps.

Lamps:

Two types of lamps are mostly used in spectroscopy: incandescent and arc. Incandescent lamps act as a blackbody radiators. At high current, high temperature tungsten filament in a bulb generate Planck's radiation (mostly in visible to infrared region) [256]. For UV applications incandescent lamps are not useful because of weak intensity in this spectral range. Arc lamps can be used to fulfil this gap. Ionised gas generate light in arc lamps using discharging energy through the gas molecules.

The most widely used arc lamps are high-pressure xenon (Xe), mercury, and deuterium lamps. The spectral output of the light source for typical lamps are shown in Figure 2-22.

Xe lamps are more common excitation light source than other lamps like mercury, because undesirable lines which appears on top of the spectral background is less in Xe lamp than Hg or D_2 lams [256].

Xe arc lamp, which has been used in this thesis, can generate continuous light as a results of recombination of electrons with ionised Xe atoms, in the range of 250 to 700 nm, see Figure 2-22.
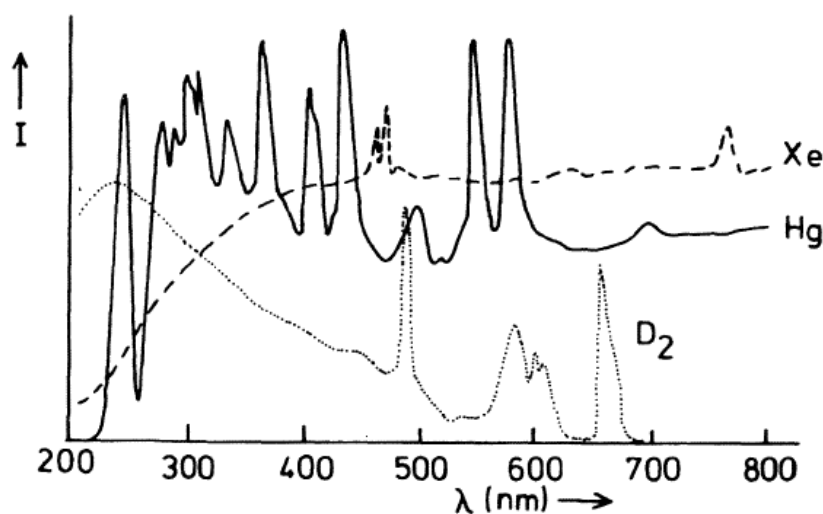
Figure 2-22 Spectral output of typical continuous Xe, Hg and D2 arc lamp [256].

Lasers:

Based on the special features of a laser sources such as coherency, ability to produce high power, small divergence, monochromaticity and capability to generate short pulses, they are perfect excitation light sources for spectroscopy in general and PL, specifically [256].

Gas lasers which use a gas as the lasing medium are very common, the most common thereby are He-Ne, Ar, Krypton, Excimer and metal vapour lasers like He-Cd.

He-Cd lasers are in the gas laser family and relatively economic light source. This type of continuous wave (CW) lasers are good monochromatic light source with excellent intensity and frequency stability for violet (441.5 nm) and UV (325 nm) emission. In this work a Kimmon made IK Series He-Cd Laser with dual wavelength of 325 nm and 442 nm (with the maximum nominal power of 25

mW and 100 mW, respectively) has been used for excitation of QWs in the UV and visible range. See Figure 2-23.

Figure 2-23 IK Series He-Cd Laser and power supply used in this thesis.

Argon lasers are another powerful continuous-wave lasers in the visible and near-ultraviolet region. Transitions on Ar ions are responsible for lasing, either in the singly ionised (Ar^+) or doubly ionised (Ar^{2+}) atoms. Wavelengths of 528.7, 514.5, 488.0, and 457.9 nm can be laser line of Ar+ and 351 and 300 nm from Ar^{2+} [256]. In this thesis Coherent Innova 300C CW argon ion laser has been used as an excitation source, mostly for UV PL spectroscopy at the wavelength of 244 nm (second harmonic of the 488 nm line). The power of the laser is nominally limited to 125 mW with the spot size of ~1.5 mm. An image of the laser system is shown in Figure 2-24.

Figure 2-24 Coherent Innova 300C CW argon ion laser.

2.4.1.3   Detection system:

To have a successful photoluminescence spectroscopy it is needed to be able to detect weak signals. Among all types of photo detectors photomultiplier tube (PMT) and the charge coupled device (CCD) are the most widely used in PL spectroscopy.

Photomultiplier tube (PMT)

The PMTs are very sensitive detectors of photons in the UV, visible, and near-IR ranges. Incident light where multiplied by detectors by the factor of 100 million times, generate current and enabling detection of individual photons when the incident flux of light is very low [256].

A photomultiplier tube consists of an input window, a photocathode, focusing electrodes, an electron multiplier an anode sealed in a glass tube which normally evacuated. The schematic construction of a PMT is shown in Figure 2-25 [257].
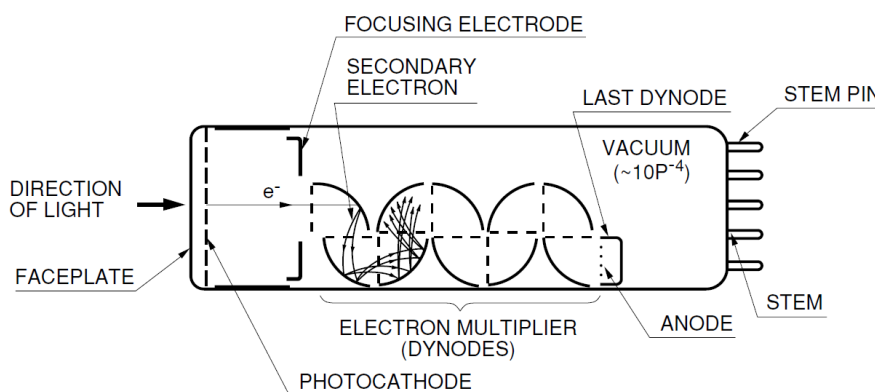
Figure 2-25 Schematic view of a photomultiplier tube [257].

Charge coupled device (CCD)

CCDs are imaging detectors with growing popularity in spectroscopy due to impressive characteristics such as remarkable sensitivity and linear dynamic range [258]. Using the CCD image detection method is back to 1970 [256]. A CCD consists of arrays of metal-oxide-semiconductor (MOS) capacitors. The MOS is a two terminal device consisting of three layers: a semiconducting layer (like silicon) called the body, a separating insulator (usually an oxide layer) and a metal gate electrode. Each pixel which consists of three gates, acts as a collector where number of electrons trapped under the gate is proportional to the number of incident photons [258]. The collected charge at each pixel point can be converted to two-dimensional image and made visible, using computer.

2.4.1.4 *Light-Dispersing Elements (LDE)*

In luminescence spectroscopy in general, light dispersing elements are used for two main reasons: Light monochromation and analysing the wavelength distribution of emitted light [256].

Here we use *monochromators* based on diffraction gratings to disperse light. A typical *monochromator* system consists of tunable entrance and exit slits, a grating, and focusing mirrors. Monochromator selects a narrow band of wavelengths λ from a source of the light. The spectral band is centred on this wavelength, which can be tuned. Therefore monochromator can work as a tunable filter with a band pass λ and resolution Δλ/λ depending on reciprocal dispersion of the grating or prism used and slits widths. Light enters the monochromator through a narrow entrance slit. It is then dispersed after hitting the prism or grating, breaking into its spectral components, by the nature of wavelength-dependent refractive index. Light reflection from grating depends on wavelength, incident angle and groove spacing [248].

A reflection diffraction grating is an optical component with periodic structure (grooves) made by etching or ruling a series of lines onto a polished reflecting surface. The density of grooves varies typically from 300 to 3600 lines/mm [256]. Figure 2-26 shows the schematic view of a typical grating.
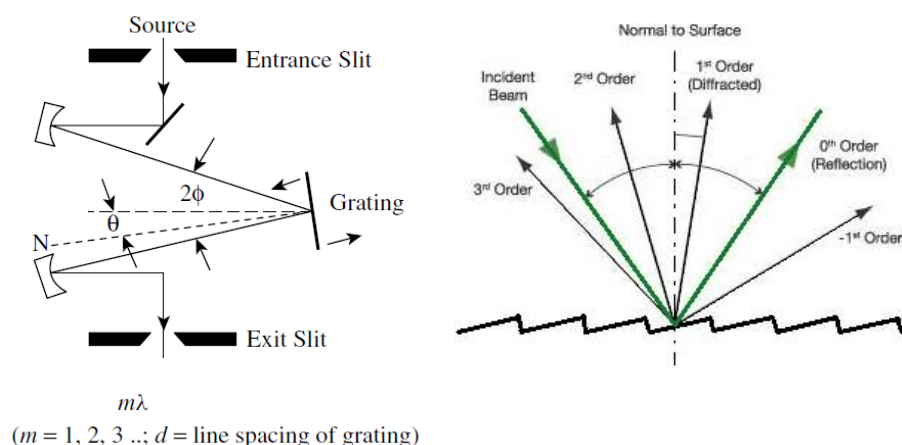
Figure 2-26. Schematic view of a monochromator and a typical grating [248].

When monochromator is located between the light source and the emitting sample, ensuring that only selected wavelengths are able to pass through and hit the sample, it is part of excitation system. Otherwise it can be placed between the studied sample and detector (single channel one like PMT or photodiode), in this case it is part of detection system. If all wavelengths allowed to be incident on the detector (CCD in this case) at once (when exit slit is absent or fully open) after being spectrally resolved by transmitting through a prism or reflecting from a grating, then the instrument is known as a *spectrometer,* see Figure 2-27.

One of the critical parameters in PL spectroscopy is stray light level. Stray light is defined as any light with undesired wavelengths which passes through monochromator [258]. If we consider Xe lamp as an exciting light source, the UV intensity of the lamp spectrum, which is used for excitation,

is much weaker than that for visible region, therefore longer wavelengths passed by monochromator can be comparable or even stronger than emitted light itself. That's why double-grating monochromator is very popular in spectroscopy, especially in excitation source, although light output intensity is getting weaker [258]. Another difficulty would be with scattered light from excitation source which path through emission monochromator and can contribute to the luminescence intensity and invalidate the measurement. Double-grating in spectrometer or using holographic grating can be a solution for this [258].

Horiba iHR-320 spectrometer with grating monochromator and Horiba MicroHR and Gemini 180 with double planar grating monochromator have been utilised for PL and PLE spectroscopy of this thesis.
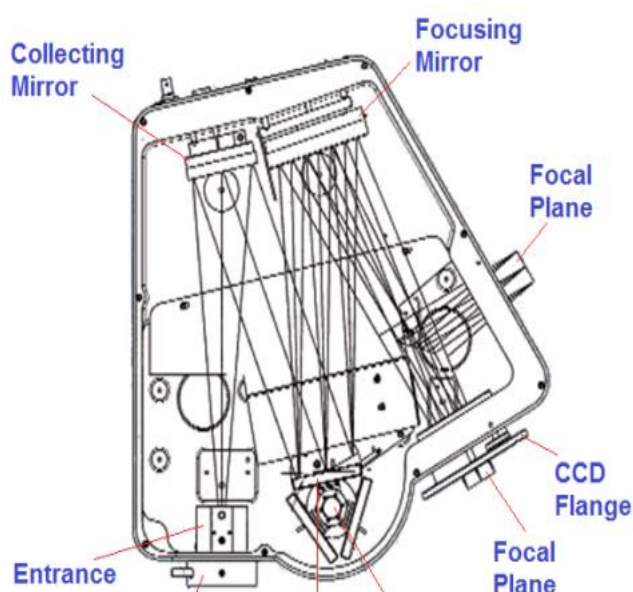
Figure 2-27. Horiba iHR320) spectrometer [259].

2.4.1.5   Temperature control system

A Closed Cycle Helium Janis cryostat system was used in this work as a temperature control system which enables variation of sample temperature nominally in the range of from 10 to 500 K.

2.4.1.6   General description of PL setup

The schematic of the PL set up used in this thesis is depicted in Figure 2-28 (*a*). The sample is mounted on sample holder in a variable temperature cryostat and is excited with either laser beam or a monochromatised emission of Xe lamp typically with the photon energy of higher than the band-

gap energy of the studied material. The emitted light is then collected using two lenses and focused onto the entrance slit of the spectrometer. Here the grating based single monochromator (Horiba iHR320) spectrometer has been used to collect and disperse the emitted light as shown in Figure 2-28(*b*). The PL spectrum is detected with either a PMT in wavelength-by-wavelength scanning mode or with CCD by 60-120 nm segments (depending on different grating used).
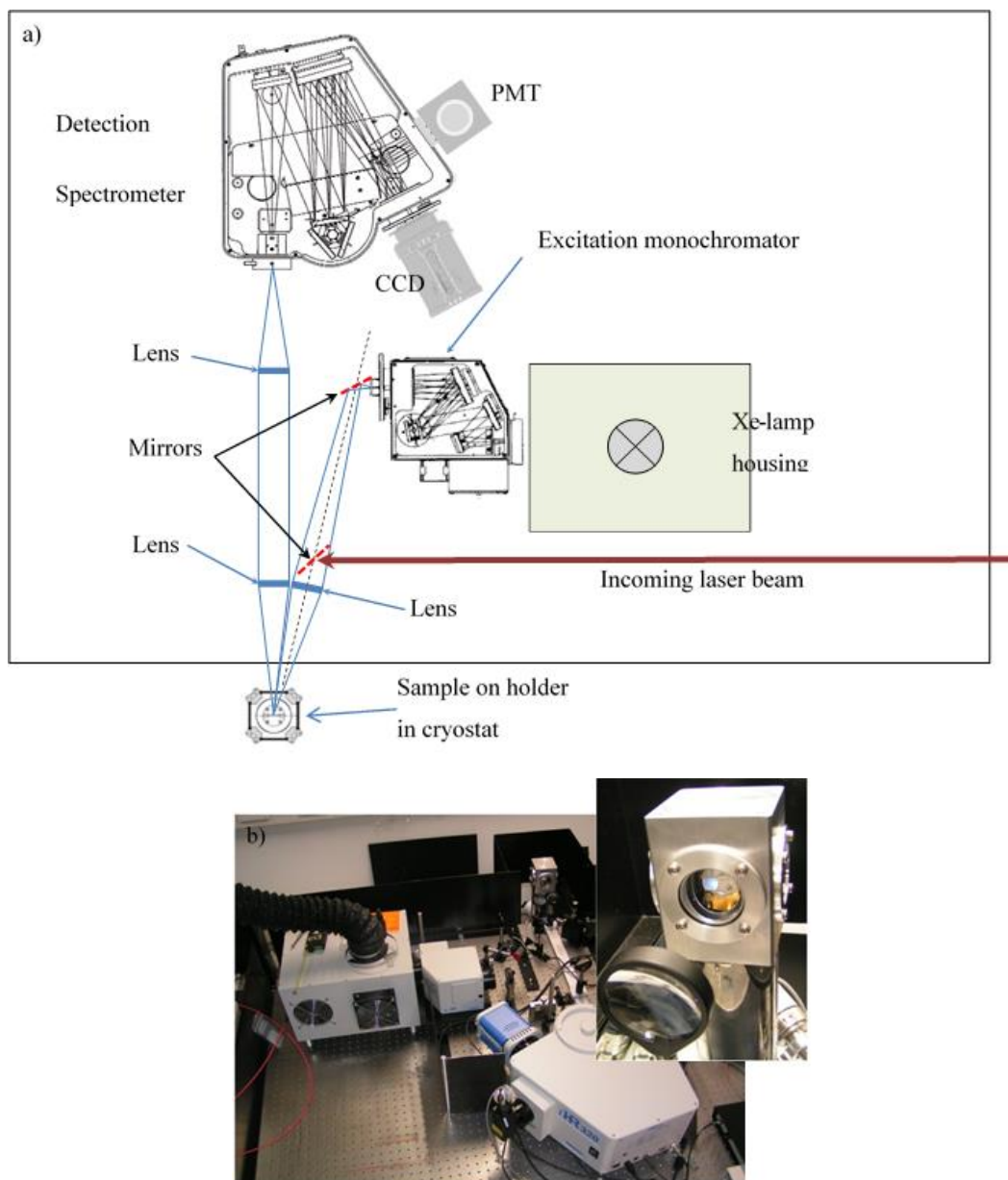
Figure 2-28 a) Schematic view of PL set-up with instrumentation used in this thesis. b) Top view image of the PL set-up.

The typical PL spectrum of an AlGaN sample is shown in Figure 2-29 with indications of the near-band-edge and a defect-related emission. Useful information can be deduced from PL spectra such as: band-gap measurement, recombination mechanism (radiative and non-radiative), material quality, impurity levels [260].
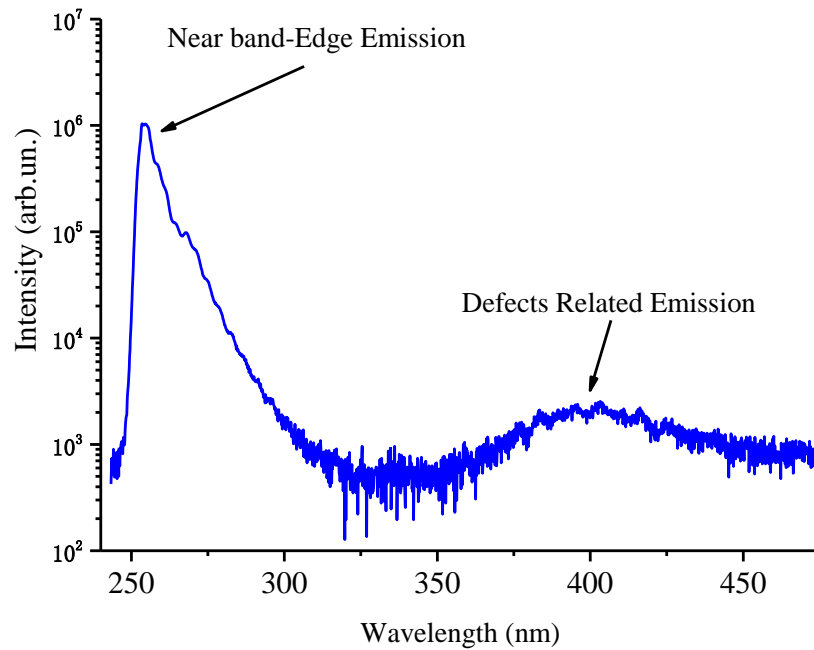
Figure 2-29. Photoluminescence spectrum of a typical AlGaN sample done in our group at low temperature (10 K).

2.4.2 Photoluminescence Excitation Spectroscopy

While in conventional PL spectroscopy excitation source wavelength is fixed and emission spectrum is measured, another scheme can also be useful. When detection system is fixed at a certain wavelength corresponding to PL spectrum of studied sample, the excitation wavelength (energy) can be varied, and the effect of this variation on the intensity of the detected signal is measured. This technique is called PL excitation or PLE spectroscopy. PL and PLE are very connected and it can be very beneficial to apply both test on a specimen

This technique offers some advantages in characterization of semiconductors because it shows resonant excitation at important PL features such as exciton peaks etc. As shown in Figure 2-28 (a) the Xe-lamp source with the low energy density of ~10^{-4} Wcm^{-2}, illuminates the sample for absorbance measurements and it is known that absorption and PL are closely linked. So, it is valuable to be able to perform both PL and PLE on a given sample [261]. Since the PL signal detected in PLE is proportional to the portion of absorbed excitation light, to some degree PLE is equivalent of absorption spectroscopy with advantages of being able to gain signals from thin layers. Based on simple calculation shown below, there is a limitation of absorbance (and thus thickness) allowing for

measurement of the absorption spectrum. Ignoring reflection, incident and transmitted signals are related with Beer–Lambert–Bouguer law:

$$I = I_0 e^{-\alpha x}$$

Equation 2-14

To be able to detect signal and measure absorption reliably, the ratio between transmitted and incident lights should be roughly between 1 to 10 %, i.e.:

$$0.01 \leq \frac{I}{I_0} \leq 0.1,$$

Equation 2-15

resulting in the requirement of $2.3 \leq \alpha x \leq 4.6$ which for the material like GaN ($\alpha_{(350\ nm)} \approx 10^5 cm^{-1}$ [262]) [170] corresponds to the following thickness limitation $230\ nm \leq x \leq 460\ nm$. This means that at least ~200 nm thick GaN layer needed to get the reliable signal, and, therefore, the absorption spectrum of much thinner layers, like quantum wells, is strongly complicated by the direct measurement but still accessible by mean of PLE spectroscopy.

A typical PL, PLE and absorption spectrum of beryllium doped gallium nitride (GaN:Be) at room temperature is illustrated in Figure 2-30.
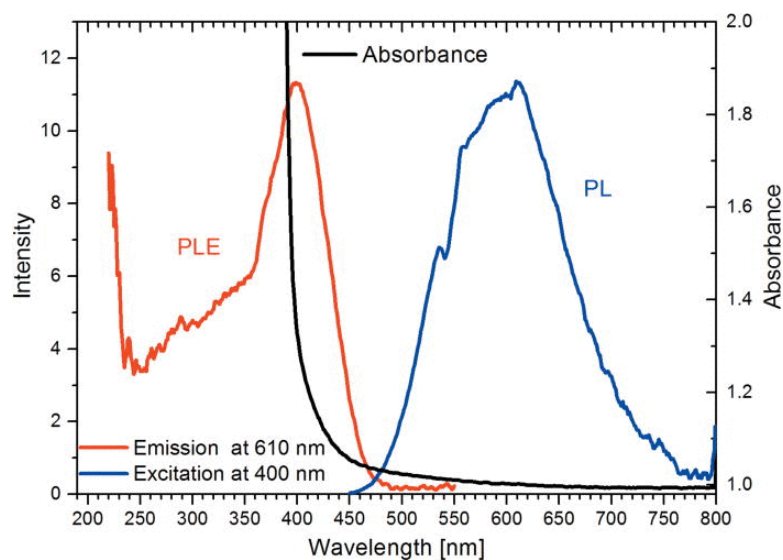
Figure 2-30 Typical PL, PLE and absorption spectrum of beryllium doped gallium nitride (GaN:Be), for PL sample, was excited below band gap at 400 nm [263].

Information that can be collected from a given sample using PLE and PL includes band-gap, degree of defects and disorder, and internal quantum efficiency (IQE).

The effective band-gap of nitride semiconductors can be determined using sigmoidal fitting of PLE spectra [161]:

$$I(hv) = \frac{I_0}{1 + exp\left(\dfrac{E_{g,\,eff} - hv}{\Delta E}\right)}$$

Equation 2-16

where I_0 is the intensity at 0 K, $E_{g,eff}$ is effective band-gap and ΔE is broadening parameter. Another factor which is affected by composition (therefore band-gap) is shift on the peak emission energy. For a given bandgap of a material, ΔE is an indicator of the material quality and a factor of non-uniformity of composition. With combination of PL and PLE, Stokes Shift of spectra and a degree of excitonic localisation can be determined. This is very valuable especially to examine the In content of the III-Ns, InGaN and InAlN. A room temperature PL and PLE (absorption) emission spectra of an InGaN sample is depicted in Figure 2-31. It can be seen from Figure 2-31 that both emission and absorption spectra increase with increasing of In content due to immiscibility of InN in GaN and thus composition fluctuation at higher indium incorporations (higher emission energies). Also, it shows that the Stokes' shift depends on emission energy and therefore alloy composition, which is an indication of degree of localisation of excitons [184]. Both these observations are indications of material disorder where obtained from photoluminescence spectroscopy.
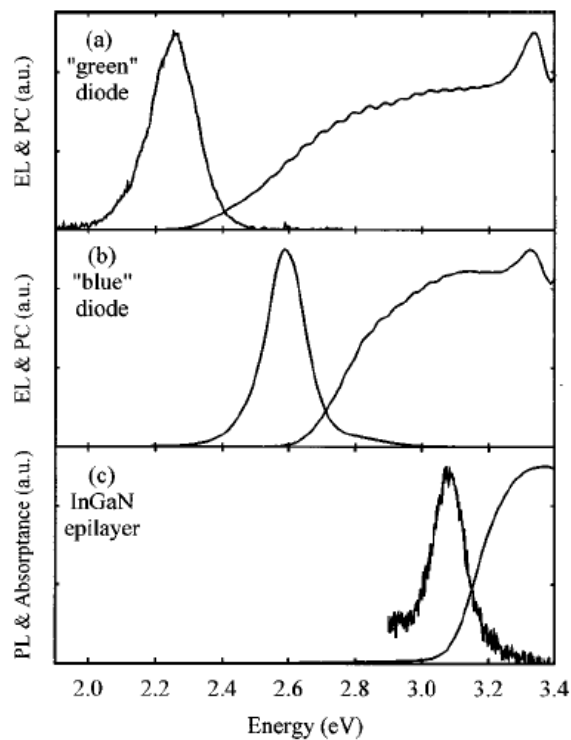
Figure 2-31. PL and PLE (absorption) emission spectra of emission and absorption spectra of InGaN at room temperature [161]).

Another valuable factor that is obtained from photoluminescence is quantum efficiency of emitting material. One straight forward technique to measure the apparent IQE is to divide integrated intensity PL (or PLE) ta low temperature to its value at room temperature:

$$IQE \approx \eta(T) = \frac{I^{int}(RT)}{I^{int}(LT)}$$
<div align="right">Equation 2-17</div>

where $I^{int}(RT)$ and $I^{int}(LT)$ denote the integrated intensity at room and low temperature, respectively.

2.4.3   Cathodoluminescence Spectroscopy

Cathodoluminescence (CL), similar to other optical characterisation techniques, is a non-destructive contactless method based on the emission of light from a specimen excited by an electron beam. CL spectroscopy is very similar to PL most of the futures, except for the excitation source. The electron source utilised in cathodoluminescence could be the electron beam gun used in SEM, an advantage is that a CL spectrum can be accompanied by an SEM picture of the same sample.

Like PL spectra, CL spectra shows useful information, some of those listed in section 2.4.1 as examples. Another advantage of CL is the absence of scattered exciting light, which is especially important for samples with rough surface morphology [264].

2.4.4   Electroluminescence Spectroscopy

Another spectroscopy technique similar to PL is *electroluminescence* (EL), which can be used to examine the light-emitting devices such as LEDs. Apart from many similarities, the main difference between EL and PL is that in photoluminescence the excitation source is light while in EL the excitation is electrical current. In both cases, luminescence from the specimen is detected. As mentioned earlier in section 2.4.1, in PL, electron-hole generation results from the photon excitation, while, in EL, the electrons are electrically injected into the conduction band and holes into the valence band. PL and EL spectra may be similar for the same sample but not necessarily identical, because of different excitation mechanisms[265].

Sharp emission lines, sometimes observed in the PL/EL spectra which could be related to the exciton recombination from a high quality, single crystal material or a single quantum dot. Such devices,

which are able to emit excitonic single photon are promising for developing electrically driven single-photon emission sources, utilised in many photonic applications such as optical communication [265].

2.5 Electrical Characterisation of Materials and Interfaces

The electronic properties of the materials (here especially semiconductors) needed to be well understood for any electronic and photonic devices. There is a variety of methods that focus on different perspective of the electronic structure of semiconductor materials and explore different effects. Some of these techniques are briefly discussed here and more descriptions can be found in the affiliated references.

2.5.1 Contact Resistance Measurement

Resistivity is one of the most important electrical parameters of semiconductor materials. In electronic and photonic devices, the contacts are critical parts of the device, and it is very useful to measure the contact resistance to be able to know how it might affect device performance. Contact resistance can be determined using an extension of the conventional technique like a simple resistor. Metal-semiconductor contacts consist of two basic categories, vertical and horizontal (or lateral), based on the current flow directions. These two types of contacts can behave differently. Generally, the total resistance between two metal contacts over a semiconductor (see Figure 2-32) can be calculated using the following equation:

$$R_T = 2R_m + 2R_c + R_{semi} \qquad \text{Equation 2-18}$$

Where R_m is the resistance of the metallic connector, R_c contact resistance and R_{semi} is semiconductor resistance [248].

The contact resistance itself depends on the size of the contact, hence contact resistivity can be used, instead. If a small region in the vicinity of the contact be considered, then the contact resistivity would be:

$$R_c = \rho \frac{\Delta x}{A_c} \rightarrow \rho_c = \lim_{\Delta x \to 0} (\rho \Delta x) = R_c A_c \qquad \text{Equation 2-19}$$
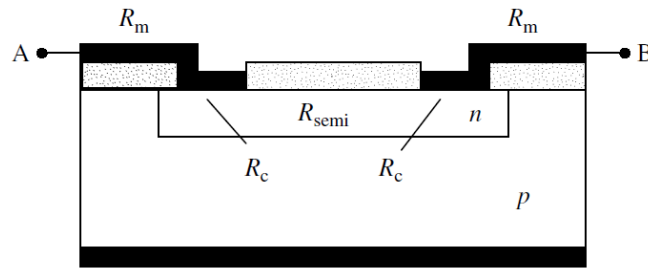
Figure 2-32. A schematic diagram of a semiconductor device with two metallic contacts [248].
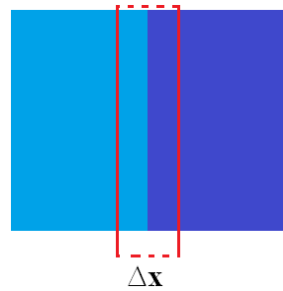
Figure 2-33 A schematic view of a metal-semiconductor contact.

Where ρ_c and A_C are resistivity and the area of the contact, respectively. With typical ρ_c values in the range of 10^{-3} to $10^{-8} \Omega \cdot cm^2$. The contact resistance of an active device and interface connection becomes larger as the dimensions are scaled down.

The current flow through the semiconductor is almost uniform, but it is not in the case when the current flows into the contacts. At the edge of the contacts, the current flow density becomes very high locally, as shown schematically in Figure 2-34 (a). This is known as "current crowding". In this case, the current drop-off from the edge of the contacts will be [248]:

$$I(x) \propto exp\left(-\frac{x}{L_T}\right),: L_T = \sqrt{\frac{\rho_c}{R_S}}$$

Equation 2-20

The distance in which most of the current travels from the semiconductor into the metal or from the metal into the semiconductor is defined as *transfer length (L_T)*. R_S is sheet resistance. The transfer length is normally about or less than 1 μm, some part of the metal contacts are inactive for such contacts bigger than 1 μm [248].
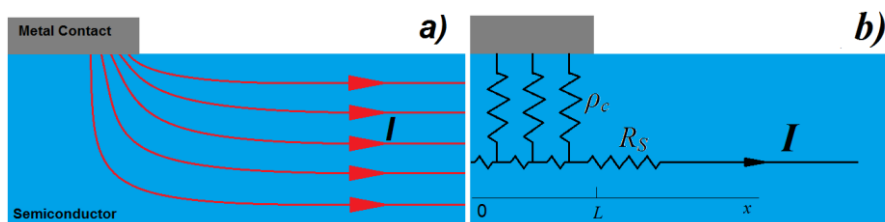
Figure 2-34 a) Schematic diagram of the current crowding effect, b) equivalent circuit of the current crowding effect.

Now, let us consider the contact configurations used in this thesis, called transmission line method test structure (TLM). Here voltage and current are measured across the same contacts from contact 1 to contact 2. In this geometry the effective area of the contact will be $L_T W$, then contact resistance R_C would be:

$$R_C = \frac{\rho_c}{L_T W} = \frac{R_S L_T}{W} \rightarrow R_T = \frac{R_S}{W}(L + 2L_T)$$

<div align="right">Equation 2-21</div>

The plot of R_T against resistor length, L, transfer length can be measured, using extrapolation of the plot back to the horizontal axis, where the intercept is equal to $-2L_T$, see Figure 2-36. Consequently, the contact resistance can be calculated.
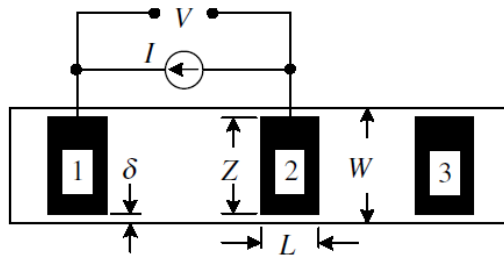
Figure 2-35 TLM contact resistance test structure [248].
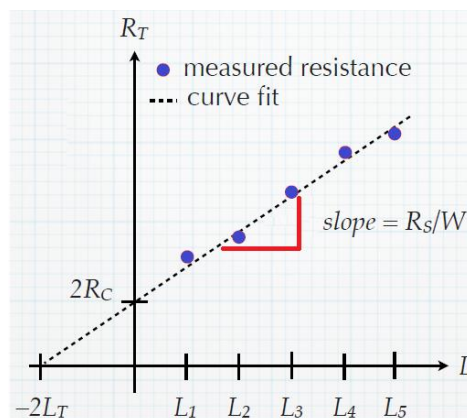
Figure 2-36 R_T versus L and measurement of contact resistance.

In addition to the technique discussed above, another geometry with the same basics can be used to measure the contact resistance which circular features are used, as depicted in Figure 2-37. This is so-called Circular Transmission Line Measurements (CTLM) technique. Then, for $d/L \ll 1$ we will have [248]:

$$R_T = \frac{R_S}{2\pi L}(d + 2L_T)$$

<div align="right">Equation 2-22</div>

And contact resistance can be calculated using the same technique as in TLM. Using circular test pattern allows elimination of the errors introduced by lateral current crowding and gap effect, which normally occur in linear TLM structure [266].
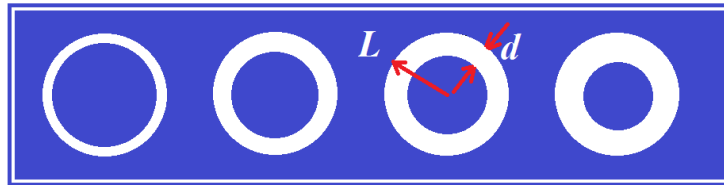
Figure 2-37 Circular contact resistance test structure.

2.5.2   Current-Voltage Characteristics

The current–voltage characteristics of an electronic device can be defined as the relationship between the DC current and the DC voltage through an electronic device. These techniques are used to measure and model the basic parameters of a device and its behaviour.

Semiconductor devices like diodes and transistors are all made of PN junctions. In such a devices I-V characteristics curves will indicate the operation of these PN junctions [267].

A typical diode characteristic is shown in Figure 2-38. For a light emitting diode (LED) the operating region is in forward-bias.
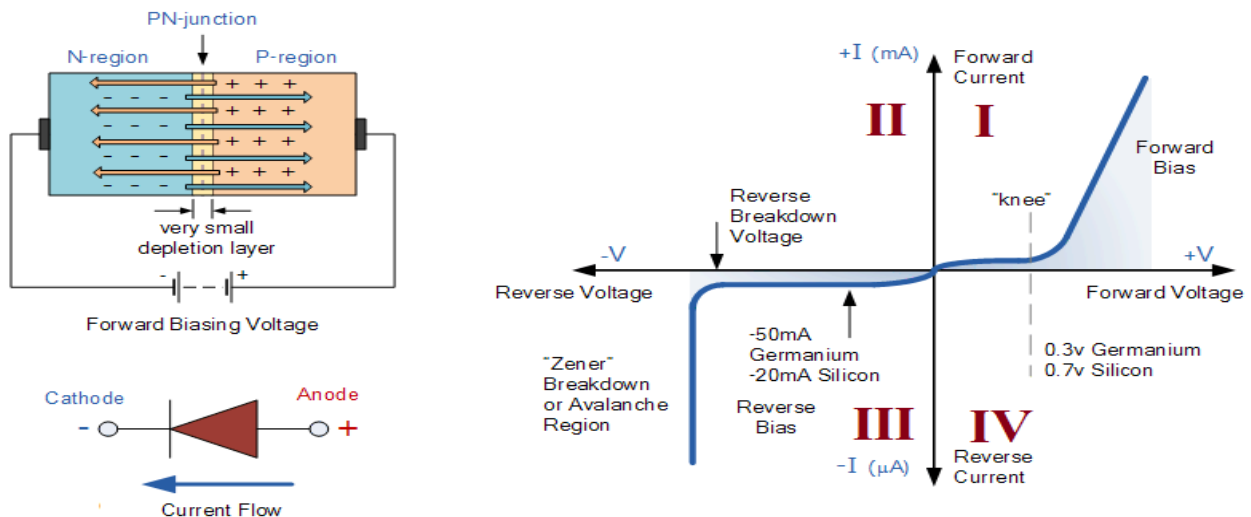
Figure 2-38 I-V characteristic curve of a Diode [267].

2.6   Fabrication of Light Emitting Devices

After GaN epitaxy, LED processing generally includes two main phases; *frontend* and *backend* processes. The LED front-end fabrication process involves mesa etch, metallization and electrode contact formation and passivation. Backend processing includes some stages like grinding, dicing, and binning.

To have a better view of these processes in the following section we will briefly discuss the technologies used for fabrication of LEDs in this project.

2.6.1   Photolithography

The fabrication of an LED requires a variety of chemical and physical processes performed on a semiconductor (here nitrides) wafer. By creating structures of the components, several devices can be built. One of the fundamental processes to make these devices is optical lithography or photolithography.

The word lithography comes from the Greek words of *lithos* and *graphia*, meaning stones and to write, respectively. Which literally means writing on stones. In the matter of lithography in this thesis, our stones are GaN wafers and the patterns are written with a light sensitive polymer called photoresist. The photoresist is exposed to the light (normally UV) via a designed mask and developed to form an image on the wafer. Ideally, photoresist image has the exact shape of the designed mask, with vertical walls across the width of the resist. The final resist pattern is including two regions; parts which uncovered completely while other parts are covered with the resist, this is necessary for pattern transfer, because the parts which covered with resist will be protected from processing (e.g. etching).

The steps for a typical optical lithography process are including: substrate preparation, photoresist spin-coating, pre-bake, exposure, post-exposure bake, development and post-bake and finished with resist stripping after the resist pattern transferred on the underlying wafer via etching. When the exposed regions of the photoresist become more soluble after optical exposure (typically UV), it called *positive photoresist*. On the other hand, there are *negative photoresists* which resist becomes insoluble to the photoresist developer, see Figure 2-39.
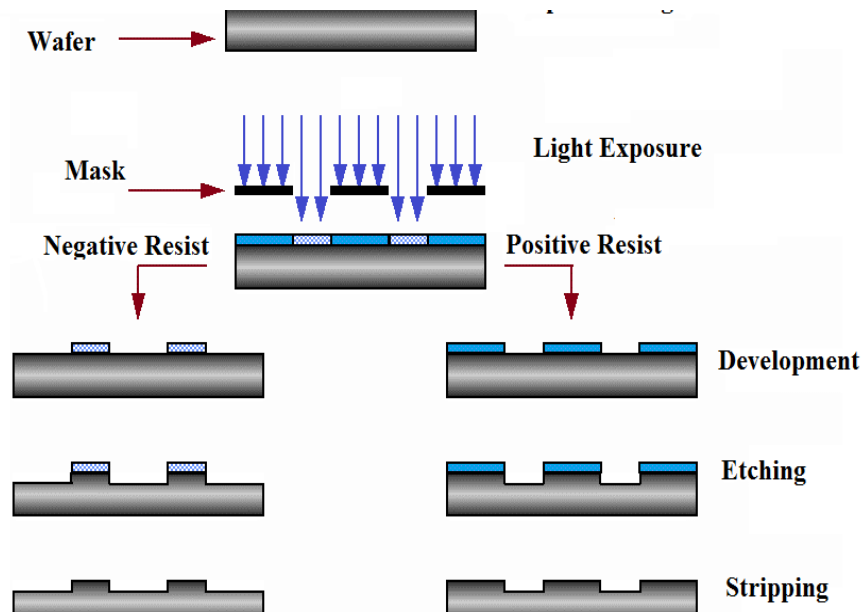
Figure 2-39 Schematic view of a typical photolithography.

2.6.2   Electron Beam Lithography

One of the key fabrication techniques which allows creating nanoscale patterns is Electron Beam Lithography (EBL). EBL started to develop by modifying the scanning electron microscopes in the late 1960s [268]. The EBL basic is very similar to photolithography: A focused beam of electrons is exposed to a wafer through a designed mask covered by a resist which sensitive to electron exposure. Electron beam exposure changes the solubility of the resist. Just like photolithography, two classes of the resist can be employed in EBL. Positive tone resists become more soluble upon exposure to electrons. The classic example of positive resist is polymethyl methacrylate (PMMA), another common positive resist is ZEP resist. Both of these resists consist of a long chain polymer. In a negative tone resist, the exposure of electrons converts the material to lower solubility. Hydrogen silsesquioxane (HSQ) is the first example here. Several other positive and negative resists have been recently developed [269], [270].

Before starting the work, the device must be designed to define the geometry and dimensions of the final device. This information is translated into a special format to be able to be read by the system, so it knows what writing fields and what beam currents are needed. The pattern for exposing is designed using a CAD package. A GDS file is the format generally accepted by industry and most of the available CAD packages are able to make files in GDS format.

Fracturing is a process which is necessary before exposure, where system's software converter translates the GDS data into the language of the EBL system, which contains all the instructions needed for the patterning [268].

Due to multiple elastic and inelastic scattering of the primary electron beam from the resist and substrate exposure, electron dose is distributed through the surface of the sample; this causes the resist outside the scanned pattern to receive a non-zero dose, therefore the developed pattern becomes wider than the scanned pattern. This phenomenon is called the *proximity effect*. The higher doses required at high energies can overcome this problem. On the other hand, low voltage electrons in the range of 1–3 keV causing electron losing most of their energy in the resist, resulting a dramatic decrease of the proximity effect and also less substrate damage [268-270].

2.6.3   Selective Area Etching

The successful achievements of the growth and fabrication of the wide band-gap group-III nitrides have enabled the realisation of several types of devices over the last decade.

Performance improvement in these devices depends on the device processing technologies along with material quality. Especially, effective etching methods are critical to create facets for GaN LEDs, forming mesas, and gate recessing in HEMTs. In comparison with III-V semiconductors, III-nitride materials and alloys have higher bond energies: e.g. 8.9 eV/atom for GaN, 7.7 eV/atom for InN and 11.5 eV/atom for AlN compared to 6.5 eV/atom for GaAs. High bond strengths with wide band-gap make these materials basically chemically inert and resistant to acids and bases at room and elevated temperatures. Therefore different kinds of dry and wet etching methods have been studied for the processing of III-nitrides. Also, external energy is required for the dissociation of the bonds. Ion and electron and optical radiation assisted etching methods are examples of external energetic sources for etching of nitrides. In this thesis, some of these etching methods are applied and will be discussed as follows [271].

Different techniques involving ion-assisted mechanisms, as a dry etch, have been utilized for the processing and fabrication of III-nitrides. This includes reactive ion etching (RIE) and inductively coupled plasma reactive ion etching (ICP-RIE), see Figure 2-40. Optical sources with photon energies higher than the band-gap of the semiconductors can also be applied. In an ICP-RIE system a high-density-plasma confines electrons using a magnetic field to generate very high ion densities. Large

ion fluxes at low energies (or biases) in these systems enhances etch rates and prevents higher damage to sample in comparison with conventional RIE [272].

Inductively coupled plasmas (ICP) were developed to overcome the difficulties regarding high aspect ratio (AR) oxide etch with high selectivity in the early 1990s [273]. As most of the input RF power is consumed by electrons, the electron density is much larger ($> 5 \times 10^{11} cm^{-3}$) in comparison with other plasma etching techniques. Additionally, a second RF source is normally used in ICP reactors to bias the substrate during etching and deliver energy to bombarding ions [272]. For the dry etching of III-nitrides mostly halogen-based, especially chlorine-based chemicals have been mostly utilised. For nitrides etched in Cl-based gases, $GaCl_x$, $InCl_x$, and $AlCl_x$ for the Group III elements are etch products, and NCl_3 or N_2 for nitrogen. The etch rates for GaN using ICP-RIE with different etching chemicals have been reported in the range of ~100 to ~1000 nm/min, depend strongly on the bias voltage. GaN etch rates of 688 nm/min at $-280\ V$ and 980 nm/min at $-450\ V$ have been reported for $Cl_2/H_2/Ar$ and Cl_2/Ar plasmas, respectively [271].
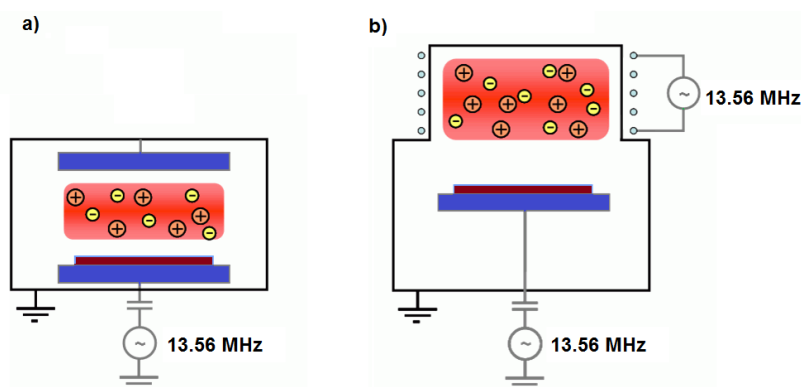
Figure 2-40 Schematic illustration of the conventional RIE (a) and ICP-RIE (b).

For selective area growth (SAG) of gallium nitride and its family silicon nitride (Si₃N₄) is used as a hard mask in this work. To pattern the Si₃N₄ as a hard mask using ICP system with high selectivity over III-nitrides usually fluorine-based chemicals such as CHF_3, CF_4, SF_6 are applied. [274, 275].

2.6.4   Metal Contact

Metal contacts are required to link the semiconductor device to the circuit via wires. Such metal contacts are generally deposited using physical vapour deposition (PVD) techniques such as evaporation or sputtering. In PVD metal physically vaporises either by sputtering process or heating and condenses again on the substrate surface of the wafer to form a solid layer. PVD is very important in semiconductor manufacturing. In sputtering a metal target (for example Al which is typically

alloyed with 1% Si and 4% Cu to improve the electrical and metallurgical properties of the Al [276]) is placed in Ar plasma and bombarded with ionic atoms. Metal atoms are then physically sputtered because of momentum transfer leading to this deposition on the surface of the wafer [276]. Sputtering is the dominant method in metallization due to high purity, better adhesion and uniformity [277].

In evaporation the wafer is located inside a vacuum chamber, where the metal to be deposited is also located. Metal is then heated to the vaporisation point and starts to evaporate. The basics of all evaporation techniques are generally similar. Resistive (thermal) evaporation and e-beam evaporation are two main categories of evaporation, based on the heating method. In resistive evaporation, the material container (normally a tungsten boat), is electrically heated using the high current to make the metal evaporate. Thermal evaporation is useful for metals with lower melting points, like Al. On the other hand, in e-beam evaporation, the electron beam is directed to the material causing local heating and evaporation. E-beam evaporation is applicable for almost all metals and especially for high melting point metals where it is not possible to use resistive evaporation.

Ohmic Contact to Nitrides: One of the challenges facing the fabrication of the GaN-based devices is to have low resistance metal contact to these semiconductors to improve reliability and efficiency of GaN-based optical and electronic devices. High quality Ohmic contact is essential to have lower applied voltage and minimum dissipation of the power. Also, as the dimension of the devices continues to decrease this low resistance metal-semiconductor contact will be more critical. It is actually affected by a number of device processing steps, specially depends on the quality of the GaN epilayer, surface treatment, metal deposition technique and post metallisation treatment [266].

In addition to the crystal quality, the conductivity of GaN epilayer has a significant influence on the on the resistivity of the metal-semiconductor (MS) contact. The conductivity of the epilayer can be enhanced by doping. It has been shown that by heavily doping of GaN epilayer directly beneath the metal contact with the thickness comparable to the width of the depletion region, contact resistance could be minimised [278]. Aside from doping, post annealing can affect MS interface to create an overall metal like region with good Ohmic contact [266]. To enhance the electrical integrity of the Ohmic contact, other ways of interfacial modification can be utilised, such as the bombardment of the GaN surface with energetic ions prior to metal deposition to achieve clean and oxide free with donor-like damaged surface, resulting in a very high interfacial conductivity [279]. Cleaning and removing the native oxide layer on the surface of GaN epilayer (with play as an electrical barrier) is

essential to achieve reliable Ohmic contact. Aside from ion etching, wet chemical etching using common acids and bases like the phosphoric acid solution, NaOH solution, BHF can also effectively remove oxides and other contamination on the surface [266].
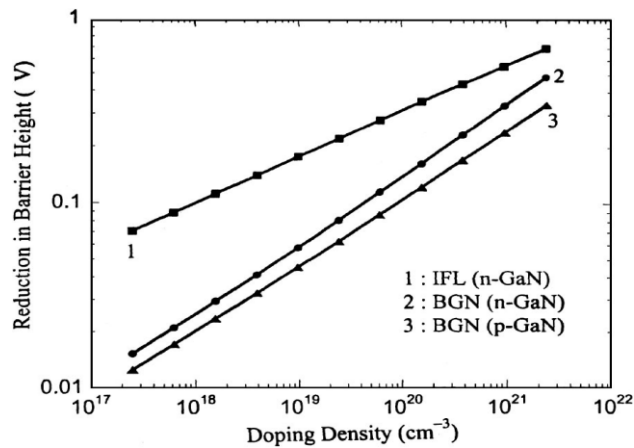
Figure 2-41 Reduction in barrier height as a function of doping density [278].

Also, metallization design, metal selection and deposition technique affect the properties of Ohmic contact. Ohmic contact to n-type GaN, can be made using the metals with the work function (Φ_m) lower than that of n-GaN, Although, in practical conditions, maybe a reaction occurs between metal and semiconductor at the interface and form a new compound with new electronic properties. Work function of Al is 4.08 eV [280], as an example, $\Phi_m(Ti) = 4.33$ eV, $\Phi_m(Ta) = 4.25$ eV and $\Phi m(V) = 4.3$ eV [281]. Using the above mentioned metals and their compounds, low contact resistance with n-GaN have been achieved, as low as in the range of $10 - 5 \times 10^{-8} \Omega \cdot cm^{-2}$, which low enough for optoelectronic applications [281]. Although there were plenty of designs for metallization, multilayer composite and compound intermetallics are the most common. Ti/Al/X/Au stack followed by around 800°C thermal annealing is the most widely used design for Ohmic contacts to *n*-type material in the fabrication of GaN devices, where X is a diffusion layer for Au which for instance can be Ti, Ni, Pd, or Mo [282, 283]. In contrary to n-type GaN, to form an ohmic contact to p-type GaN principally a metal with larger work function is needed. In addition to this property, there are other problems which makes it difficult to form an ohmic contact to p-type GaN with resistivity lower than 10^{-4} $\Omega \cdot cm^2$ [281][Song 2010]. Due to large activation energy of around 170meV [284] of magnesium atoms (as acceptors) in p-GaN and also creation of Mg-H complexes during growth, it is very difficult to dope p-GaN heavily. Another difficulty is arise from the fact that based on p-GaN electronic properties (Eg=3.4 eV and electron affinity of around 4.1 eV [285]), there is lack of suitable metals with higher work function than p-GaN. Therefore, it is critical to form a low resistance ohmic contact to p-GaN for optoelectronic applications with the special case of gallium nitride based LEDs here. Scientist have tried several ways and techniques to be able to get a good quality ohmic contact to p-GaN,

including using metals with large work function, such as Ni/Au alloy [286, 287], Ni/Cu alloy [288] and Pt/Pd/Au [289] with the contact resistance in the range of around 10^{-6}-10^{-3} $\Omega \cdot cm^2$ after annealing at 350 °C to 600 °C in pure nitrogen ambient. Also by treatment of surface of the semiconductor, there have been reported the improvement of the ohmic contact and resistivity. This is mostly because of susceptibility of the bare semiconductor to oxygen and air, and it is crucial to have ohmic contact by removing the oxide layer on the surface. Cleaning with dilute HCl [290, 291], KOH [290], dilute HF [292] and $(NH_4)_2S_x$ [293] are examples of achieving better contact using surface treatment using chemical solutions. Surface treatment using Cl_2 plasma [294] and KrF excimer pulsed laser [295] have also showed great improvement in contact resistivity. Using metals like Ti and Ta to de-passivate the Mg atoms by extracting hydrogen atoms, is the another way of improving ohmic contact [296].

Chapter 3

Growth and Characterization of InAlN Epilayers

3 GROWTH AND CHARACTERIZATION OF INALN EPILAYERS

3.1 Introduction

In this chapter, PLE spectroscopy is used for a detailed study of the room temperature $In_xAl_{1-x}N$ band-gap for the $0 < x < 0.11$ range. There is only a little data in the literature on the band-gap of low indium content InAlN [149], due to the focus of attention in this material system being on compositions close to the lattice-matching condition with GaN ($x = 0.17$-0.18). Hence the majority of discussion on the variation and strength of the bowing parameter for $x < 0.1$ has been based on extrapolation of the InAlN band-gap dependence in the range $0.1 < x < 0.25$ to the low x region. This extrapolation has been based on the rather scattered array of published data available for such indium contents [159], or else on theoretical calculations [128, 146], which still need to be supported by experiment.

Good quality InAlN in this range should be grown on thick (>1 µm) AlN templates. This causes difficulties in estimation of the band-gap by most of the available techniques particularly for low x, in addition to the general complications of working in the deep ultraviolet spectral range. Absorption/transmittance measurements are hampered due to a strong contribution from the sub-band-gap absorption tail of the much thicker AlN layer. Any ellipsometry measurement of the InAlN/AlN heterostructure is also mostly defined by the thicker AlN layer and its analysis becomes complicated/less reliable for low indium content InAlN. Reflectance spectra will also be dominated by AlN excitonic features. Band-gap estimation from the onset of interference fringes in reflectance spectra can be carried out only for relatively thick InAlN layers, which are difficult to controllably prepare [297].

Our report of the $In_xAl_{1-x}N$ band-gap for $x < 0.11$ is free of the disadvantages of the above-mentioned methods because no room temperature PL is detected from the AlN templates under the weak excitation conditions used, while fairly strong PL was observed from the InAlN epilayers. This makes our PLE measurement insensitive to the presence of the thick AlN template and allows precise analysis of the InAlN absorption edge. We first present the procedures used to prepare the material and then to determine the InAlN composition and band-gap. Particular attention is paid to the presence of valence band intermixing and the effect this has on the PLE spectra. Finally, a discussion is presented of the nature of the change in the band-gap with increasing In composition. We show

that the observed behaviour can be well described and understood using a band-anticrossing (BAC) model to treat the interaction of In-related localised states with the alloy conduction and valence band edges.

3.2   Experimental Details

The 80-100 nm thick $In_xAl_{1-x}N$ epilayers were grown using the MOVPE system on 2.5 μm AlN-templates on $c-Al_2O_3$ prepared by colleagues and already reported [298]. The In composition, x, was varied from below 0.01 to 0.224 using growth temperatures T_g in the range 940°C to 730°C. A high V/III ratio of 3600, TMIn/TMAl ratio of 0.5, pressure of 70 mbar and nitrogen ambient were used for InAlN; the growth rate at such conditions was about 0.05 nm/s, decreasing slightly with increasing temperature.

It has been proved that, MOVPE grown InAlN often suffers from Ga auto-incorporation [164, 165, 299]. We undertook a number of measures to almost completely eliminate this unwanted process in our samples: First, the showerhead was thoroughly cleaned, reactor glassware changed, and the susceptor baked at high temperature prior to growth of the sample series. This was followed by the growth of a number of AlN-templates to coat the reactor chamber. No deposition using trimethylgallium was undertaken until the last sample in this reported series had been grown. This reduced the Ga content in our samples down to negligible levels, as confirmed by secondary ion mass spectrometry measurements for the $In_{0.045}Al_{0.955}N$ sample, where a value of less than 0.001 (0.1%) was estimated. Taking into account an AlGaN band-gap bowing parameter of 1 eV [64], this would lead to no more than 4 meV of additional narrowing of the band-gap in comparison to the case of an absolutely Ga-free InAlN layer. All samples were characterised by XRD using a PANalytical X'pert PRO XRD system (by my colleague Dr Duc V. Dinh). Symmetric 0002 ω-2Θ scans and asymmetric $(10\bar{1}5)$ reciprocal space maps were carried out to determine the indium content and strain status of the samples. Photoluminescence (PL) was excited using a double monochromator coupled Xe-lamp at room temperature (RT, 295 K). PL and PLE spectra were detected using an iHR320 Horiba imaging spectrometer equipped with a photomultiplier. PL spectra were excited with the wavelengths corresponding to the maxima of their PLE spectra and divided by the intensity of the Xe-lamp at the same wavelengths. Sometimes it would be more useful if PL spectra is shown with respect to photon energy as opposed to wavelength. However one must remember that the value of luminescence intensity is actually *per unit wavelength* not *per unit energy*. Because of inverse relation between energy and wavelength, the spaces between each step in the wavelength spectrum ($\Delta\lambda$) are not equally

stretched across the energy spectrum. Therefore, to replot the PL spectra versus photon energy, the measured spectra were divided by the square of the photon energy:

$$E = \frac{hc}{\lambda} \rightarrow \frac{dE}{d\lambda} = hc \frac{d}{d\lambda}\left(\frac{1}{\lambda}\right) \rightarrow I_{PL}(hv) = \frac{I_{PL}(\lambda)}{hv^2} \qquad \text{Equation 3-1}$$

The relative PL efficiencies of the samples were calculated as integrals of their PL spectra plotted using Equation 3-1 divided by intensities of the Xe-lamp emission at wavelengths used for their excitation. The PL spectrum position hv_{PL} used here was defined as the centre-weighted PL spectrum position given by Equation 3-2:

$$hv_{PL} = \frac{\int_{hv_{min}}^{hv_{max}} \xi \cdot I_{PL}(\xi)d\xi}{\int_{hv_{min}}^{hv_{max}} I_{PL}(\xi)d\xi}, \qquad \text{Equation 3-2}$$

where hv_{min} and hv_{max} are the minimum and maximum measured photon energy range respectively, which $I_{PL} > 0$ within, and ξ is an integration variable. The PLE spectra were fitted with a sigmoidal function (Equation 3-3) [184] to derive the effective band-gap $E_{g, \text{eff}}$ of the samples studied, where I_0 is the intensity at low temperature ($\leq 12K$), $E_{g,eff}$ is effective band-gap and ΔE is broadening parameter.

$$I_{PL}(hv) = \frac{I_0}{1 + exp\left(\dfrac{E_{g, eff, 1} - hv}{\Delta E}\right)} \qquad \text{Equation 3-3}$$

A double sigmoidal function (Equation 3-4) was used to analyse the PLE spectra of those samples which exhibited a double absorption edge in PLE.

$$I_{PL(hv)} = \frac{I_1}{1 + exp\left(\dfrac{E_{g, eff, 1} - hv}{\Delta E_1}\right)} + \frac{I_2}{1 + exp\left(\dfrac{E_{g, eff, 2} - hv}{\Delta E_2}\right)} \qquad \text{Equation 3-4}$$

3.3 Estimation of In Content

The change in the composition of the $In_xAl_{1-x}N$ layers determined by XRD with growth temperature is presented by the square and circle data points in Figure 3-1. In the temperature range $T_g > 800°C$, x was found to decrease exponentially with T_g. The growth rates for nitrides of each III group metal

are proportional to the difference between the rates of metal adsorption onto the growth surface and desorption from it. One can neglect the temperature dependence of the growth rate for AlN, since the Al ad-atoms sticking coefficient is considered to be unity in the studied temperature range [300]. However, the InN growth rate should drop with T_g much faster than exponentially. This is because, although the indium adsorption rate does not depend strongly on T_g, its desorption rate increases rapidly with T_g. Thus, the InN growth rate should also rapidly decrease with growth temperature, reaching even negative values when the In desorption rate exceeds that of its adsorption. This would lead to a similar rapid decrease of x with T_g in our samples. Due to high desorption rate of indium atoms with temperature, it is expected that indium content will decrease exponentially with temperature. The relatively lower decreasing rate of x observed in our experiment than expected, may be due to a decreased desorption rate of In adatoms once they are surrounded by Al ones. The indium content x is therefore driven by the probability of an In adatom being surrounded by Al atoms before desorption can occur, rather than being determined by the pure In ad-atom desorption rate. It is reasonable that even at fairly high T_g a small amount of In ad-atoms has a chance to be surrounded by Al atoms before their desorption.

It was found from analysis of symmetric 0002 ω-2Θ and asymmetric $(10\bar{1}5)$ reciprocal space map XRD measurements that In$_x$Al$_{1-x}$N layers of ~100 nm thickness are fully strained if $T_g > 825°C$, corresponding to $x < 0.054$, with samples in the range (805°C $\leq T_g \leq$ 825°C; 0.105 $\geq x \geq$ 0.054) showing only slight relaxation (about 25% for the $x = 0.105$ sample).
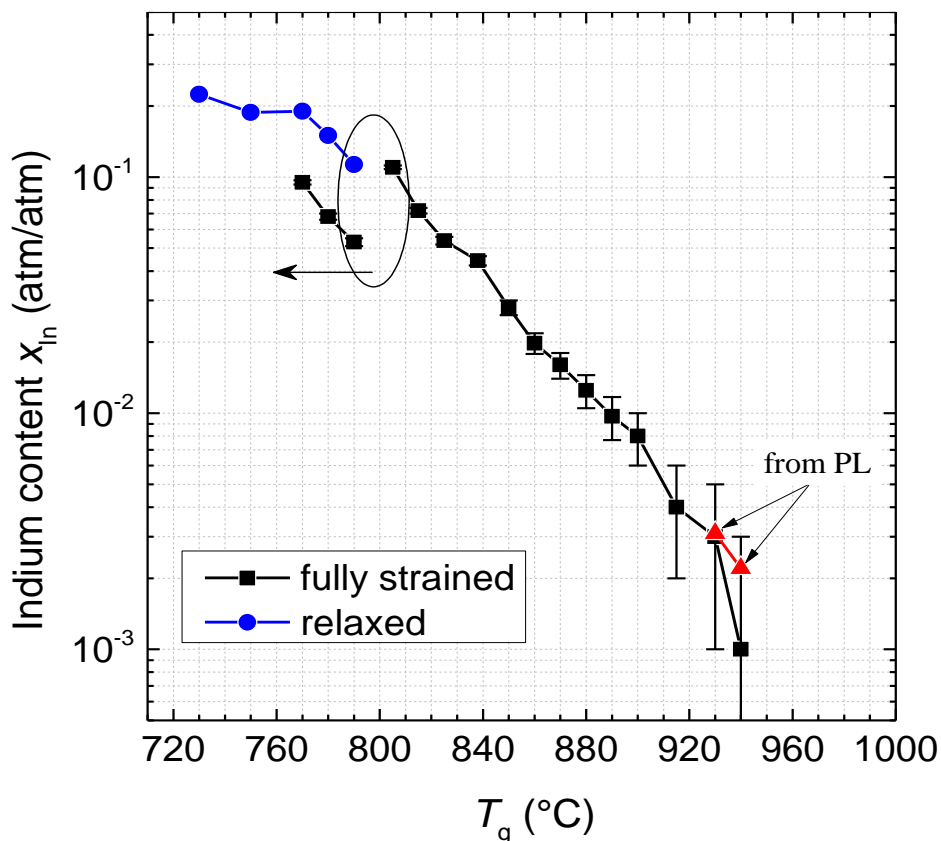
Figure 3-1 Dependence of InAlN indium content on growth temperature as determined from XRD (squares and circles) and PL measurements (triangles). For an explanation of the data from PL, see text below.

3.4 PL Properties

A strong RT PL band was observed for these strained InAlN layers, centred between 310 and 370 nm and with full width at half maxima (FWHM) within the 0.66-0.97 eV range, as depicted in Figure 3-2. As shown in squares and circles in Figure 3-1, at growth temperatures lower than 805°C, the material splits into two subsystems with different stress status and composition.

No luminescence was observed from the samples with $x > 0.11$, which is attributed to the high defect density in these mismatched and relaxed layers implied by the XRD data. This appears in a strong broadening of 0002 and especially $(1\bar{1}01)$ ω-scans of this relaxed layers relative to those for AlN-templates used (250-350" and 550-650" for (0002) and $(1\bar{1}01)$ reflectance, respectively), while the strained layers are characterised by FWHMs within only 10% difference from them. It is worth noting that the relative RT PL efficiency of the UV band, having a maximum at around $x = 0.01$ (Figure 3-3),

starts to drop significantly even before *x* reaches the value beyond which relaxation is clearly detected by XRD. This may indicate that the decrease in PL efficiency is not only due to an initial relatively weak relaxation not yet clearly seen in XRD, but also due to a possible increase of point defect concentration at lower growth temperatures [301].
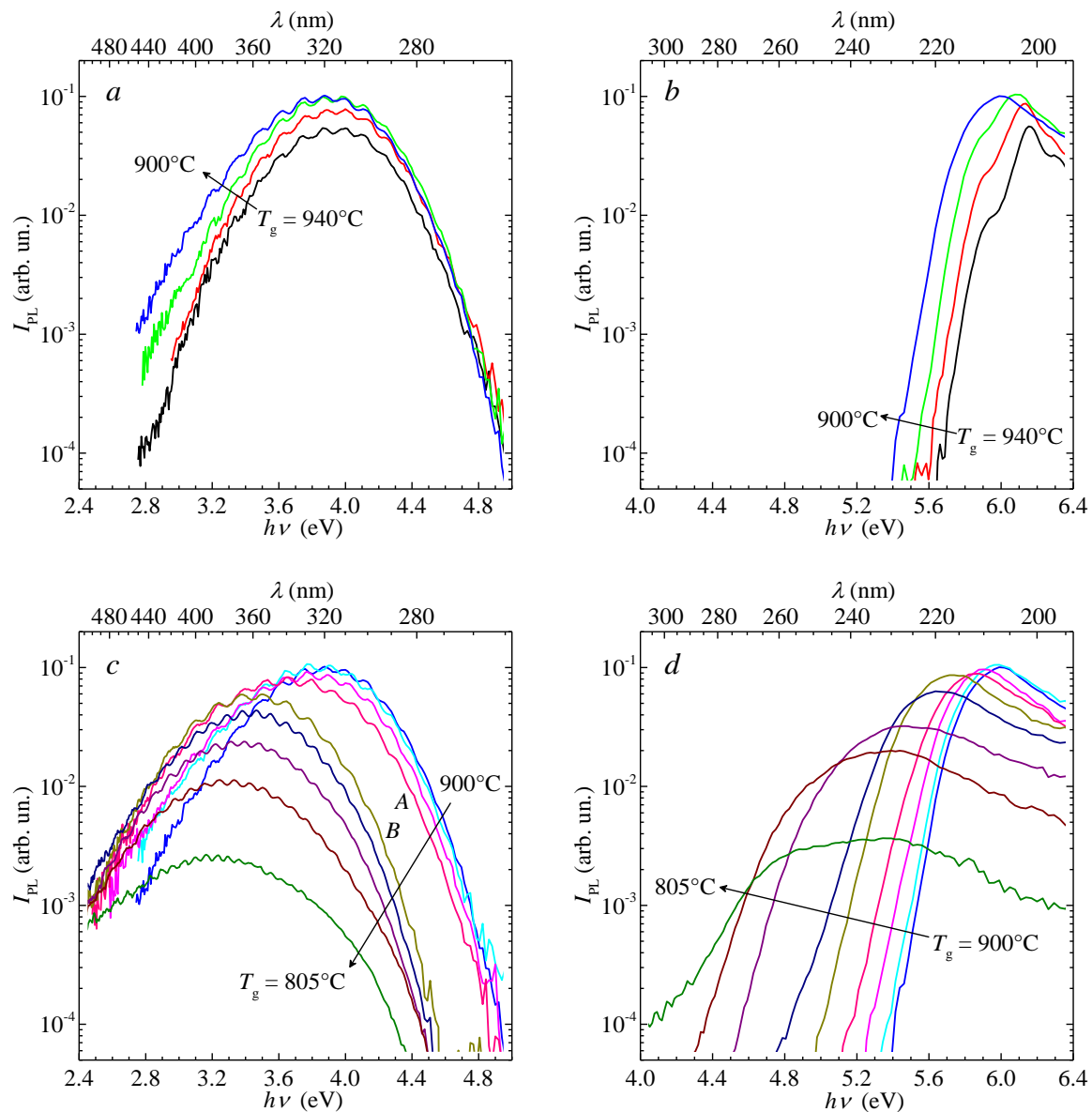
Figure 3-2 RT PL (a, c) and PLE (b, d) spectra of InAlN layers grown at different temperatures.

Chichibu et al. [302] recently observed a similar near-UV band in *m*-plane $In_{0.02}Al_{0.98}N$ samples, which they proposed to be possibly due to carbon or Al vacancies. To investigate if this is the origin of the PL in our case, we analysed AlN layers grown firstly under optimised conditions for our AlN template (see Ref. [298] for more details), and secondly under the conditions used to prepare the InAlN samples (only neglecting the TMIn flow rate, i.e. *x* = 0). In both cases, the AlN samples were

found to be optically inactive (no PL signal detected) under the weak excitation conditions used ($\sim 10^{-5}$ W/cm^2 power density at 198 nm emission wavelength from the spectrometer coupled Xe-lamp). At the same time, the samples become immediately luminescent if even a small fraction of Al atoms is substituted by In atoms as shown in Figure 3-2. We thus consider a luminescence centre involving In, possibly in complex with carbon or with Al vacancies, as the origin of the luminescence, rather than carbon or Al vacancies individually. Taking into account the very large PL Stokes shift of about 1.9 eV in these low x samples, it is difficult to interpret the observed PL band as a band-edge emission; the exact nature of this band is currently unknown.

Figure 3-4 shows that the InAlN PL spectrum blue-shifts with increasing T_g until 915°C, but then saturates as the temperature is further increased, as can also be seen in…, a and c. The PL band FWHM decreases from 0.81 eV at $T_g = 870$°C to 0.66 eV at $T_g = 915$°C, with this decrease saturating for higher T_g. Thus, the PL spectrum shape and position becomes in essence independent of growth temperature and therefore of indium content for $T_g \geq 915$°C ($x \leq 0.004$). At the same time the PL efficiency, having been nearly stable across the 870°C $< T_g <$ 915°C range, starts to drop distinctly with further increasing T_g. The absence of the UV PL band for the AlN samples, combined with its presence in the InAlN samples, and the correlation of its efficiency with indium content at small x support our argument that In-related centres are involved in the luminescence mechanism.
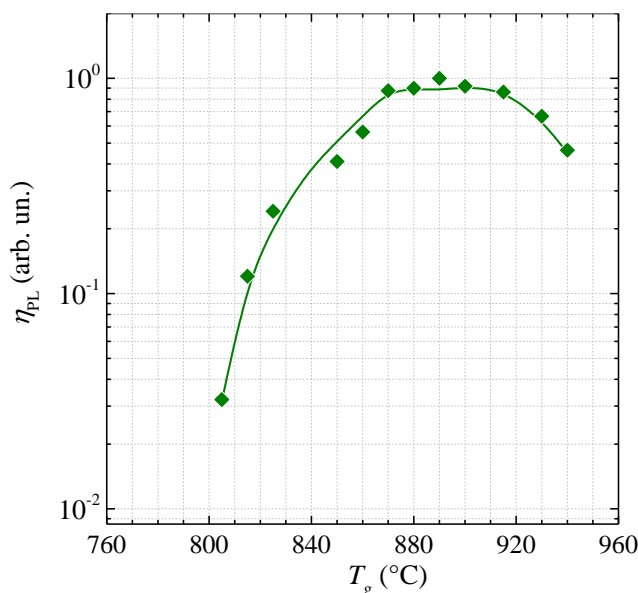
Figure 3-3 Growth temperature dependent PL efficiency.

Moreover, it is reasonable to assume that the PL efficiency of the InAlN samples grown at the highest temperatures (≥ 915°C) is proportional to the indium content in them, therefore allowing a second

method to estimate composition. Using the $In_{0.004}Al_{0.996}N$ sample as a reference and assuming a linear dependence of the PL efficiency with indium content, the x values of the two highest growth temperature samples were estimated using the simple expression:

$$x = x_0 \frac{\eta_{PL,\,x}}{\eta_{PL,\,x_0}}, \qquad\qquad \text{Equation 3-5}$$

where x_0 and $\eta_{PL,\,x_0}$ are 0.004 and the PL efficiency of the $In_{0.004}Al_{0.996}N$ sample, respectively, and $\eta_{PL,\,x}$ is the PL efficiency of the sample for which the x value is being estimated. These indium composition estimates are included in Figure 3-1 (triangular data points marked as "from PL"). It is clear that a key challenge in examining such low composition alloys is the determination of the composition at such small values, leading to the increasing error bars shown in Figure 3-1. Using the monotonic decrease in efficiency as a predictor, the additional estimate of x can be made for the samples grown at highest T_g, where the error in estimation of x from XRD is ±0.002 and thus exceeds 50% of the absolute value of x. It is worth noting that the "from PL" x value for the sample grown at 930°C and its XRD estimate are very close, while the PL based estimate for the sample grown at the highest T_g is still within the error bar of the XRD measurement. The "from PL" values also lie close to what might be predicted based on extrapolation of composition with temperature for the series as a whole, based on the data in Figure 3-1. We, therefore, use these "from PL" x values for the samples grown at the two highest T_g as our best estimate of the composition.
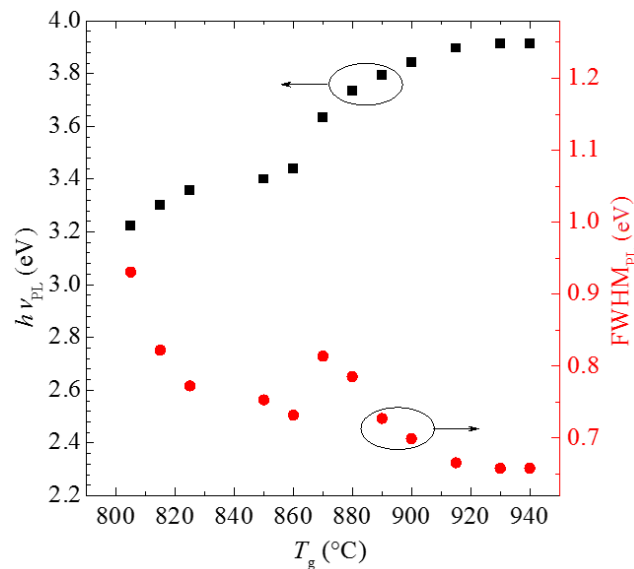
Figure 3-4 PL spectrum position (squares) and FWHM (circles) of InAlN layers as a function of growth temperature.

There is a significant jump in the evolution of the PL spectra with T_g between 860°C and 870°C (as plotted in Figure 3-2, c, curves A and B, respectively) with a change in peak position and, more dramatically, FWHM being observed (Figure 3-4). The samples were grown sequentially, with no

essential change in growth conditions identified other than the change in growth temperature. The reason for the sudden change in behaviour is unclear, though it is likely, given the behaviour of the PL FWHM in particular, that the band is made of two different sources: for example deep centres involving single In atoms for higher T_g and those involving multiple ones for lower T_g, with competition between them leading to the single In atom-related one collapsing at lower T_g due to a higher occurrence of clusters of multiple In atoms and carrier localisation in them. To support this conjecture it is worth noting that for low x, $In_xAl_{1-x}N$ can be considered as an ensemble of separate In atoms in the AlN matrix and therefore the PL spectra observed for $x \leq 0.004$ are associated with the presence of such atoms. This would explain why both PL peak position and FWHM become independent of x for such low In compositions.

For samples grown at $805°C \leq T_g \leq 825°C$ ($0.105 \geq x \geq 0.054$) the PL FWHM is observed to broaden rapidly, with this broadening accompanied by a rapid decrease in PL efficiency. This is attributed to the effects of the onset of initial small strain relaxation (as opposed to the spinodal decomposition of the material into two subsystems: fully relaxed and only slightly relaxed, observed for $T_g < 800°C$) and increasing point defect concentration, as discussed above.

3.5 Band-gap Determination

3.5.1 InAlN Band-gap at room temperature

As seen from the PLE spectra in Figure 3-5, the native centre-like PL band is excited via the host matrix, which is consistent with that observed for doped centres in InAlN [303] and native defects found in other III-N alloys [304]. This allows the PL bands observed here to be used as a reliable probe of semiconductor band-gap. The InAlN effective band-gaps $E_{g, eff}$ derived from the PLE spectra using the sigmoidal expression [184], are plotted in Figure 3-5 as a function of indium content. As can be seen from the spectra in Figure 3-2(*b*), the samples were grown at $T_g > 900°C$ clearly exhibit a double edge absorption, leading to their characterisation using double sigmoidal expression and thus with two $E_{g, eff}$ values. In most cases the error bar in the determination of the band-gap is less than 10 meV; the only exception from this is the double sigmoidal fit of the $x = 0.008$ sample ($\delta E_g = \pm 30$ meV), for which the double absorption band is barely detectable. We attribute the double edge PLE spectra observed for samples with $x \leq 0.008$ to the relative contributions to the PL of carriers photo-generated from different valence bands uniaxially split due to the wurtzite crystal field. The

energy difference between the higher and lower band-edges (~0.22 eV) for these very low indium content samples matches typically published values for crystal field splitting in AlN [74], further corroborating our assertion. It should be noted that such a double-edge PLE behaviour has been reported previously by Feneberg et al. [304] in $Al_{1-y}Ga_yN$, and attributed to the same mechanism. However, in that case, the effect exists for Ga contents up to at least $y = 0.06$, whereas here it is only observable for $In_xAl_{1-x}N$ where $x \leq 0.008$, i.e. approximately one order of magnitude smaller. This is consistent with recent theoretical analysis [146, 305] showing that In atoms cause a strong intermixing of the valence band states in the material. The finding is also consistent with the PLE double-absorption edge of InAlN samples disappearing rapidly with increasing In as the absorption of the material is dominated by the lower (fundamental) band-gap for 'high' x ($x > 0.02$) despite the nominally forbidden nature of the transition for c-plane material. Consequently, if the wave function character of the highest valence state switches at much higher AlN contents than one would predict from a linear interpolation of the valence band parameters, access to a significantly larger range of TE emitting structures might be expected. This finding is important for designing InAlN-based devices operating in the UV spectral region since the light polarisation characteristics affect the light extraction efficiency of the device. Similarly, for polar AlN-based photodetectors [306] it is clear that small amounts (<1%) of In will significantly modify the effective absorption edge due to a combination of this effect and the high bowing giving a high degree of sensitivity for photon energies around 6 eV.
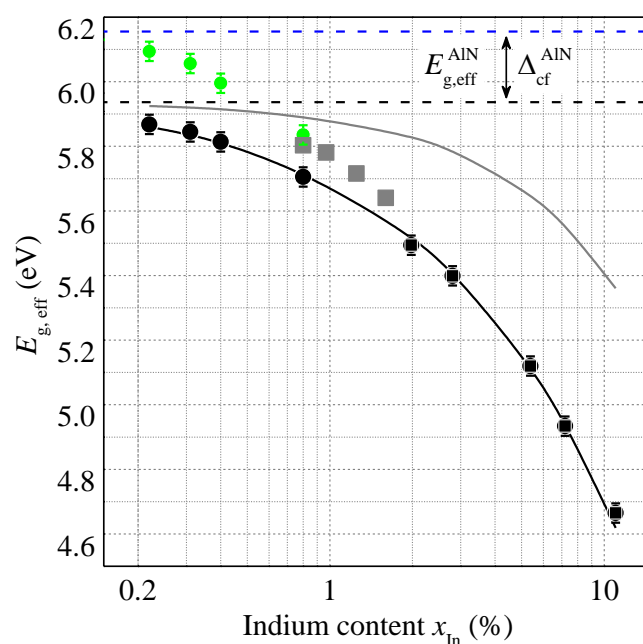
Figure 3-5 Composition dependent effective band-gaps derived from PLE spectra by fitting with the single (squares) or double sigmoidal expressions (circles). Black solid line – fit using band-anticrossing (BAC) model (see text below). Grey solid line – fit using linear interpolation between AlN and InN band-gaps

3.5.2 InAlN band-gap at low temperature

Low temperature, 10 K, PL and PLE spectra of typical 0.4% $In_XAl_{1-X}N$ is shown in Figure3-6. Similar to the RT data, it can be seen that there is strong PL emission from strained layers and very big Stokes shift, ~1-2 eV, depending on In content. Normalised PL spectra of InAlN alloys with different indium contents are shown in Figure3-7.
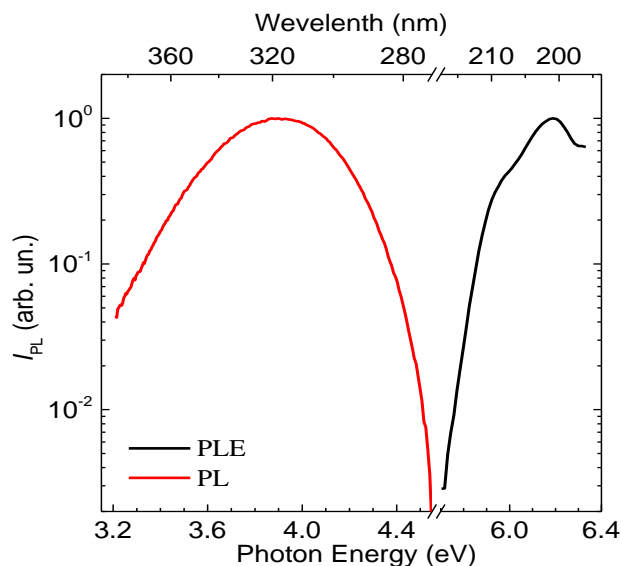
Figure3-6 Low temperature PL and PLE spectra of $In_{0.004}Al_{0.996}N$
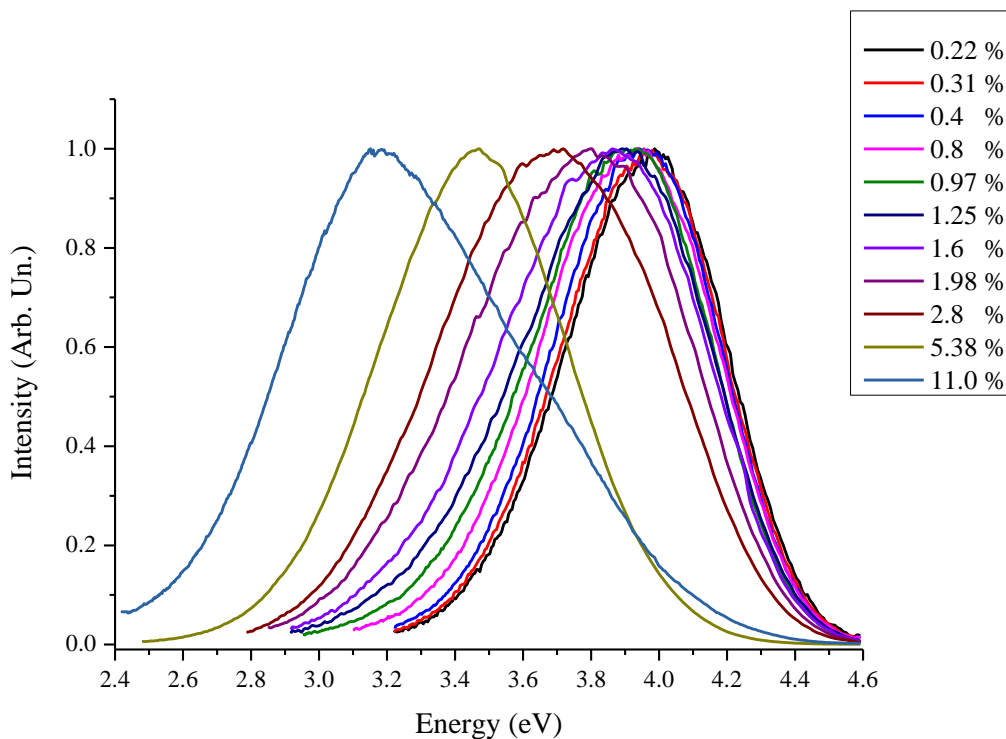
Figure3-7 Low temperature (10 K) PL spectra of InAlN at different compositions

As depicted in Figure3-8, PL emission is showing a blue shift with decreasing In content and at the same time PL emissions are getting broader. The point is the intensity decreases almost linearly with indium content for x<= 5.38. This is not a similar behaviour to the room temperature results we have got and reported previously in section 3.5.1, where emission energy is almost unchanged for very low indium contents, In<=0.8 %. As described earlier, based on the analysis, we conclude that emission at low In contents is associated to the single In atoms spread in the AlN matrix, therefore until overlapping of the wave-function of the In atoms, they will behave similar to dilution in AlN host material.

Here it seems that the situation of RT analysis is not the case. Although at RT it was possible to observe just emission from single In atoms, due to higher efficiency, there are still positions in alloy with clustered In atoms. These clusters are dim and inefficient at RT, but at low temperatures they are activated with much more radiative recombination and become a dominant source of emission at low temperature. Both emission peaks associated with single and clustered In atoms are relatively broad. This is because of coupling with phonons and alloy like behaviour and fluctuation of In atoms in each separated cluster, respectively. Therefore, PL emission which is a product of the overlapping of the two peaks is a broad emission, moving with composition change. Typical PL spectrum of typical $In_{0.008}Al_{0.992}N$ alloy is shown in Figure3-9. PL spectra are simulated using double sigmoidal fitting by Origin software. The higher energy emission at around 4.110 eV is associated with single In atoms and the peak at ~3.810 eV is from clustered In. Simulation of all other spectra shows that the higher energy emission, associated with In atoms, approximately remains unchanged, although integrated intensity is rapidly decreasing, until disappearing of the peak at the compositions of about ≤1 %.

Contribution from single In atoms in emission continued until around $x_{In} \approx 2\%$, and FWMH reduction occurs afterward as shown in Figure3-8 (red triangles).

Additionally, as can be seen in Figure3-8, for highest indium content of 11 %, the emission energy variation with composition is off from linearity. This is because of creation of an additional peak, which is visible in PL spectrum in Figure3-10. It is also causing the broadening of the PL spectrum. This additional emission peak is associated with phase separation which starts to occurs at this composition where material start to change from fully strained to fully relax phase, as described in section 3.3.
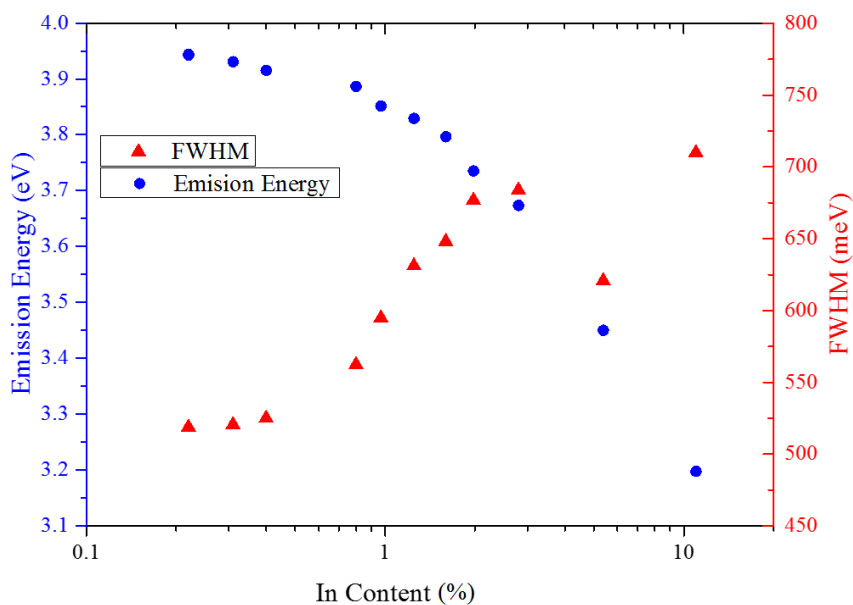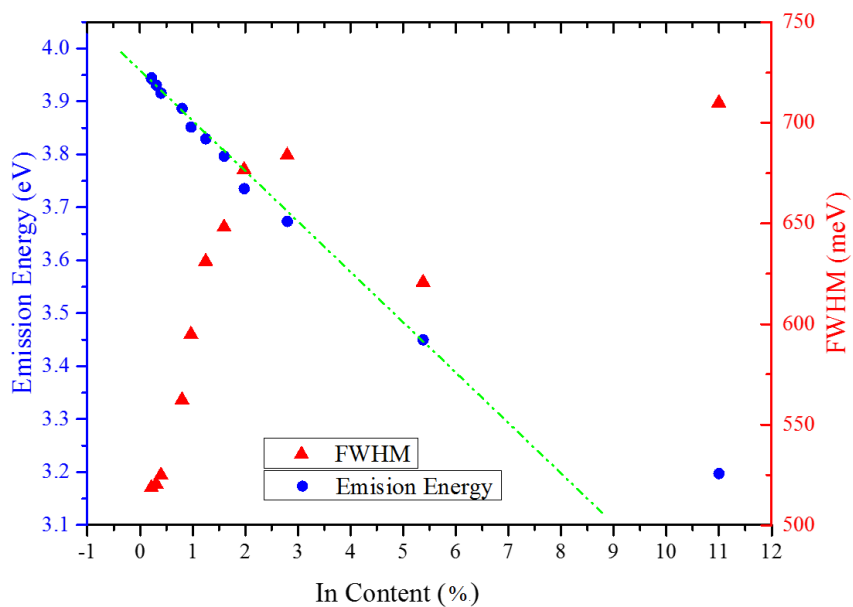
Figure3-8 Low temperature (10 K) PL emission energy and FWMH with respect to In content in linear (top) and log (bottom) scale..
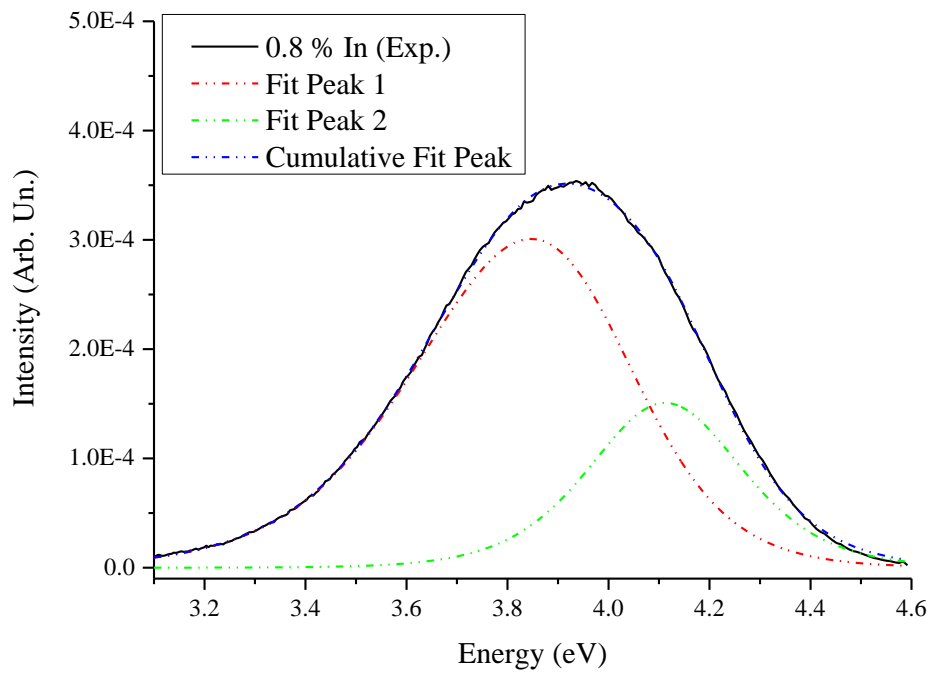
Figure3-9 LT PL spectra of In0.008Al0.992N layer with asymmetric sigmoidal fittings.
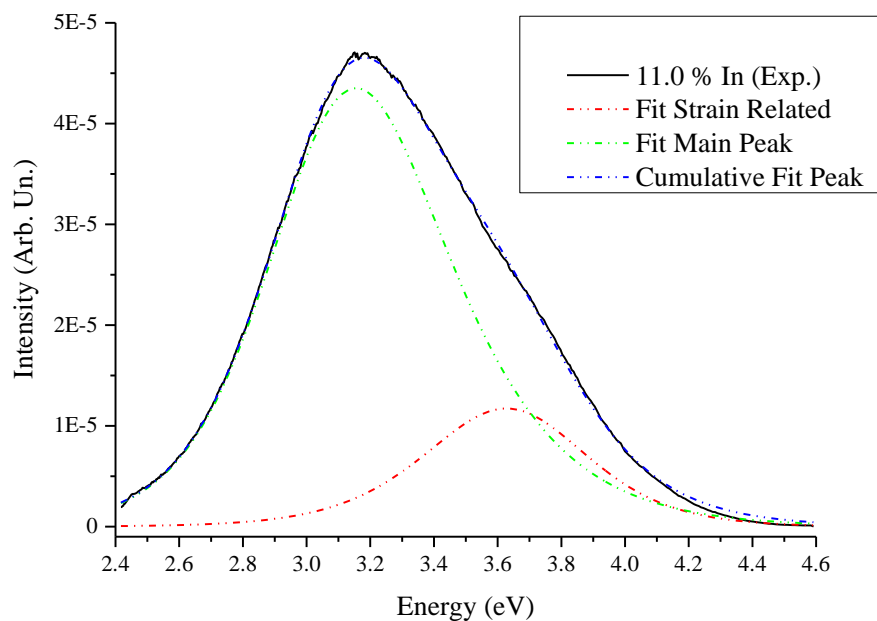
Figure3-10 LT PL spectra of In0.11Al0.89N layer with asymmetric sigmoidal fittings.

PLE spectra of In$_x$Al$_{1-x}$N layers with different In contents are exhibited in Figure3-11. Shifting the band-edge towards lower energies is obviously can be seen with increasing the indium content. Other two interesting behaviour of these PLE spectra are double band-edge at low In contents, x < 0.1, and appearance of the excitonic peak at the lowest indium content.
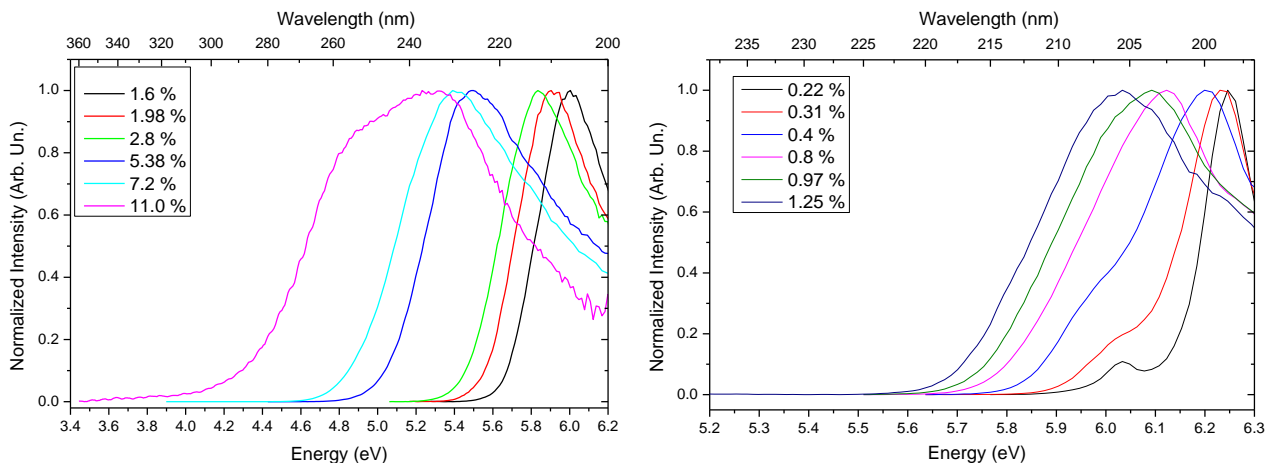
Figure3-11 Low temperature PLE spectra of InAlN layers with different composition.

As shown in our previous report at room temperature [83], the double band emission is associated with valence-band splitting in wurtzite crystal field. At room temperature we are able to see these double edge up to 0.8% indium content, while at low temperature, it is detectable up to 0.97%. This phenomenon has previously been reported for AlN and AlGaN by Feneberg and colleagues [304].

The higher band edge is attributed to $\Gamma_{7c} \to \Gamma_{7v}/\Gamma_{9v}$ and the lower one to $\Gamma_{7c} \to \Gamma_{7vbm}$, with vbm standing for valence band maximum, as schematically illustrated in Figure 3-12. The difference between Γ_{7vbm} and Γ_{9v} (levels which define the crystal field splitting Δ_{cf}), is ~202 meV at low temperature for the lowest indium content sample, 0.22 % In, which is close to the reported values for AlN, 219 meV [74], 212 meV [307].
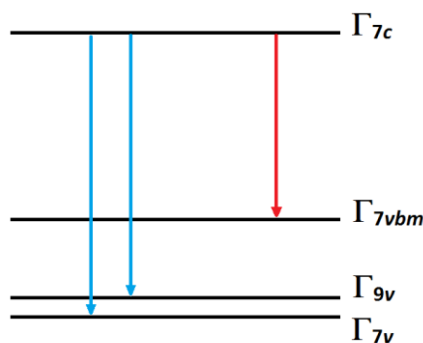
Figure 3-12 Schematic illustration of carrier transition Al rich InAlN alloy.

To obtain the effective band gap from PLE spectra, single and double sigmoidal expressions have been used to fit the single and double edge spectra, respectively. The single sigmoidal equation is as [184]:

$$I_{PL}(h\nu) = \frac{I_0}{1 + exp\left(\dfrac{E_{g,\,eff,\,1} - h\nu}{\Delta E}\right)}$$

Equation 3-6

where I_0 is the intensity at low temperature ($\leq$12K), $E_{g,eff}$ is effective band-gap and ΔE is broadening parameter. This formula can be generalised for a double sigmoidal expression, and typical fitting of both systems is shown in Figure 2-9.

The low-temperature fundamental band-gap of the In$_x$Al$_{1-x}$N alloy is driven by the combination of lower energy band-gap from double sigmoidal fit (corresponds to $\Gamma_{7c} \rightarrow \Gamma_{7vbm}$ transition) for lower indium contents and single sigmoidal fit data for higher x_{In}, as could be seen in Figure 3-14. Starting from 5.998 eV for 0.22% In content, and rapidly decreasing to 4.709 eV for 11% indium. It seems that for x=0.0125 and x=0.016 the values of fundamental band-gap are overestimated due to the mixing of band edges at this compositions.
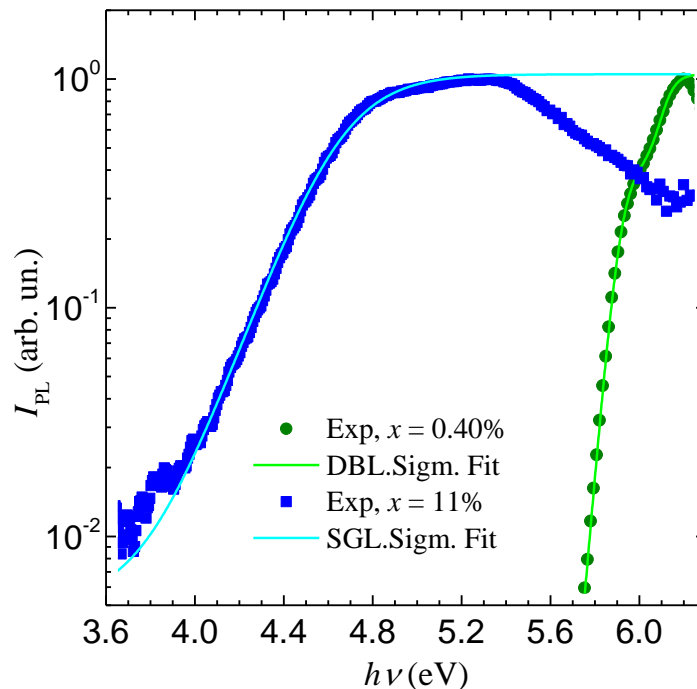
Figure 3-13 Typical room temperature PLE spectra of InAlN/AlN samples and their fit using single and double sigmoidal expression.
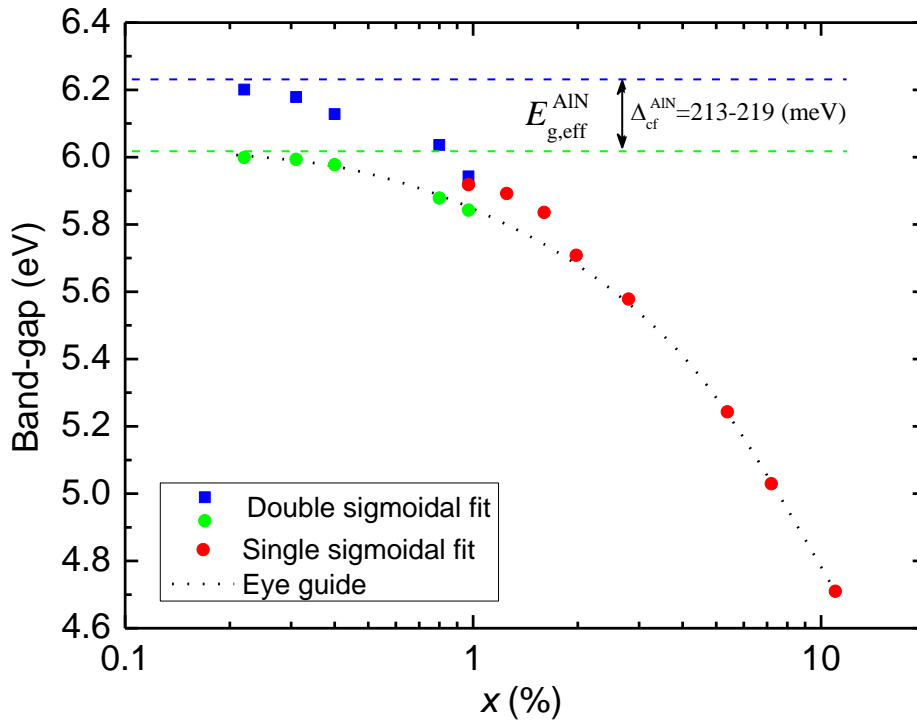
Figure 3-14 Low temperature (10 K) fundamental band-gap of strained InAlN layers at In contents. Higher band edge due to valence band splitting is shown with blue squares.

3.5.3 Determination of an AlN band-gap reference

As mentioned previously, RT PL was not observed from the AlN samples under low-intensity lamp excitation, leaving no opportunity to measure its PLE spectrum. We, therefore, required an alternative approach to determining a value of the AlN $E_{g,\,eff}$, compatible with our InAlN $E_{g,\,eff}$ plotted in Figure 3-5. This was performed by extracting the AlN $E_{g,\,eff}$ value from PLE spectra of two identical InAlN layers, one of which was overgrown with 150 nm of AlN. This additional thin AlN layer acted as an optical filter for the InAlN, with its PLE spectrum modified accordingly for photon energies above the AlN band-gap, while below AlN band-gap the top layer becomes transparent leaving the PLE signal unaffected (Figure 3-15). If one ignores any difference in the amount of reflected light, which is marginal in comparison to the absorption of light in the AlN cap, these two spectra are related by the simple expression:

$$I_{\text{PLE, capped}}(h\nu) = I_{\text{PLE, uncapped}}(h\nu) \cdot e^{-\alpha_{\text{AlN}}(h\nu)\cdot d_{\text{AlN}}}, \qquad \text{Equation 3-7}$$

where $\alpha_{\text{AlN}}(h\nu)$ is the AlN absorption spectrum and d_{AlN} is the thickness of the AlN layer grown on top of InAlN.

From Equation 3-7 we estimated the AlN absorption spectrum as:

$$\alpha_{AlN}(h\nu) = \ln\left(I_{PLE,\,uncapped}(h\nu)/I_{PLE,\,capped}(h\nu)\right)/d_{AlN} \qquad \text{Equation 3-8}$$

This is plotted in Figure 3-15, along with the above-mentioned PLE spectra. Next the effective band-gap $E_{g,\,eff}^{AlN}$ was derived from the absorption spectrum using the same methodology as for the InAlN PLE spectra. Although this is rather an exotic method to estimate the homogeneous binary compound band-gap, giving a value most probably underestimated by at least the exciton binding energy [304], this value is most appropriate to be compared to our InAlN $E_{g,\,eff}$ values given the similarity in the method used to determine it. The $E_{g,\,eff}^{AlN}$ value obtained is 6.155 eV, which matches well to the classical ~6.2 eV RT AlN band-gap corresponding to the $\Gamma_{7c}\rightarrow\Gamma_{9v}$ transition after deduction of the exciton binding energy (~0.051 eV [308]). The fundamental effective band-gap $E_{g,\,eff}^{AlN}$ corresponding to the $\Gamma_{7c}\rightarrow\Gamma_{7vbm}$ transition (where "vbm" indicates valence band maximum) was not seen in the absorption spectrum, so it was taken as the difference of the $\Gamma_{7c}\rightarrow\Gamma_{9v}$ transition energy and the AlN crystal field splitting Δ_{cf}. Both values are shown by horizontal dashed lines in Figure 3-5.
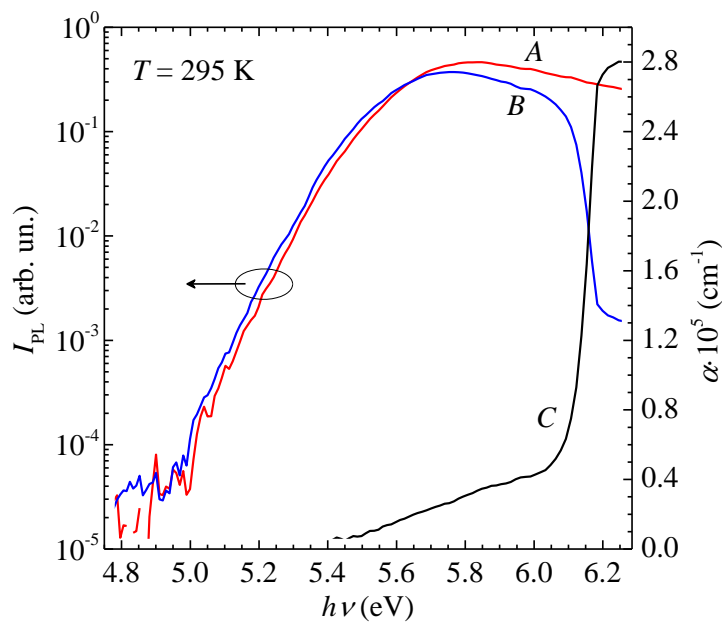
Figure 3-15 PLE spectra of uncapped (curve A) and AlN-capped (curve B) In$_{0.019}$Al$_{0.981}$N layers as well as the resulting absorption spectrum of AlN (curve C) determined from Equation 3-8.

3.5.4   Band anti-crossing model

The rapid reduction in energy gap observed here with increasing In composition (Figure 3-5) is consistent with the theoretical results in [146], where a strong band-gap bowing was also observed

for small x_{In}. The first-principles calculations undertaken in [305] showed that In-related localised states are formed in the conduction and the valence band in $In_xAl_{1-x}N$ for low In composition, x, and that these resonant localised states dominate the evolution of the band structure with increasing x. The variation of the conduction band-edge (CBE) energy with x in III-V alloys where one of the alloy components introduces resonant defect states above the CBE can be well described in low x range (dilute limit) by the BAC model [309-311]. In the BAC model, the evolution of the CBE energy is given by the lower eigenvalue of the 2×2 Hamiltonian matrix [309, 310, 312]:

$$H(x) = \begin{pmatrix} E_D(x) & V_{D,c} \\ V_{D,c} & E_c(x) \end{pmatrix}$$

Equation 3-9

where $E_D(x) = E_{In}^0 - \gamma \cdot x$ is the assumed variation of the mean In-related resonant defect energy with composition, and $E_c(x) = E_{c,0} - \alpha \cdot x$ describes the virtual crystal approximation (VCA) variation of the host matrix CBE state with In composition x. Here $E_{c,0}$ is the CBE for AlN, which was taken as the difference between $E_{g,eff}$ for AlN estimated above and AlN crystal field splitting (6.155 eV – 0.219 eV = 5.936 eV) to take into consideration the $\Gamma_{7c} \rightarrow \Gamma_{7vbm}$ transition. $V_{D,c}$ describes the interaction between the levels, which varies with x as $\beta\sqrt{x}$, where the $\sqrt{x}$ dependence arises because the interaction is between a localised defect and extended conduction states [312]. The change of the CBE energy with In composition x is then given by the lower eigenvalue E_- of the Hamiltonian in Equation 3-9.

$$E_-(x) = \frac{E_c + E_D}{2} - \sqrt{\left(\frac{E_c - E_D}{2}\right)^2 + V_{D,c}^2}.$$

Equation 3-10

As T_g decreases from 940°C, the relative contribution of the lower energy edge to PL is observed to increase (Figure 3-2, b). The lower energy edge values determined from the double sigmoidal fit of PLE spectra for samples with $x \leq 0.008$ (Figure 3-5, black circles) form a smooth x-dependence of the band-gap together with those obtained using the single sigmoidal fit for samples with $x \geq 0.02$ (Figure 3-5, black squares) for which, taking into account the above-mentioned tendency (Figure 3-2, b), the lower band-edge transition is expected to be dominant. We chose to fit these experimentally measured data for the variation in energy gap using Equation 3-10. It can be seen that

the BAC model (black solid curve in Figure 3-5) gives a very good fit over the full composition range considered. The fit shown is obtained by assuming that the isolated In-related defect level E_{In}^0 is 0.3 eV above the AlN CBE, that $\alpha = \gamma = 3$ eV, and that $\beta = 3.4$ eV. We note that the values used here are slightly larger than those used to fit the theoretical conduction band data in [305]. In [305] a non-parabolicity was found in both the valence and the conduction band edges of InAlN. Here, we have basically constructed an "effective" BAC model. Effects arising from the evolution of both the conduction and the valence band with composition x are condensed into one set of BAC parameters. Hence, it is not unexpected that the parameters extracted here are larger than the values our colleagues got for the conduction band alone [305]. In addition, with four free parameters in Equation 3-7, it is clear that a range of other values could have been chosen to fit the experimental data. Nevertheless, the overall analysis strongly supports our previous theoretical work [305] stating that localised In states, both in the valence and the conduction band, significantly affect the composition dependence of the InAlN band-gap, E_g and give rise to the nonparabolicity of E_g reported here.

The grey solid line in Figure 3-5 shows the expected variation of energy gap with the composition in $In_xAl_{1-x}N$ assuming a linear interpolation between the energy gaps of AlN and InN (i.e. ignoring any band-gap bowing). As discussed earlier in section 1.2.2, such a linear variation significantly overestimates the energy gap; while the excellent fit with the solid black line confirms that the evolution of the band-gap in $In_xAl_{1-x}N$ can be very well described for low values of x using a BAC model to take account of the interaction between localised In states and the host matrix band edges. It should be noted that the rapid change of band-gap with x for the samples reported here cannot be combined with previous results for higher values of x to obtain a "classical" composition independent parabolic bowing parameter, consistent with previously reported analyses [157, 159].

3.5.5   Composition dependent band-gap bowing parameter

Since the data in Figure 3-5 represent the composition dependence of the effective band-gap $E_{g, eff}(x)$, it is worth converting the data to provide an x-dependent band-gap bowing parameter $b(x)$, using the following expression:

$$b(x) = \frac{(1 - x) \cdot E_{g,eff}^{AlN} + x \cdot E_{g,eff}^{InN} - E_{g,eff}^{InAlN}(x)}{x \cdot (1 - x)}.$$

Equation 3-11

As seen from the above formula, the term $b(x)$ becomes extremely sensitive to the $E_{g,\,eff}^{AlN}$ value chosen at small indium contents. Even though AlN has been studied for a long time, there is still some discrepancy in the RT band-gap values (6.01-6.22 eV) reported in the literature [36] and references therein]. Partly this is caused by the fact that only the higher energy transition $\Gamma_{7c} \rightarrow \Gamma_{9v}$ can be effectively "seen" for commonly used *c*-plane AlN epitaxial samples, which is then sometimes considered to be the fundamental transition, instead of $\Gamma_{7c} \rightarrow \Gamma_{7vbm}$, as discussed by Li et al. [74]. There is another more important impediment when using data from the literature for $E_{g,\,eff}^{AlN}$: Because InAlN has a fairly "soft" absorption edge, similar to InGaN [184], it can be characterised only by an effective band-gap value, while values for AlN in the literature are claimed to be defined conventionally. We, therefore, need (and indeed already have from the AlN band-gap analysis obtained from the PLE spectra presented in Figure 3-15 and discussed earlier) a value which is compatible with our $E_{g,\,eff}^{InAlN}(x)$ data. At the same time, as seen from Equation 3-11, $b(x)$ is much less dependent on $E_{g,\,eff}^{InN}$ for low indium containing InAlN; hence, it is sufficient to use literature data for $E_{g,\,eff}^{InN}$, despite there also being a fairly large scatter in experimental values for $E_{g,\,eff}^{InN}$ (varying between 0.62 and 0.8 eV [313, 314]. As a compromise, we used a value of 0.65 eV for $E_{g,\,eff}^{InN}$. Experimental values of b were then determined using Equation 3-11 and are plotted as a function of x in Figure 3-16(squares).
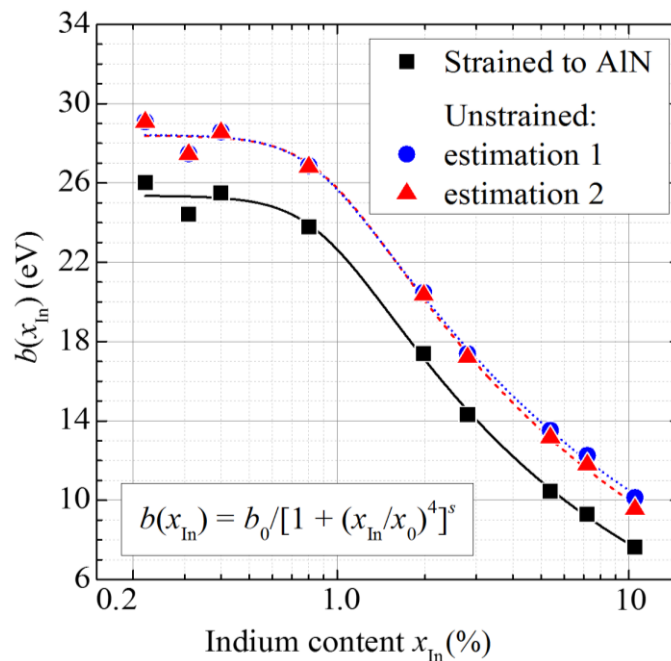
Figure 3-16 Composition dependent band-gap bowing parameter for InAlN strained to AlN (squares) and corrected for the unstrained case (circles and triangles). The lines plotted using the specified empirical expression with parameters listed in the Table 3-1 are guides to the eye.

3.5.6   Taking into account the strain conditions

It should be noted that the experimental data presented in Figure 3-5 relate to the band-gap of InAlN compressively strained to AlN; therefore, the band gap is expected to be overestimated in comparison to that of unstrained InAlN. To correct the data for the unstrained material one needs to take into account the strain dependence of the InAlN band-gap. Unfortunately, data regarding this strain dependence are not directly available in the literature; however, an estimate can still be made based on the relevant data currently available for AlN, InN and $In_xAl_{1-x}N$.

The variation with the strain of the AlN direct energy gap $E_{g,A}$ (due to transition $\Gamma_{7c} \rightarrow \Gamma_{7vbm}$) and of the $E_{g,B/C}$ energy gap ($\Gamma_{7c} \rightarrow \Gamma_{9v}/\Gamma_{7v}$ transitions) are given respectively by [139]:

$$E_{g,A} = E_{g,A,0} + \left(a_{cz}^{AlN} - D_1^{AlN}\right) \cdot \varepsilon_{zz} + \left(a_{ct}^{AlN} - D_2^{AlN}\right) \cdot \left(\varepsilon_{xx} + \varepsilon_{yy}\right) \quad \text{Equation 3-12}$$

and

$$E_{g,B/C} = E_{g,B/C,0} + \left(a_{cz}^{AlN} - D_1^{AlN} - D_3^{AlN}\right) \cdot \varepsilon_{zz} + \left(a_{ct}^{AlN} - D_2^{AlN} - D_4^{AlN}\right) \cdot \left(\varepsilon_{xx} + \varepsilon_{yy}\right), \quad \text{Equation 3-13}$$

where $E_{g,A/B/C,0}$ are energy gaps of unstrained material, ε_{xx} and ε_{yy} are the in-plane strain components, ε_{zz} is the strain along the c-axis direction, and a_{cz}^{AlN}, a_{ct}^{AlN} and D_i^{AlN} are AlN deformation potentials, with D_3^{AlN} and D_4^{AlN} the deformation potentials describing the strain dependence of the crystal field splitting. For biaxially strained layers, such as those considered here, $\varepsilon_{yy} = \varepsilon_{xx}$ and $\varepsilon_{zz} = -R_c \varepsilon_{xx}$, where the biaxial relaxation coefficient $R_c = 2C_{13}/C_{33}$, with C_{13} and C_{33} elastic constants. For $In_xAl_{1-x}N$ at low In composition ($x <\sim 10\%$), R_c has a very weak dependence on x [315], so we use the AlN value $R_c = 0.62$ from [315] in our analysis below, independent of In composition.

Taking into account the above relations between strain components, expressions (9) and (10) can be simplified to the form:

$$\Delta E_g(\varepsilon_{xx}) = E_g(\varepsilon_{xx}) - E_{g,0} = k \cdot \varepsilon_{xx} \quad \text{Equation 3-14}$$

with $k_A = 2 \cdot (a_{ct} - D_2) - R_c \cdot (a_{cz} - D_1)$

and

$$k_B = 2 \cdot (a_{ct} - D_2 - D_4) - R_c \cdot (a_{cz} - D_1 - D_3) \quad \text{Equation 3-15}$$

for $\Gamma_{7c} \rightarrow \Gamma_{7vbm}$ and $\Gamma_{7c} \rightarrow \Gamma_{7v}/\Gamma_{9v}$ transitions respectively.

Assuming for now that k varies linearly with In composition x, ($k_{InAlN} = k_{InN} + (k_{AlN} - k_{InN}) \cdot x$) and using as endpoints k_A values of $k_{InN} = -6.9$ eV and $k_{AlN} = -22$ eV, based on the deformation potentials from [139], a band-gap correction can be made for each sample. For instance, taking into account the strain value of -1.15% for our ~20% relaxed $In_{0.105}Al_{0.895}N$ sample, and using $k_A = 20.4$ eV gave a reduction in the energy gap of 0.235 eV for unstrained $In_{0.105}Al_{0.895}N$ compared to the value measured here (estimation 1, "linear").

However, two factors are likely to lead to a smaller actual difference in energy gap between the strained and unstrained alloys. Firstly, it has been shown both theoretically and experimentally that the hydrostatic pressure dependence of the energy gap, dE_g/dp is dramatically reduced for $In_xAl_{1-x}N$ with low In composition compared to that of AlN [316]. Depending on the type of alloy assumed, the calculated band-gap pressure coefficient reaches that of InN already at 40% and 15% In, in the case of homogeneously ordered and clustered alloys respectively. This indicates a strongly nonlinear composition dependence of the deformation potentials a_{ci} and D_i in $In_xAl_{1-x}N$. Therefore our assessment using a linear composition dependence of k most likely overestimates the energy gap reduction. There is insufficient information in the literature to deduce the nonlinear composition dependence of the deformation potentials in Equation 3-12. However, it can be expected that much of the reduction in deformation potentials should occur at very low In compositions, consistent with what is observed using the BAC model in other alloys such as $GaInN_xAs_{1-x}$ [309]. If we assume that most of the reduction in deformation potentials occurs by 25% indium (consistent with the data on dE_g/dp in [316]) this would then give a reduction in the energy gap of 0.18 eV for the $In_{0.105}Al_{0.895}N$ layer here (estimation 2, "bowing").

Correcting our band-gap data for the strain using these two assumptions led to the revised bowing parameters plotted in Figure 3-16 as circles ("linear") and triangles ("bowing"). The experimental data in Figure 3-16 were fitted with an empirical equation, Equation 3-16. The best fit was achieved using parameters listed in Table 3-1 for each case.

$$b(x_{In}) = \frac{b_0}{[1 + (x_{In}/x_0)^n]^s} \qquad \text{Equation 3-16}$$

Secondly, even the assessment taking into account bowing of InAlN deformation potentials may still overestimate the change in the energy gap. From the PLE data, it can be seen that Γ_{9v} character starts

to mix into the highest valence states in $In_xAl_{1-x}N$ for very low In content x. If we assume that the Γ_{9v} character dominates the strain dependence of the band edge states, then we should use Equation 2-20 to estimate the change in the band-gap. Using a linear interpolation gives $k_B = -8.14$ eV and an energy gap change of only 94 meV for the $x = 10.5\%$ sample.

Table 3-1 Parameters of empirical expression specified in Figure 3-16 allowing for the best fit of the data presented there.

Parameter Case	b_0 (eV)	x_0 (atm/atm)	s	n
Strained to AlN (experimental)	25.4±0.3	0.0090±0.0009	0.122±0.007	4
Unstrained (estimation 1, "linear")	28.4±0.3	0.0087±0.0008	0.102±0.006	4
Unstrained (estimation 2, "bowing")	28.4±0.3	0.0091±0.0008	0.109±0.006	4

The InAlN band-gap can be now calculated applying the conventionally used equation:

$$E_g^{InAlN}(x) = E_g^{AlN} - x \cdot \left(E_g^{AlN} - E_g^{InN}\right) - b(x) \cdot x \cdot (1-x). \qquad \text{Equation 3-17}$$

It should be noted in the above that it is critical to use the lower $\Gamma_{7c} \rightarrow \Gamma_{7vbm}$ measure of the band-gap for AlN irrespective of the crystallographic orientation of the sample under consideration. Using the empirical expression for bowing parameter in Figure 3-16 and Equation 3-17, one can accurately estimate the band-gap of low In containing InAlN alloys.

3.5.7   Peculiarities of temperature dependence of InAlN band-gap

To investigate further, we measured temperature dependence of the InAlN absorption edge of the low indium content samples. It was found that InAlN band-gap shift $\Delta E_g = E_g(10\text{ K}) - E_g(300\text{ K})$ does not change monotonically between AlN and InN, but that ΔE_g initially increases from the 89 meV value of pure AlN, measured using absorption of a specially designed sample, to a value in excess of 110 meV, Figure 3-17. The error bar range of measurement for all samples are less than 10 meV, except the sample with 0.97% of In content, in which the point that double sigmoidal converted to single sigmoidal fitting, as discussed earlier in section 3.5.2. The data in this range is challenging to examine due to the impact of valence band interactions, leading to the use of double sigmoidal fits for $x_{In} < 0.01$ and single sigmoidal analysis, as discussed earlier. However, the trend to increasing temperature dependent band-gap shrinkage for these low In content samples is clear, both from the rise in ΔE_g in

the range 0.0022≤x_{In}≤0.0042 for which a good double sigmoid fit is made and also from PLE data taken at intermediate temperatures.

This behaviour is unlike that reported for other III-nitrides [64], nor can it be explained by the reported band-gap shrinkage observed for dilute nitrides (e.g. GaAsN). While such dilute nitrides also exhibit strong band-gap non-parabolicity with composition, this is typically also associated with a *reduction* rather than the *increase* in the band-gap shrinkage with temperature [317, 318]. This unexpected behaviour is currently unexplained but it is another evidence of the unusual behaviour of the InAlN alloy and its difference from other III-nitrides materials.
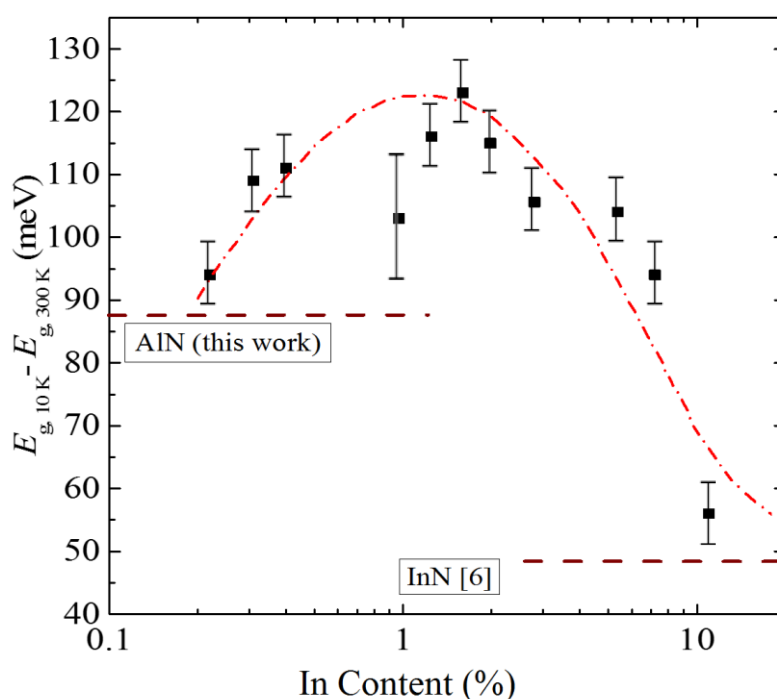
Figure 3-17 Composition dependence of InAlN temperature band-gap shrinkage between 10 K and 300 K (line is a guide to the eye).

One reason for this behaviour could be the fact that at low In content (<1%) this material behaves differently from higher In contents which is counted as an alloy. As mentioned in section 3.4, for low In content (below 1%) PL peak position is remaining unchanged and just intensity is reducing by decreasing indium. In this situation In atoms can act as individual particles inside AlN crystal which are not feeling each other (no wave-function overlap) due to relatively small exciton radius. The reason for broad PL emission at these compositions can be due to the coupling of the In exciton with crystal phonons and/or possibly of a complex with carbon or with Al vacancies.

3.6 Optical properties of InAlN across the full range of composition

3.6.1 Band-gap and bowing parameter

The band-gap of InAlN, as a ternary material, like many other ternary materials such as InGaN and InGaAs, has proven to be non-linear with composition. As a result we can define a nonlinearity factor of b, or bowing parameter for calculation of band-gap, as described in Equation 1-9.

As mentioned in section 1.2.2 bowing parameter, b, has been reported for the most of the nonlinear materials to be a small constant and composition independent factor like other nitride ternary alloys AlGaN and InGaN, but this is not in case for InAlN as showed theoretically [146, 153, 158] and proved experimentally [146, 157, 159] that it is a composition dependent parameter. But the challenges that still remain, are the exact value of the bowing parameter and hence band-gap for the whole composition range, especially for low indium content, x < 0.10, and the most interesting region in terms of technology which $In_xAl_{1-x}N$ is lattice matched to GaN, x≈0.18 .

Here I report the band-gap and bowing parameter of $In_xAl_{1-x}N$ for a whole composition range and the effects of temperature and introducing a new formula for bowing parameter using our data along with other previous and available data, for the full range of composition. Experimental details have been reported earlier in the previous section (3.5).

The composition dependent bowing parameter $b(x)$ can be calculated using Equation 3-11. Using a combination of our experimental $E_g(x)$ data with previously reported data for band-gap of InAlN for higher compositions than 10%. As a result we have managed to obtain an empirical expression for the bowing parameter for the full composition range of $In_xAl_{1-x}N$ alloy, using Equation 3-16. We should notice that as InAlN on AlN at low In contents are under compressive stress and it will affect the band-gap and hence bowing parameter, therefore for the understanding of actual parameters of free standing InAlN, these facts should be taking into account. There is the lack of enough information in this area but based on discussion in section 3.5 and reported previously [83], there is a non-linear reduction of the band-gap due to compressive strain. Also, theoretical calculations showed the band gap pressure coefficients, dE_g/dp, exhibit large bowing with composition [316, 319]. This indicates a strongly non-linear composition dependence of the deformation potentials which allow us to use non-linear estimation. Therefore we will end up with the parameters of $b_0 = 28.3 \pm 0.7$ eV; $x_{In,0} = 0.010 \pm 0.002$; n=4, $s = 0.118 \pm 0.005$ in Equation 3-16, see Figure 3-18. Here we used $E_{g,\ eff}^{AlN}$=6.015 eV for the band gap for AlN [320] which is compatible to our experimental

measurement, and for the band-gap of the InN, despite very scattered data due to different quality of materials [89, 313, 314] we came to the conclusion of using a value of $E_{g,\,eff}^{InN}$=0.65 eV. The non-parabolic variation of the band-gap and high composition dependence of bowing parameter in InAlN alloy has already been explained based on band anti-crossing (BAC) model in section 3.5.4.
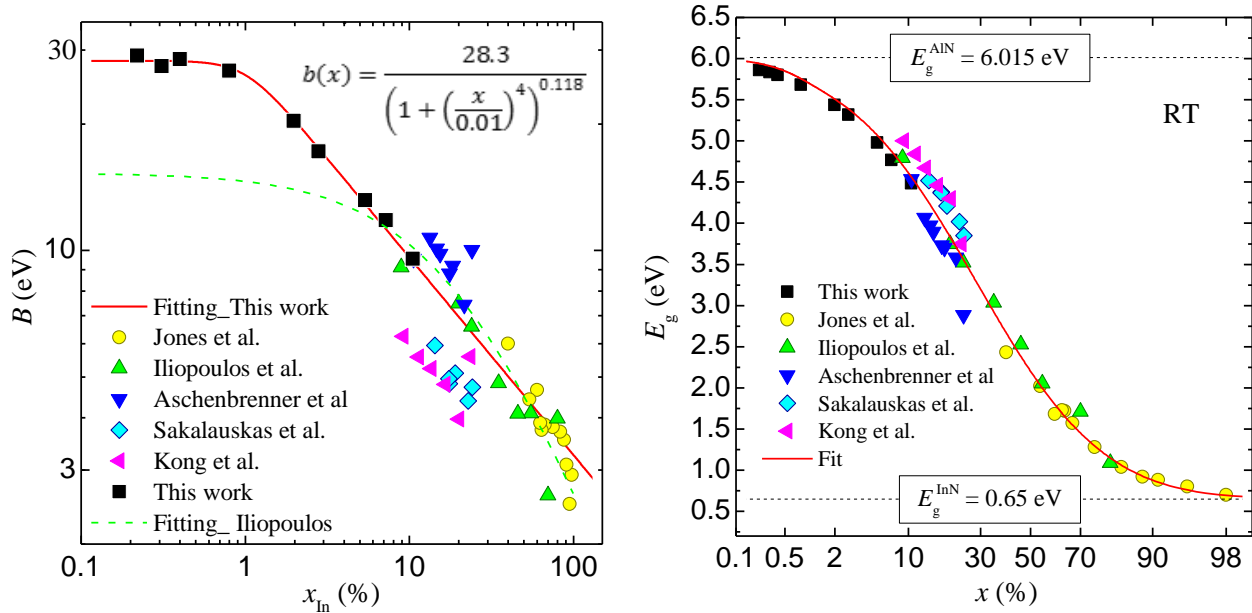
Figure 3-18 InAlN bowing parameter and bang gap with their best fit (using b(x) equation) in full range of In contents, in combination with other previously reported data [154, 155, 157, 159, 321].

To bring all information about band-gap variation of III-nitride semiconductors together we can use previous reports from other groups to be able to estimate and plot InGaN and AlGaN band-gap variation with composition and eventually with lattice parameter. Based on the latest results given by our colleagues in Tyndall National Institute, which is in good agreement with previous experiments and theoretical results (see [146] and references within), the bowing parameter of InGaN alloy for the whole composition range can be estimated. Using our empirical equation of Equation 3-16, and assuming saturation of bowing parameter at very low indium contents, similar to this situation for InAlN alloy, a non-linear and composition dependent bowing parameter of InGaN alloy is estimated. Using Origin software fitting to the theoretical data shown in Table 3-2, we could end up with the parameters of: $b_0 = 2.85\pm0.1$ eV; $x_{In,0} = 0.10\pm0.02$; $n=2$, $s = 0.12\pm0.005$ in Equation 3-16. Here we used $E_{g,\,eff}^{GaN}$=3.438 eV for the band gap for GaN (see section 1.1.2.1), and a value of $E_{g,\,eff}^{InN}$=0.65 eV.

Table 3-2 Composition dependent band-gap bowing parameter b(x) of In$_x$Ga$_x$N alloy [146].

x (%)	5	10	15	25	35	50	65	75	85
b (eV)	2.77	2.6	2.42	2.28	2.13	1.94	1.82	1.78	1.82

For AlGaN alloys, the bowing parameter is assumed to be small and composition independent [36]. Here, based on all previous researchers, the value of $b = 0.94$ is used which is recommended by Coughlan et al (2015) [130] and compatible with other previous reports, see also section 1.2.2 and references there. Also, the lattice parameter of all ternary alloys were derived by Vegard's law, see section 1.2.1 and Equation 1-8.

Based on this results, the interesting InAlN/GaN lattice matching occurs at the indium composition of 17.8 %. Assembling all these data and information, we are in position to be able to plot a new version of energy band-gap of wurtzite structure binary and ternary III-nitride semiconductors as a function of lattice constance, as depicted in Figure 3-19. An another interesting point here is lower band of InAlN alloy than AlGaN at the compositions lower than critical point of P, where both lattice and band-gap of InAlN and AlGaN are matched. This is due to very high bowing parameter of InAlN than AlGaN alloy at this range of compositions, as shown earlier in this thesis.
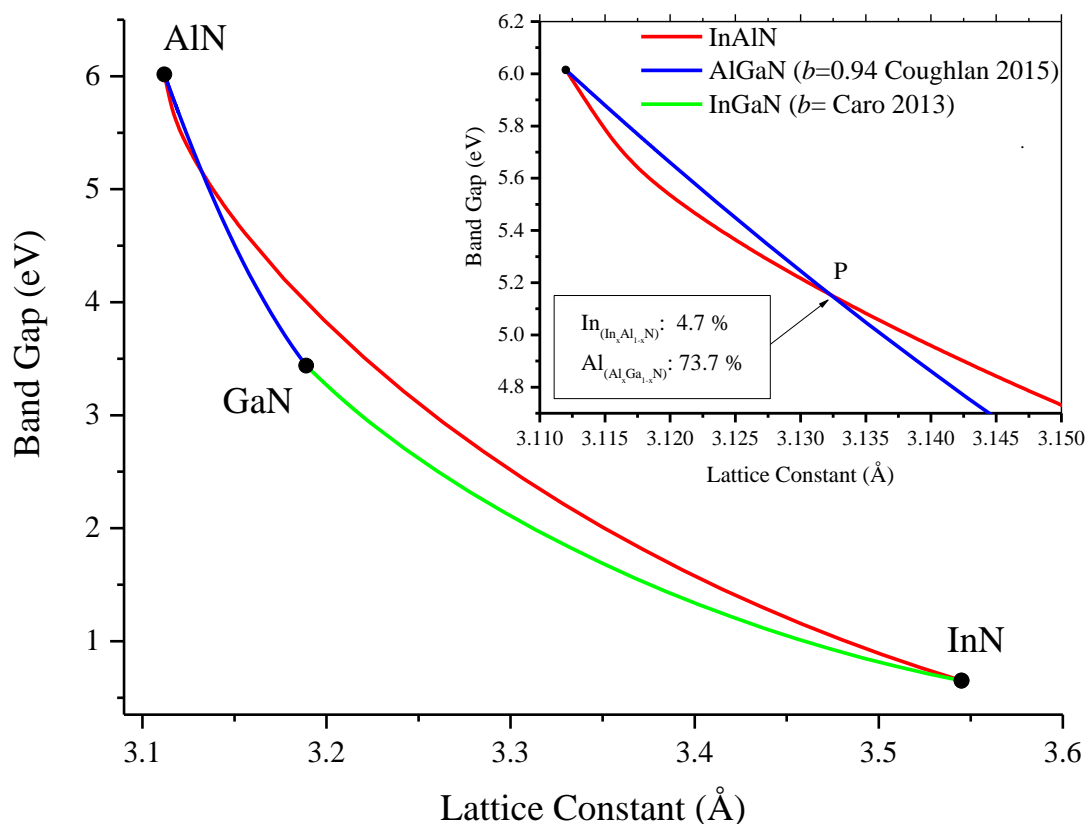
Figure 3-19 RT energy band-gap of wurtzite structure binary and ternary III-nitride semiconductors as a function of lattice constant.

3.6.2 Band offsets

Knowing the band offsets of the binary and ternary III-nitrides is also very crucial for designing the devices for photonic and electronic applications. Thus, it attracts a lot of attention both theoretically and experimentally [36, 322, 323]. Band offsets of InN-AlN and GaN-AlN are shown schematically in Figure 3-20 based on the data reported by Westmeyer et. al [323] and King et. al [322].
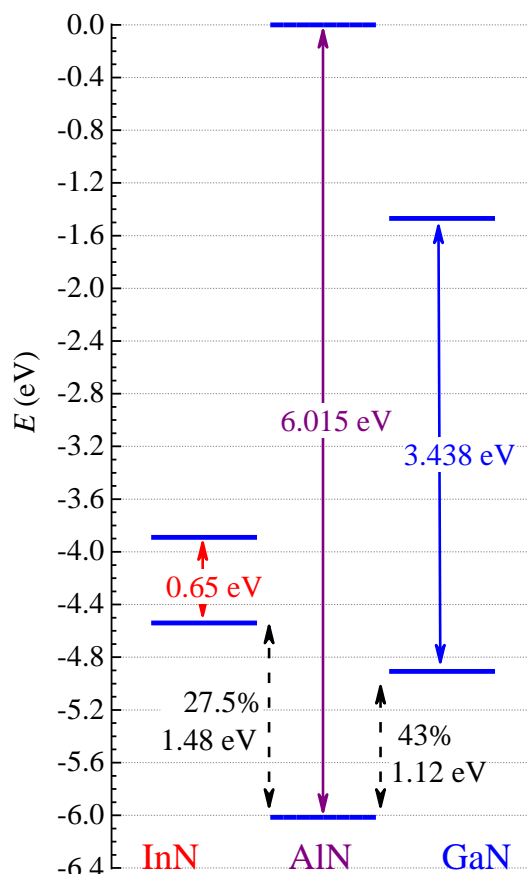
Figure 3-20 Schematic view of InN-AlN and GaN-AlN band-offsets.

A simple calculation taking into account InAlN and AlGaN band-gap composition dependencies and using band offset ratios ($\Delta E_c/\Delta E_v$) of 1.33 for the AlN–GaN system [323] and 2.63 for the AlN–InN system [322], the composition dependence band-offsets of ternary alloys can be calculated. Based on these calculations, estimated valance and conductive band offsets of InAlN and AlGaN are plotted in Figure 3-21. At the critical point of 'P' band-offsets of InAlN and AlGaN are determined and shown in Figure 3-21. It is shown that:

$$|\Delta E_c| = |E_c^{InAlN} - E_c^{AlGaN}| = \cong 165 \pm 5 \text{ meV}$$

$$|\Delta E_v| = |E_v^{InAlN} - E_v^{AlGaN}| \cong 125 \pm 5 \text{ meV}$$

Equation 3-18

There are still discrepancies in the band offsets of binary nitrides and the relationship of ternary compounds is even more uncertain. Here we assume that $\Delta E_c/\Delta E_v$ remains constant for each ternary alloy system with respect to a binary end point as a method to make a reasonable estimate. This is normally the case for most materials, though the implications of the composition dependent bowing parameter for InAlN does introduce additional uncertainty.

For point 'P' our results indicates the type-II line up in this structure, where electrons can be confined in InAlN with confinement energy of about 165 meV, while holes would be confined in AlGaN with the confinement energy of about 125 meV. This behaviour could be potentially useful for UV detector applications.
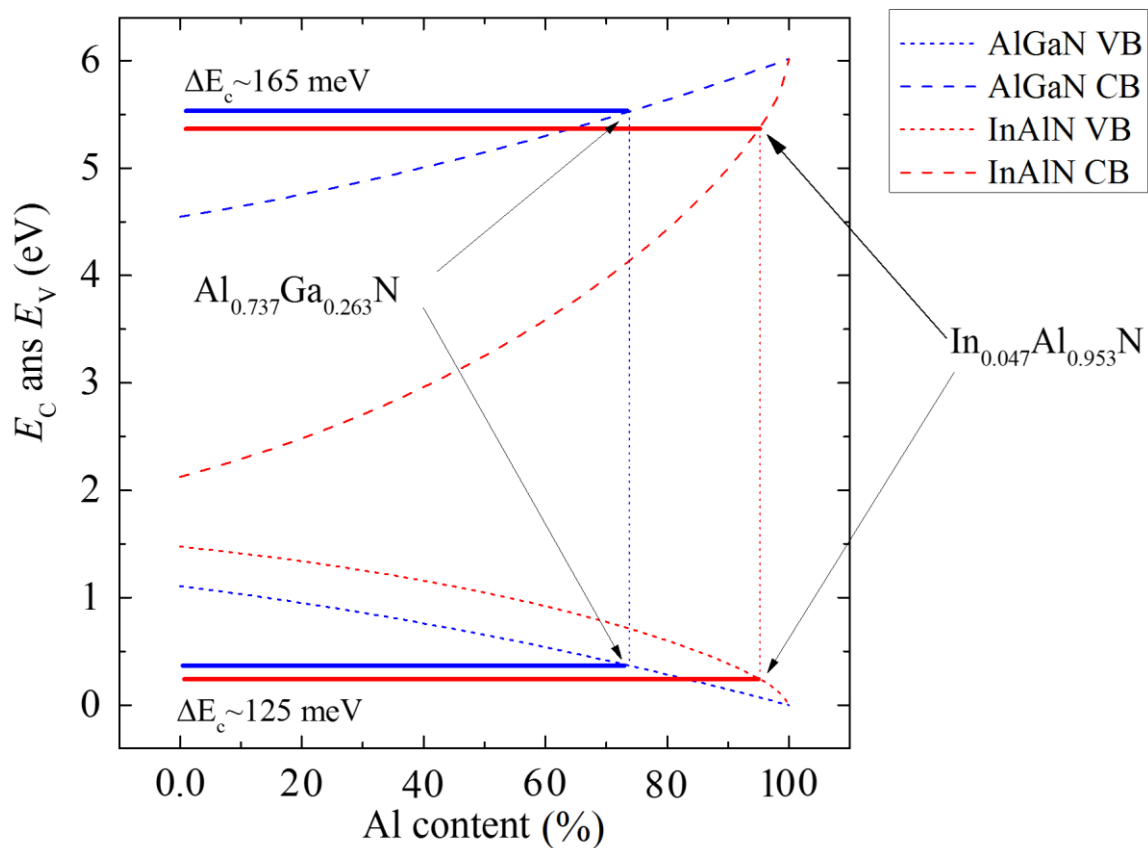
Figure 3-21 Composition dependent band offsets (dash lines) and the positions of valance and conductive bands (solid lines) of InAlN and AlGaN.

3.6.3   Refractive index

In addition to the band-structure properties of InAlN/AlGaN stack, (especially lattice matched InAlN/GaN structure) refractive index of the materials and index contrast ($\frac{\Delta n}{n}$) is a key point of interest for design and application of electronic and photonic devices such as DBRs [324-326] and laser

waveguides [326]. As shown in Equation 1-21, to calculate the index contrast we need the wavelength dependent variation of refractive index of both AlGaN and InAlN.

$$\frac{\Delta n}{n} = \frac{n_{InAlN} - n_{AlGaN}}{n_{AlGaN}}$$

Equation 3-19

There are several techniques suggested by scientists to determine refractive index of semiconductors and therefore index contrast of a stack. Using an empirical oscillator model it is very common to determine the dispersion of refractive index, for energies lower than the band-gap energy [327]. Sellmeier equation is regularly used for derivation of wavelength dependent refractive index of dielectric materials [328]:

$$n(\lambda)^2 = A + \frac{\lambda^2}{\lambda^2 - B}$$

Equation 3-20

where λ is the incident wavelength (in μm). A and B are parameters determined by fitting. To find these coefficients for compound semiconductors, Sellmeier parameters has been interpolated. For $Al_xGa_{1-x}N$ alloys, Takeuchi et. al. [328] suggested the composition dependent parameters A(x) and B(x) as below:

$$A(x) = 4.27 - 1.07x$$

Equation 3-21

$$B(x) = 0.092 - 0.065x$$

Parameters A(x) and B(x) were taken by fitting the experimental values and managed to deal effectively with AlGaN alloys [328, 329]. However, based on our knowledge, there are no such a systematic values for InAlN and InGaN materials so far.

Two main problems are still remaining regarding to determination of refractive contrast of the alloys; first, they are covering limited composition ranges and second is they are just valid for specific wavelengths. Another concern is that Sellmeier coefficients used in Equation 3-20 are pure fitting parameters without actual physical meaning.

A model for determination of dielectric function of dielectric materials was proposed by Adachi in 1982 [330]. This model which is more physics based, worked well for semiconductors as well, for energies lower that band-gap energy ($hv < E_g$) [327].

$$n^2(hv) = a(x) * \left(\frac{hv}{E_g}\right)^{-2} \left[2 - \left(1 + \left(\frac{hv}{E_g}\right)\right)^{\frac{1}{2}} - \left(1 - \left(\frac{hv}{E_g}\right)\right)^{\frac{1}{2}} \right] + b(x) \quad \text{Equation 3-22}$$

where E_g denotes the band-gap energy of the material, h is Planck's constant, v is incident light frequency and $a(x)$ and $b(x)$ are fitting parameters. This formula has been used with a good agreement with experimental data for III-nitride binary materials (AlN, GaN and InN). Parameters $a(x)$ and $b(x)$ are also showing good agreement with experimental measurements of refractive index of the ternary alloys by linear interpolation of those for binary materials [52, 331-333].

Peng and Piprek obtained the fitting parameters by linear interpolation from binary AlN, GaN and InN nitrides for ternary compounds in 1996 [150, 331]. The parameters proposed by Peng and Piprek for Parameters of wurtzite GaN, AlN and InN are summarised in Table 3-3. For a III-nitride ternary $A_xB_{1-x}N$ these parameters are obtained using generic equations as follows:

$$a(x)_{ABN} = a_{AN}x + a_{BN}(1 - x)$$

$$\text{Equation 3-23}$$

$$b(x)_{ABN} = b_{AN}x + b_{BN}(1 - x)$$

Later on 1999, Piprek et. al. [334] proposed a non-linear interpolation for $Al_xIn_{1-x}N$ alloy:

Table 3-3 Parameters of wurtzite GaN, AlN and InN used by Peng and Piprek [331].

Material	Eg (eV)	a	b
InN	1.9	53.57	-9.19
GaN	3.4	9.31	3.03
AlN	6.2	13.55	2.05

Although the parameters and formulas proposed by Peng and Piprek were worked well in some levels of accuracy, but they were still far from good values to be used in advanced application like laser. It

was mostly due to choosing the wrong values for band-gap of binary materials, specially using the large value for InN band-gap (1.9 eV) which later proved to be much smaller [87]. Therefore it was introducing errors for the values of refractive index. For example at the wavelength of 589 nm it gave the value of n=2.36, which is substantially larger than values reported later for AlN [328, 333, 335] .

To get the higher level of accuracy, Laws et. al. introduced the modified non-linear expressions for parameters a(x) and b(x). For $Al_xGa_{1-x}N$ in the range of $0 < x < 0.38$ formula would be as below:

$$a(x)_{AlGaN} = 9.827 - 8.216x - 31.59x^2$$

Equation 3-24

$$b(x)_{AlGaN} = 2.736 + 0.842x - 6.29x^2$$

The accuracy and functionality of these parameters are still inadequate, because it is not using state-of-the-art values for band-gap and limited range of composition covered.

Here to determine the refractive index of ternary nitrides we are applying the Adachi model. To attain the accurate values, the most recent band-gap values for binary and ternary nitride are used. Therefore for band-gap value (Eg) in Equation 3-22, the values obtained from our experiments are used, especially for fundamental band-gap value of Eg=6.015 eV for AlN, as shown in section 3.6.1. Using the previous experimental data for refractive indexes of AlN [332], GaN [127] and InN [336] enabled us to obtain a and b parameters of these binary nitrides. Energy band-gap and all fitting parameters of wurtzite AlN, GaN and InN are summarised in Table 3-4 .

Table 3-4 Band- gap Energy and Adachi model fitting parameters of wurtzite InN, GaN and AlN.

Material	Eg (eV)	a	b
InN	0.65	7.44±0.3	4.58±0.2
GaN	3.438	9.64±0.2	2.85±0.05
AlN	6.015	14.61±0.1	0.45±0.03

To obtain the Adachi parameters for ternary alloys, a linear interpolation from binary nitrides is utilised. Generic expressions are defined to drive the $a(x)$ and $b(x)$ for a III-nitride ternary $A_xB_{1-x}N$ alloy (Equation 3-23).

The photon energy dependence refractive index of gallium nitride is shown in Figure 3-22. As can be seen, the calculation of refractive index based on our model is in a very good agreement to other previous experimental results [52, 157, 328, 332, 337-340], and fits well to the average empirical values in the combined data set.

Figure 3-22 Refractive index of GaN as a function of photon energy. Comparison of our new model with previous experimental results and theoretical models.

The incident photon energy and composition dependence refractive index of InAlN and AlGaN were derived using the parameters in Table 3-4. Our data, reported in section 3.6.1, is used for band-gap energy of InAlN across the full compositional range. For the AlGaN alloy, a bowing parameter of 0.94 is applied to calculate the band-gap at different compositions, as described in section 3.6.1.

The results for refractive index of $In_xAl_{1-x}N$ and $Al_yGa_{1-y}N$ alloys as a function of photon energy (below band-gap) at different compositions are depicted in Figure 3-23. Also the variation of refractive index at different compositions using theoretical models proposed by Tacheuchi et al. [328]

are added to the graph for comparison. Our new model shows good agreements with previous experimental results. Slight differences could be related to material quality and techniques used for growth and characterisation.
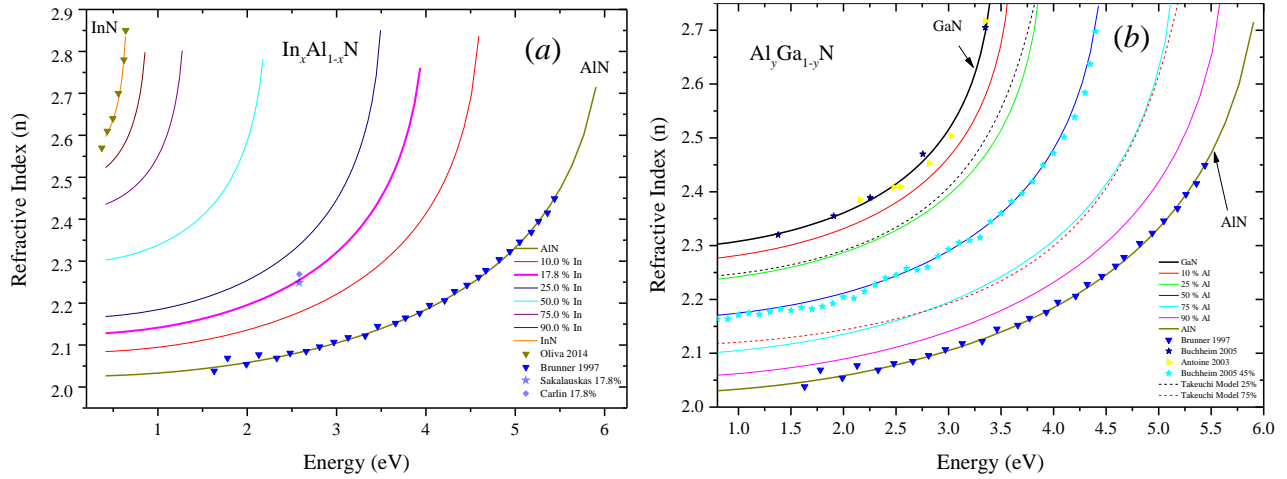
Figure 3-23 Refractive index of InAlN (a) and AlGaN (b) alloys as a function of photon energy at different compositions. Comparison of our new model with previous experimental results.

Figure 3-24-*a* shows the refractive index of InAlN with varying indium content at four different incident light wavelengths of 480 nm, 633 nm, 950 nm and 1064 nm. Based on our knowledge this would be the first systematic estimate for InAlN alloy for this wide composition range.

In terms of index contrast there were some works done for InAlN/GaN due to technological interests of this structure. Carlin et al. [324], using experimental spectroscopic set-up obtained the refractive index experimentally and based on those results they proposed an empirical equation for determining the *Δn/n* for indium composition within the 6% to 21% range using optical reflectance:

$$\frac{\Delta n}{n}(In_xAl_{1-x}N/GaN) = -0.127 + 0.35 * x \qquad \text{Equation 3-25}$$

Later, Sakalauskas and colleagues [157] suggested a modified formula for *Δn/n* with a good agreement with previous expression and covering the wider composition range ($0 \leq x < 0.2$).

$$\frac{\Delta n}{n}(In_xAl_{1-x}N/GaN) = -0.125 + 0.29 * x \qquad \text{Equation 3-26}$$

Although these expression are in good agreement, they are still insufficient due to limited compositions they cover and also the formula is just valid for a wavelength of 480 nm.

Based on our proposal, refractive index contrast ($\Delta n/n$) of the any two III-nitride binary or ternary compounds can be modelled and calculated. $\Delta n/n$ of the lattice matched InAlN-GaN as a function of energy is plotted and illustrated in Figure 3-24-*b*. It can be seen that the index contrast $|\Delta n/n| \approx 7\%$ at low energy side transparent region, then rises rapidly as energy approaches the band-gap energy of GaN, due to the fact that that refractive index is increasing close to the band-edge because of higher absorption coefficient.
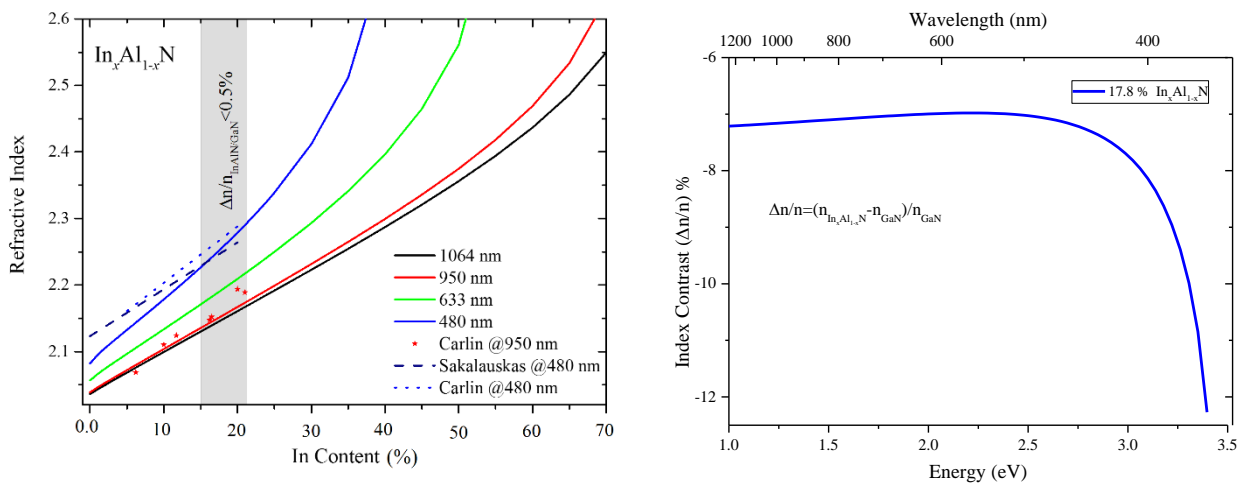
Figure 3-24 a)Refractive index of InAlN at whole composition range at different incident light wavelengths in comparison with other models. b) Refractive index contrast of the lattice matched InAlN-GaN as a function of energy.

As mentioned earlier, there is a tremendous interest regarding the InAlN-GaN refractive index contrast, especially for lattice matched pair and most of the research and reported results are focused on this. Therefore, here, based on our proposed model, indium content dependent index contrast of InAlN-GaN at four different incident light wavelengths is shown in Figure 3-25. Also the inset picture presents an expanded picture including experimental data close to the lattice matched condition. Two models proposed by Carlin et al and Sakalauskas et al. are also shown in the inset picture for comparison. Our results are consistent with those results and $\Delta n/n$ remains between ~7% to ~8% at compositions close to lattice match ($\Delta a/a<0.1\%$). In addition to these, Feltin et al. showed $|\Delta n/n|\sim10\%$ between $In_{0.15}Al_{0.85}N$ and $Al_{0.2}Ga_{0.8}N$ at 343 nm, whilst our model gives value about 7.5%, which is still in a good agreement with experimental data. It is indicating and proving that this structure is a good choice for diffractional Bragg reflectors (DBR) applications and even low In content InAlN/AlGaN stacks are able to be utilised for UV mirrors.
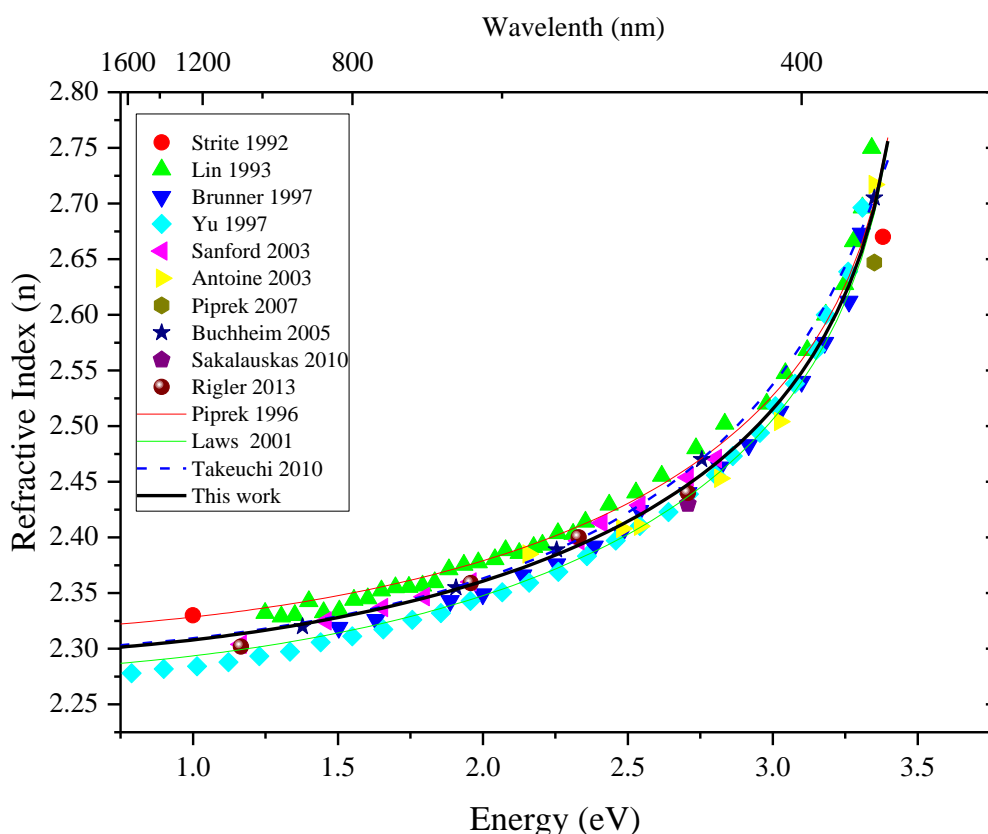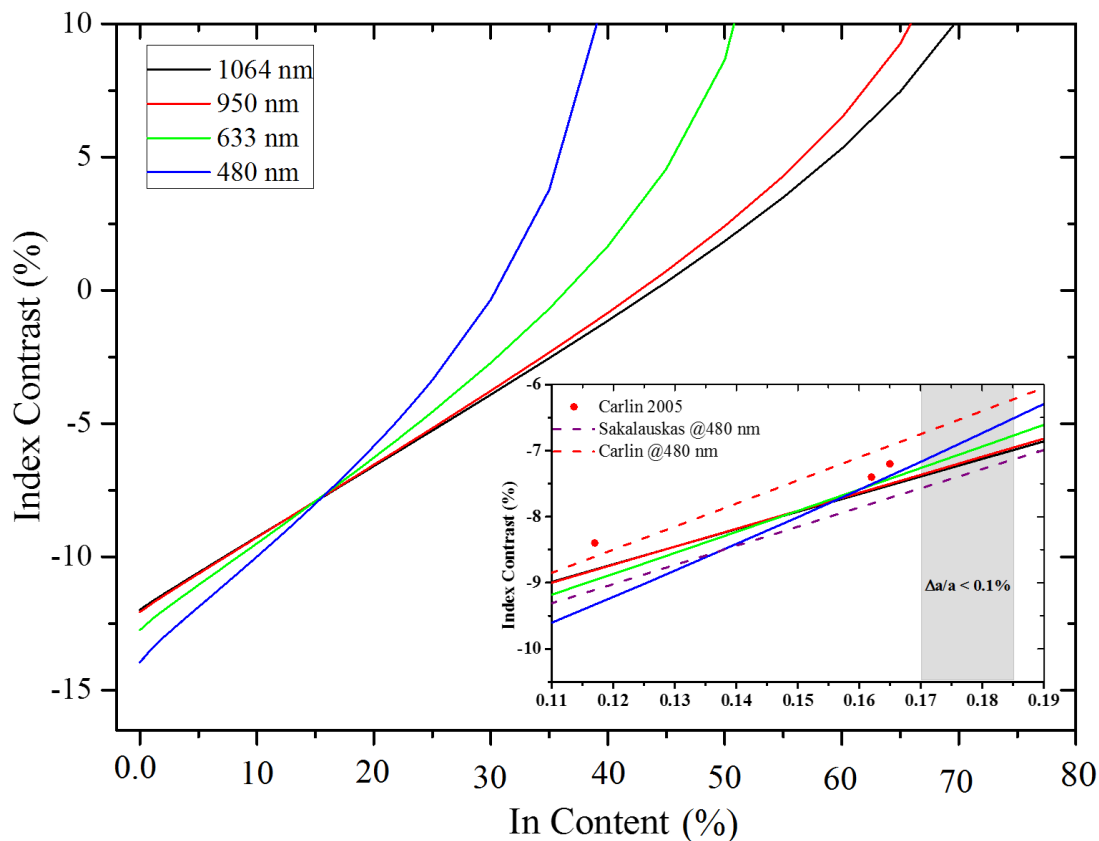
Figure 3-25 Refractive index of GaN as a function of photon energy. Comparison of our new model with previous experimental results and theoretical models.

3.7 Summary

In summary, we reported on the optical properties of 80-120 nm thick $In_xAl_{1-x}N$ epitaxial layers prepared on AlN templates with low In content. The layers were found to be nearly fully strained for In compositions less than about 0.10. While no luminescence was observed for relaxed samples ($x > 0.11$) those that were fully strained exhibited strong near UV luminescence with maximum efficiency for indium content in the range $0.004 \leq x \leq 0.016$. The luminescence centre(s) responsible for the band are currently not identified, though a clear association with the presence of In is observed. Using the band as a probe for photoluminescence excitation spectroscopy a detailed determination of the variation of the room temperature $In_xAl_{1-x}N$ effective band-gap with indium content in the range $0.0022 \leq x \leq 0.11$ was obtained. The band-gap was found to decrease rapidly with indium content resulting in $In_xAl_{1-x}N$ band-gap bowing parameter of above 25 eV in the $x{\rightarrow}0$ limit. The obtained evolution of the $In_xAl_{1-x}N$ band-gap in the $x < 0.11$ range can be well described

using a band-anticrossing model to take account of the interaction between localised In states and the host matrix conduction and valence band edges. This data allows determination of the potential of InAlN for active region design and reflector stacks in the UV, as well as for modelling of InAlN based heterostructure field effect transistors. Furthermore, the presented data shows the strong impact of a small (<1%) content of InN in an AlN matrix on the selection rules governing surface emission and absorption in InAlN, of direct relevance in the consideration of such alloys for UV emitter applications.

Using our low In content data in combination with data reported by other scientists, band-gap and bowing parameter of InAlN alloy at the full composition range were determined. Applying the provided accurate band-gap data, band-offset and refractive index of the alloys were driven using Adachi model for all binary and ternary III-nitride materials. The results are in good agreement with previous experimental data reported for refractive index of GaN, AlN and AlGaN. Also, although there were no experimental data for InAlN alloys, the index contrast obtained for InAlN/GaN is in a very good agreement with other experimental and models, especially at the InAlN compositions lattice matched to GaN.

Chapter 4

InAlN Alloys as an Active Region for Light Emitting Applications

4 INALN ALLOY AS AN ACTIVE REGION FOR LIGHT EMITTING APPLICATIONS

As already mentioned previously, InAlN alloy potentially can be a good candidate for light emitting applications especially in the blue and UV range. In the previous chapter band-gap and bowing parameter of this material, as critical parameters in semiconductors had been investigated particularly for the low indium composition range. In this chapter the possibility of using this material as an active region will be studied. This study includes optimisation of the InAlN QWs from luminescence point of view as well as effects of composition, temperature and excitation power on the luminescence properties of the InAlN.

4.1 Optimisation of InAlN QWs from luminescence point of view

InAlN/AlGaN multiple quantum wells (MQWs) emitting between 300-350 nm have been prepared by metalorganic chemical vapour deposition on planar AlN templates. To obtain strong room temperature luminescence from InAlN QWs a two-temperature approach was applied [187]. The intensity decayed weakly as the temperature was increased to 300 K, with ratios $I_{PL}(300\ K)/I_{PL}(T)_{max}$ up to 70%. This high apparent internal quantum efficiency is attributed to the exceptionally strong carrier localisation in this material, which is also manifested by a high Stokes shift (0.52 eV) of the luminescence. Based on these results InAlN is proposed as a robust alternative to AlGaN for ultraviolet emitting devices.

4.1.1 Experimental

All samples studied here were grown on c-Al_2O_3 substrates by the MOVPE reactor using trimethylgallium, trimethylindium, trimethylaluminum and ammonia as precursors. The choice of the substrate was determined by the need to have UV transparency in the practical light emitting devices, and to ensure the III-nitride growth was also c-oriented, which gives the most reliable structural and morphological quality in this material system, see section 2.2.3. The InAlN/$Al_{0.53}Ga_{0.47}N$ 5QW stacks were grown on 2 μm $Al_{0.53}Ga_{0.47}N$ templates, which were deposited on 2.5 μm AlN on c-Al_2O_3 as described above. The In composition of the wells was modified in the range 12 to 18% using growth temperatures in the range 790°C to 730°C, an approach used for our InAlN epilayers (see 2.2). For the InAlN QW growth, the molar ratios of the group III precursors (TMIn/TMAl) was set equal to

0.5 and the V/III ratio was 3600 and a growth rate of around 0.05 nm/s was obtained, slightly decreasing with increasing temperature. The MQW growth was carried out at a pressure of 70 mbar under a nitrogen atmosphere, while a hydrogen atmosphere was used in the preparation of the AlGaN/AlN-templates. After growth of the last barrier, the samples were cooled under an NH_3 flow.

Samples were characterised by XRD using a PANalytical X'pert PRO XRD system as described earlier. PL was excited using a 244 nm laser or monochromator coupled Xe-lamp in the temperature range 11-325 K. PL and PL excitation (PLE) spectra were detected using iHR320 Horiba imaging spectrometer equipped with a CCD camera and a photomultiplier.

4.1.2   Effect of Cap Layer Thickness

As is known for InGaN/GaN QWs, there is a trade-off between the In composition and crystalline quality [341]. One method to obtain higher efficiency is to grow the quantum barriers (QBs) at temperatures higher than those of the QWs ($T_{QB} > T_{QW}$) [342], so-called "quasi-2T" approach [343]. Here we adopted a similar approach to the growth of InAlN/AlGaN MQWs, whereby the QWs were capped with a thin layer of AlGaN at T_{QW} before the ramp to T_{QB} at which the main part of QB was grown. To clarify, growth structure and temperature profile of InAlN/AlGaN MQWs is schematically depicted in Figure 4-1.
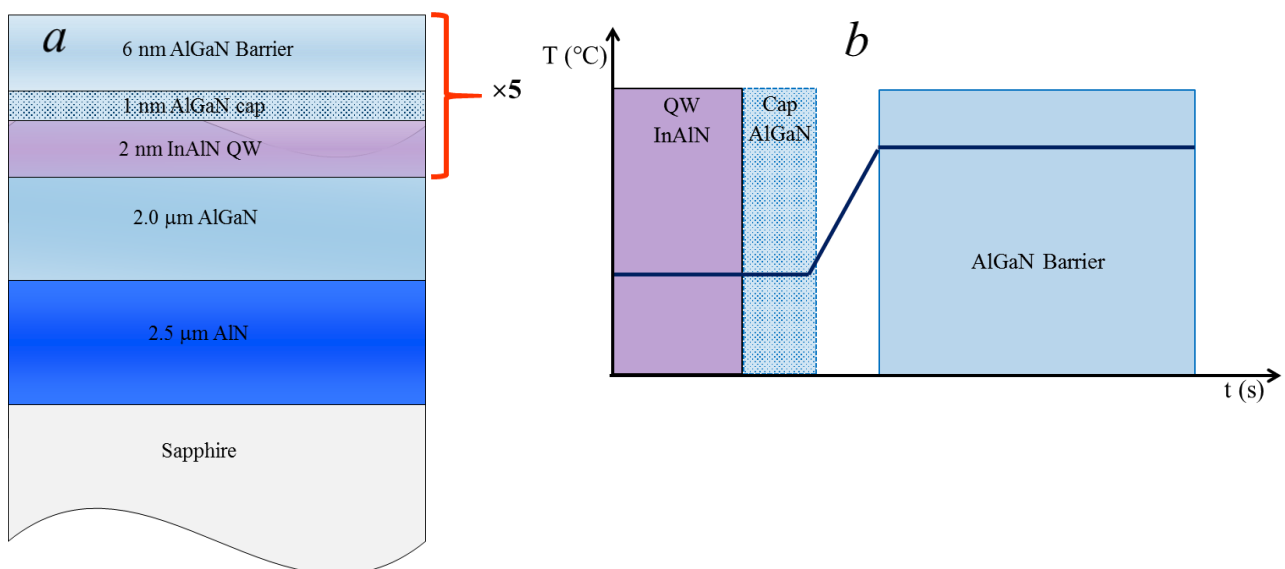
Figure 4-1 Schematic illustration of growth structure (a) and temperature profile during growth (b) of InAlN/AlGaN MQWs.

To examine the impact of AlGaN cap thickness on InAlN/AlGaN 5QW luminescence, otherwise, identical structures with nominal caps of 0, 1, 2, 3 nm were prepared. As shown in Figure 4-2,

reduction of intensity and blueshift in luminescence of the sample with "1 nm" cap layer is observed, this is due to an inadequate protection by the thinner cap. The "3 nm" cap seems to be excessive since there is no further PL redshift in comparison to the "2 nm" cap while there is a drop of PL intensity. A possible reason for the reduction of the PL intensity of the "3 nm" cap sample is that there will be wells/barriers created inside thicker wide band-gap part of QBs and prevent carriers to transport from QBs to QWs [187].
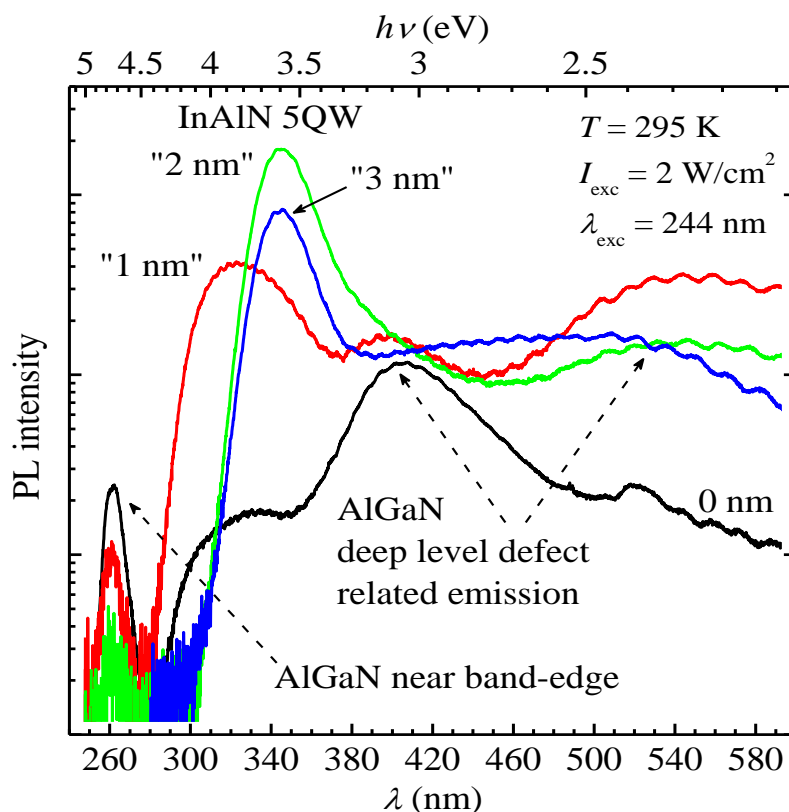
Figure 4-2 RT PL spectra of InAlN/AlGaN 5QW structures with different nominal QW cap layer thicknesses[187].

4.1.3   Effect of QWs Thickness

Two sets of QW samples with thicknesses (d_{QW}) of 1.1, 1.4, 2.0, 2.6 nm and 1.0, 2.0, 3.0, 4.0 nm were grown at T_{QW} of 730°C and 790°C, respectively. Using data from section 3.5, the indium composition of the quantum wells at 730°C and 790°C would be 22.4 % and 11.3 %, respectively. The in-plane mismatch between AlGaN QBs and InAlN QWs can be calculated using Equation 2-6, where summarised in Table 4-1.

Table 4-1 Lattice constants of InAlN QWs and AlGaN QBs and their in-plane lattice mismatch.

	$a_{(InAlN)}$ (Å)	$a_{(AlGaN)}$ (Å)	Mismatch (%)
730°C	3.209	3.153	~1.8
790°C	3.161	3.153	<1

The results for RT PL wavelength and integrated PL intensity are plotted in Figure 4-3. We describe the initial rise of PL intensity with d_{QW} with a better carrier confinement in the thicker QWs, assuming only a weak carrier transport from QBs to QWs. For the $T_{QW} = 730$°C series, it was found that the highest PL intensity corresponds to d_{QW} between 1.4 and 2.0 nm. Increasing d_{QW} from 2.0 nm to 2.6 nm led to a sharp decrease in PL intensity with a much smaller redshift of the corresponding PL band in comparison to that observed for $d_{QW} < 2.0$ nm thick QWs. The same sort of behaviour is observed for samples from the $T_{QW} = 790$°C series but the sharp drop in PL intensity occurs for wider QWs (between 3.0 and 4.0 nm). The possible reasons for the PL efficiency saturation and then drop include a quantum-confined Stark effect (QCSE) in wider QWs and a partial strain relaxation (via defect formation) [343, 344]. QCSE would be expected to lead to a consistent redshift with increased well width contrary to our observation. Furthermore, initial modelling work done by my colleague showed that such structures are nearly polarisation matched and as a result should have reduced internal fields. Therefore, we believe the latter mechanism is dominant as it may also explain why the observed PL efficiency drop occurs earlier for QWs grown at 730°C. The $Al_{0.53}Ga_{0.47}N$ buffer and barriers are nearly fully strained to AlN (only 8-10% relaxation), therefore, QWs with higher indium content suffer from stronger compressive strain and as a result may start to relax at lower thicknesses. Another possible reason for earlier drop in efficiency with respect to the well thickness in samples grown at 730°C in comparison with 790°C, is higher in-plane lattice mismatch, therefore, stronger compressive stress in the QWs, see Table 4-1. With increasing well thickness, formation of defects due to strain relaxation would be higher in the samples with higher in-plane lattice mismatch.
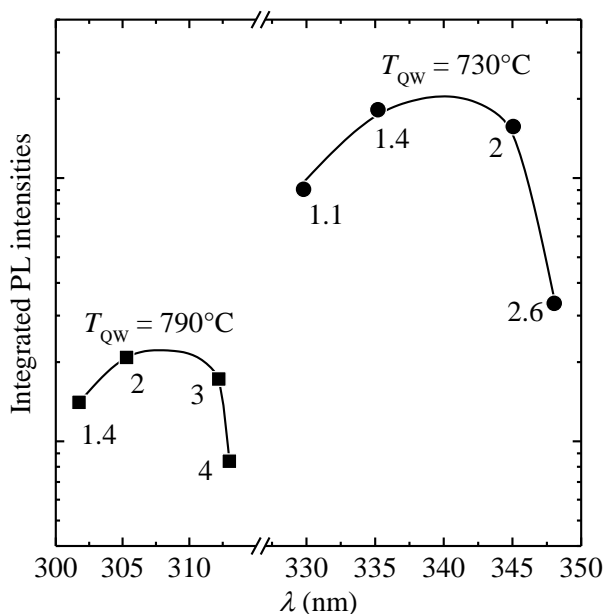
Figure 4-3 RT PL intensities as a function of PL peak position for the MQW heterostructures grown at different T_{QW}. The numbers close to the data points are QW thicknesses in nm [187].

4.1.4   PLE of InAlN/AlGaN QW heterostructures

RT PLE spectroscopy was applied to an InAlN/AlGaN sample with five 2 nm-wide QWs grown at $T_{QW} = 750°C$ to confirm the origin of each PL band present in its PL. The PLE spectrum of the InAlN-related peak, at the detecting energy of ~3.701 eV ($\lambda_{det} = 335$ nm, Figure 4-4) shows contributions from both AlGaN and InAlN. The feature around 4.64 eV correlates well with the band-gap of compressively strained $Al_{0.53}Ga_{0.47}N$ [345], while a "soft" edge at $hv < 4.5$ eV relates to the absorption edge of InAlN which is expected to be broad due to the nature of the alloy. Similar results have been reported for InGaN QWs. Fitting of the InAlN absorption edge with a sigmoidal expression [184] allowed determining the effective band-gap $E_{g,eff}$ of 4.25 eV and broadening parameter ΔE of 136 meV. As reviewed in section 1.2.2 and later showed with our experimental data in section 3.5 for bulk InAlN alloy, our effective band gap, $E_{g,eff} = 4.25$ eV, obtained for $In_{0.16}Al_{0.84}N$ QWs stands within the range of reported values. Both the Stokes shift ($E_{g,eff} - E_{PL}$) of 0.52 eV and broadening parameter are higher than those in InGaN with similar indium fraction x $\approx$ 16% [184], which can be expected given the higher value of the derivative $dE_g(x_{In})/dx_{In}$ in InAlN. This in its turn suggests that the carrier localisation is as expected much stronger in InAlN than in InGaN. The lowering of QW PLE signal at $hv>4.55$ eV where QBs become opaque decreasing the amount of exciting light absorbed directly in QWs indicates a weak carrier transport from QBs to QWs, which possible reason was discussed above [187].

The PLE spectra of the deeper luminescence bands measured at detection energies of ~3.024 eV (λ_{det}=410 nm) and ~2.567 eV (λ_{det}=483 nm) show that the corresponding PL bands are effectively excited by light with photon energies above the AlGaN band-gap confirming our ascription above. There is some lower photon energy ($h\nu < 4.5$ eV) excitation of the AlGaN bands in the PLE spectra that might be due to some contribution from the QWs or a sub-band-edge absorption in AlGaN.
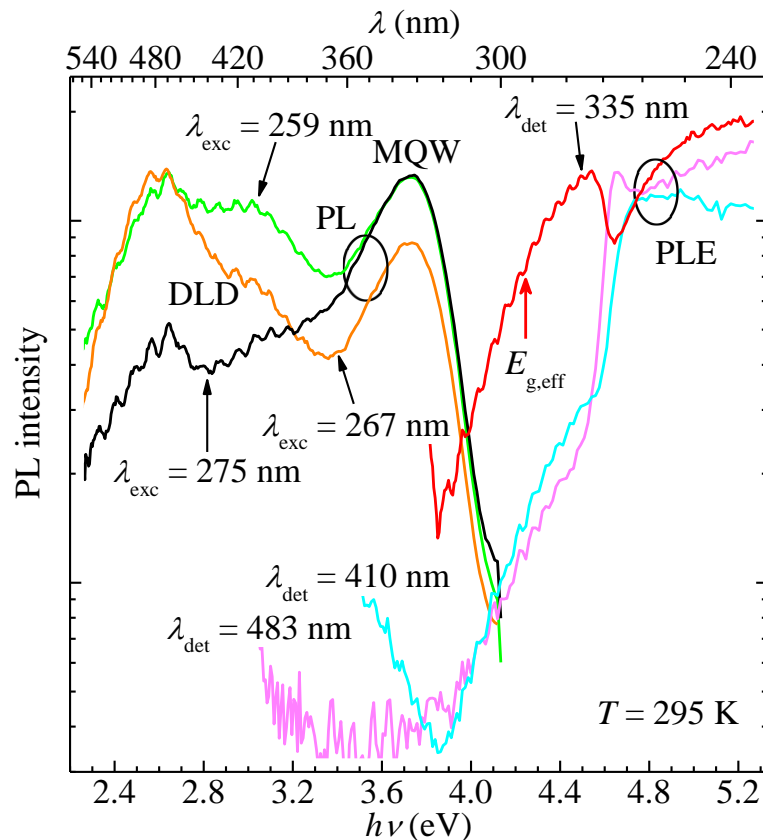
Figure 4-4 RT PL and PLE spectra of InAlN/AlGaN 5QW structure with 2 nm thick QWs grown at T_{QW} = 750°C.

4.1.5   Temperature Dependent Photoluminescence Spectroscopy

The same sample was also characterised by temperature dependent PL under 244 nm excitation shown in Figure 4-5. Notably the maximum integrated QW PL does not occur at low temperature (LT) but between 120 and 150 K. Furthermore the "apparent internal quantum efficiency (IQE)", defined here as the ratio between the RT PL integrated intensity and the highest measured value of it, is around 38% suggesting a strong thermal resilience of the luminescence. It is worth noting that AlGaN/AlGaN QWs are usually characterised by much lower "apparent IQE" values [346]. This demonstrates that InAlN-based emitters can potentially be more efficient at RT than their AlGaN-based counterparts at least in near UV region.
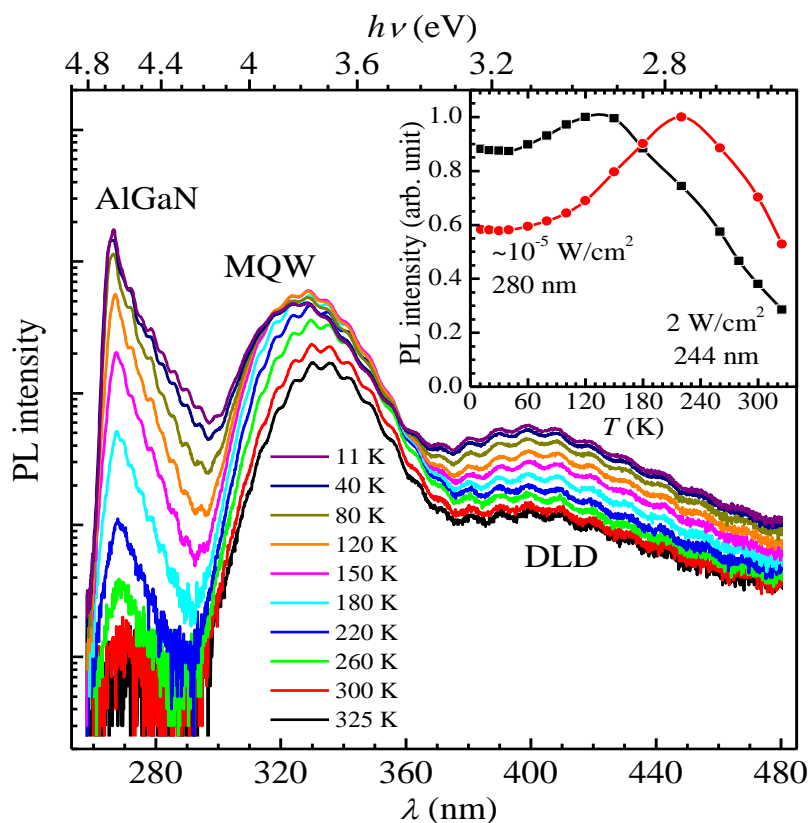
Figure 4-5 Temperature-dependent PL spectra of the InAlN/AlGaN MQW heterostructure at 244 nm laser emission excitation. Inset: normalised integrated intensities of the QW-related band under different excitation conditions as a function of temperature [187].

All the QW samples showing good RT PL are found to exhibit maximum PL intensities at elevated temperature, typically 60-200 K. The reason for this behaviour is the subject of investigation and we will explain it later in this thesis in section 4.3. Theoretical work performed by Schulz et al. [305] have indicated that in bulk InAlN the lowest hole and electron energy states may not be spatially co-located. This would lead to a reduced radiative efficiency until the carriers have sufficient thermal energy to hop from one local minimum to another. A second argument is that carrier transport from QBs to QWs may be further degraded at LT caused by stronger carrier localisation in the QBs. As it was discussed earlier in 4.1.2, the thin Al-rich cap causes a non-uniform composition profile in the barrier potentially leading to a carrier trap location.

To investigate further, temperature-dependent PL measurements were performed using monochromated 280 nm Xe lamp emission for selective excitation of QWs. The maximum PL efficiency shifted to even higher temperature (220 K) indicating that carrier transport from QBs to

QWs is not responsible for this behaviour, but the localisation effect (spatial non-co-location) likely is. PL "apparent IQE" in the case of selective excitation of QWs was found to be 70%.

4.2   Composition dependence of PL properties of $In_xAl_{1-x}N$/AlGaN QWs

A series of InAlN/AlGaN five QW heterostructures was prepared by MOVPE system to investigate their photoluminescence properties as a function of indium content in QWs with the aluminium content in the barriers fixed at 59%.

4.2.1   Experimental

The InAlN/AlGaN 5QW samples studied here were grown by MOVPE, as described in section4.1. The growth of the active region in N_2-ambient was preceded by deposition of a 2 µm thick undoped AlGaN-buffer layer on pre-prepared AlN/sapphire templates. The indium content in QWs was varied by changing QW growth temperature T_{QW} in the 710-790°C range while keeping the barrier growth temperature fixed at 1110°C. The same spectrometer system described in section 3.2 was used for PLE measurements whereby luminescence was excited by Xe lamp emission after the double additive grating scanning monochromator.

4.2.2   Results

In general, the RT PL spectra of InAlN/AlGaN MQWs grown using high-temperature QBs, proper cap layers and optimised QW thicknesses are dominated by near-UV emission corresponding to the QWs. The peak position is principally dependent on T_{QW}. Besides the main PL band and the AlGaN buffer near-band-edge emission at 260-270 nm, there are two additional bands at 390-410 and 470-550 nm. The exact peak positions vary from sample to sample, and the relative intensities depend on excitation condition. Comparison of InAlN/AlGaN MQW PL spectra with that of AlGaN templates shows these bands can be attributed to the deep level defect (DLD) emission in the underlying AlGaN buffer layers [347]. Room temperature RT PL spectra of the InAlN/AlGaN MQW samples are presented in Figure 4-6. According to the results from 4.1.4, the weak shortest wavelength band at around 265 nm corresponds to the band-edge emission from AlGaN bulk buffer. A somewhat broader and in some cases dominant near-UV band is the emission from QWs. Two broad peaks in the visible are defect-related emission bands from AlGaN layers.

It can also be seen in Figure 4-6 that the QW-related PL band redshifts with decreasing QW growth temperature, which is consistent with the higher indium incorporation and thus lower band-gap of the

resulting InAlN. With taking into account the In compositions in samples grown at two lowest temperatures, the overall PL redshift is nearly linear with x and is of about 6.5 nm per one percent of composition, as shown in Figure 4-7.
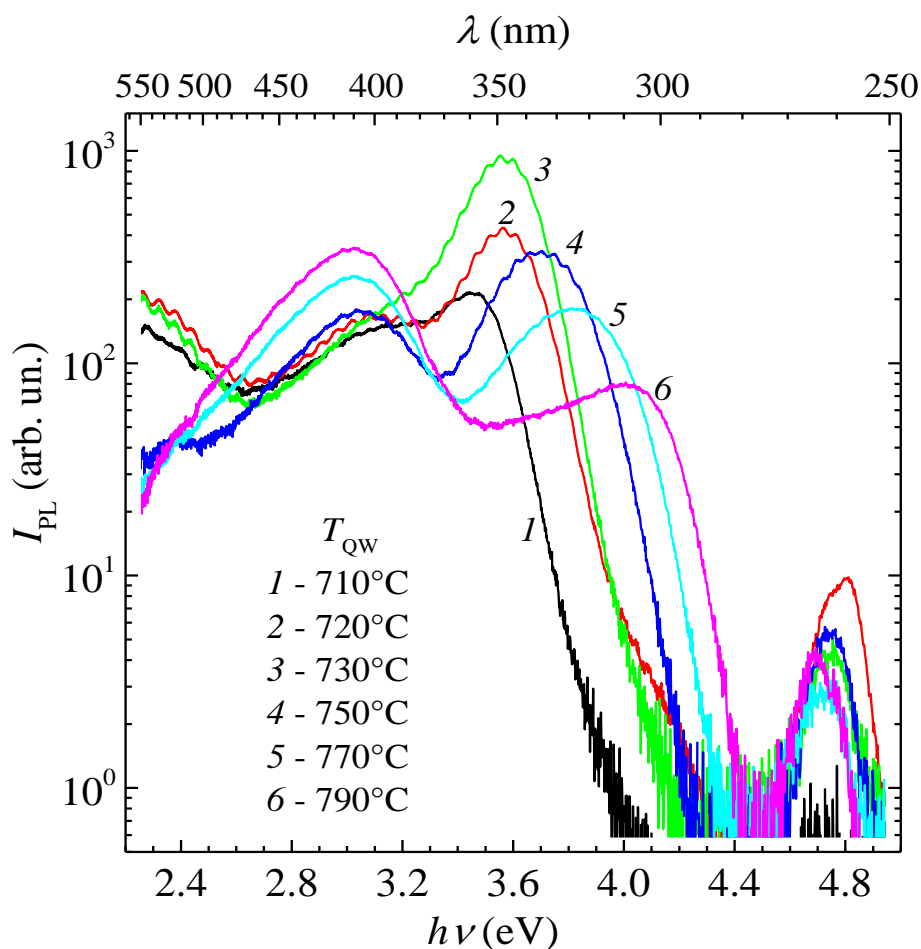
Figure 4-6 PL spectra of InAlN/AlGaN MQW samples grown at different QW temperatures.

The composition dependence of PL FWHM is also presented in Figure 4-7. Unlike InGaN QWs, which typically demonstrate an increasing PL bandwidth with indium composition [348, 349] due to an enhanced material inhomogeneity and thus band-gap fluctuations, our InAlN QWs shows an opposite behaviour up to about 18% of indium. Only a further increase of indium content apparently leads to the expected PL band broadening, though the differences in FWHM in this region are fairly small. The reason for the observed behaviour is most probably related to the indium content dependent PL efficiency, therefore we will first explore the effect of alloy composition (whereby PL peak position) on luminescence intensity (PL efficiency).
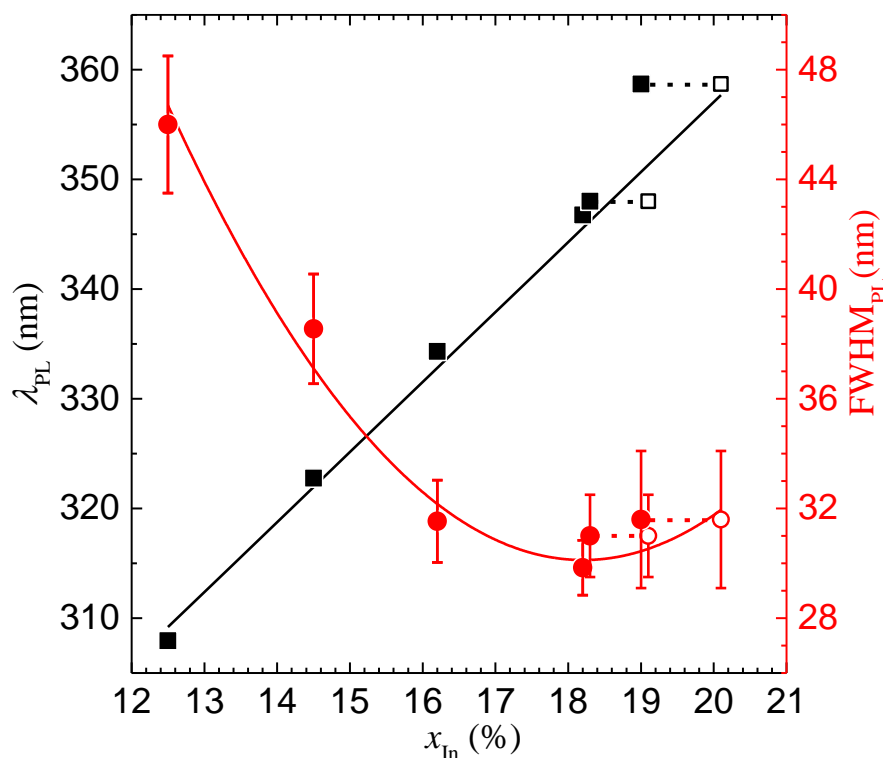
Figure 4-7 PL peak position (squares) and bandwidth (circles) as a function of indium content. Open symbols are plotted for two samples grown at lowest temperatures using x values estimated assuming partial InAlN relaxation. Lines are a linear fit for PL peak position and a second order polynomial fit for PL bandwidth; both are guides to the eye.

There are two notable features of the indium content dependence of PL efficiency of the studied samples, which can be seen in Figure 4-8: the highest PL efficiency is for $In_xAl_{1-x}N$ QWs with $x \sim$ 0.18 with a gradual decrease with reducing In content and a more sudden fall at higher contents. The rapid decrease of PL efficiency for $x > 0.18$ correlates with the point where the rate of change in determined In content (assuming fully strained MQWs) with growth temperature alters, as shown in reference [188], which we have attributed to the onset of plastic deformation in the QWs. Such plastic deformation (dislocation formation within the QW structure) leads to the reduction in optical efficiency. It is worth noting that we have observed no significant correlation of the MQW-related PL with the crystalline quality of AlGaN/AlN-templates in any study we have conducted in this system. However, new dislocations generated within QW material are very critical from this point of view. This is because the threading dislocations intersecting QW plane from the buffer 'corrupt' apparently arbitrary regions of QW and not necessarily In-rich ones, leaving a lot of them dislocation-free where carriers can be localised and recombine radiatively. On the other hand, QW based misfit dislocations happen in the most strained and thus most indium-rich regions of those QWs. These dislocated In-rich regions are still good traps for non-equilibrium carriers but unfortunately being localised there they have obviously a much lower chance of radiative recombination. We, therefore,

conclude that the onset of mechanical strain relaxation during growth of InAlN/AlGaN MQW stack is the main reason of the rapid PL degradation at $x > 18\%$. It is worth noting that, as mentioned earlier in Section 4.1.3, we observed a decrease of PL efficiency due to the same mechanism at two fixed indium compositions when QW widths were increased instead. The mechanical strain relaxation via misfit dislocation formation occurred at above critical QW widths of about 2 nm and 3 nm for samples grown at 730°C and 790°C, respectively.
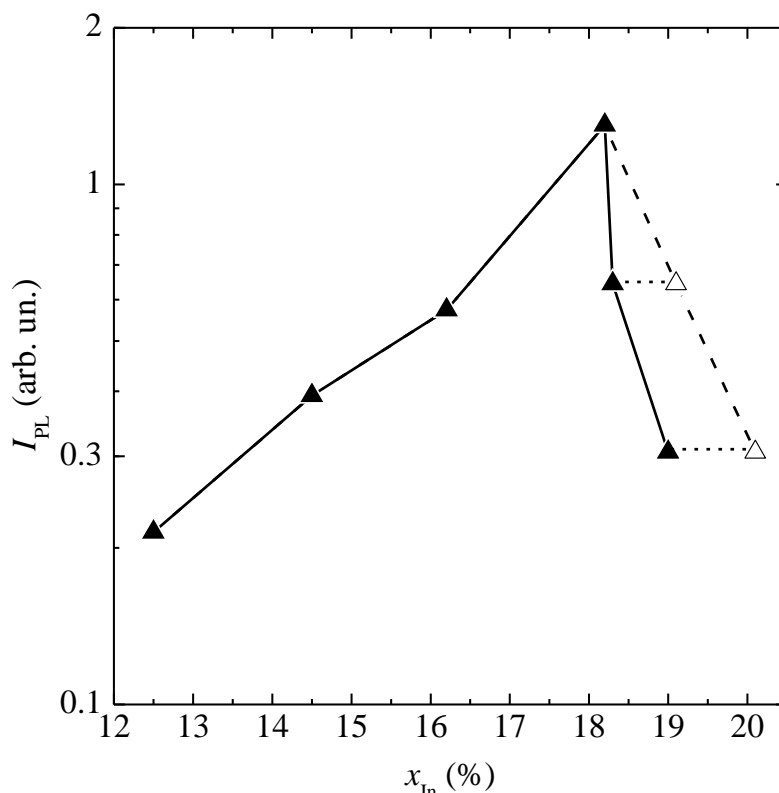
Figure 4-8 – Relative PL efficiency of InAlN/AlGaN MQWs as a function of indium content. Open symbol data points are plotted in the same way as explained previously in Figure 4-7.

Let us now consider the gradual decrease of PL efficiency as x falls from 0.18 to 0.12 in our material. Such a behaviour has been observed in InGaN [350, 351] where a reduction in luminescence efficiency with decreasing In content was explained by carriers being localised away from defects in In-rich regions, as already discussed above. This behaviour was observed however for low indium content InGaN [350], for moderate indium contents of around 10% and higher, the tendency is usually the opposite [348, 352]. Moreover, this initial increase of PL efficiency in InAlN has been already observed for indium contents in the range $0 < x < 0.01$, as discussed in 3.4. This is consistent with much stronger expected carrier localisation in InAlN in comparison to InGaN due to the higher

difference in band-gap and especially due to high band-gap bowing parameter (> 25 in the $x \rightarrow 0$ limit), see section 1.1.2 which in combination makes the value of dE_g/dx exceptionally high in this content range. The high dEg/dx results in strong band-gap variations at relatively low fluctuations of alloy composition. This is why, small indium contents in InAlN can generate sufficient localised states to suppress nonradiative recombination, and a further increase of density of localised states does not help improve efficiency anymore.

As the QW band-gap gets closer to that of the barriers, obviously carrier confinement within them becomes weaker. For the 12.5% InAlN sample, the QW band-gap (4.38 eV) is still significantly lower than that of their barriers (4.74 eV). However, it is possible in the InAlN–AlGaN system that a type II band line-up can occur, whereby the holes are confined to the $Al_yGa_{1-y}N$ while the electrons are confined as desired in $In_xAl_{1-x}N$. A simple calculation taking into account InAlN and AlGaN band-gap composition dependencies and band offset ratios $\Delta E_c/\Delta E_v$ of 1.33 for the AlN–GaN system [323] and 2.63 for the AlN–InN system [322] indicates a transition from type I $In_xAl_{1-x}N/Al_{0.59}Ga_{0.41}N$ QWs to a type II line-up at $x_{tr} \approx 0.15$. In this case for $x > x_{tr}$ both electrons and holes are confined in InAlN QW, but for $x < x_{tr}$, type II band line-up occurs and holes would be confined in the AlGaN barrier [188].

Therefore, the observed non-monotonic dependence of luminescence efficiency on indium content with the maximum at about $x = 0.18$ can be explained as a trade-off between a strain relaxation for higher indium contents and a switch from type I to type II quantum well band alignment at lower indium contents. It may explain the unusual broadening of the quantum well luminescence band observed, as the x decreases through the stronger luminescence contribution of electrons in deeper localised states (type I line-up) in InAlN, while most of the hole population tends to be confined in AlGaN barriers (type II line-up) for the lower In content QW samples.

4.3   Temperature and Excitation Power Density Photoluminescence of QWs

4.3.1   Experimental

In this work, $In_{0.18}Al_{0.82}N/Al_{0.59}Ga_{0.41}N$ MQWs were grown on $Al_{0.53}Ga_{0.47}N$ templates, which were deposited on 2.5 μm AlN on c-Al_2O_3 as already reported in section 4.1 and schematically shown in Figure 4-1.

For PL measurements, a cw Ar-ion laser ($\lambda = 244$ nm) was used as an excitation source. PL spectra were detected using iHR-320 Horiba imaging spectrometer equipped with a thermoelectrically cooled CCD matrix array. The sample to be measured was placed in a cryostat cold head to control the ambient temperature (10-450 K). The effect of excitation power density on the photoluminescence properties of InAlN MQWs was evaluated at 10 K and 300 K. Excitation power density (I_{exc}) was attenuated and tuned using a pair of neutral variable optical density filters, in the range of 1 to $10^{-6}W/cm^2$, see Figure 4-9.
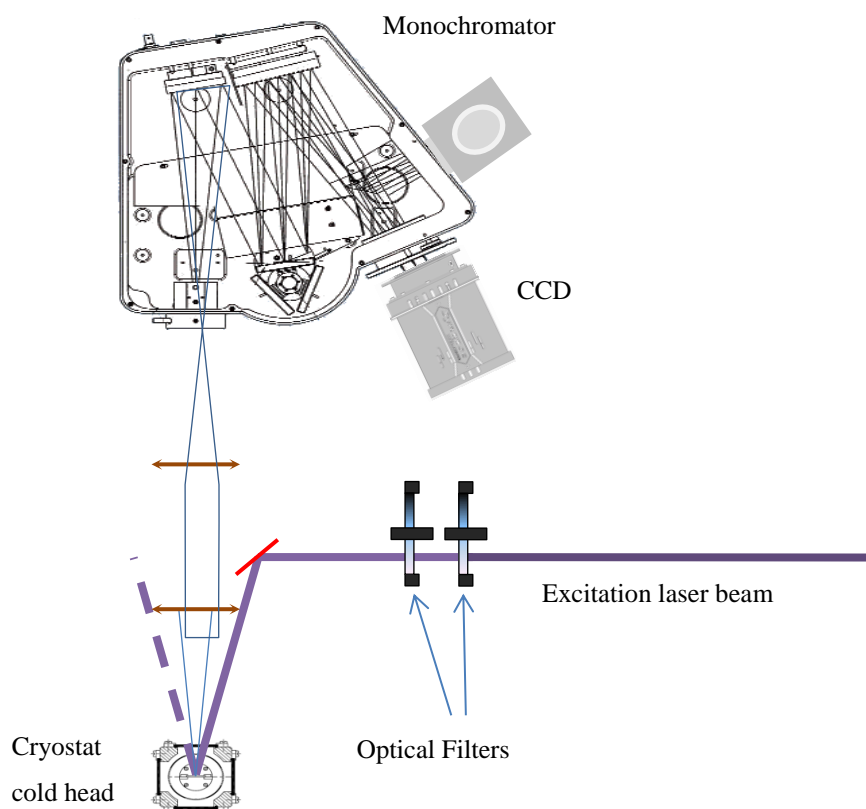
Figure 4-9 Set-up of temperature and excitation power dependent photoluminescence.

4.3.2   Results and discussion

Typical spectra of temperature dependent PL at 5 mW (1 W/cm^2) and excitation dependent PL at 10 K, are shown in Figure 4-10 for indication.
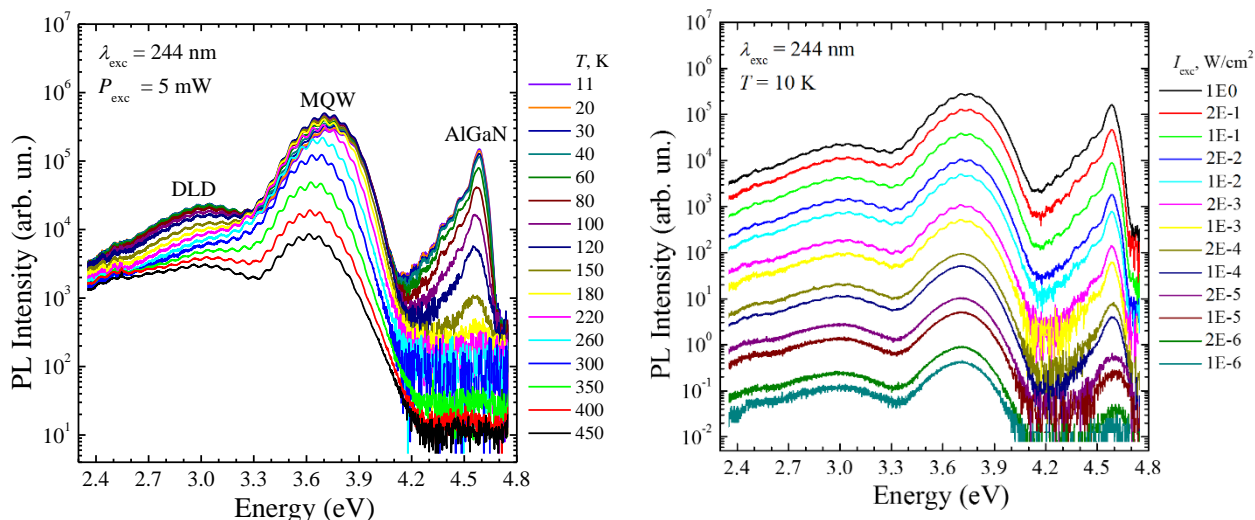
Figure 4-10 Temperature (left) and excitation power (right) dependence PL spectrum of InAlN/AlGaN MOWs.

The emission peak position energies, full width at half maximum (FWHM), and emission intensities are determined by fitting the PL spectra, using the Asymmetric Double Sigmoidal (Asym2Sig) function, allowing modelling of asymmetric peak line-shape[353]. The peak position energy and FWHM of the PL emission as a function of the excitation power density at 10 and 300 K are illustrated in Figure 4-11.

At 300 K, as shown in Figure 4-11a, the emission energy peak position (E_p) shows an initial small redshift, along with the broadening of the linewidth as excitation power density increases from 10^{-6} to $10^{-5} W/cm^2$. At high temperatures, nonradiative recombination centres are thermally activated; therefore, carrier lifetime is low due to the recombination in the defects especially at low excitation power densities. Thus a relatively high fraction of carriers recombine (both radiatively and non-radiatively) while still at extended states (i.e. before attaining lower energy localised states). As the excitation level increases (particularly in the range of $10^{-6} - 10^{-5} W/cm^2$), carriers with higher concentration can partially saturate the nonradiative channel, which leads to an improvement in their total lifetime [354], hence increasing the localisation degree of carriers which would manage to recombine radiatively. As a result, a redshift of the peak energy of the PL band is observed. Furthermore, a small broadening of the spectrum is also observed at this range with increasing excitation power density. While the contribution of localised carriers in InAlN QWs contribute more in luminescence which is causing the redshift, there is still the high population of carriers recombining radiatively in the extended states, before saturation of centres, causing the broadening of line-width in the combination of carriers being localised.
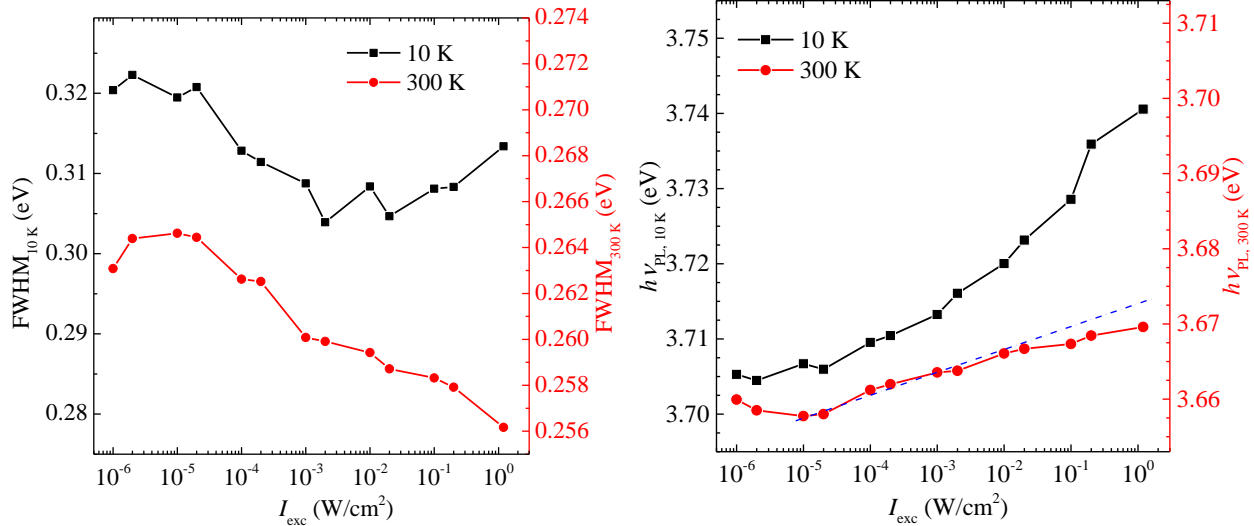
Figure 4-11 Emission peak energy and full width at half maximum (FWHM) as a function of excitation power density for the InAlN/AlGaN MQWs at 10 K and 300 K.

With further increasing excitation power density higher than $10^{-5} W/cm^2$, the nonradiative centres are saturated further, hence, almost all carriers would have time to localise before recombination. Carriers captured in the localised states start then to fill the band which causes the observed blueshift of the emission energy. The approximate linearity of the peak position energy with log (I_{exc}) can be explained by the fact that band filling is exponentially increasing (with energy) tail of density of states function [355]. The narrowing of the linewidth at room temperature and excitation power densities higher than $10^{-5} W/cm^2$ can be explained as follows: as we know that PL spectrum (analogues of occupied density of states) is a product of density of states and Fermi function (probability of occupation) and normally density of states in the tail region is assumed to change exponentially with energy i.e. $\rho(hv) \sim \exp(hv/\Delta E)$, where ΔE is a parameter equivalent to the broadening parameter in the sigmoidal expression [184], (see Figure 4-12*a*) then it can be shown that while PL spectrum position blue-shifts linearly with excitation intensity, the FWHM would remain unchanged, as shown in Figure 4-12*b*.
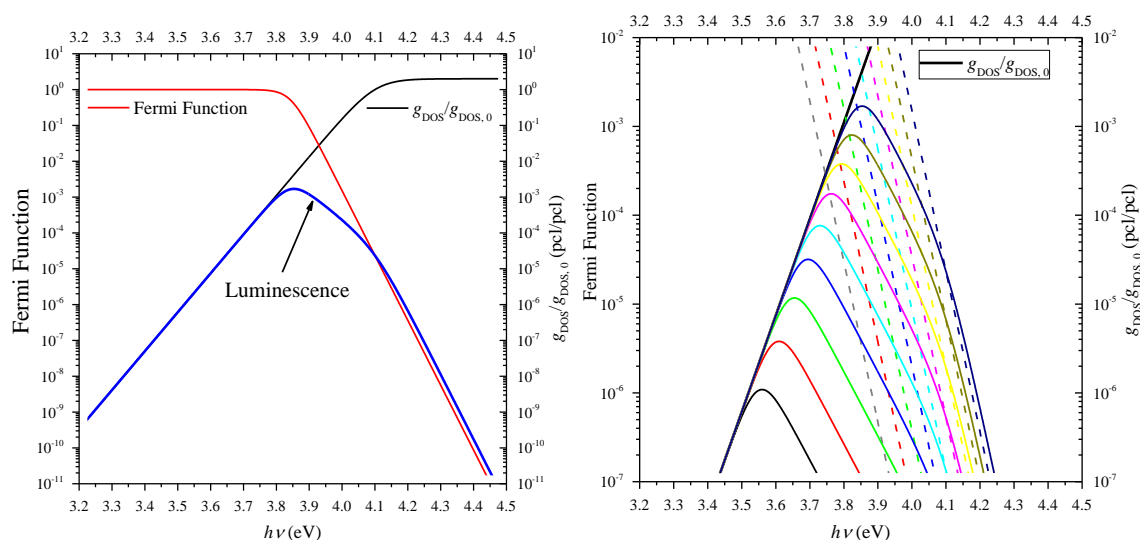
Figure 4-12 Modelling of luminescence produced from the exponentially changed density of states function with energy (black line) and varied Fermi-Dirac Function at different Fermi levels.

However, if one assumes that the broadening parameter ΔE (therefore the exponent $1/\Delta E$) depends on $h\nu$, then PL FWHM will also vary with I_{exc}. Particularly, an increase of $1/\Delta E$ (i.e. faster than the single exponential increase of density of states in the tail region) will lead to a reduction of PL FWHM and sublinear (with $\ln(I_{exc})$) blue-shift and vice versa. Such a behaviour is demonstrated in Figure 4-13, where the luminescence is calculated as a product of the density of states function and varied Fermi-Dirac Function at different Fermi levels to show how peak energy and linewidth will change if the density of available states follows the Boltzmann function (as an example) other than exponentially. This seems to be our case where PL bandwidth slightly reduces with the excitation power density (Figure 4-11 *b*, "300 K" curve). The faster than the single exponential increase of the density of states should also lead to a sublinear with $\log(I_{exc})$ PL blue-shift, and it is indeed slightly sublinear in our case (Figure 4-11 *a*, "300 K" curve, blue dash line is a guide to the eye).

At 10 K, as shown in Figure 4-11, the behaviour of both PL spectrum position and FWHM is quite different from room temperature and cannot be described in such a way. The peak energy increases gradually with increasing excitation power density, while the linewidth first decreases at the low excitation energy densities, $I_{exc} < 10^{-3}$ W/cm^2, then increases with further excitation power density enhancement.
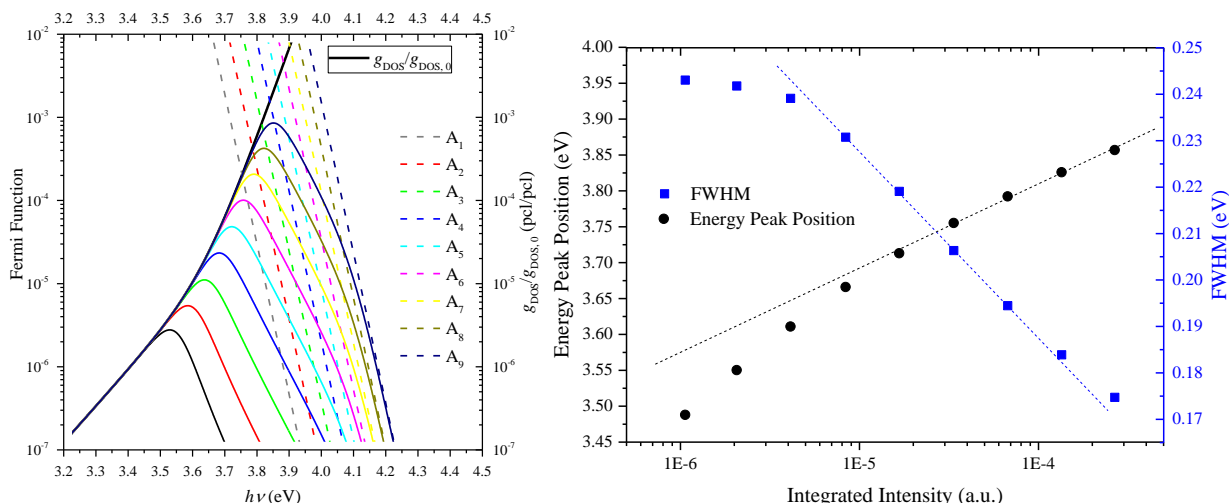
Figure 4-13 a) Modelling of luminescence produced from the density of states function (black line), and varied Fermi-Dirac Function at different Fermi levels and b) energy peak position and linewidth (FWHM) derived from modelling.

An explanation for the low-temperature luminescence behaviour of the material can be as follows: First of all, the initial (at low I_{exc}) redshift of PL spectrum and PL broadening observed at RT are not seen at low temperature (Figure 4-11, *a* and *b*, "10 K" curves). This is attributed to the fact that at low temperature, non-radiative channels are frozen, therefore carriers can move to the localisation states before recombination. Also, these carriers are forced to localise in the nearby and shallow states due their low kinetic energy at low temperature.

In this situation, the band filling of these states leads to the PL blue-shift and narrowing of PL bandwidth at the lowest excitation levels applied. However, with further increase of the excitation level ($I_{exc} > 10^{-3}$ W/cm^2) a stronger blue-shift occurs. This blue-shift cannot be only due to the band filling effect. This is because its rate of variation depends only on the density of states available for carriers to occupy, independent from temperature, which is the case for our results.

Due to the quite strong difference in band offsets in the InAlN-AlN and AlGaN-AlN systems, this is likely to be a type I →type II transition in the In$_x$Al$_{1-x}$N-Al$_y$Ga$_{1-y}$N system [188, 356]. Using information mentioned in section 4.2 composition dependent band offset of In$_x$Al$_{1-x}$N-Al$_y$Ga$_{1-y}$N alloys are plotted and presented in Figure 4-14, for indication. It can be seen from Figure 4-14*a* that the type I →type II transition for Al$_{0.59}$Ga$_{0.41}$N barriers should occur at around 15% of indium in InAlN QWs. In our sample with the average indium content of 18% QWs, there is more likely to have the type I band line-up. However, due to miscibility of InN in AlN and composition fluctuation it is

likely to have some In depleted regions where valance band of the InAlN QWs is locally lower than the AlGaN barriers, allowing occurrence of a type II line-up, as shown in Figure 4-14*a* and *b*. Contribution of holes localised in AlGaN to luminescence is very weak at ambient temperatures, since holes can easily propagate to or even be confined in barriers and very quickly recombine there nonradiatively. However, at low temperature and particularly at high excitation levels, the PL efficiency of AlGaN improves essentially due to a partial freezing of some non-radiative centres and partial saturation of the rest of the centres. This can be observed from in the strong increase of AlGaN related PL band in the spectra, as shown in Figure 4-10. The increased total carrier lifetime in AlGaN makes the holes available from two sources (escaped from QWs to AlGaN and directly generated there) to recombine with electrons in QWs. For lower average indium contents in QWs this effect is stronger, and the emission corresponding to this recombination appears as a distinct shoulder or even as a separate PL band [188], but in this case it only shifts the total PL further towards higher energies and broadens the emission spectrum (Figure 4-11, *a* and *b*, "10 K" curves). This observation thus may serve as another indication of proximity of type I →type II transition in our QWs.

Figure 4-15*a* shows the temperature dependence of the PL peak position at two (maximum and minimum applied) excitation power densities. The anomalous temperature behaviour of peak position is obviously visible in the both curves measured at 10^{-4} and $1\ W/cm^2$. Although both curves are somewhat similar to the very well-known *S*-shape variation of energy over temperature in InGaN QWs, in the case of InAlN QWs we appear to have two turning points so that one can speculate about a *W*-shaped dependence. An initial red-shift of the peak position was observed here in this experiment for both excitation power densities, although, based on Varshni expression, there is almost no initial red shift with temperature estimated for In$_{0.18}$Al$_{0.82}$N using a linear interpolation between InN and AlN., [89, 357]. This is consistent with localisation of carriers in the sample.

This behaviour is related to the decreasing of the contribution of In-depleted QW regions with temperature in the condition close to type II band line-up. A stronger initial redshift observed for $1\ W/cm^2$ is clearly due to the stronger contribution of those In-depleted QW regions at higher excitation densities, as discussed above. Similar to what normally observed for InGaN QWs [355], the high-temperature turning point of PL peak position (E_p) is observed for InAlN but at significantly higher temperatures. This is an indication of deeper localisation, in comparison with InGaN, where the thermionic emission of carriers into shallower localised states happens at essentially higher temperatures. Finally, a Varshni-like variation of PL peak position is expected for InAlN if the experiment to be continued to the elevated temperatures, as high as more than 450 K.
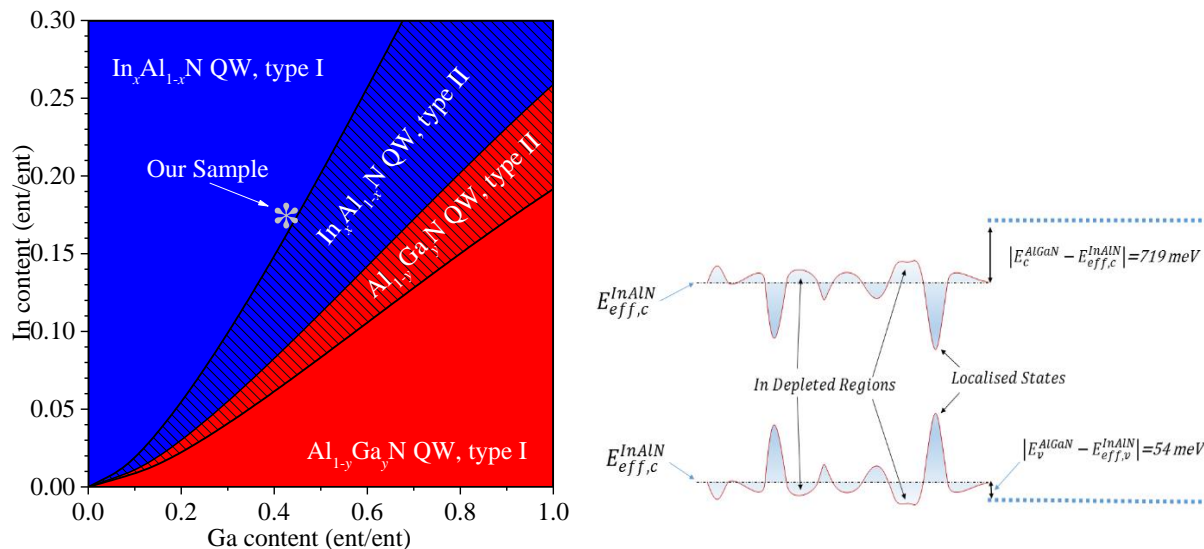
Figure 4-14 a: Composition dependent band offset of InAlN and AlGaN alloys, b: Schematic band structure of In$_{0.18}$Al$_{0.82}$N/Al$_{0.59}$Ga$_{0.41}$N and an indication of localised states and In depletion regions.

For the excitation power density of 10^{-4} W/cm^2, the PL linewidth is nearly stable up to 100 K then shows a $\sim$27 meV reduction up to 350 K, followed by a linear increase. On the other hand, the linewidth power density of 1 W/cm^2 shows a continuous decrease up to 300 K followed by a linear increase over the rest of the temperature range. Decreasing the FWHM over the temperature range of 100 to 300 K corresponds to the redshift of E_p.
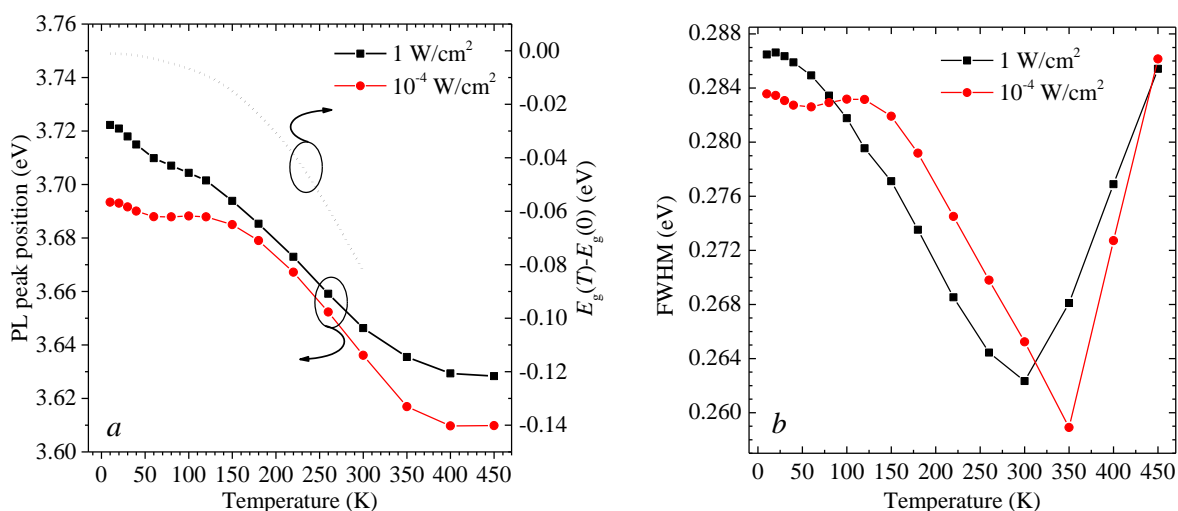
Figure 4-15 Temperature dependence PL peak energy position (a) and FWHM (b) for excitation power densities of 1 and 10^{-4} W/cm^2. Dotted curve in (a) is given for reference and represents the temperature dependence of In$_{0.18}$Al$_{0.82}$N band-gap calculated using a linear interpolation between the corresponding binary compounds [89, 357] (solid lines are a guide to the eye).

Figure 4-16 shows the Arrhenius plot of the integrated PL emission intensity of InAlN MQWs for low and high excitation power densities, over the temperature range from 10 to 450 K. It is quite noticeable to point that an anomalous enhancement of emission intensity appears over the low-temperature range. In the case of higher excitation, the maximum emission intensity at 120 K is raised by 40% in comparison to that at 10 K. Using Equation 4-1, an apparent internal quantum efficiency (IQE) can be calculated. As we don't have the spectra for excitation power dependence at the degrees between 100 K to 120 K where the highest temperature dependence intensity observed, integrated emission intensity at 10 K counted as the reference. This choice may not be the best but very common among scientists for obtaining apparent IQE. Apparent IQE is defined by the ratio of emission intensity at room temperature (300 K) in which divided by the excitation power density at each point and the maximum value of intensity at low temperature (10 K) which is also divided by the excitation power density for normalisation, assuming the radiative recombination is dominant at adequately low temperature:

$$IQE = \eta = \frac{I_{PL,300K}/I_{exc}}{I_{PL,10K}^{max}}$$ Equation 4-1

where $I_{PL,300K}$ is the integrated intensity of the PL spectrum at 300K, I_{exc} is excitation power density (mW/cm^2) and $I_{PL,10K}^{max}$ is the maximum intensity of the PL spectrum at 10 K. Using Equation 4-1, apparent IQE of more than 40% is obtained, assuming 10 K spectrum as a reference. If reference point changes, other than 10 K, the behaviour of IQE with respect to excitation power intensity would not change as it is just a matter of dividing to a number. However, the maximum IQE could drop to but not to be lower than around 25 %.
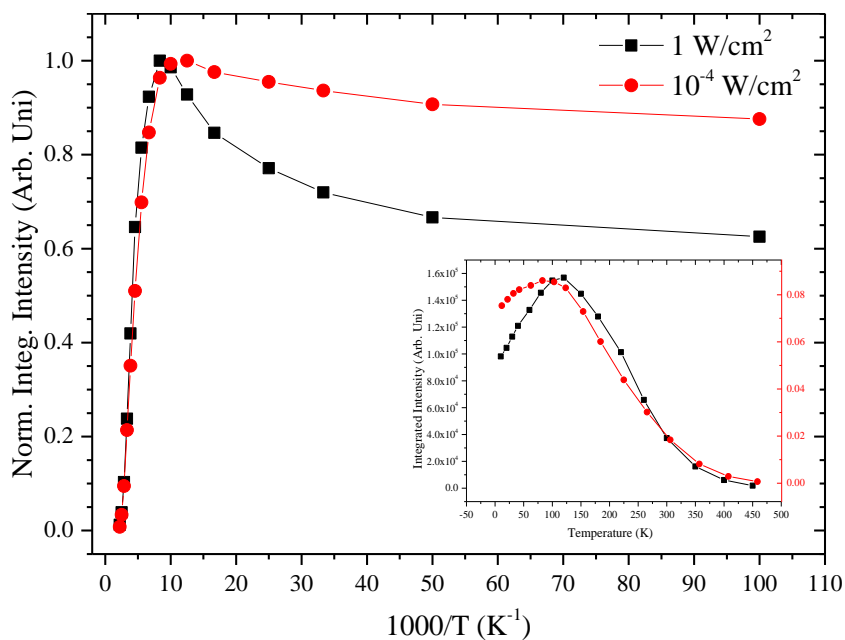
Figure 4-16 Arrhenius plot of the integrated PL intensity for 1 W/cm^2 and 10^{-4} W/cm^2. Inset: temperature dependence integrated PL intensity at two excitation power densities.

In Figure 4-17, using the values obtained from Equation 4-1, the apparent internal quantum efficiency in respect of excitation power density is illustrated.
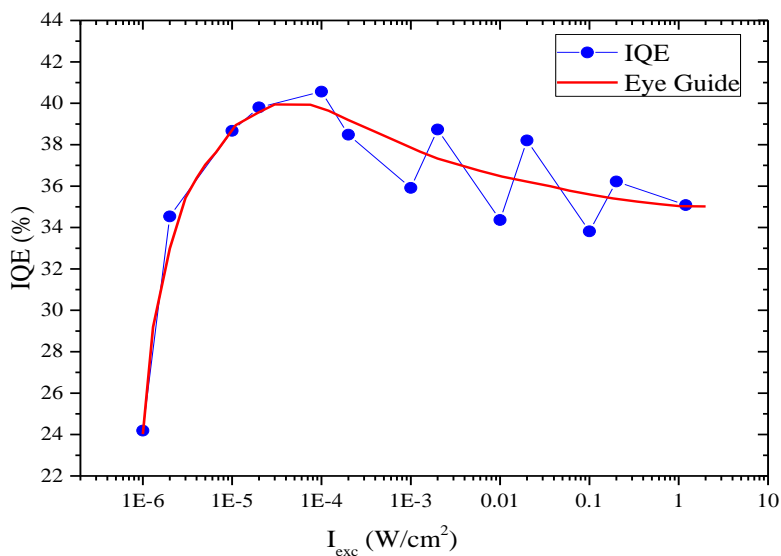
Figure 4-17 Apparent internal quantum efficiency as a function of excitation power density.

To explain the observed anomalous behaviour of InAlN QWs in the variation of emission intensity, more detailed evaluations are needed. The probable explanation for this observation is that at the elevated temperatures, from 10 K to 100 K, kinetic energy of holes in valence band (in both InAlN QWs and AlGaN) are increasing, tend to find the lateral wave-function overlap with electrons in

InAlN QWs and have a radiative recombination accordingly. At the temperatures higher than 100 K, nan-radiative channels starts to activate, capturing the carriers and prevent them to recombine radatively, therefore emission intensity decreases.

4.3.3 Summary

In summary, in this section, 5×InAlN/AlGaN MQWs were studied using temperature and excitation power resolved photoluminescence. Super-linearity of peak position variation with Ln(I_{exc}) at low temperature is attributed to the combination of both band filling and type I →type II band-gap line-up transition, where carriers localised in AlGaN are also contributing to luminescence. For High temperature, on the other hand, the non-single exponential (faster) increase of variation of density of states in the tail region is proposed for reduction of PL FWHM and sublinear (with ln(I_{exc})) blue-shift of peak position.

Temperature dependence PL emission at low and high excitation densities with the anomalous increase in integrated intensities at elevated temperatures (>100 K) and variation of emission energy are another indications of very high localisation of InAlN alloy which is desired for luminescing materials.

Chapter 5

Growth and Characterization of InGaN QWs on Nano-Structured GaN

5 GROWTH AND CHARACTERIZATION OF INGAN QWS ON NANO-STRUCTURED GAN

InGaN-based visible LEDs have revolutionised general lighting and other related industries, such as displays and communication, with special interest formed in micro- or nanostructured emitter-based displays [358-360]. As mentioned in chapter 0, differences in the in-plane lattice constants of GaN and the sapphire substrate leads to strained epilayers. This is actually causing threading dislocation (TDD) going through InGaN/GaN QWs, which is one route of causing the increasing nonradiative recombination, therefore, responsible for decreasing the IQE of LEDs.

The built-in piezoelectric field in polar material, on the other hand, leads to reduction of carrier recombination due to separation of electron-hole wavefunctions. This especially important issue for development of high power LEDs, which are suffering from efficiency droop. Thus, it is became very critical to overthrow these efficiency-limiting issues, by dealing with the stress.

Nanoscale materials have attracted a lot of attention due to their ability to decrease dislocations as well as built-in field reduction. Another noticeable properties of using nanostructured materials, especially III-nitrides, is to provide possible growth on foreign as well as native materials [15-17]. Nanostructured LEDs also offered the possibility of achieving integration of efficient emitters in photonic circuits [361, 362].

GaN nanostructures (especially, nano-rods and nano-pyramids), have been used as the template for InGaN MQW growth. These nanostructures can provide templates free of dislocations and that are strain relieved, due to the large surface-to-volume ratio [18-21], accordingly, increasing the quantum efficiency [22, 23]. Additionally, GaN-based nanostructured LEDs are reported to have potentially higher light extraction efficiency [230, 363-365].

There are three main category of techniques to produce GaN nanostructures for light emitting applications: *a)* top-down techniques (dry and wet etching), *b)* bottom up growth techniques such as selective area growth (SAG) [366-370], vapour liquid solid (so-called hybrid approach)

[371, 372] and spontaneous self-assembly epitaxy [373] and *c*) combination of top-down/bottom-up techniques [24, 374].

Despite many successful advances, there are still challenges and limitations regarding to growth and fabrication of these nanostructures. For instance, although the top-down approach with physical dry etching method presents an effective control of fabrication of nanostructures, surface damage during the etching process affects the quantum efficiency [375]. Chemical wet etching (as an another top-down technique), on the other hand, benefits from advantages such as high selectivity for different materials and insignificant deterioration of crystal quality during etching [376], which made this technique very common for fabrication of nanostructured semiconductors such as GaAs, ZnO and Si [374]. Apart from advantages of using wet etch to fabricate nanostructures, it is not very suitable for III-nitrides, especially for Ga-polar (0001) GaN, due to high chemical stability [377-379]. Using bottom-up (like SAG), on the other hand, there are many successful reports about formation of high quality III-nitride nanostructures and a good control over diameter and aperture distances, but still challenges from patterning process would place the limitation to use this technique more commonly [374].

In this thesis, two techniques were used to prepare nanostructured GaN template for InGaN/GaN MQW heterostructures, selective area growth (SAG) and a combination of top-down/bottom-up techniques by selective area dry etch followed by MOVPE growth.

5.1 Preparation of Nano-Structures Using top-down/bottom-up Technique

5.1.1 Introduction

Combination of top-down and bottom-up techniques by selective dry etch of GaN template followed by MOVPE growth, allows us to use benefits of both top-down (ability to growth planar material with low impurity and controlled doping) and bottom-up (strain free and low density of dislocation) methods. Also, using this technique allows us to growth nano-rods separately without coalescence, as already reported by our group for AlN [24]. This technique also makes the possibility of growing high density, therefore high filling factor LEDs based on GaN nano-columns (NCs) to be able to overcome efficiency droop by lowering the current density [380].

5.1.2   Experimental

5.1.2.1   *Growth of gallium nitride template*

Silicon doped GaN was grown on c-plane sapphire substrates (Kyma template) using an Aixtron close coupled showerhead 3 × 2″ MOCVD reactor. TMGa and Ammonia precursors were used as gallium nitrogen sources, respectively. A ~1.5 µm bulk GaN layer was grown at the V/III ratio (TMIn/TMAl) of ~1200 and growth temperature of 1045 °C. Hydrogen used as the carrier gas, at the pressure of 100 mbar, during growth and the growth rate at such conditions was about 6 Å/s.

5.1.2.2   *Nanolithography using sphere scooping transfer approach*

The grown GaN template, was then patterned using scooping transfer lithography technique. A monolayer of silica spheres, synthesised by the Stöber method [381], was coated on the GaN template using a transfer from a liquid surface to the wafer.

First, a diluted suspension of silica nanospheres (at two diameters of 120 nm and 210 nm ± 5%) prepared in ethanol with the concentration of 10% w/v. Then suspension mixed with chloroform at a volume ratio of 1:1 and stirred for 30 min. Then, few drops of the mixture were introduced on the surface of the Milli-Q water [https://en.wikipedia.org/wiki/Milli-Q] until about 80 % of the surface covered with spheres. This would allow spheres to diffuse freely across the surface to find the lowest energy configuration, therefore developing of self-assembly process and crystallisation of silica nanospheres on the surface [382].

Second, the container with the submerging GaN/Sapphire template was mechanically and gently lowered, allowing the silica spheres to be transferred to the emerging surface of the wafer, as schematically shown in Figure 5-1.

After evaporation of the liquids from nanosphere monolayer, the silica nanospheres were adhered to the surface of the wafer by capillary action [383]. Figure 5-2 shows the images of the nearly closed packed monolayer of the silica nanospheres coated on a GaN template obtained by a FEI Quanta 650 field emission gun (FEG) high resolution SEM.
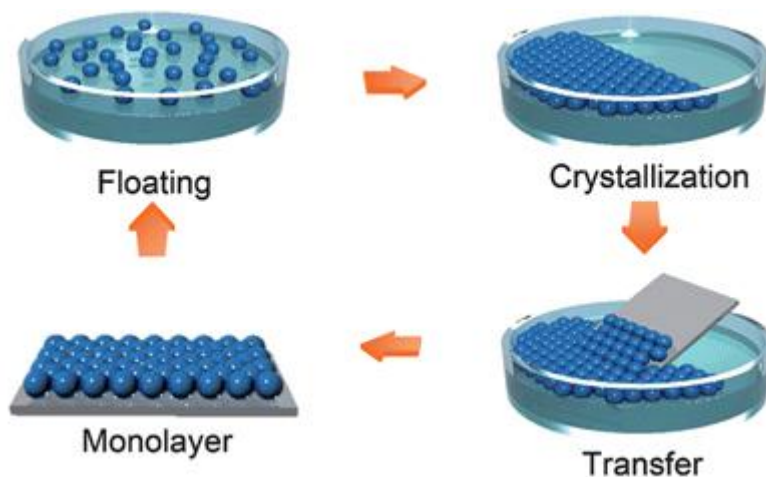
Figure 5-1. Schematic view of scooping transfer technique (picture is modified from reference [382]) .
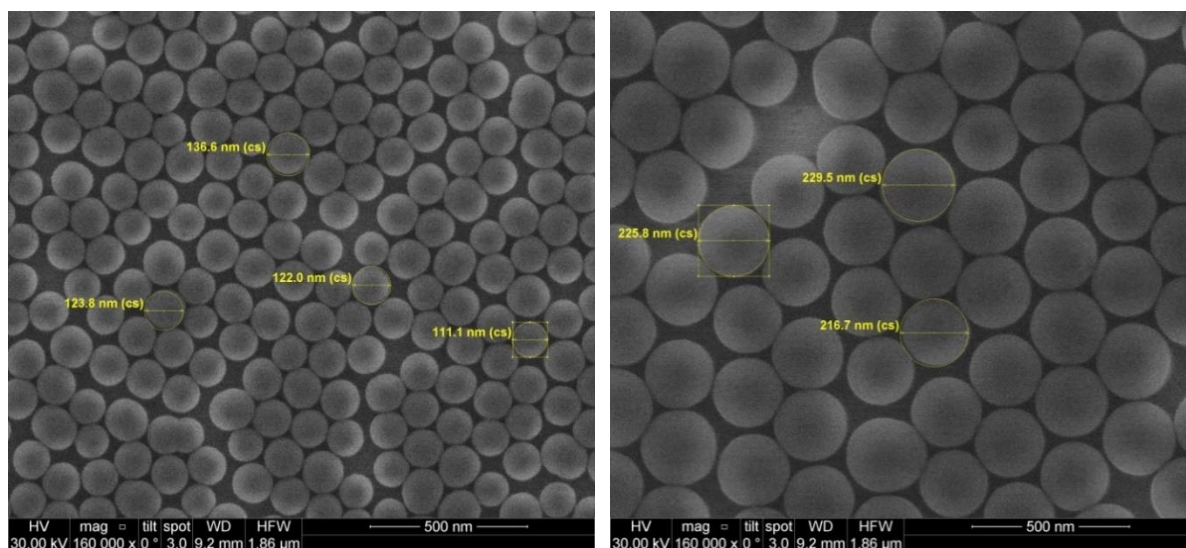
Figure 5-2. SEM top image of silica nanospheres GaN/Sapphire template at two nominal sizes of 120 nm and 210 nm.

5.1.2.3   *Formation of nano-columns using ICP dry etch*

A chlorine based inductively coupled plasma (ICP) etching process was used to transfer pattern into underlying GaN template to form nano-columns, using Oxford Instruments Plasmalab 100. Parameters used for the ICP dry etch is summarised in Table 5-1.

Table 5-1 ICP dry etch parameters.

Parameter	Cl$_2$ Flow	Pressure	ICP Power	RF Power	Temperature	Duration
	sccm	mTorr	W	W	°C	sec
	50	9	700	120	60	45

Before placing the sample back in the reactor, the residual silica mask after GaN etch was removed by immersing the wafer in a Sigma Aldrich ammonium fluoride–hydrofluoric acid (10:1) mixture (so called buffered oxide etch (BOE) solution) for 5 minutes.
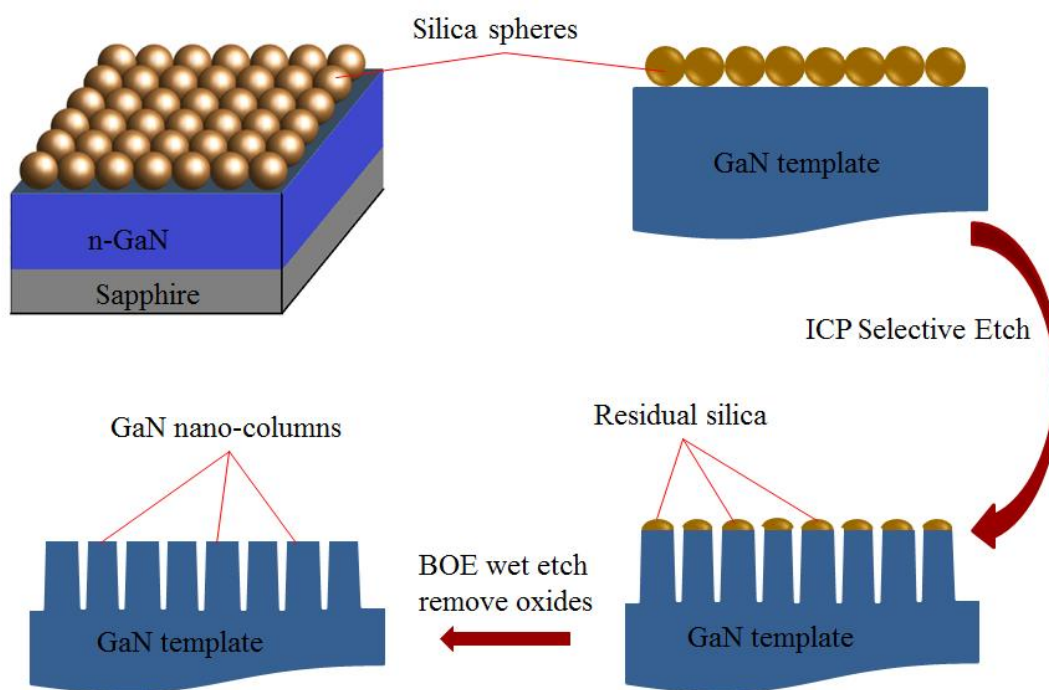
Figure 5-3. Schematically shown experimental method to fabricate nano-columns.

SEM top view and cross section images of fabricated NCs are shown in Figure 5-4. Top view SEM images indication almost uniform and closed packed NCs were fabricated in both 210 and 120 nm sizes. Some attachments of the columns in smaller nanostructure is probably due to overlapping of nanospheres during scooping therefore making a shadow for GaN dry etch, see Figure 5-4 *a* and *c*. Figure 5-4-*b* showing the cross section of 210 nm NCs with obvious remaining and flattened silicon dioxide on top of the columns. On the other hand, Figure 5-4-

d shows no residual oxide on top of columns after BOE wet etch, indicating that 5 min wet etch was enough to remove silica.
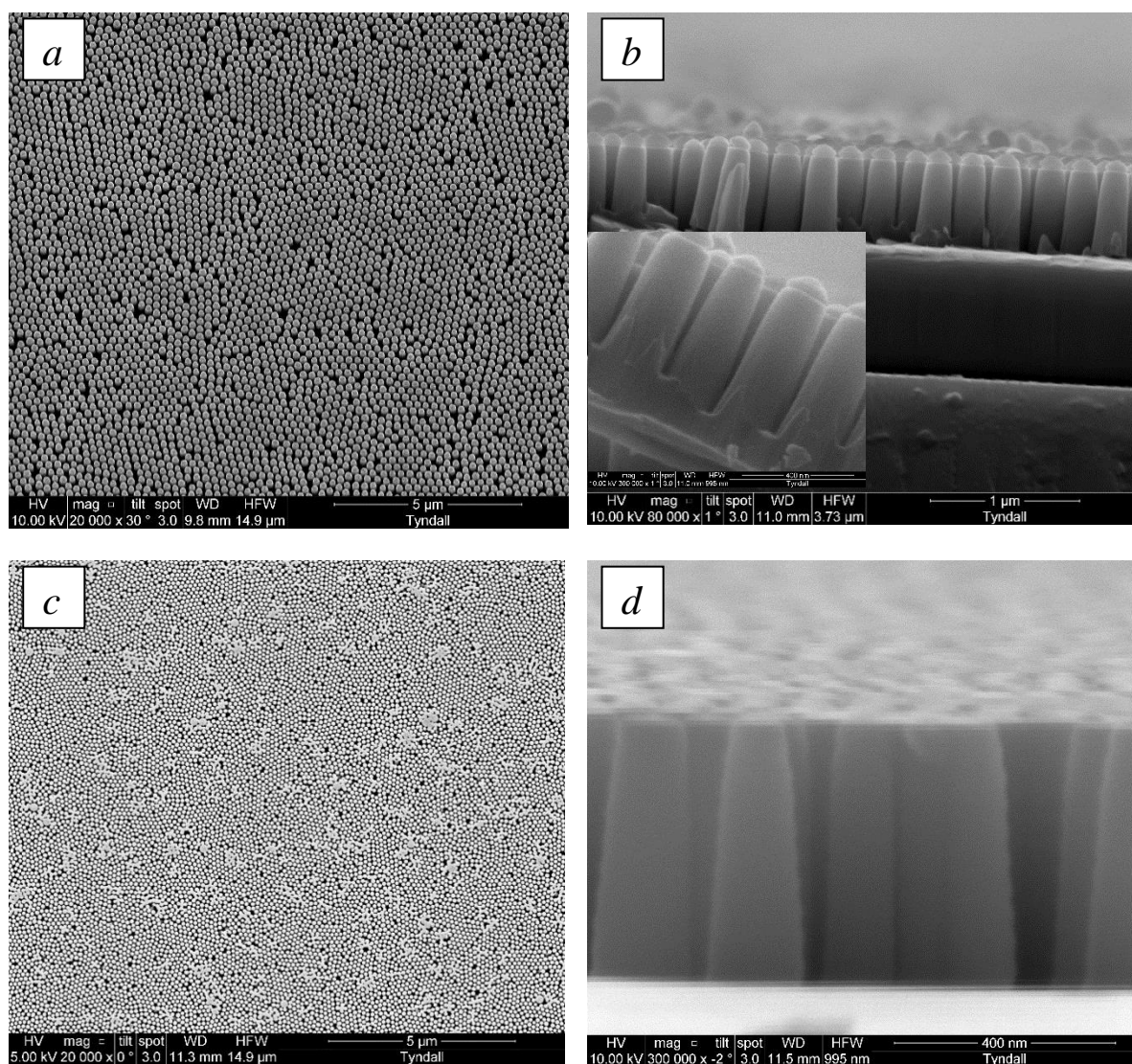
Figure 5-4. SEM top view and cross section images of fabricated GaN nano-columns; top (a) and cross section (b) view of 210 nm nano-columns before removal of residual silicon oxide. Top (c) and cross section (d) view of 120 nm nano-columns after 5 min we etch of oxide using BOE.

To check the effect of the temperature on dry etching of GaN, a sample coated with 120 nm nanospheres selectively etched using ICP process with the same parameters as mentioned in Table 5-1, except with an etch temperature of 150 °C applied. Figure 5-5 shows the SEM images of NCs prepared by ICP dry etching at 150 °C. Similar to low temperature, there are still some attachments of the NCs due to overlapping of nanospheres during scooping. In comparison with the ICP etching at the lower temperature of 60 °C (see Figure 5-4 c and d), verticality of columns was improved with the decreasing of the average sidewall angle from 6-

7° to 1-3°. Also, instead of rounded NCs at low temperature, hexagonal shaped NCs were obtained with a lower average diameter of 90 nm. This is believed to be related to passivation of NCs during etching due to formation of a layer of GaCl$_3$ in Chlorine based ICP etching [384, 385]. The volatility of the GaCl$_3$ by-product is increased by rising the temperature up to 150 °C [385, 386], therefore it will be removed at higher temperature, allowing further etch of NCs.
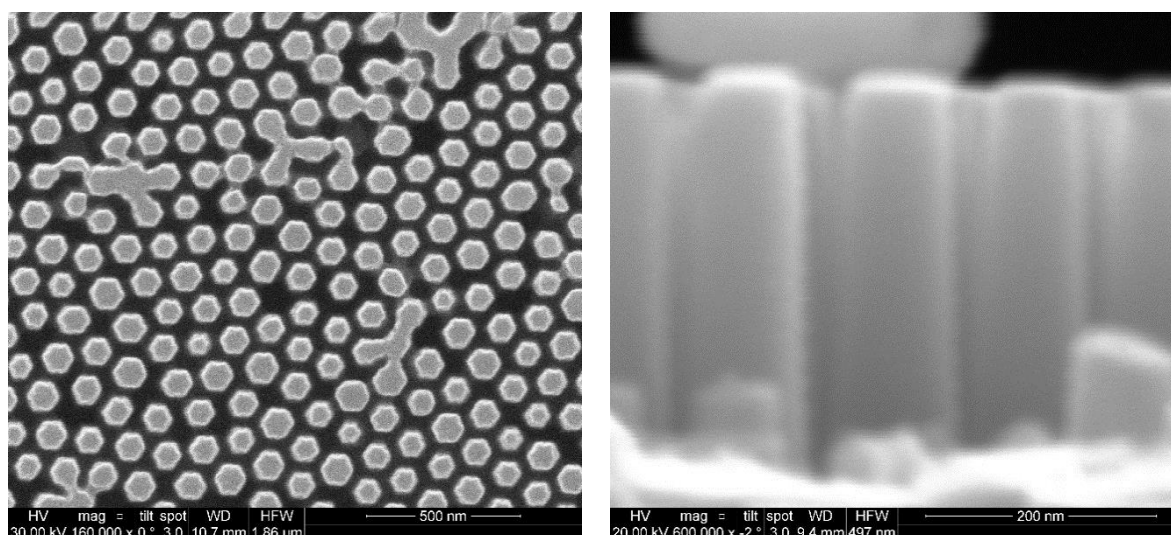
Figure 5-5. SEM images of GaN NCs (using 120 nm nanospheres) after ICP etch at high temperature.

5.1.2.4   InGaN/GaN structure growth

Growth was performed in the Aixtron 3×2 inch close-coupled vertical flow showerhead MOVPE reactor, as described previously in Section 2.1.2. Trimethyindium (TMIn), Trimethylgallium (TMGa) and ammonia (NH3) were used as Ga, In and N sources, respectively. Samples were initially heated up to 1200°C and annealed for 1 minute in an ammonia atmosphere. Afterwards, the reactor temperature was reduced to the Si-doped GaN growth temperature of 1035 °C, which performed using hydrogen as a carrier gas under a pressure of 150 hPa and V/III ratio of 1,000. The reactor ambient was then switched to nitrogen at a pressure of 400 hPa during cooling to 735 °C corresponding to InGaN growth temperature, which was measured by an in-situ Laytec pyrometer. An InGaN single QW was grown on the n-GaN pyramids using a TMIn flux of 8 μmol/min and a TMGa flux of 8 μmol/min. The NH$_3$ flux was maintained at 270 mmol/min with the V/III ratio of 17000. GaN barriers were grown at 860 °C in the nitrogen ambient. InGaN/GaN SQW structure was also grown on a planar

(0001) GaN template, for comparison. The nominal thickness of the QW on c-plane as a reference point was ~2.5 nm.
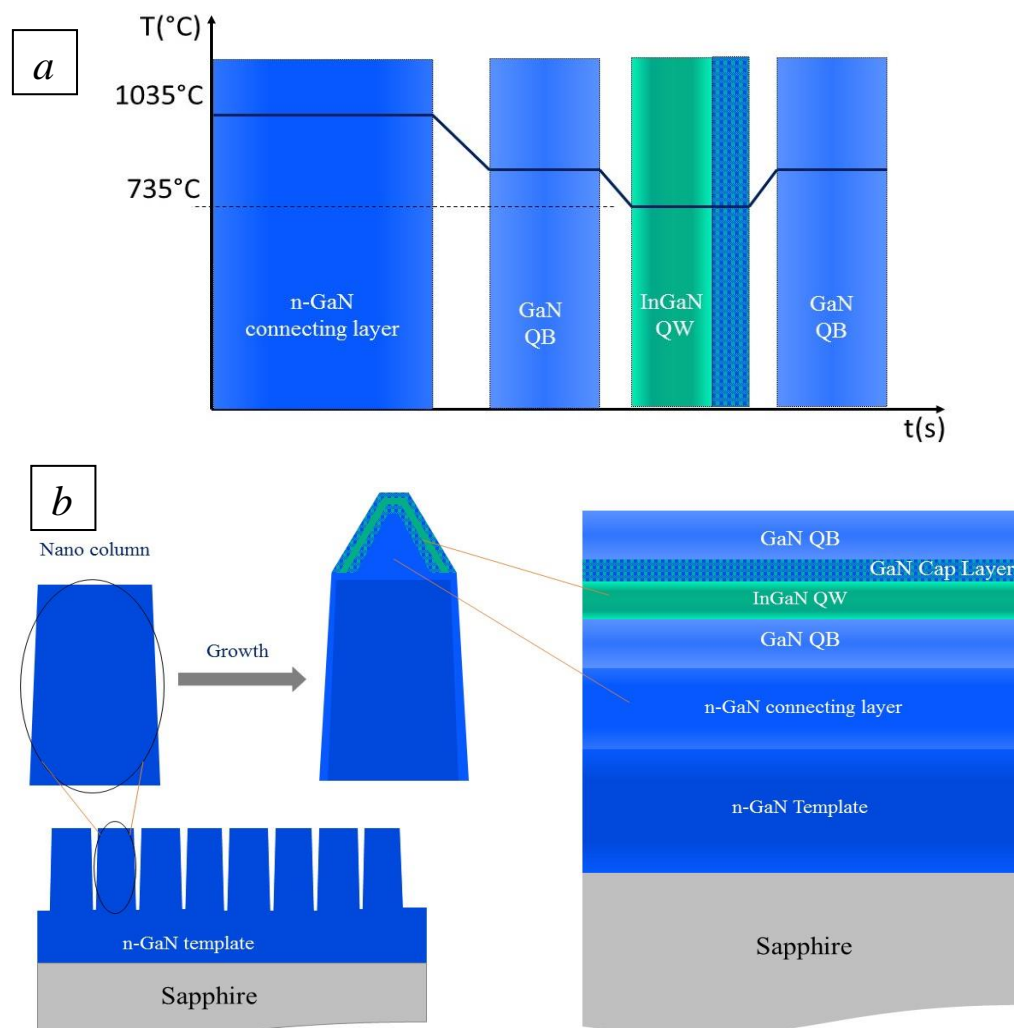
Figure 5-6. Schematic illustration of growth structure (a) and temperature profile during growth (b) of InGaN/GaN NCs.

5.1.3   Results

The effect of n-GaN connecting layer growth time is studied here. Figure 5-7 shows the top and cross section view of NCs prepared using 210 nm NSs after growth. Nano-columns after 7.5 minutes of n-GaN growth showing apex tips and almost separate and isolate NCs with hexagonal shape. By increasing growth time to 15 min diameter of NCs starts to increase with indication of some attachments, as shown in Figure 5-7*b*. By increasing growth time to 25 and 60 minutes, NCs coalescence starts to happen, with the formation of locally flat areas the top surface at a longer time, see Figure 5-7 *c* and *d*.
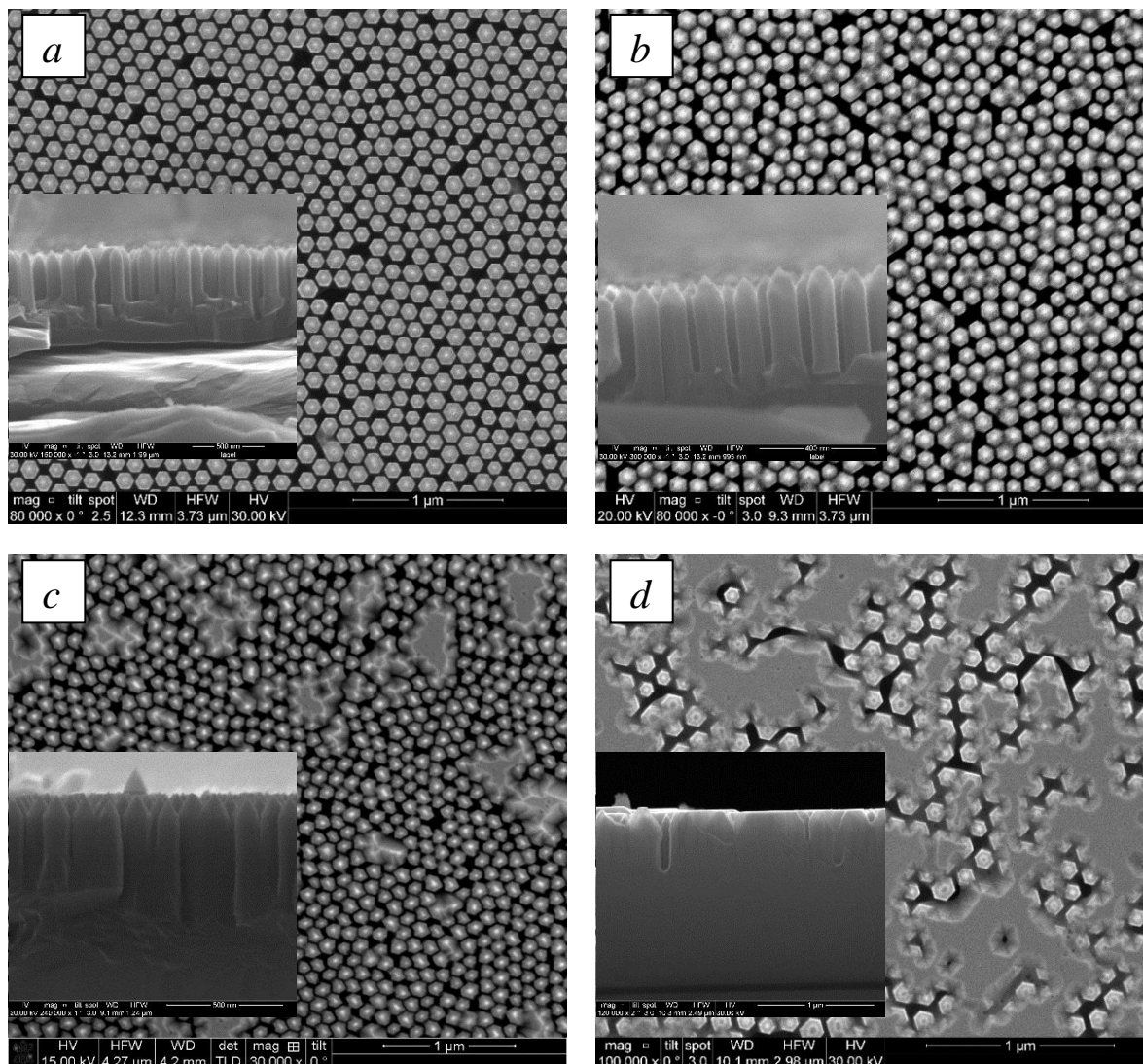
Figure 5-7. SEM top view and cross section images of InGaN/GaN 210 nm nano-columns with different growing time of n-GaN connecting layer; (a) 7.5 minutes, (b) 15 min, (c) 25 min and (d) 60 min.

High resolution TEM (HR-TEM) images of NCs grown at 7.5 and 25 minutes are shown in Figure 5-8. It can be seen that, first of all, 7.5 minutes of n-GaN connecting layer growth was not enough to get the apex tip and top of the NCs are still flat and sharpness of the of them get better at longer growth time of 25 minutes. Another interesting point is that the longer the growth time, the lower the dislocation density is. The NCs which grown at longer time is almost free of dislocations. This results alongside previous results, helping us to estimate the amount of material needed to be grown to have less dislocation and not to have coalescence. Also, HRTEM images of both NCs showing almost no or invisible QW, indication that InGaN QW growth time was short and needed to be increased. It is worth mention that InGaN growth rate

on semipolar facets of GaN is lower than polar ones, as shown schematically in Figure 5-9 [118, 387].

Figure 5-8. TEM images of InGaN/GaN 210 nm nano-columns with different growing time of n-GaN connecting layer; (a) 7.5 minutes, (b) 25 min.
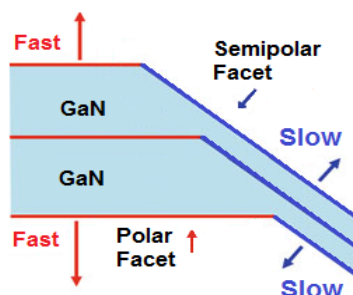
Figure 5-9. Schematic diagram of growth rate on polar and semipolar facets.

Photoluminescence spectroscopy of these two samples along with the reference sample which grown on planar (polar) sample, are plotted and shown in Figure 5-10. There are three main peaks visible in all three samples. A peak at around 365 nm, related to GaN, at 430 nm from QW and at around 550 nm associated with deep level defects (DLDs) in GaN. GaN emission from NCs are stronger than planar one, due to better quality on nano-structures after growth and also probably because of better light extraction efficiency from NCs. The weaker emission from QWs in both nano-structure samples, in comparison with planar one is mainly due to very low thickness of or even no creation of QW on semipolar facets on top of NCs. DLDs emission intensity in all samples are almost the same. This is because most of the defects are created in GaN templates underneath which are literally similar.

This experiment showed that growing time of QW needs to be modified and increased.
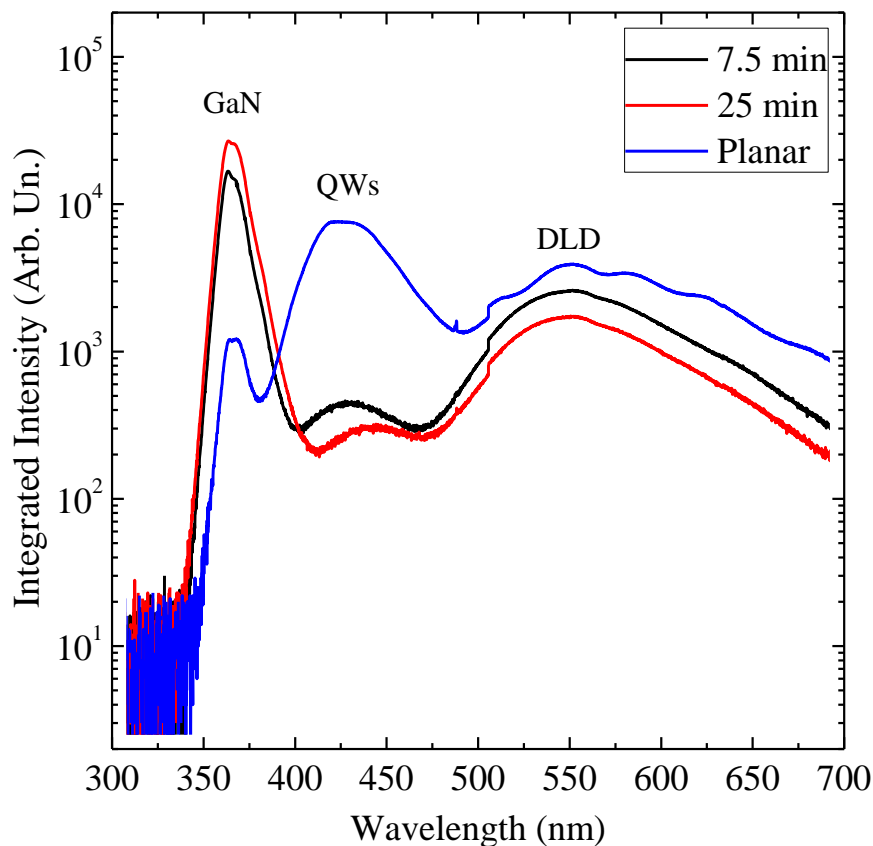
Figure 5-10. RT-PL spectroscopy of InGaN/GaN 210 nm nano-columns with different growing time of n-GaN connecting layer; in comparison with planar sample.

The effect of the growth time was also done using the NCs with smaller diameter of 120 nm. Based on the previous experiment on 210 nm NCs, where QWs were very thin on semipolar facets than the reference point on polar facets, to achieve thicker QWs, the growth time of QWs on 120 nm NCs were doubled.

Figure 5-11 shows the SEM images of two sets of InGaN/GaN samples with different thickness of n-GaN connecting layer, on NCs fabricated using 120 nm nanospheres. In both samples there are indications of coalesced regions of NCs which could be related to the overlapping of NSs during scooping transfer, or coalescence of NCs during growth. Because of short growing (5 minutes) time in the first sample, it is more probable that this issue is related to the overlapping of NSs. For longer growth time of 25 min, the coalescence of NCs increased, similar to what was observed for the 210 nm set of samples. Another interesting point is that,

sample with shorter growth time is flat-topped, as shown in inset cross section image in Figure 5-7-*a*. This is indicates that n-GaN connecting layer growth time was insufficient to create apex tips.
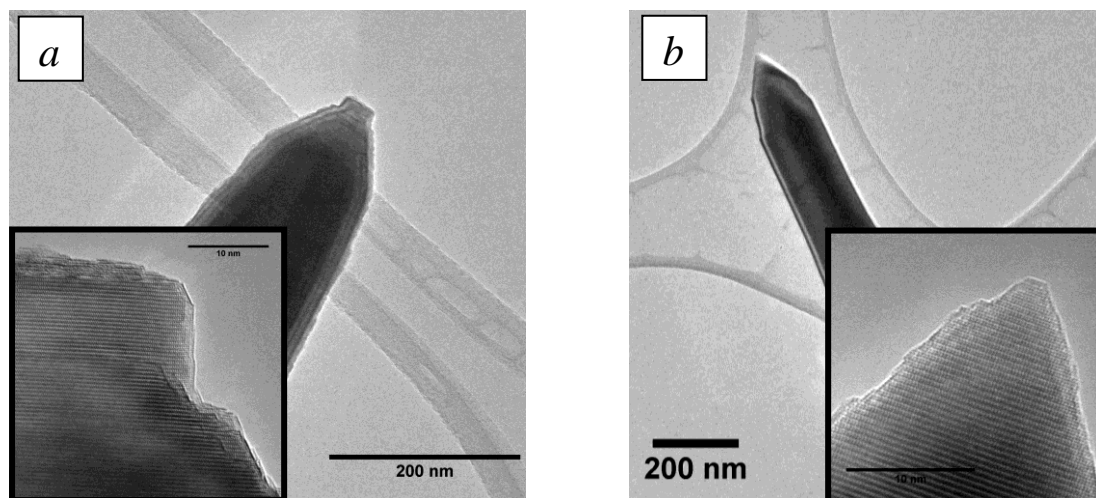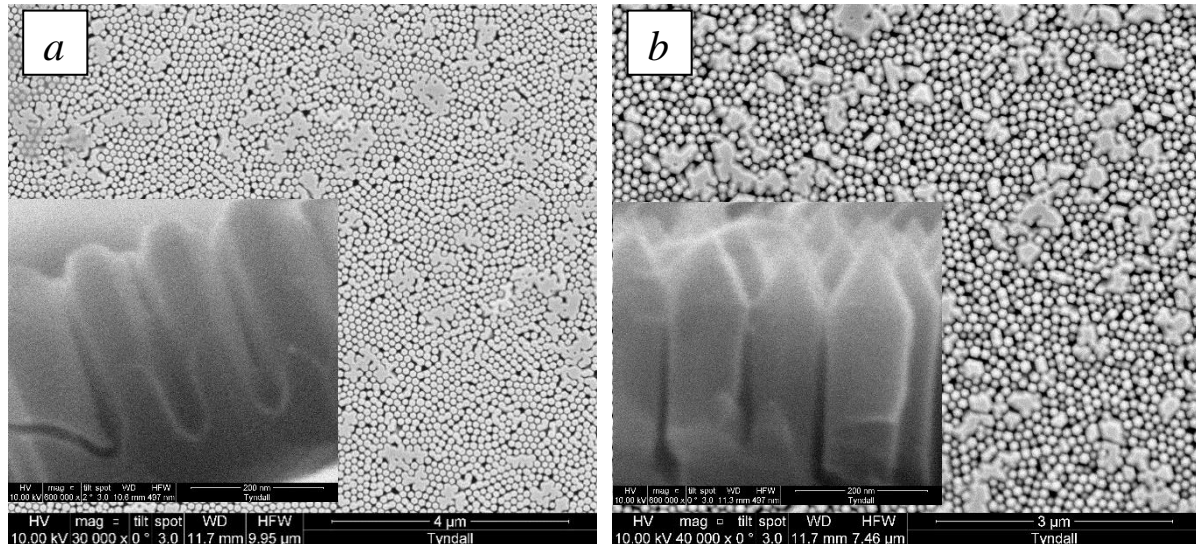

Figure 5-11. SEM top view and cross section images of InGaN/GaN 120 nm nano-columns with different growing time of n-GaN connecting layer; (a) 5 minutes, (b) 25 min.

Room temperature PL spectroscopy of the 120 nm set of samples along with reference planar sample is plotted in Figure 5-12. Generally there are three emission peaks visible in all samples, emitted from GaN, QWs and DLDs. Similar to the larger diameter NCs, the GaN emission intensity is higher in nanostructured samples than planar and flat one.

Another interesting observation is the variation of emission wavelength of the QWs. QWs in planar, 5 min and 25 min samples are emitting light at 464 nm, 436 nm and 408 nm, respectively. Obviously apex tipped sample is emitting light at shorter wavelength and flat topped sample is emitting at longest wavelength. Emission from planar (c-plane) sample is the weakest and has the longer wavelength in comparison with QWs on nanostructured samples. This behaviour is related to the fact that in these three samples there are different facets of polar and semipolar, and emission can be attributed to these facets or combination of both. In polar facets, is it well known that piezoelectric field causes band bending, therefore reduction of wavelength overlap, and hence resulting in red shift and weakened the emission intensity, as discussed earlier in Section 1.1.3. This behaviour is even getting stronger due to higher thickness of QW on polar facets than semipolar facets, see Figure 5-9. Longer emission wavelength of flat topped sample in comparison with apex tipped sample is again related to the

same origin. In apex tip sample emission expected to dominantly come from semipolar facets with less internal fields than the c-plane facets which occurred in flat top specimen. This could be another reason for shorter emission wavelength of apex tipped NCs.
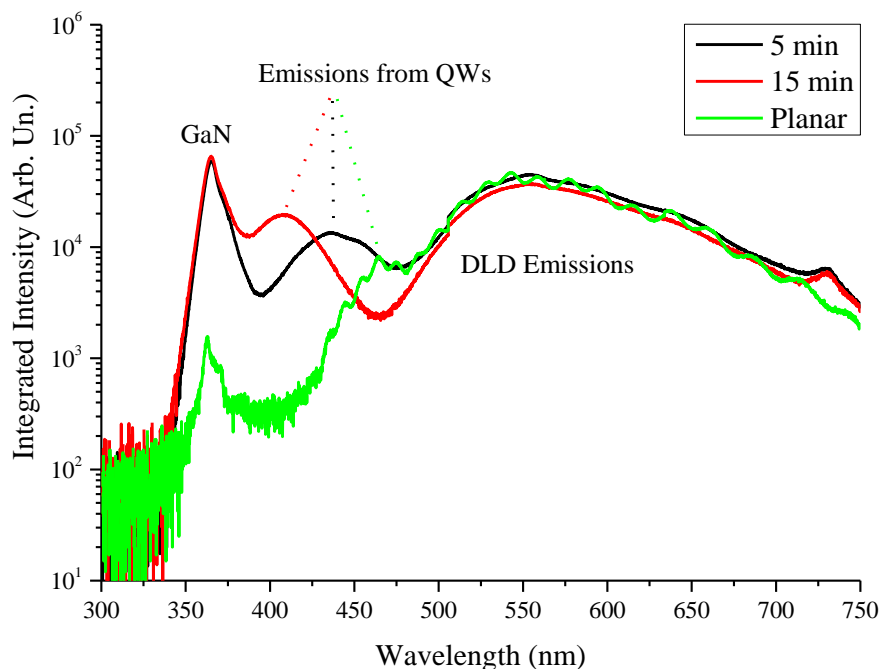
Figure 5-12. RT-PL spectroscopy of InGaN/GaN 120 nm nano-columns with different growing time of n-GaN connecting layer; in comparison with planar sample.

5.1.4 Summary

Preparation of GaN nano-columns using combination of top-down and bottom-up techniques have been made, showing that there are many factors affecting not only creation of NCs but also QWs and emission from structures. ICP dry etch of GaN at higher temperature of 150° C, helps to get better verticality of hexagonal shaped NCs due to prevention of passivation which occurred at RT ICP etching. One of the factors that affects the quality of NCs after bottom-up growth of the GaN connecting layer is growth time, which needs to be optimised to be able to have apex tip NCs and before coalescence of them. This could be shorter in smaller diameter of NCs.

Another result which needs to be concerned for processing and fabrication of LEDs using this technique is variation of growth rate on different GaN facets, polar and semipolar in this case. Growth rate of QWs and GaN on semipolar facets was much lower that it is on polar facets,

therefore very thin QW observed from TEM results of our initial QW growth experiment. Doubling the growth time of SQW helped to get emission from wells. Polarity of the material also affect the luminescence emission intensity as well as wavelength. Emission wavelength from semipolar facets seems to be shorter than those from polar/planar facets, because of weaker wavefunction overlap which is due to stronger internal piezoelectric field. Weaker wavefunction overlap would also weaken the emission intensity from polar facets of planar sample and flat topped NCs.

5.2   Preparation of Nano-Structures Using Selective Area Growth (SAG) Technique

5.2.1   Introduction

In selective area growth (SAG), areas are intentionally selected using a mask and exposed for desired material growth. This technique has been studied intensively by scientists, owing to the several advantages for the light emitting devices, including; adjustable diameter and spacing of the grown nano/micro-structures [25, 26], and the capability of growing LEDs with a variety of colours on the same substrate [25, 27]. Another most noticeable advantage of using SAG is to increase the efficiency by lowering of the defects by trap and bending the threading dislocations [28-30] and reduction of piezoelectric field on semipolar/nonpolar facets [31-35]. The SAG of III-nitrides has been studied recently more on sub-millimetre and micro-scales than nano-scales [32, 33].

Growth of InGaN quantum wells (QWs) on GaN micro-pyramids has been widely studied because it provides both dislocation density reduction and weakening of the built-in piezoelectric fields [10, 388-390], resulting in potential enhancement of recombination efficiency.

Here in this thesis, I conducted SAG GaN at nano-scales in silicon nitride as a non-selective hard mask. InGaN/GaN heterostructures were grown by the SAG technique on a 1.5 µm-thick GaN/c-sapphire template using conventional MOVPE and examined in terms of structure, morphology and luminescence behaviour.

5.2.2   Experimental

A 20 nm-thick Si_3N_4 layer was coated on 1.5 μm thick Si-doped (0001) GaN template on a sapphire substrate using plasma-enhanced chemical vapour deposition. A hexagonal array of circular apertures was patterned into the Si_3N_4 layer using the electron beam lithography (EBL) technique. ZEP520A resist was spin coated on a silicon nitride hard mask at 4000 rpm, then baked at 120 °C for 3 mins, followed by high-resolution electron beam exposure with the voltage of 50 kV and 130 $\mu C/cm^2$ doses, using JEOL JBX 6000FS system (see Figure 5-13).
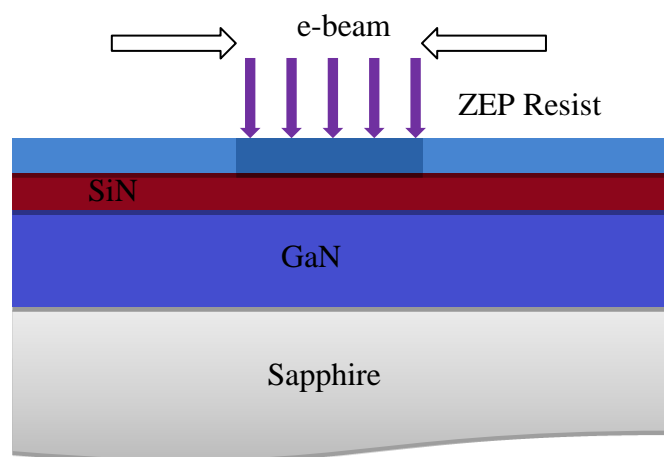
Figure 5-13. Schematic view of electron beam exposure of the sample.

 The exposed samples were ultrasonically developed as follows: the samples were immersed in a solution of ZED N50 developer (n-Amyl acetate) for 30 secs, then rinsed in isopropyl alcohol (IPA) for 30 seconds. The developed samples were dried using high purity nitrogen immediately afterwards. In order to etch the Si_3N_4 layer to create nano-sized apertures (100-1000 nm ±2.5%), an anisotropic fluorine-based (CHF_3/CF_4 etch recipe) inductively coupled plasma (ICP) reactive ion etch (RIE) process was carried out for 10 seconds using an SPTS ICP Multiplex Etcher. To strip the resist and clean the surface from residual materials an oxygen plasma asher was utilised just after the dry etch, to give the resultant pattern shown in Figure 5-14.

Silicon doped gallium nitride was then grown through the apertures under appropriate growth conditions leading to the formation of hexagonal pyramids with apex tops, as illustrated schematically in Figure 5-15.

mag □ | tilt | spot | WD | HFW | HV | 2 µm
60 000 x | 0 ° | 3.0 | 10.5 mm | 4.97 µm | 30.00 kV | label
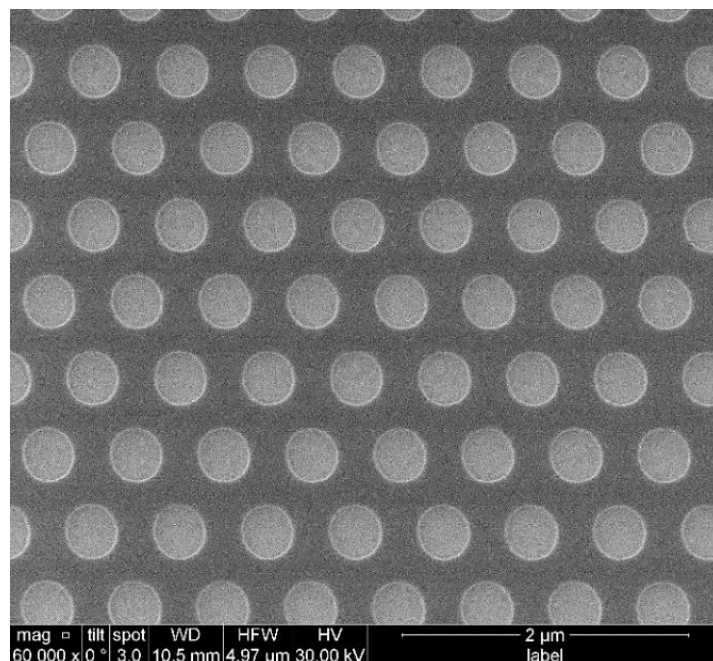
Figure 5-14. Top view SEM image of apertures through silicon nitride hard mask.

SiN
n-GaN
GaN Cap layer
MQWs
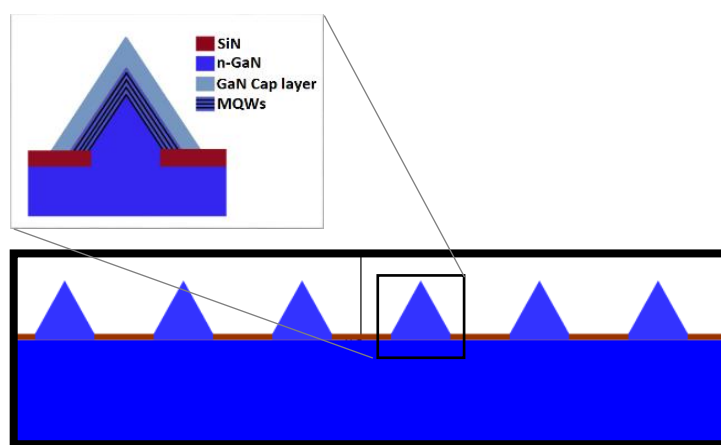
Figure 5-15. Growth Schematic

Growth was performed in the Aixtron 3×2 inch close-coupled vertical flow showerhead MOVPE reactor, as described previously. Trimethylaluminum (TMAl), trimethylgallium (TMGa), and ammonia (NH3) were used as Al, Ga, and N sources, respectively. Samples were initially heated up to 1200°C and annealed for 1 minute in an ammonia atmosphere. Afterwards, the reactor temperature was reduced to the Si-doped GaN growth temperature of 1035 °C, which performed using hydrogen as a carrier gas under a pressure of 150 hPa and V/III ratio of 1000, for 6 minutes. The reactor ambient was then switched to nitrogen at a

pressure of 400 hPa during cooling to 735 °C corresponding to InGaN growth temperature, which was measured by an in-situ Laytec pyrometer. The InGaN QWs were grown on the n-GaN pyramids using a TMIn flux of 8 μmol/min and a TMGa flux of 8 μmol/min. The NH_3 flux was maintained at 270 mmol/min with the V/III ratio of 17000. GaN barriers were grown at 860 °C in the nitrogen ambient. InGaN/GaN MQWs structure was also grown on planar (0001) GaN template, for comparison. Growth parameters are summarised in Table 5-2.

Table 5-2 Summary of growth parameters of InGaN/GaN structure.

Parameter	n-GaN	InGaN QWs	GaN QB
Temperature (°C)	1035	735	860
V-III Ratio	1000	17000	1000
TMIn/TMGa	-	1	-
Reactor Pressure (mBar)	150	400	150
Carrier Gas	Hydrogen	Nitrogen	Nitrogen

Temperature dependent PL measurements were conducted using a Horiba iHR320 spectrometer and a 325 nm He-Cd continuous wave (CW) laser with power and beam size of ~5 mW and 1 mm^2 respectively, as an excitation source. A T6400 Horiba μ-Raman/μ-PL system was used for micro-PL mapping with the spatial resolution of 1.5 µm (laser spot size). Microscopic morphology was examined by an FEI Quanta FEG 650 field emission (FE) scanning electron microscopy (SEM) instrument. Micro/nano-structural properties were characterised by scanning transmission electron microscopy (STEM) with a Jeol 2100 microscope operating at an acceleration voltage of 30 kV. STEM specimens were prepared using focused ion beam FEI DualBeam Helios NanoLab 600i Focussed Ion Beam (FIB) system.

To identify the origin of emission in nano-scale, the luminescence properties were also examined by SEM cathodoluminescence (CL) and monochromatic CL mapping conducted at RT using the custom set up mounted to the SEM. CL characterisation were done in collaboration with our colleagues in Strathclyde University. As the electron beam raster across the region being imaged, an Oriel MS125 spectrometer gathers the generated CL signal via a

50µm entrance slit and analyses it using a 600 lines/mm grating blazed at 400 nm, before it is collected by an Andor Newton electron multiplying (EM-) CCD. The exit slits are defined by the width of the pixel columns of the detector, which operated at 2x horizontal binning to give an effective width of 32 µm. CL mapping measurements were performed at an acceleration voltage of 5 kV and 20 nm step size.

5.2.3   Optical Characterisation

 GaN pyramids grown on the nano-patterned template are observed to be broadly uniform as shown in Figure 5-16.
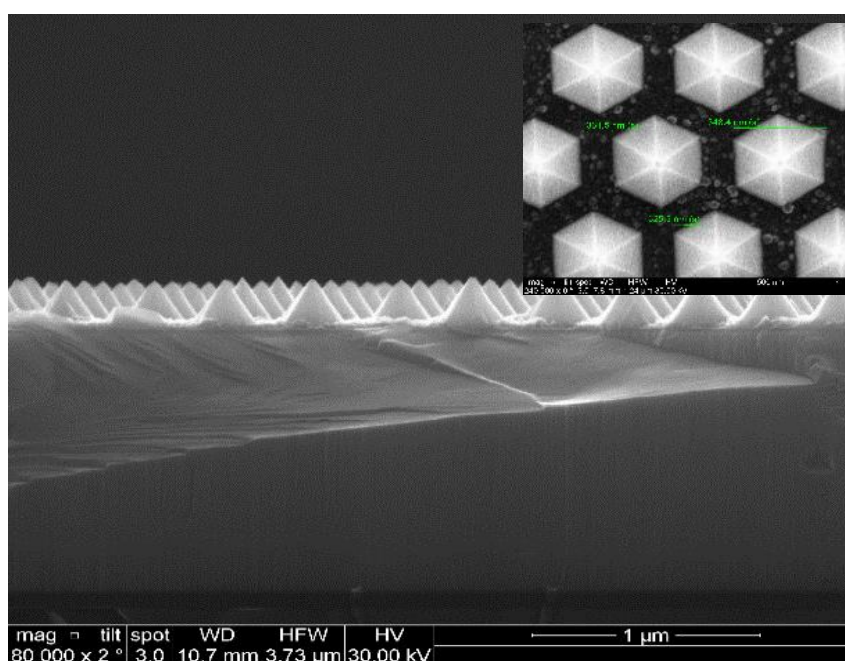
Figure 5-16 SEM cross section and top view (inset) images of selective area growth InGaN/GaN heterostructure on GaN nano-pyramids.

The STEM images show almost no defect and there are indications of dislocation bending in pyramids with some increased rounding of the apex tops with InGaN growth (Figure 5-17). Also, it reveals that InGaN QWs and GaN barriers are thinner compared to those on simultaneously grown c-plane reference material. Using PL spectroscopy, the active regions have been observed to emit light in the blue spectral region.

The thermal behaviour is a crucial factor in LED applications, therefore, the temperature-dependent PL of InGaN quantum dots/wells was carried out in the range of 10 to 450 K, as shown in Figure 5-18-*a*. In order to measure intensity, emission energy position and full width

at half maximum height (FWHM) of the PL spectra, the Gaussian peak function of OriginPro software were utilised to simulate each spectrum for all temperatures. Using data collected from Gaussian fitting, the peak position energy emission was plotted as a function of temperature with a weak indication of an S-shaped behaviour, where attributed to the localisation of excitons [391, 392], see Figure 5-18-*b*. The solid red line is the fitting of the peak position variation using Varshni equation (Equation 1-2). To fit the data with Varshni equation, the α and β parameters were calculated using linear interpolation from binary GaN and InN. The experimental data for GaN were taken from Nepal et. al. [64] (*α=0.94 meV/K* and *β=791 K*) and for InN were also taken from Holtz et. al [99] (*α=0.31 meV/K* and *β=650 K*). Hence for the estimated composition of 17±2 % the fitting parameter values of: $\alpha = (8.3 \pm 0.1) \times 10^{-4} \ eV \ K^{-1}$ and $\beta = 760 \pm 5 \ K$, were used to fit the data, which gives an effective band gap of $E_g(0) = 2.798 \pm 0.005 \ eV$.
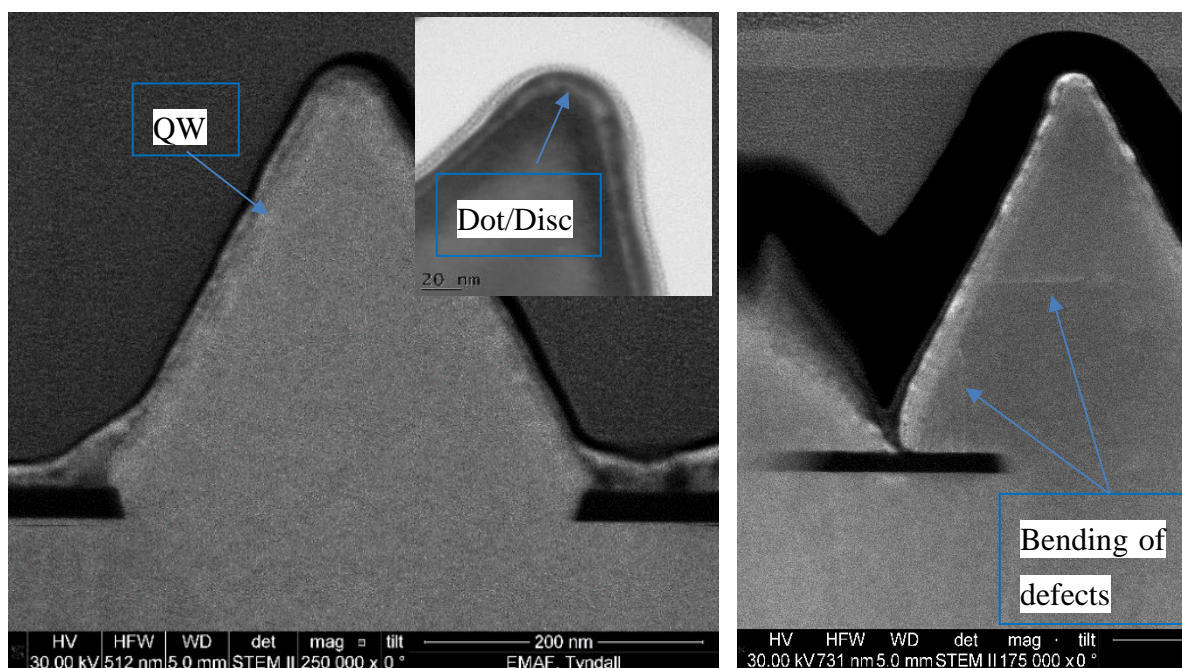
Figure 5-17. STEM image of GaN nano-pyramids with an InGaN /GaN structure grown on, the indication of defect bending and rounding of apex top.

In addition to the peak position of the energy emission, FWHM or linewidth is another key parameter which also carries important information on localisation mechanism of carriers. Here the FWHM reduces from around 255 meV to 230 meV with increasing temperature from 10 K to 180 K, followed by a gradual increase to 302 meV at higher temperatures.

At low temperatures, injected carriers are confined in the localisation potential of the quantum wells or dots. With increasing temperature, the carriers gain enough energy to overcome the potential barriers and recombine at non-radiative centres in the barrier.

Figure 5-18-c shows PL integrated intensity as a function of temperature. The ratio of the integrated PL intensity at 10 and 300 K (I_{300K}/I_{10K}) is an approximate measure of internal quantum efficiency (IQE), η_{int}, an IQE value of ~38% has been observed.

From Figure 5-18-c variation of the integrated intensity versus with $1000/k_BT$, two different temperature regimes can be seen: at very low temperatures, up to around 50 K, which the intensity remains almost constant. Above this value, a very rapid reduction is observed, indicating activation of localised carriers. This data can be well fitted and analysed using the well-known Arrhenius equation:

$$I(T) = I_0 \left[1 + A_1 exp\left(-\frac{E_{a1}}{k_BT}\right) + A_2 exp\left(-\frac{E_{a2}}{k_BT}\right) \right]^{-1} \qquad \text{Equation 5-1}$$

The Arrhenius plot of the integrated PL intensity gives the activation energy E_{a1} and E_{a2} of the non-radiative channels for carrier recombination. In Equation 5-1, I_0 is the integrated intensity at low temperature, A_1 and A_2 are two constants corresponding to the density of non-radiative recombination centres and k_B is Boltzmann constant [393-395].

The thermal activation energy E_a is related to the energy that localised carriers need to thermally escape from their localised states, which also gives us the meaningful information about localisation degree [396]. Any defect in the material acts as the nonradiative channel and consequently reduce the thermal activation energy. Higher activation energy signifies that the non-radiative quenching is more difficult to achieve. The best fit of experimental data with an Arrhenius equation is achieved with the values of activation energies $E_{a1} = 15 \pm 2 \, meV$ and $E_{a2} = 74 \pm 8 \, meV$ with the rate constants of 1.3 ± 0.3 and 15.6 ± 2, respectively (see Figure 5-18-c). An interesting point that E_{a1} value correlates roughly with the energy difference between the experimental peak position at 15 K and the E_g derived from Varshni fitting at the low temperature which can be defined as a sign of carrier localisation [397].
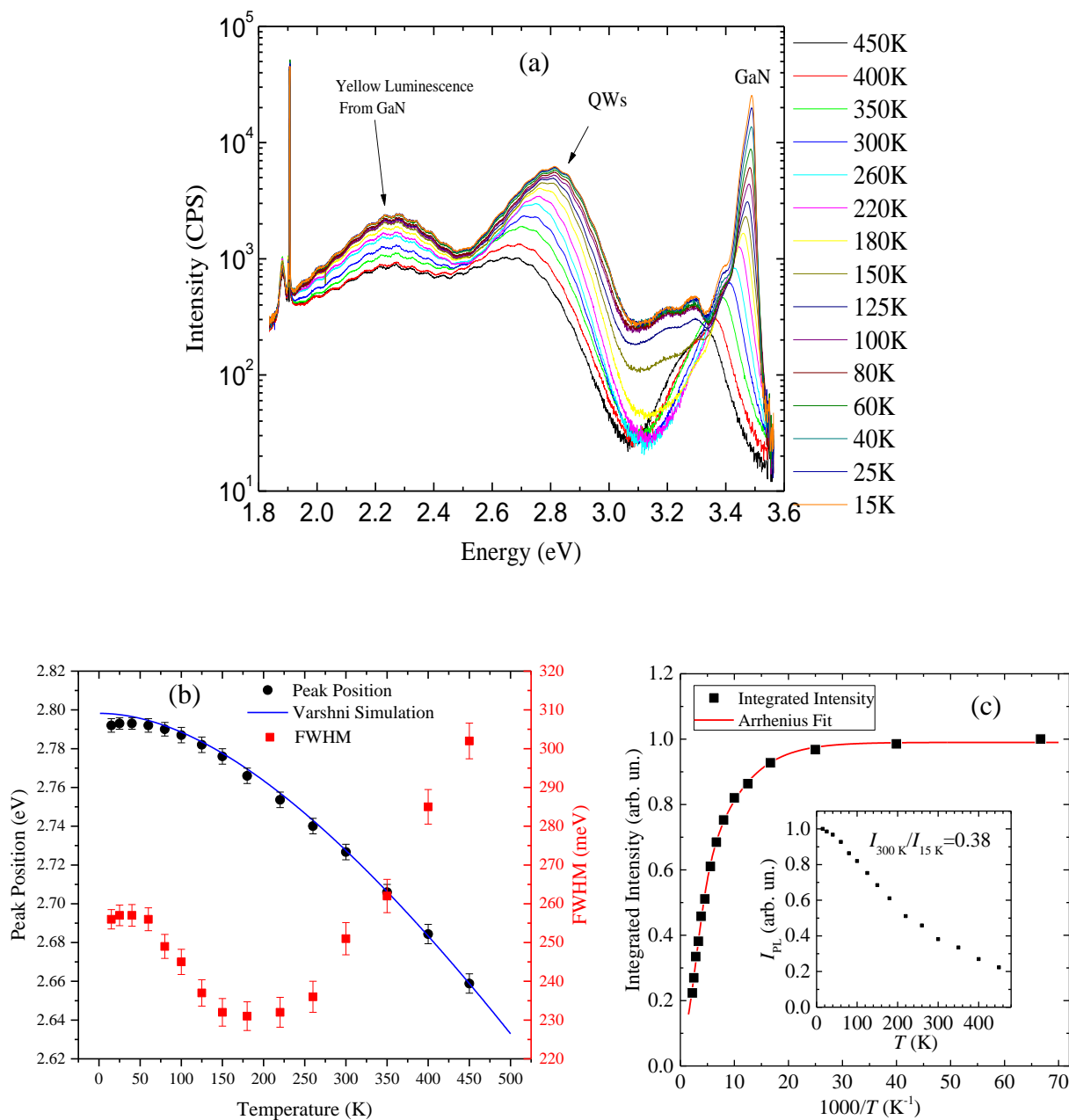
Figure 5-18. Temperature dependent PL spectroscopy of nano-pyramids using the 325nm laser from 10K to 450K (a), peak energy position (b) and integrated emission intensity (Arrhenius plot) (c) as a function of temperature.
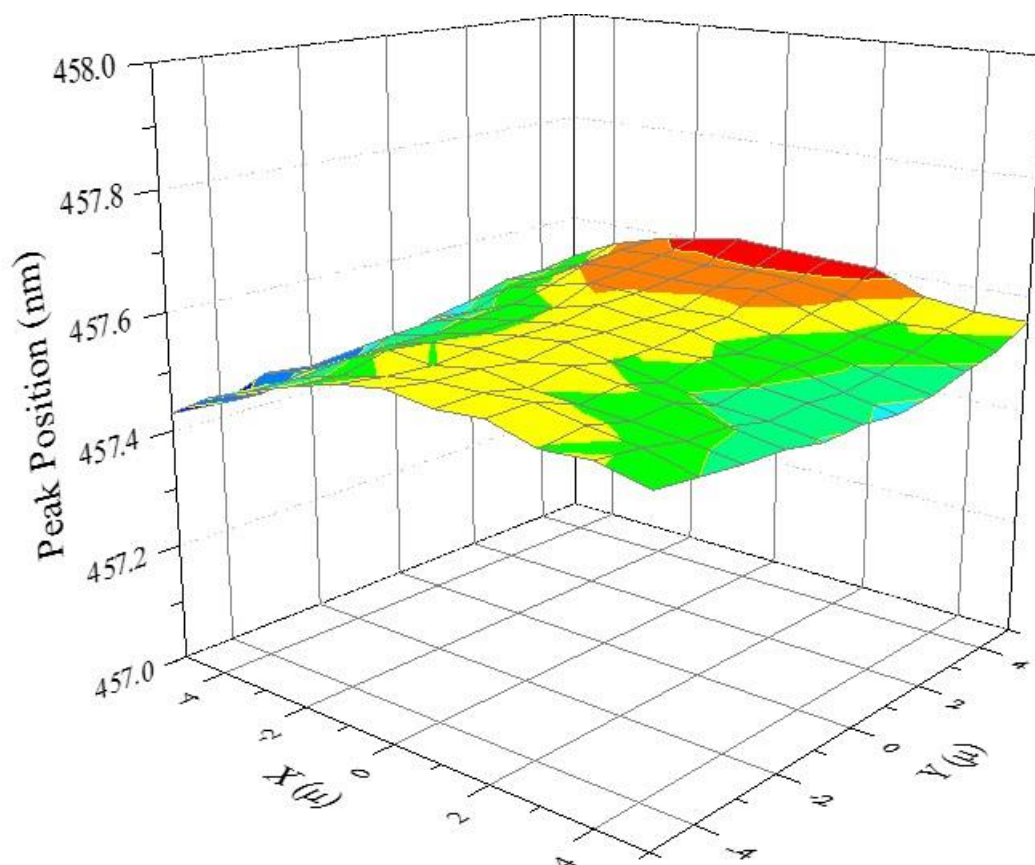
Figure 5-19. Mapping μ-PL (5×5 μm) using 325 nm laser and T6400 Horiba μ-Raman/μ-PL system.

Micro-PL mapping was applied to investigate the level of uniformity of the emission from the nano-pyramids. Based on the laser beam spot size (~1.5 µm in diameter) and distance between pyramids (450 nm), it would be around 3×3 pyramids covered with the beam and hence one is measuring the average emission of 9 pyramids at a time. A uniform emission from the structure over the area of 5×5 µm has also been observed with emission wavelength discrepancy of less than 0.2 nm over the area (λ_{emis}=457.5 ±0.1 nm)see Figure 5-19.

Room temperature CL shows double emission peaks at around 2.55 and 2.75 eV, although there was only a single emission peak (~ 2.73 eV) in PL, as can be seen in Figure 5-20. This additional lower energy peak may be related to either higher indium nitride content or polar (c-plane) quantum dot/discs on apex tips. The reason for detection of this additional peak is because of more intense electron beam excitation in CL which causes to excite the discs/dots, with the smaller and lower cross section, harder. In the case of possibility of higher In content in these sites, it is obvious to see the red-shift in the energy emission due to the smaller band-gap of the InGaN alloy. In the case of possible polar discs/dots on top of the apex tips, the

bending of the band-gap due to piezoelectric field in c-plane InGaN/GaN structure cause the red shift in comparison to the semi-polar plane, with the similar indium content, which is getting even stronger at the thicker QW on polar facet than semipolar one. [111].
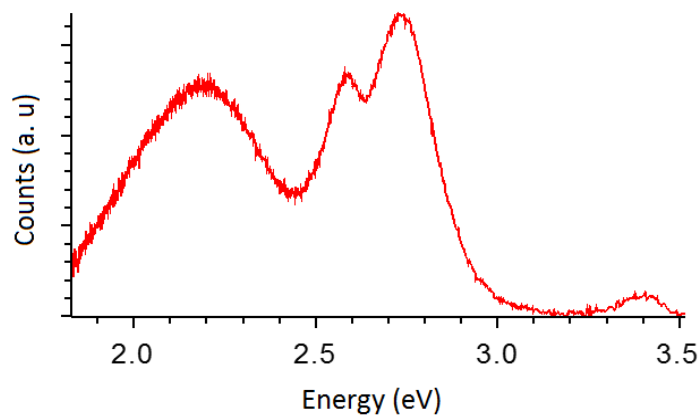
Figure 5-20 Mean spectrum CL at room temperature showing double peak emission.
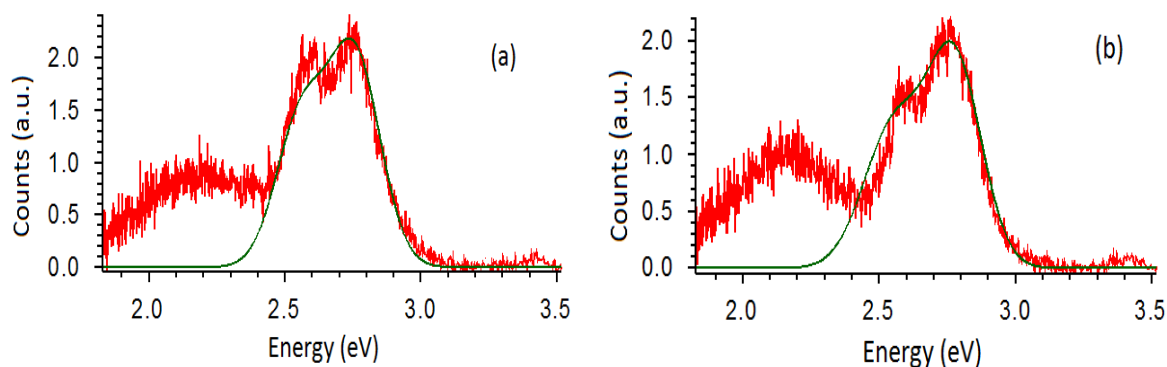
Figure 5-21 CL of InGaN/GaN structure showing relatively different luminescence intensity from both apex tips (a) and facets (b) of nano-pyramids.

Additionally, when each nano-pyramid excited at different positions it can be seen that the lower energy CL peak is relatively more intense when exciting the pyramid apex tips rather than the side facets (Figure 5-21). It is another indication of the higher indium nitride content in c-plane quantum dots/discs formed on the apex tips. In Figure 5-22 centroid and spatially assigning CL mapping of nano-pyramids are depicted. It can be obviously seen that the lower

emission energy range (2.44 – 2. 64eV) is more intense from apex tips than in which from facets. This is another indication of high indium content regions on top of apex tip pyramids
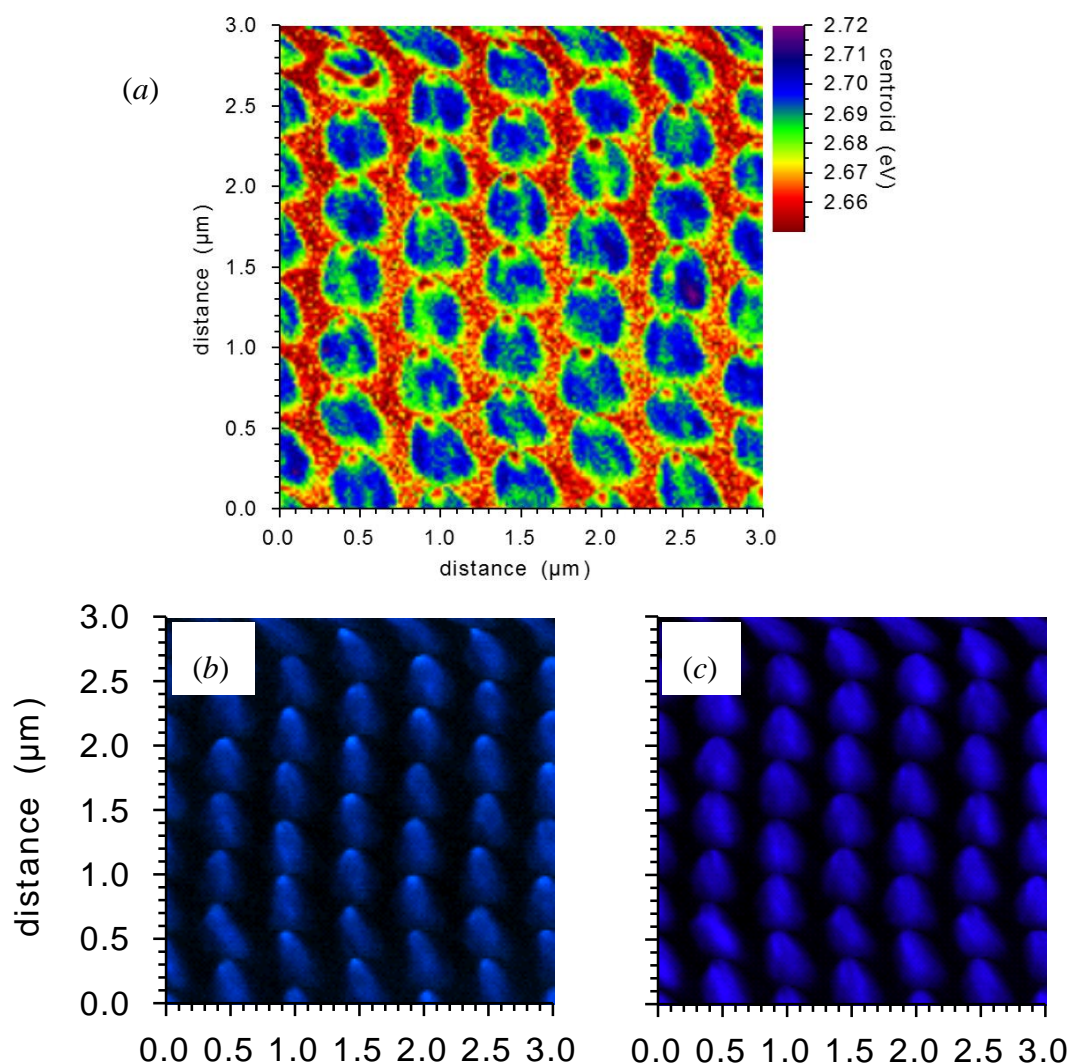
Figure 5-22 Centroid CL mapping, between 2.46eV and 3.00eV (a) and spatially assigning CL mapping of two emission peaks from nano-pyramids, 2.44 – 2. 64eV (b) and 2. 64 – 3.10eV (c) range.

5.2.4   Full LED Device Fabrication

To fabricate the full LED a mask was designed using CleWin layout software. The Mask set contained 7 layers for the purpose of photolithography, coatings and metallisation. The sequence of layers for fabrication of the LED is as follows: n-GaN (mesa) etch, p-metal coating, SiO_2 coating/etching, n-metal coating and bond-pad coating. Palladium (Pd) was used as a p-contact with the thickness of 30 nm on semipolar facets. A Ti/Al/Ti/Au (20:170:50:100 nm) stack has been used for the n-contact. Both p and n contacts were bonded with gold coating as

the bond-pad. More details about LED fabrication and metallisation can be find in section 2.6. A schematic cross view of a fabricated LED is shown in Figure 5-23.
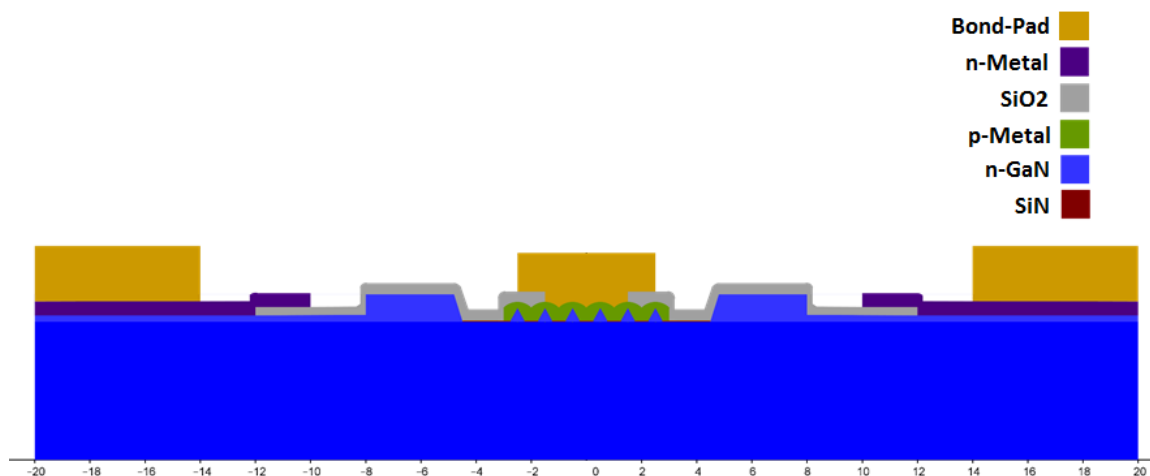
Figure 5-23 Schematic cross view of a fabricated nano-structured LED.

The final mask for LED fabrication is shown in Figure 5-24. In addition to the devices, this mask contains alignment marks, CTLM test features, isolation test sites and LED test sites on planar surfaces.
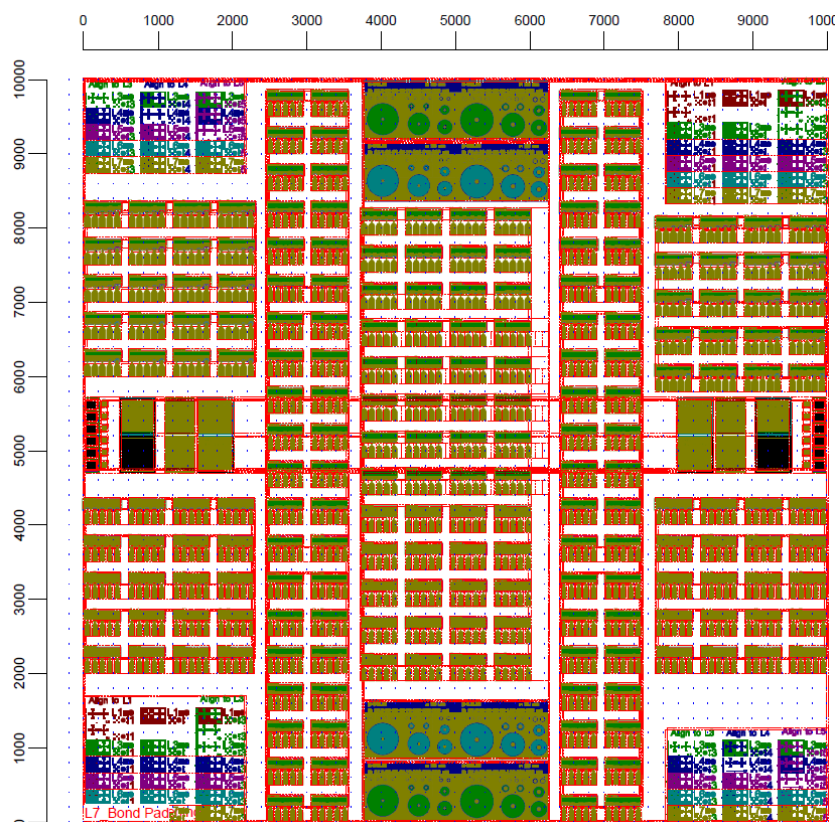
Figure 5-24 Schematic cross view of a fabricated nano-structured LED.

Optical Nomarski images of devices after n-contact deposition is shown in Figure 5-25. It is indicating a good alignment and uniform metal coating over n-GaN.
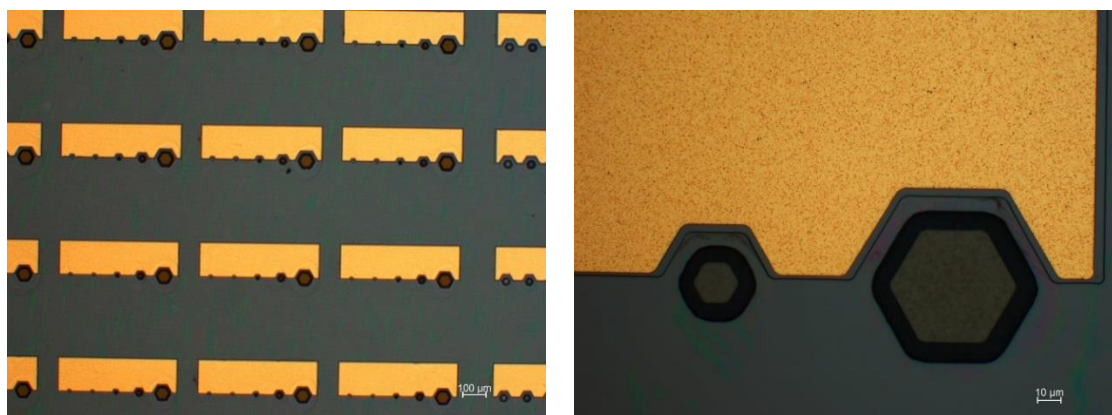
Figure 5-25 Nomarski images of LED devices after n-contact deposition at two different magnifications.

SEM images of p-contact (30 nm Pd) deposition of two different samples are depicted in Figure 5-26. It is also showing uniform metal coating and good alignment at these scales (<10 μm)
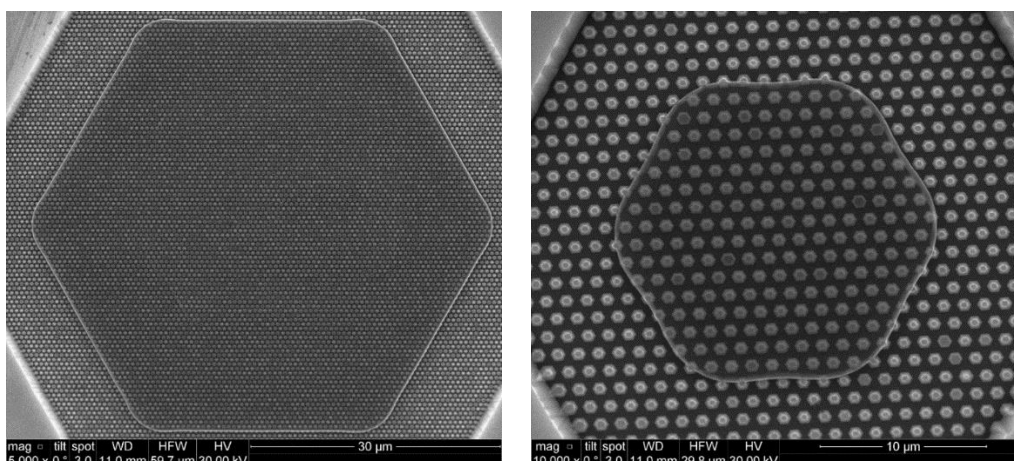
Figure 5-26 Top view SEM images of p-metal deposition of two different samples are depicted.

High resolution TEM (HRTEM) images of a typical nano-pyramid LED is shown in Figure 5-27. There is no obvious defect visible in the pyramid. The thickness of p-GaN is thinner (~8 nm) than that of the reference planar sample grown simultaneously (~35 nm). The thickness of the SQW is ~2 nm. P-contact Pd deposition is thinner on semipolar facets than planar sites with no diffusion of Pd into the nitride.
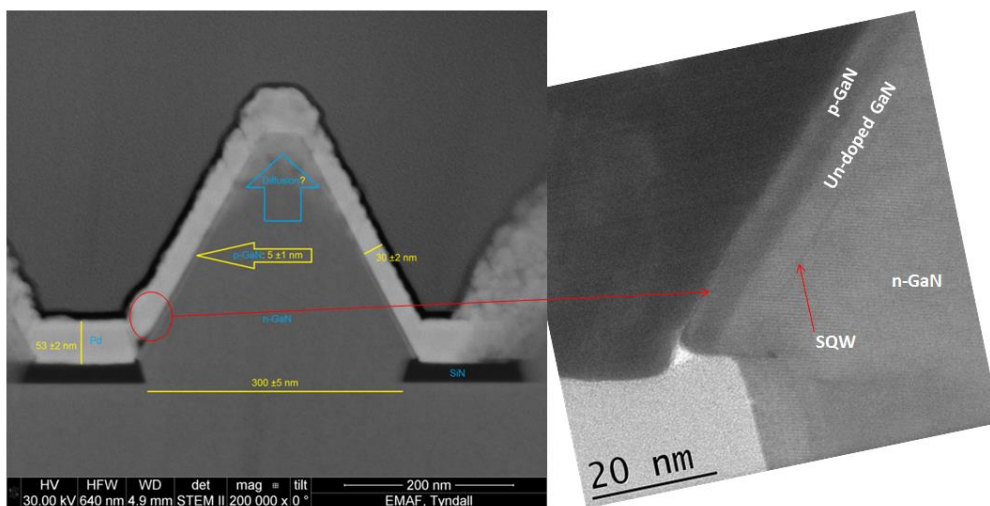
Figure 5-27 HRTEM images of a nano-pyramid LED.

Photoluminescence spectroscopy of samples with different diameter (D in nm) and pitches (W in nm) was performed using μ-PL system exciting with 325 nm laser, as plotted in Figure 5-28. Emission from QWs at the wavelength around 455 nm has been observed. There was no obvious and systematic effect either with variation of aperture size or the pitch on the emission energy of InGaN/GaN nano-pyramids observed.
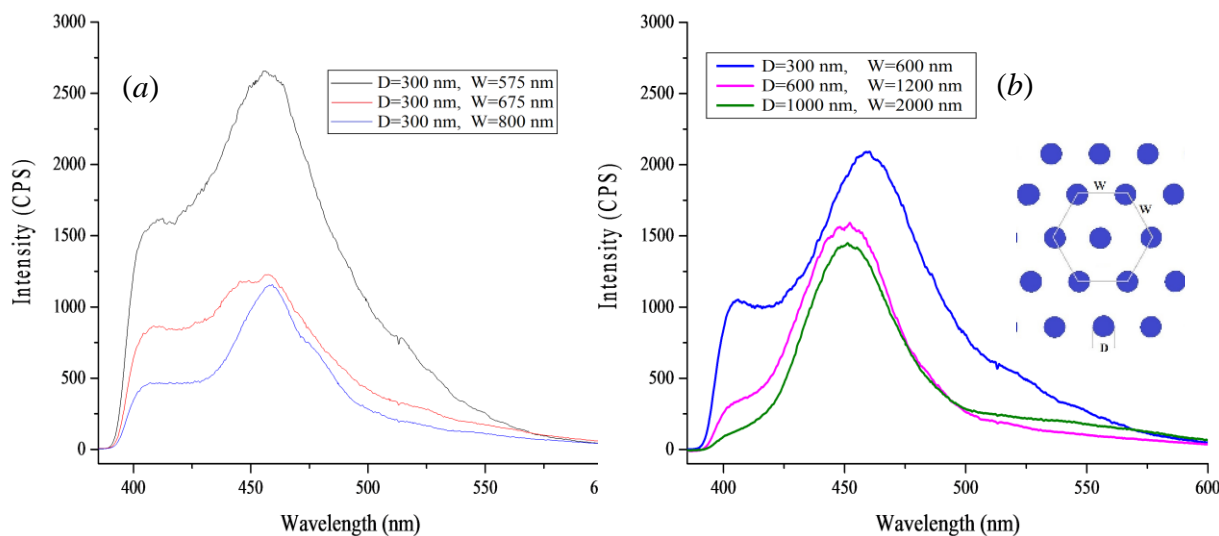
Figure 5-28 μ-PL spectroscopy of nano-structured LED. The effects of pitch (a) and size (b).

Unfortunately, no light emission detected using light-current-voltage (LIV) test. As there was PL emission observed, the problem must be related to injection efficiency of the carriers to QWs. High concentration of p dopants and over doping of Mg in p-GaN on semipolar facets [398] could be one reason for this. Thin p-GaN and accumulation of Mg on semipolar facets could be another reason for high Mg concentration, therefore overdoping of p-GaN.

SUMMARY AND CONCLUSIONS

In summary, we reported on the optical properties of 80-120 nm thick $In_xAl_{1-x}N$ epitaxial layers prepared on AlN templates with low In content. The layers are found to be nearly fully strained for In compositions less than about 0.10. While no luminescence was observed for relaxed samples ($x > 0.11$), those that were fully strained exhibited strong near UV luminescence with maximum efficiency for indium content in the range $0.004 \leq x \leq 0.016$. The luminescence centre(s) responsible for the emission band are currently not identified, though a clear association with the presence of In is observed. Using the band as a probe for photoluminescence excitation spectroscopy, an accurate determination of the variation of the room temperature $In_xAl_{1-x}N$ effective band-gap with indium content in the range $0.0022 \leq x \leq 0.11$ was obtained. The band-gap was found to decrease rapidly with indium content resulting in $In_xAl_{1-x}N$ band-gap bowing parameter of above 25 eV in the $x \rightarrow 0$ limit. The obtained evolution of the $In_xAl_{1-x}N$ band-gap in the $x \leq 0.11$ range can be very well described using a band-anticrossing model to take account of the interaction between localised In states and the host matrix conduction and valence band edges. This data allows determination of the potential of InAlN for active region design and reflector stacks in the UV, as well as for modelling of InAlN based heterostructure field effect transistors. Furthermore, the presented data shows the strong impact of a small (<1%) content of InN in an AlN matrix on the selection rules governing surface emission and absorption in InAlN, of direct relevance in the consideration of such alloys for UV emitter applications.

Using our low In content data in combination with data reported by other scientists, band-gap and bowing parameter of InAlN alloy at the full composition range were determined. Additionally, applying the InAlN band-gap data, band-offset and refractive index of the alloys were driven using Adachi model for all binary and ternary III-nitride materials. These results in a very good agreement with previous experimental data reported for the refractive index of GaN, AlN and AlGaN. Also, although there were no experimental data for InAlN alloy, index contrast obtained for InAlN/GaN is in a very good agreement with other experimental and models, especially at the InAlN compositions lattice matched to GaN.

There is lack of reliable data for the band-gap and bowing parameter of InGaN at low indium contents, <10%. Therefore similar experiment on InGaN could be interesting to provide the full spectrum for InGaN as well.

It was found to be critical for PL properties of InAlN/AlGaN QW heterostructures to implement a high growth temperature (1110°C) barrier with a capping procedure to prevent In desorption during the temperature ramp. We investigated the dependence of luminescence on QW thickness and found optimal values that are a trade-off between the weaker carrier confinement and less amount of light absorbed in thinner QWs and effects of the polarisation fields and partial strain relaxation in wider ones. As a result of the optimisations made, a strong RT luminescence from InAlN/AlGaN QWs that decays relatively weakly with temperature has been observed. Based on these results we believe that InAlN can provide an attractive alternative active region for UV light emitters in the 300-350 nm wavelength range.

The photoluminescence properties of $In_xAl_{1-x}N/Al_{0.59}Ga_{0.31}N$ five quantum well heterostructure, where indium content in wells was tuned by varying their growth temperature, has been studied. The observed non-monotonic dependence of luminescence efficiency on indium content with the maximum at about 18% was explained as a trade-off between a strain relaxations for higher indium contents and a change to type II line-up for lower In content InAlN. An unusual broadening of quantum well luminescence band (while absorption edge expectedly sharpens as indium content decreases) is attributed to the stronger contribution of deeper localised states due to a higher availability of holes, which tend to be confined in AlGaN barriers when quantum well band alignment is type II.

Optimal InAlN QWs show promising results in the luminescence point of view, especially in UV range due to high localisation degree leading to the high radiative recombination ratio. Therefore it can be a potential of UV emitters technology for UVB wavelengths. Further works could be done focusing on LED fabrication based on InAlN active regions. Preparation of GaN nano-columns using top-down/bottom-up technique showing that many factors are affecting not only creation of NCs but also QWs and emission from structures. ICP dry etch of GaN at the higher temperature of 150° C, helps to get better verticality of hexagonal shaped NCs due to the prevention of passivation which occurred at RT ICP etching. One of the factors affecting the quality of NCs after bottom-up growth is the (GaN connecting layer) is growth time, which needs to be optimised to be able to have apex tip NCs and before coalescence of them. The growth duration could be shorter for smaller diameter of NCs.

The growth rate of QWs and GaN on semipolar facets was found to be much lower that it is on polar facets, therefore very thin QW observed from TEM results of our initial QW growth experiment. Doubling the growth time of SQW helped to get emission from wells. Polarity of the material also affects the luminescence emission intensity as well as wavelength. Emission wavelength from semipolar facets is to be shorter than those from polar/planar facets. This attributed to a combination of factors including the increased confinement (thinner well), reduced band bend (semipolar) and potentially less In (due to In desorption at growth temperature).

Uniform luminescence has been observed from InGaN/GaN structure on the low defect uniformly shaped hexagonal array of GaN nano-pyramids. The temperature dependent PL emission energy following the predictions of the Varshni equation. CL spectra showing second emission peaks in addition to one detected by PL indicate of an accumulation of high indium content InGaN in the form of quantum dots or discs at the pyramid apexes. This perception is consistent with observations from STEM images.

TEM results from fabricated full LED showing the reasonable QW thickness with very thin p-GaN, ~8 nm in comparison with the expected thickness of the reference point of the planar sample which was ~35 nm. Also, no apparent defects were detected from HRTEM analysis. Luminescence at around 450 nm was observed by PL spectroscopy No obvious and systematic change in PL emission energy observed from the variation of the size and distance of the nano-pyramids.

LIV characterisation was showing no light emission, maybe due to a high concentration of Mg dopants in p-GaN because of the lower growth rate of GaN on semipolar facets. As it is likely that this issue is also related to the injection efficiency, optimisation of the growth time for the hole injection layers, and an electron blocking structure should be considered carefully.

Future work can be done on the investigation of growth and characterisation of QDs or quantum discs on top of defect-free nano-pyramids provided.

REFERENCES

1.   Nakamura, S. and S.F. Chichibu, *Introduction to Nitride Semiconductor Blue Lasers and Light Emitting Diodes*. 2000: Taylor & Francis.

2.   Khan, A., K. Balakrishnan, and T. Katona, *Ultraviolet light-emitting diodes based on group three nitrides.* Nat Photonics, 2008. **2**.

3.   Nakamura, S., T. Mukai, and M. Senoh, *Candela‐class high‐brightness InGaN/AlGaN double‐heterostructure blue‐light‐emitting diodes.* Applied Physics Letters, 1994. **64**(13): p. 1687-1689.

4.   Fiorentini, V., F. Bernardini, and O. Ambacher, *Evidence for nonlinear macroscopic polarization in III–V nitride alloy heterostructures.* Applied Physics Letters, 2002. **80**(7): p. 1204-1206.

5.   Lahnemann, J., et al., *Direct experimental determination of the spontaneous polarization of GaN.* Physical Review B, 2012. **86**(8): p. 5.

6.   Wood, C. and D. Jena, *Polarization Effects in Semiconductors: From Ab Initio Theory to Device Applications*. 2008: Springer.

7.   Ren, C., *Polarisation fields in III-nitrides: effects and control.* Materials Science and Technology, 2016. **32**(5): p. 418-433.

8.   Corbett, B., et al. *Development of semipolar (11-22) LEDs on GaN templates*. in *SPIE OPTO*. 2016. International Society for Optics and Photonics.

9.   Dinh, D.V., et al., *Semipolar (112─2) InGaN light‐emitting diodes grown on chemically–mechanically polished GaN templates.* physica status solidi (a), 2015. **212**(10): p. 2196-2200.

10.   Weijie, C., et al., *High-performance, single-pyramid micro light-emitting diode with leakage current confinement layer.* Applied Physics Express, 2015. **8**(3): p. 032102.

11.   Nakamura, S., *The roles of structural imperfections in InGaN-based blue light-emitting diodes and laser diodes.* Science, 1998. **281**(5379): p. 956-961.

12.   Oliver, R.A., et al., *Microstructural origins of localization in InGaN quantum wells.* Journal of Physics D: Applied Physics, 2010. **43**(35): p. 354003.

13.   Vegard, L., *Die konstitution der mischkristalle und die raumfüllung der atome.* Zeitschrift für Physik, 1921. **5**(1): p. 17-26.

14.   Morkoç, H., *Handbook of Nitride Semiconductors and Devices, Materials Properties, Physics and Growth*. Vol. 1. 2009: John Wiley & Sons.

15.   Kumaresan, V., et al., *Epitaxy of GaN Nanowires on Graphene.* Nano Letters, 2016. **16**(8): p. 4895-4902.

16.   Heilmann, M., et al., *Vertically Oriented Growth of GaN Nanorods on Si Using Graphene as an Atomically Thin Buffer Layer.* Nano Letters, 2016. **16**(6): p. 3524-3532.

17.   Sarwar, A., et al., *Semiconductor Nanowire Light‐Emitting Diodes Grown on Metal: A Direction Toward Large‐Scale Fabrication of Nanowire Devices.* Small, 2015. **11**(40): p. 5402-5408.

18.   Coltrin, M.E., et al., *Energy Frontier Research Center for Solid-State Lighting Science: Exploring New Materials Architectures and Light Emission Phenomena.* The Journal of Physical Chemistry C, 2014. **118**(25): p. 13330-13345.

19.   Jonathan, J.W., Jr., et al., *III-nitride core–shell nanowire arrayed solar cells.* Nanotechnology, 2012. **23**(19): p. 194007.

20.   Guo, W., et al., *Catalyst-Free InGaN/GaN Nanowire Light Emitting Diodes Grown on (001) Silicon by Molecular Beam Epitaxy.* Nano Letters, 2010. **10**(9): p. 3355-3359.

21.   Yan, R., D. Gargas, and P. Yang, *Nanowire photonics.* Nat Photon, 2009. **3**(10): p. 569-576.

22.   Kim, H.-M., et al., *High-Brightness Light Emitting Diodes Using Dislocation-Free Indium Gallium Nitride/Gallium Nitride Multiquantum-Well Nanorod Arrays.* Nano Letters, 2004. **4**(6): p. 1059-1062.

23.   Zang, K. and S.J. Chua, *GaN based nanorod light emitting diodes by selective area epitaxy.* physica status solidi (c), 2010. **7**(7-8): p. 2236-2239.

24.   Conroy, M., et al., *Epitaxial lateral overgrowth of AlN on self-assembled patterned nanorods.* Journal of Materials Chemistry C, 2015. **3**(2): p. 431-437.

25.   Sekiguchi, H., K. Kishino, and A. Kikuchi, *Emission color control from blue to red with nanocolumn diameter of InGaN/GaN nanocolumn arrays grown on same substrate.* Applied physics letters, 2010. **96**(23): p. 231104.

26.   Musolino, M., et al., *Compatibility of the selective area growth of GaN nanowires on AlN-buffered Si substrates with the operation of light emitting diodes.* Nanotechnology, 2015. **26**(8): p. 085605.

27.   Bergbauer, W., et al., *Continuous-flux MOVPE growth of position-controlled N-face GaN nanorods andembedded InGaN quantum wells.* Nanotechnology, 2010. **21**(30): p. 305201.

28.   Hiramatsu, K., et al., *Fabrication and characterization of low defect density GaN using facet-controlled epitaxial lateral overgrowth (FACELO).* Journal of Crystal Growth, 2000. **221**(1): p. 316-326.

29.   Jamil, M., et al., *Mechanism of large area dislocation defect reduction in GaN layers on Al N/ Si (111) by substrate engineering.* Journal of Applied Physics, 2007. **102**(2): p. 023701.

30.   Zheleva, T.S., et al., *Dislocation density reduction via lateral epitaxy in selectively grown GaN structures.* Applied Physics Letters, 1997. **71**(17): p. 2472-2474.

31.   Tanikawa, T., et al., *Growth of semi-polar (11-22) GaN on a (113) Si substrate by selective MOVPE.* physica status solidi (c), 2008. **5**(9): p. 2966-2968.

32.   Tanaka, A., et al., *Strong geometrical effects in submillimeter selective area growth and light extraction of GaN light emitting diodes on sapphire.* Scientific reports, 2015. **5**.

33.   Wunderer, T., et al., *Three-dimensional GaN for semipolar light emitters.* physica status solidi (b), 2011. **248**(3): p. 549-560.

34.   Rishinaramangalam, A.K., et al., *Semipolar InGaN/GaN nanostructure light-emitting diodes on c-plane sapphire.* Applied Physics Express, 2016. **9**(3): p. 032101.

35.   Tendille, F., et al., *Successive selective growth of semipolar (11-22) GaN on patterned sapphire substrate.* Semiconductor Science and Technology, 2015. **30**(6): p. 065001.

36. Vurgaftman, I. and J.R. Meyer, *Band parameters for nitrogen-containing semiconductors.* Journal of Applied Physics, 2003. **94**(6): p. 3675-3696.

37. Available from: http://mini.physics.sunysb.edu/~marivi/TEACHING-OLD/PHY313/doku.php?id=lectures:4.

38. Yao, T. and S.K. Hong, *Oxide and Nitride Semiconductors: Processing, Properties, and Applications.* 2009: Springer Berlin Heidelberg.

39. Dinh, D.V., *MOVPE growth of InN and InGaN with different surface orientations*, in *Mathematics and Natural Sciences.* 2012, Technical University of Berlin. p. 145.

40. Nakamura, S., S. Pearton, and G. Fasol, *The Blue Laser Diode: The Complete Story.* 2013: Springer Berlin Heidelberg.

41. Akasaki, I., et al., *Shortest wavelength semiconductor laser diode.* Electronics Letters, 1996. **32**(12): p. 1105-1106.

42. Akasaki, I. and H. Amano, *Widegap Column‐III Nitride Semiconductors for UV/Blue Light Emitting Devices.* Journal of the Electrochemical Society, 1994. **141**(8): p. 2266-2271.

43. Eastman, L.F. and U.K. Mishra, *The toughest transistor yet [GaN transistors].* IEEE spectrum, 2002. **39**(5): p. 28-33.

44. Mishra, U.K., P. Parikh, and Y.-F. Wu, *AlGaN/GaN HEMTs-an overview of device operation and applications.* Proceedings of the IEEE, 2002. **90**(6): p. 1022-1031.

45. Erol, A., *Dilute III-V Nitride Semiconductors and Material Systems: Physics and Technology.* 2008: Springer Berlin Heidelberg.

46. Kolnik, J., et al., *Electronic transport studies of bulk zincblende and wurtzite phases of GaN based on an ensemble Monte Carlo calculation including a full zone band structure.* Journal of Applied Physics, 1995. **78**(2): p. 1033-1038.

47. Dingle, R., et al., *Stimulated emission and laser action in gallium nitride.* Applied Physics Letters, 1971. **19**(1): p. 5-7.

48. Fritsch, D., H. Schmidt, and M. Grundmann, *Band-structure pseudopotential calculation of zinc-blende and wurtzite AlN, GaN, and InN.* Physical Review B, 2003. **67**(23): p. 235205.

49. Lagerstedt, O. and B. Monemar, *Luminescence in epitaxial GaN: Cd.* Journal of Applied Physics, 1974. **45**(5): p. 2266-2272.

50. Monemar, B., *Fundamental energy gap of GaN from photoluminescence excitation spectra.* Physical Review B, 1974. **10**(2): p. 676.

51. Volm, D., et al., *Exciton fine structure in undoped GaN epitaxial films.* Physical Review B, 1996. **53**(24): p. 16543.

52. Piprek, J., *Nitride Semiconductor Devices: Principles and Simulation.* 2007: Wiley.

53. Rodina, A., et al., *Free excitons in wurtzite GaN.* Physical Review B, 2001. **64**(11): p. 115204.

54. Merz, C., et al., *Free and bound excitons in thin wurtzite GaN layers on sapphire.* Semiconductor science and technology, 1996. **11**(5): p. 712.

55. Morkoc, H., *Nitride semiconductors and devices.* Vol. 32. 2013: Springer Science & Business Media.

56. Persson, C., et al., *Effective electronic masses in wurtzite and zinc-blende GaN and AlN.* Journal of Crystal Growth, 2001. **231**(3): p. 397-406.

57. Xin-he, J., et al., *Enhancement of TE polarized light extraction efficiency in nanoscale (AlN) m /(GaN) n (m > n) superlattice substitution for Al-rich AlGaN disorder alloy: ultra-thin GaN layer modulation.* New Journal of Physics, 2014. **16**(11): p. 113065.

58. Kirilyuk, V., *Optical Characterization of Gallium Nitride*. 2002, Radboud University Nijmegen.

59. Varshni, Y.P., *Temperature dependence of the energy gap in semiconductors.* Physica, 1967. **34**(1): p. 149-154.

60. Teisseyre, H., et al., *Temperature dependence of the energy gap in GaN bulk single crystals and epitaxial layer.* Journal of applied physics, 1994. **76**(4): p. 2429-2434.

61. Petalas, J., et al., *Optical and electronic-structure study of cubic and hexagonal GaN thin films.* Physical Review B, 1995. **52**(11): p. 8082.

62. Shan, W., et al., *Temperature dependence of interband transitions in GaN grown by metalorganic chemical vapor deposition.* Applied physics letters, 1995. **66**(8): p. 985-987.

63. Salvador, A., et al., *Properties of a Si doped GaN/AlGaN single quantum well.* Applied physics letters, 1995. **67**(22): p. 3322-3324.

64. Nepal, N., et al., *Temperature and compositional dependence of the energy band gap of AlGaN alloys.* Applied Physics Letters, 2005. **87**(24): p. 242104.

65. Yim, W., et al., *Epitaxially grown AlN and its optical band gap.* Journal of Applied Physics, 1973. **44**(1): p. 292-296.

66. Perry, P. and R. Rutz, *The optical absorption edge of single‐crystal AlN prepared by a close‐spaced vapor process.* Applied Physics Letters, 1978. **33**(4): p. 319-321.

67. Strite, S. and H. Morkoç, *GaN, AlN, and InN: a review.* Journal of Vacuum Science & Technology B, 1992. **10**(4): p. 1237-1266.

68. Guo, Q. and A. Yoshida, *Temperature dependence of band gap change in InN and AlN.* Japanese journal of applied physics, 1994. **33**(5R): p. 2453.

69. Vispute, R.D., H. Wu, and J. Narayan, *High quality epitaxial aluminum nitride layers on sapphire by pulsed laser deposition.* Applied Physics Letters, 1995. **67**(11): p. 1549-1551.

70. Jiang, L., et al., *Temperature dependence of the optical properties in hexagonal AlN.* Journal of applied physics, 2003. **94**(9): p. 5704-5709.

71. Onuma, T., et al., *Exciton spectra of an AlN epitaxial film on (0001) sapphire substrate grown by low-pressure metalorganic vapor phase epitaxy.* Applied Physics Letters, 2002. **81**(4): p. 652-654.

72. Chen, J., et al., *Critical point transitions of wurtzite AlN in the vacuum–ultraviolet spectral range.* Applied physics letters, 2004. **84**(24): p. 4866-4868.

73. Chen, G.D., et al., *Fundamental optical transitions in GaN.* Applied Physics Letters, 1996. **68**(20): p. 2784-2786.

74. Li, J., et al., *Band structure and fundamental optical transitions in wurtzite AlN.* Applied Physics Letters, 2003. **83**(25): p. 5163-5165.

75. Rezaei, B., A. Asgari, and M. Kalafi, *Electronic band structure pseudopotential calculation of wurtzite III-nitride materials.* Physica B: Condensed Matter, 2006. **371**(1): p. 107-111.

76.   Wei, S.H. and A. Zunger, *Valence band splittings and band offsets of AlN, GaN, and InN.* Applied physics letters, 1996. **69**(18): p. 2719-2721.

77.   de Carvalho, L.C., et al., *Valence-band splittings in cubic and hexagonal AlN, GaN, and InN.* Appl. Phys. Lett, 2010. **97**(23): p. 232101.

78.   Silveira, E., et al., *Excitonic structure of bulk AlN from optical reflectivity and cathodoluminescence measurements.* Physical Review B, 2005. **71**(4): p. 041201.

79.   Rodina, A. and B. Meyer, *Anisotropy of conduction band g values and interband momentum matrix elements in wurtzite GaN.* Physical Review B, 2001. **64**(24): p. 245209.

80.   Pugh, S., et al., *Electronic structure calculations on nitride semiconductors.* Semiconductor Science and Technology, 1999. **14**(1): p. 23.

81.   Rinke, P., et al., *Consistent set of band parameters for the group-III nitrides AlN, GaN, and InN.* Physical Review B, 2008. **77**(7): p. 075202.

82.   Zhang, J., H. Zhao, and N. Tansu, *Effect of crystal-field split-off hole and heavy-hole bands crossover on gain characteristics of high Al-content AlGaN quantum well lasers.* Applied Physics Letters, 2010. **97**(11): p. 111105.

83.   Zubialevich, V.Z., et al., *Strongly nonparabolic variation of the band gap in In x Al1− x N with low indium content.* Semiconductor Science and Technology, 2015. **31**(2): p. 025006.

84.   Nam, K., et al., *Optical properties of AlN and GaN in elevated temperatures.* Applied physics letters, 2004. **85**(16): p. 3489-3491.

85.   Berland, K., et al., *Temperature stability of intersubband transitions in AlN/GaN quantum wells.* Applied Physics Letters, 2010. **97**(4): p. 043507.

86.   Tansley, T. and C. Foley, *Optical band gap of indium nitride.* Journal of Applied Physics, 1986. **59**(9): p. 3241-3244.

87.   Wu, J. and W. Walukiewicz, *Band gaps of InN and group III nitride alloys.* Superlattices and Microstructures, 2003. **34**(1–2): p. 63-75.

88.   Matsuoka, T., et al., *Optical bandgap energy of wurtzite InN.* Applied Physics Letters, 2002. **81**(7): p. 1246-1248.

89.   Wu, J., et al., *Temperature dependence of the fundamental band gap of InN.* Journal of Applied Physics, 2003. **94**(7): p. 4457-4460.

90.   Rinke, P., et al., *Band gap and band parameters of InN and GaN from quasiparticle energy calculations based on exact-exchange density-functional theory.* arXiv preprint cond-mat/0610141, 2006.

91.   Davydov, V.Y., et al., *Absorption and emission of hexagonal InN. Evidence of narrow fundamental band gap.* physica status solidi (b), 2002. **229**(3): p. r1-r3.

92.   Trybus, E., et al., *Growth of InN on Ge substrate by molecular beam epitaxy.* Journal of crystal growth, 2005. **279**(3): p. 311-315.

93.   Chen, T.-C.P., et al., *Growth of InN films by RF plasma-assisted MBE and cluster beam epitaxy.* Journal of crystal growth, 2006. **288**(2): p. 254-260.

94.   Bhuiyan, A.G., et al., *Single-crystalline InN films with an absorption edge between 0.7 and 2 eV grown using different techniques and evidence of the actual band gap energy.* Applied physics letters, 2003. **83**(23): p. 4788-4790.

95.   Wu, J., et al., *Effects of the narrow band gap on the properties of InN.* Physical Review B, 2002. **66**(20): p. 201403.

96.   Bhuiyan, A.G., A. Hashimoto, and A. Yamamoto, *Indium nitride (InN): A review on growth, characterization, and properties.* Journal of Applied Physics, 2003. **94**(5): p. 2779-2808.

97.   Manabu, U., et al., *Band Structures of Wurtzite InN and Ga 1- x In x N by All-Electron G W Calculation.* Japanese Journal of Applied Physics, 2004. **43**(3B): p. L407.

98.   Walukiewicz, W., et al., *Optical properties and electronic structure of InN and In-rich group III-nitride alloys.* Journal of Crystal Growth, 2004. **269**(1): p. 119-127.

99.   Holtz, M., et al., *Influence of phonons on the temperature dependence of photoluminescence in InN with low carrier concentration.* Journal of Applied Physics, 2009. **105**(6): p. 063702.

100.   Yeo, Y., T. Chong, and M. Li, *Electronic band structures and effective-mass parameters of wurtzite GaN and InN.* Journal of applied physics, 1998. **83**(3): p. 1429-1436.

101.   Ambacher, O., et al., *Pyroelectric properties of Al(In)GaN/GaN hetero- and quantum well structures.* Journal of Physics-Condensed Matter, 2002. **14**(13): p. 3399-3434.

102.   Stutzmann, M., et al., *Playing with polarity.* Physica Status Solidi B-Basic Research, 2001. **228**(2): p. 505-512.

103.   Waltereit, P., et al., *Nitride semiconductors free of electrostatic fields for efficient white light-emitting diodes.* Nature, 2000. **406**(6798): p. 865-868.

104.   Harrison, P., *Quantum Wells, Wires and Dots: Theoretical and Computational Physics of Semiconductor Nanostructures.* 2010: Wiley.

105.   Miller, D., et al., *Band-edge electroabsorption in quantum well structures: The quantum-confined Stark effect.* Physical Review Letters, 1984. **53**(22): p. 2173.

106.   O'Reilly, E., *Quantum Theory of Solids.* 2003: Taylor & Francis.

107.   Fiorentini, V., et al., *Effects of macroscopic polarization in III-V nitride multiple quantum wells.* Physical Review B, 1999. **60**(12): p. 8849-8858.

108.   Chichibu, S.F., et al., *Origin of defect-insensitive emission probability in In-containing (Al, In, Ga) N alloy semiconductors.* Nature Materials, 2006. **5**(10): p. 810-816.

109.   Dinh, D.V., S.N. Alam, and P.J. Parbrook, *Effect of V/III ratio on the growth of ( ) AlGaN by metalorganic vapour phase epitaxy.* Journal of Crystal Growth, 2016. **435**: p. 12-18.

110.   Masui, H., et al., *Nonpolar and semipolar III-nitride light-emitting diodes: achievements and challenges.* IEEE Transactions on Electron Devices, 2010. **57**(1): p. 88-100.

111.   Feezell, D.F., et al., *Semipolar (202-1-) InGaN/GaN Light-Emitting Diodes for High-Efficiency Solid-State Lighting.* Journal of Display Technology, 2013. **9**(4): p. 190-198.

112.   Romanov, A., et al., *Strain-induced polarization in wurtzite III-nitride semipolar layers.* Journal of Applied Physics, 2006. **100**(2): p. 023522.

113.   Koester, R., et al., *M-plane core–shell InGaN/GaN multiple-quantum-wells on GaN wires for electroluminescent devices.* Nano letters, 2011. **11**(11): p. 4839-4845.

114.   Wang, Q., et al., *Influence of strain relaxation on the optical properties of InGaN/GaN multiple quantum well nanorods.* Journal of Physics D: Applied Physics, 2011. **44**(39): p. 395102.

115.   Liu, C., et al., *Light emission from InGaN quantum wells grown on the facets of closely spaced GaN nano-pyramids formed by nano-imprinting.* Applied physics express, 2009. **2**(12): p. 121002.

116.   Chang, J.-R., et al., *Fabrication and luminescent properties of core-shell InGaN/GaN multiple quantum wells on GaN nanopillars.* Applied Physics Letters, 2012. **100**(26): p. 261103.

117.   Kim, T., et al. *Polychromatic white LED using GaN nano pyramid structure*. 2013.

118.   Girgel, I., et al. *Investigation of facet-dependent InGaN growth for core-shell LEDs*. 2015.

119.   Liou, B.-T., S.-H. Yen, and Y.-K. Kuo, *Vegard's law deviation in band gap and bowing parameter of AlxIn1-xN.* Applied Physics A, 2005. **81**(3): p. 651-655.

120.   Liou, B.-T., et al., *First-principles calculation for bowing parameter of wurtzite InxGa1−xN.* Optics Communications, 2005. **249**(1–3): p. 217-223.

121.   Kuo, Y.-K., et al., *Vegard's law deviation in lattice constant and band gap bowing parameter of zincblende In x Ga 1− x N.* Optics Communications, 2004. **237**(4): p. 363-369.

122.   Liou, B.-T., S.-H. Yen, and Y.-K. Kuo. *Vegard's law deviation in band gaps and bowing parameters of the wurtzite III-nitride ternary alloys*. in *Photonics Asia 2004*. 2005. International Society for Optics and Photonics.

123.   Nam, K.B., et al., *Unique optical properties of AlGaN alloys and related ultraviolet emitters.* Appl Phys Lett, 2004. **84**.

124.   Jmerik, V.N., E.V. Lutsenko, and S.V. Ivanov, *Plasma-assisted molecular beam epitaxy of AlGaN heterostructures for deep-ultraviolet optically pumped lasers.* physica status solidi (a), 2013. **210**(3): p. 439-450.

125.   Teofilov, N., et al., *Optical investigation of AlxGa1−xN epitaxial films grown on AlN buffer layers.* Diamond and Related Materials, 2002. **11**(3–6): p. 892-895.

126.   Koide, Y., et al., *Energy band‐gap bowing parameter in an AlxGa1−x N alloy.* Journal of Applied Physics, 1987. **61**(9): p. 4540-4543.

127.   Buchheim, C., et al., *Dielectric function and critical points of the band structure for AlGaN alloys.* physica status solidi (b), 2005. **242**(13): p. 2610-2616.

128.   Pelá, R.R., et al., *Accurate band gaps of AlGaN, InGaN, and AlInN alloys calculations based on LDA-1/2 approach.* Applied Physics Letters, 2011. **98**(15): p. 151907.

129.   Neuschl, B., et al., *Composition dependent valence band order in c-oriented wurtzite AlGaN layers.* Journal of Applied Physics, 2014. **116**(11): p. 113506.

130.   Coughlan, C., et al., *Band gap bowing and optical polarization switching in Al1−xGaxN alloys.* physica status solidi (b), 2015. **252**(5): p. 879-884.

131.   Parker, C.A., et al., *Determination of the critical layer thickness in the InGaN/GaN heterostructures.* Applied Physics Letters, 1999. **75**(18): p. 2776-2778.

132.   Ponce, F.A., et al., *Microstructure and electronic properties of InGaN alloys.* physica status solidi (b), 2003. **240**(2): p. 273-284.

133.   Islam, M.R., et al., *MOVPE Growth of InxGa1−xN (x ∼ 0.4) and Fabrication of Homo-junction Solar Cells.* Journal of Materials Science & Technology, 2013. **29**(2): p. 128-136.

134.   Wu, J., et al., *Small band gap bowing in In1−xGaxN alloys.* Applied Physics Letters, 2002. **80**(25): p. 4741-4743.

135.   Shan, W., et al., *Optical properties of InxGa1−xN alloys grown by metalorganic chemical vapor deposition.* Journal of Applied Physics, 1998. **84**(8): p. 4452-4458.

136.   Wright, A.F. and J.S. Nelson, *Bowing parameters for zinc‐blende Al1−xGaxN and Ga1−xInxN.* Applied Physics Letters, 1995. **66**(22): p. 3051-3053.

137.   Moret, M., et al., *Optical, structural investigations and band-gap bowing parameter of GaInN alloys.* Journal of Crystal Growth, 2009. **311**(10): p. 2795-2797.

138.   Kurouchi, M., et al., *Growth and properties of In-rich InGaN films grown on (0001) sapphire by RF-MBE.* physica status solidi (b), 2004. **241**(12): p. 2843-2848.

139.   Yan, Q., et al., *Effects of strain on the band structure of group-III nitrides.* Physical Review B, 2014. **90**(12): p. 125118.

140.   Wu, J., et al., *Universal bandgap bowing in group-III nitride alloys.* Solid State Communications, 2003. **127**(6): p. 411-414.

141.   Orsal, G., et al., *Bandgap energy bowing parameter of strained and relaxed InGaN layers.* Optical Materials Express, 2014. **4**(5): p. 1030-1041.

142.   Gedam, V., A. Pansari, and B. Sahoo, *Macroscopic Polarization Effect on Bowing Constant of Thermal Parameters of In^ sub x^ Ga^ sub 1-x^ N.* Journal of Electronic Materials, 2015. **44**(4): p. 1035.

143.   Naranjo, F.B., et al., *Structural and optical characterization of thick InGaN layers and InGaN/GaN MQW grown by molecular beam epitaxy.* Materials Science and Engineering: B, 2002. **93**(1–3): p. 131-134.

144.   Feng, Z.C., et al., *Photoluminescence characteristics of low indium composition InGaN thin films grown on sapphire by metalorganic chemical vapor deposition.* Thin Solid Films, 2006. **498**(1–2): p. 118-122.

145.   Li, Q., et al., *Origin of the 'S-shaped' temperature dependence of luminescent peaks from semiconductors.* Journal of Physics: Condensed Matter, 2005. **17**(30): p. 4853.

146.   Schulz, S., et al., *Composition-dependent band gap and band-edge bowing in AlInN: A combined theoretical and experimental study.* Applied Physics Express, 2013. **6**(12): p. 121001.

147.   Kubota, K., Y. Kobayashi, and K. Fujimoto, *Preparation and properties of III-V nitride thin films.* Journal of Applied Physics, 1989. **66**(7): p. 2984-2988.

148.   Guo, Q., H. Ogawa, and A. Yoshida, *Growth of AlxIn1−xN single crystal films by microwave-excited metalorganic vapor phase epitaxy.* Journal of Crystal Growth, 1995. **146**(1): p. 462-466.

149.   Kim, K.S., et al., *Determination of the band-gap energy of Al1−xInxN grown by metal–organic chemical-vapor deposition.* Applied Physics Letters, 1997. **71**(6): p. 800-802.

150.   Peng, T., et al., *Band gap bowing and refractive index spectra of polycrystalline AlxIn1−xN films deposited by sputtering.* Applied Physics Letters, 1997. **71**(17): p. 2439-2441.

151.   Lukitsch, M.J., et al., *Optical and electrical properties of Al1−xInxN films grown by plasma source molecular-beam epitaxy.* Applied Physics Letters, 2001. **79**(5): p. 632-634.

152.   Goano, M., et al., *Band structure nonlocal pseudopotential calculation of the III-nitride wurtzite phase materials system. Part I. Binary compounds GaN, AlN, and InN.* Journal of Applied Physics, 2000. **88**(11): p. 6467-6475.

153. Ferhat, M. and F. Bechstedt, *First-principles calculations of gap bowing in InxGa1−xN and InxAl1−xN alloys: Relation to structural and thermodynamic properties.* Physical Review B, 2002. **65**(7): p. 075213.

154. Aschenbrenner, T., et al., *Optical and structural characterization of AlInN layers for optoelectronic applications.* Journal of Applied Physics, 2010. **108**(6): p. 063533.

155. Jones, R.E., et al., *Band gap bowing parameter of In{sub 1-x}Al{sub x}N.* Journal Name: Journal of Applied Physics; Journal Volume: 104; Journal Issue: 12; Other Information: DOI: 10.1063/1.3039509; (c) 2008 American Institute of Physics; Country of input: International Atomic Energy Agency (IAEA), 2008: p. Medium: X; Size: page(s) 123501-123501.6.

156. Wang, K., et al., *Optical energies of AlInN epilayers.* Journal of Applied Physics, 2008. **103**(7): p. 073510.

157. Sakalauskas, E., et al., *Dielectric function and optical properties of Al-rich AlInN alloys pseudomorphically grown on GaN.* Journal of Physics D: Applied Physics, 2010. **43**(36): p. 365102.

158. Dridi, Z., B. Bouhafs, and P. Ruterana, *First-principles investigation of lattice constants and bowing parameters in wurtzite AlxGa1− xN, InxGa1− xN and InxAl1− xN alloys.* Semiconductor science and technology, 2003. **18**(9): p. 850.

159. Iliopoulos, E., et al., *Energy bandgap bowing of InAlN alloys studied by spectroscopic ellipsometry.* Applied Physics Letters, 2008. **92**(19): p. 191907.

160. Vurgaftman, I., J. Meyer, and L. Ram-Mohan, *Band parameters for III–V compound semiconductors and their alloys.* Journal of applied physics, 2001. **89**(11): p. 5815-5875.

161. Wu, J., *When group-III nitrides go infrared: New properties and perspectives.* Journal of Applied Physics, 2009. **106**(1): p. 011101.

162. Zhang, L., et al., *Solar-blind ultraviolet AlInN/AlGaN distributed Bragg reflectors.* Applied Physics Letters, 2013. **102**(24): p. 242112.

163. Matsuoka, T., *Calculation of unstable mixing region in wurtzite In1−x−yGaxAlyN.* Applied Physics Letters, 1997. **71**(1): p. 105-106.

164. Taylor, E., et al., *Structural and optical properties of Ga auto-incorporated InAlN epilayers.* Journal of Crystal Growth, 2014. **408**: p. 97-101.

165. Kim, J., et al., *Origins of unintentional incorporation of gallium in InAlN layers during epitaxial growth, part II: Effects of underlying layers and growth chamber conditions.* Journal of Crystal Growth, 2014. **388**: p. 143-149.

166. Seong Jae, L., et al., *Band structure of ternary compound semiconductors beyond the virtual crystal approximation.* Journal of Physics: Condensed Matter, 1990. **2**(14): p. 3253.

167. Ryu, H.-Y., *Large enhancement of light extraction efficiency in AlGaN-based nanorod ultraviolet light-emitting diode structures.* Nanoscale Research Letters, 2014. **9**(1): p. 1-7.

168. Shan, W., et al., *Band anticrossing in dilute nitrides.* Journal of Physics: Condensed Matter, 2004. **16**(31): p. S3355.

169. Wu, J., W. Shan, and W. Walukiewicz, *Band anticrossing in highly mismatched III–V semiconductor alloys.* Semiconductor Science and Technology, 2002. **17**(8): p. 860.

170. Muth, J.F., et al., *Absorption coefficient, energy gap, exciton binding energy, and recombination lifetime of GaN obtained from transmission measurements.* Applied Physics Letters, 1997. **71**(18): p. 2572-2574.

171.   Hui, R., et al., *III-nitride-based planar lightwave circuits for long wavelength optical communications.* IEEE journal of quantum electronics, 2005. **41**(1): p. 100-110.

172.   Bennett, B.R., R.A. Soref, and J.A. Del Alamo, *Carrier-induced change in refractive index of InP, GaAs and InGaAsP.* IEEE Journal of Quantum Electronics, 1990. **26**(1): p. 113-122.

173.   Sze, S.M. and M.K. Lee, *Semiconductor Devices: Physics and Technology, 3rd Edition: Physics and Technology.* 2012: John Wiley & Sons.

174.   Jayaprakash, R., et al., *Extraction of absorption coefficients from as-grown GaN nanowires on opaque substrates using all-optical method.* Optics Express, 2014. **22**(16): p. 19555-19566.

175.   Morkoç, H., *Nitride Semiconductors and Devices.* 2013: Springer Berlin Heidelberg.

176.   Fox, M., *Optical Properties of Solids.* 2010: OUP Oxford.

177.   Morkoç, H., *Nitride Semiconductors and Devices.* 1999: Springer Berlin Heidelberg.

178.   Bergman, L. and J.L. McHale, *Handbook of Luminescent Semiconductor Materials.* 2016: CRC Press.

179.   Taniyasu, Y., M. Kasu, and T. Makimoto, *Radiation and polarization properties of free-exciton emission from AlN (0001) surface.* Applied Physics Letters, 2007. **90**(26): p. 261911.

180.   Sakalauskas, E., et al., *Dielectric function and optical properties of quaternary AlInGaN alloys.* Journal of Applied Physics, 2011. **110**(1): p. 013102.

181.   Sedhain, A., J. Lin, and H. Jiang, *Valence band structure of AlN probed by photoluminescence.* Applied Physics Letters, 2008. **92**(4): p. 041114.

182.   Sedhain, A., et al., *Photoluminescence properties of AlN homoepilayers with different orientations.* Applied Physics Letters, 2008. **93**(4): p. 041905.

183.   Silveira, E., et al., *Excitonic structure of bulk AlN from optical reflectivity and cathodoluminescence measurements.* Physical Review B, 2005. **71**(4): p. 041201.

184.   Martin, R.W., et al., *Exciton localization and the Stokes' shift in InGaN epilayers.* Applied Physics Letters, 1999. **74**(2): p. 263-265.

185.   Chichibu, S., et al., *Effective band gap inhomogeneity and piezoelectric field in InGaN/GaN multiquantum well structures.* Applied Physics Letters, 1998. **73**(14): p. 2006-2008.

186.   Jeong, H., et al., *Carrier localization in In-rich InGaN/GaN multiple quantum wells for green light-emitting diodes.* Scientific reports, 2015. **5**: p. 9373.

187.   Zubialevich, V.Z., et al., *Enhanced UV luminescence from InAlN quantum well structures using two temperature growth.* Journal of Luminescence, 2014. **155**: p. 108-111.

188.   Zubialevich, V.Z., et al., *Composition dependence of photoluminescence properties of In x Al 1− x N/AlGaN quantum wells.* Journal of Physics D: Applied Physics, 2016. **49**(38): p. 385105.

189.   Cho, J., E.F. Schubert, and J.K. Kim, *Efficiency droop in light‐emitting diodes: Challenges and countermeasures.* Laser & Photonics Reviews, 2013. **7**(3): p. 408-421.

190.   Karpov, S., *ABC-model for interpretation of internal quantum efficiency and its droop in III-nitride LEDs: a review.* Optical and Quantum Electronics, 2015. **47**(6): p. 1293-1303.

191.   Verzellesi, G., et al., *Efficiency droop in InGaN/GaN blue light-emitting diodes: Physical mechanisms and remedies.* Journal of Applied Physics, 2013. **114**(7): p. 071101.

192.   Karpov, S.Y., *Effect of localized states on internal quantum efficiency of III-nitride LEDs.* physica status solidi (RRL)-Rapid Research Letters, 2010. **4**(11): p. 320-322.

193.   Iveland, J.S., James S., Martinelli, L., Peretti, J., Weisbuch, C., *Auger effect identified as main cause of efficiency droop in LEDs*, in *SPIE Newsroom*. 2014.

194.   Cho, E., *Gallium Nitride Based Heterostructure Growth and Application to Electronic Devices and Gas Sensors*. 2009: ProQuest.

195.   Maruska, H.P. and W.C. Rhines, *A modern perspective on the history of semiconductor nitride blue light sources.* Solid-State Electronics, 2015. **111**: p. 32-41.

196.   Nakamura, S. and M.R. Krames, *History of gallium–nitride-based light-emitting diodes for illumination.* Proceedings of the IEEE, 2013. **101**(10): p. 2211-2220.

197.   Ambacher, O., *Growth and applications of Group III nitrides.* Journal of Physics D-Applied Physics, 1998. **31**(20): p. 2653-2710.

198.   Lo, Y.H., *Emerging Optoelectronic Technologies and Applications*. 1997: World Scientific.

199.   Feng, Z.C., *III-nitride: Semiconductor Materials*. 2006: Imperial College Press.

200.   Ibach, H. and H. Lüth, *Solid-State Physics: An Introduction to Principles of Materials Science*. 2009: Springer Berlin Heidelberg.

201.   Hovel, H.J. and J.J. Cuomo, *Electrical and Optical Properties of Rf-Sputtered Gan and Inn.* Applied Physics Letters, 1972. **20**(2): p. 71-&.

202.   Zembutsu, S. and M. Kobayashi, *The Growth of C-Axis-Oriented Gan Films by Dc-Biased Reactive Sputtering.* Thin Solid Films, 1985. **129**(3-4): p. 289-297.

203.   Yadav, B.S., S.S. Major, and R.S. Srinivasa, *Growth and structure of sputtered gallium nitride films.* Journal of Applied Physics, 2007. **102**(7).

204.   Alexiev, D., et al., *A Review of Liquid Phase Epitaxial Grown Gallium Arsenide.* arXiv preprint cond-mat/0408653, 2004.

205.   Kawamura, F., et al., *Growth of a large GaN single crystal using the liquid phase epitaxy (LPE) technique.* Japanese journal of applied physics, 2003. **42**(1A): p. L4.

206.   Morishita, M., et al., *The influences of supersaturation on LPE growth of GaN single crystals using the Na flux method.* Journal of crystal growth, 2004. **270**(3): p. 402-408.

207.   Steiner, T.D., *Semiconductor Nanostructures for Optoelectronic Applications*. 2004: Artech House.

208.   Mori, Y., et al. *Growth of bulk GaN crystal by Na flux method*. in *SPIE OPTO*. 2014. International Society for Optics and Photonics.

209.   Maruska, H.P. and J.J. Tietjen, *Preparation and Properties of Vapor-Deposited Single-Crystalline GaN.* Applied Physics Letters, 1969. **15**(10): p. 327-&.

210.   *HVPE Edition for modeling of GaN, AlN or AlGaN alloy*. 2016; Available from: http://www.str-soft.com/products/cvdsim/HVPE/.

211.   Dhanaraj, G., et al., *Springer Handbook of Crystal Growth*. 2010: Springer Berlin Heidelberg.

212.   Suhara, T., *Semiconductor Laser Fundamentals*. 2004: Taylor & Francis.

213.   Kuech, T., *Handbook of Crystal Growth: Thin Films and Epitaxy*. 2014: Elsevier Science.

214.   Stringfellow, G.B., *Organometallic Vapor-Phase Epitaxy: Theory and Practice*. 1999: Elsevier Science.

215.   Manasevit, H.M., *Single Crystal Gallium Arsenide on Insulating Substrates*. Applied Physics Letters, 1968. **12**(4): p. 156-159.

216.   Nakamura, S., *Highlights in Condensed Matter Physics and Materials ScienceIII–V nitride based light-emitting devices*. Solid State Communications, 1997. **102**(2): p. 237-248.

217.   Jones, A.C. and M.L. Hitchman, *Chemical Vapour Deposition: Precursors, Processes and Applications*. 2009: Royal Society of Chemistry.

218.   Parikh, R.P. and R.A. Adomaitis, *An overview of gallium nitride growth chemistry and its effect on reactor design: Application to a planetary radial-flow CVD system*. Journal of crystal growth, 2006. **286**(2): p. 259-278.

219.   Seshan, K., *Handbook of Thin Film Deposition*. 2001: Elsevier Science.

220.   Amano, H., et al., *Metalorganic vapor phase epitaxial growth of a high quality GaN film using an AlN buffer layer*. Applied Physics Letters, 1986. **48**(5): p. 353-355.

221.   Hui, L., *Mass transport analysis of a showerhead MOCVD reactor*. Journal of Semiconductors, 2011. **32**(3): p. 033006.

222.   Ohring, M., *Materials science of thin films*. 2001: Academic press.

223.   Matthews, J. and A. Blakeslee, *Defects in epitaxial multilayers: I. Misfit dislocations*. Journal of Crystal growth, 1974. **27**: p. 118-125.

224.   Peter, Y. and M. Cardona, *Fundamentals of semiconductors: physics and materials properties*. 2010: Springer Science & Business Media.

225.   Trampert, A., O. Brandt, and K.H. Ploog, *Chapter 7 Crystal Structure of Group III Nitrides*, in *Semiconductors and Semimetals*, I.P. Jacques and D.M. Theodore, Editors. 1997, Elsevier.

226.   Paskova, T., D.A. Hanser, and K.R. Evans, *GaN substrates for III-nitride devices*. Proceedings of the IEEE, 2010. **98**(7): p. 1324-1338.

227.   Lin, H., *SiC, GaN, and other Wide Band Gap (WBG) materials for power electronics applications*. 2015, Yole Développement: France.

228.   Lin, M.E., et al., *GaN grown on hydrogen plasma cleaned 6H-SiC substrates*. Applied Physics Letters, 1993. **62**(7): p. 702-704.

229.   Dadgar, A., et al., *Growth of blue GaN LED structures on 150-mm Si(1 1 1)*. Journal of Crystal Growth, 2006. **297**(2): p. 279-282.

230.   Akihiko, K., et al., *InGaN/GaN Multiple Quantum Disk Nanocolumn Light-Emitting Diodes Grown on (111) Si Substrate*. Japanese Journal of Applied Physics, 2004. **43**(12A): p. L1524.

231.   Wong, W.S., T. Sands, and N.W. Cheung, *Damage-free separation of GaN thin films from sapphire substrates*. Applied Physics Letters, 1998. **72**(5): p. 599-601.

232.   Yoshida, S., S. Misawa, and S. Gonda, *Improvements on the electrical and luminescent properties of reactive molecular beam epitaxially grown GaN films by using AlN-coated sapphire substrates*. Applied Physics Letters, 1983. **42**(5): p. 427-429.

233.   Zhu, D., D.J. Wallis, and C.J. Humphreys, *Prospects of III-nitride optoelectronics grown on Si.* Reports on Progress in Physics, 2013. **76**(10): p. 106501.

234.   Levinshtein, M.E., S.L. Rumyantsev, and M.S. Shur, *Properties of Advanced Semiconductor Materials: GaN, AIN, InN, BN, SiC, SiGe*. 2001: John Wiley & Sons.

235.   Suzuki, R., A. Kawaharazuka, and Y. Horikoshi, *Effect of the MgO substrate on the growth of GaN.* Journal of Crystal Growth, 2009. **311**(7): p. 2021-2024.

236.   Li, N., et al. *Growth of GaN on ZnO for solid state lighting applications*. 2006.

237.   Hamdani, F., et al., *Microstructure and optical properties of epitaxial GaN on ZnO (0001) grown by reactive molecular beam epitaxy.* Journal of Applied Physics, 1998. **83**(2): p. 983-990.

238.   Weber, M.J., *Handbook of optical materials*. Vol. 19. 2002: CRC press.

239.   Alemu, A., et al., *Optical properties of wurtzite GaN epilayers grown on A-plane sapphire.* Physical Review B, 1998. **57**(7): p. 3761.

240.   Zhao, D., et al., *Stress and its effect on optical properties of GaN epilayers grown on Si (111), 6H-SiC (0001), and c-plane sapphire.* Applied physics letters, 2003. **83**(4): p. 677-679.

241.   Armitage, R. and H. Hirayama, *M-plane GaN grown on m-sapphire by metalorganic vapor phase epitaxy.* Applied Physics Letters, 2008. **92**(9): p. 092121.

242.   Ni, X., et al., *Optimization of a-plane GaN growth by MOCVD on r-plane sapphire.* Journal of Crystal Growth, 2006. **290**(1): p. 166-170.

243.   Sun, C.J., et al., *A crystallographic model of (00·1) aluminum nitride epitaxial thin film growth on (00·1) sapphire substrate.* Journal of Applied Physics, 1994. **75**(8): p. 3964-3967.

244.   Melton, W.A. and J.I. Pankove, *GaN growth on sapphire.* Journal of Crystal Growth, 1997. **178**(1–2): p. 168-173.

245.   Theeradetch, D., et al., *Relaxation Process of the Thermal Strain in the GaN/α-Al 2 O 3 Heterostructure and Determination of the Intrinsic Lattice Constants of GaN Free from the Strain.* Japanese Journal of Applied Physics, 1992. **31**(10B): p. L1454.

246.   Amano, H., K. Hiramatsu, and I. Akasaki, *Heteroepitaxial Growth and the Effect of Strain on the Luminescent Properties of GaN Films on (11 2̄0) and (0001) Sapphire Substrates.* Japanese journal of applied physics, 1988. **27**(8A): p. L1384.

247.   Potin, V., et al., *Mosaic growth of GaN on (0001) sapphire: A high-resolution electron microscopy and crystallographic study of threading dislocations from low-angle to high-angle grain boundaries.* Physical Review B, 2000. **61**(8): p. 5587-5599.

248.   Schroder, D.K., *Semiconductor material and device characterization*. 2006: John Wiley & Sons.

249.   Spring, K.R.D., M. W. . *Useful Magnification Range*. 2016; Available from: http://www.microscopyu.com/microscopy-basics/useful-magnification-range.

250.   Moram, M. and M. Vickers, *X-ray diffraction of III-nitrides.* Reports on Progress in Physics, 2009. **72**(3): p. 036502.

251.   Fewster, P.F., *X-ray Scattering from Semiconductors*. 2000: Imperial College Press.

252.   Mansuripur, M., *Classical Optics and Its Applications*. 2002: Cambridge University Press.

253. *Fundamental Concepts in DIC Microscopy*. Available from: http://www.olympusmicro.com/primer/techniques/dic/dicintro.html.

254. Lang, W., *Nomarski differential interference-contrast microscopy*. 2016, ZEISS Germany. p. 114-120.

255. Bergman, L. and J.L. McHale, *Handbook of Luminescent Semiconductor Materials*. 2011: Taylor & Francis.

256. Vij, D.R., *Luminescence of Solids*. 1998: Springer US.

257. Photonics, H., *Photomultiliier Tubes, basics and applications*. 3 ed. 2007, Japan: Hamamatsu Photonics.

258. Lakowicz, J.R., *Principles of Fluorescence Spectroscopy*. 2007: Springer US.

259. Parbrook, S.N.A.V.Z.Z.D.V.D.P.J., *Temperature Dependent BandGap and Bowing Parameter of Indium-Aluminum Nitride*, in *UKNC Winter conference*. 2016: Cambridge University, UK.

260. Razeghi, M., *Fundamentals of Solid State Engineering*. 2009: Springer US.

261. Perkowitz, S., *Optical characterization of semiconductors: infrared, Raman, and photoluminescence spectroscopy*. 2012: Elsevier.

262. !!! INVALID CITATION !!!

263. Teisseyre, H., et al., *GaN doped with beryllium—An effective light converter for white light emitting diodes.* Applied Physics Letters, 2013. **103**(1): p. 011107.

264. Yacobi, B.G. and D.B. Holt, *Cathodoluminescence Microscopy of Inorganic Solids*. 2013: Springer US.

265. Zhang, J.Z., *Optical properties and spectroscopy of nanomaterials*. 2009: World Scientific.

266. Yu, E.T., *III-V Nitride Semiconductors: Applications and Devices*. 2002: Taylor & Francis.

267. *I-V Characteristic Curves*. http://www.electronics-tutorials.ws/.

268. Altissimo, M., *E-beam lithography for micro-/nanofabrication.* Biomicrofluidics, 2010. **4**(2): p. 026503.

269. Mohammad, M.A., et al., *Fundamentals of electron beam exposure and development*. 2012: Springer.

270. Vieu, C., et al., *Electron beam lithography: resolution limits and applications.* Applied Surface Science, 2000. **164**(1–4): p. 111-117.

271. Adesida, I., et al. *Dry and wet etching for group III–nitrides*. in *MRS Proceedings*. 1998. Cambridge Univ Press.

272. Nishi, Y. and R. Doering, *Handbook of semiconductor manufacturing technology*. Second ed. 2008: CRC Press.

273. Keller, J.H., J.C. Forster, and M.S. Barnes, *Novel radio-frequency induction plasma processing techniques.* Journal of Vacuum Science & Technology A, 1993. **11**(5): p. 2487-2491.

274. Hahn, H., et al., *Oxygen addition to fluorine based SiN etch process: Impact on the electrical properties of AlGaN/GaN 2DEG and transistor characteristics.* Solid-State Electronics, 2012. **67**(1): p. 90-93.

275.   Kuryatkov, V., et al., *Analysis of nonselective plasma etching of AlGaN by CF4/Ar/Cl2.* Journal of applied physics, 2005. **97**(7): p. 73302-73302.

276.   Streetman, B. and S. Banerjee, *Solid State Electronic Devices* 2009, Prentice Hall: New Delhi.

277.   Xiao, H., *Introduction to semiconductor manufacturing technology.* Second ed. 2012: Prentice Hall Upper Saddle River, NJ.

278.   Mohammad, S.N., *Contact mechanisms and design principles for Schottky contacts to group-III nitrides.* Journal of Applied Physics, 2005. **97**(6): p. 063703.

279.   Fan, Z., et al., *Very low resistance multilayer Ohmic contact to n-GaN.* Applied Physics Letters, 1996. **68**(12): p. 1672-1674.

280.   Dobos, L., et al., *Metal contacts to n-GaN.* Applied Surface Science, 2006. **253**(2): p. 655-661.

281.   Song, J.O., J.-S. Ha, and T.-Y. Seong, *Ohmic-contact technology for GaN-based light-emitting diodes: Role of p-type contact.* IEEE transactions on electron devices, 2010. **57**(1): p. 42-59.

282.   Lee, H.-S., D.S. Lee, and T. Palacios, *AlGaN/GaN high-electron-mobility transistors fabricated through a Au-Free technology.* Electron Device Letters, IEEE, 2011. **32**(5): p. 623-625.

283.   Nebauer, E., et al., *XTEM and TFXRD investigations of ohmic Ti/Al/Ti/Au/WSiN contacts on AlGaN/GaN HFET layer systems.* Semiconductor Science and Technology, 2002. **17**(3): p. 249.

284.   Götz, W., et al., *Activation of acceptors in Mg-doped GaN grown by metalorganic chemical vapor deposition.* Applied Physics Letters, 1996. **68**(5): p. 667-669.

285.   Trexler, J., et al., *Comparison of Ni/Au, Pd/Au, and Cr/Au metallizations for ohmic contacts to p-GaN.* MRS Online Proceedings Library Archive, 1996. **449**.

286.   Nakamura, S., et al., *Room-temperature continuous-wave operation of InGaN multi-quantum-well structure laser diodes.* Applied Physics Letters, 1996. **69**(26): p. 4056-4058.

287.   Ho, J.-K., et al., *Low-resistance ohmic contacts to p-type GaN achieved by the oxidation of Ni/Au films.* Journal of Applied Physics, 1999. **86**(8): p. 4491-4497.

288.   Chu, C.-F., et al., *Low-resistance ohmic contacts on p-type GaN using Ni/Pd/Au metallization.* Applied Physics Letters, 2000. **77**(21): p. 3423-3425.

289.   Kim, H.-K., et al., *Low-resistance Pt/Pd/Au ohmic contacts to p-type AlGaN.* Applied physics letters, 2004. **84**(10): p. 1710-1712.

290.   Sun, J., et al., *p-GaN surface treatments for metal contacts.* Applied Physics Letters, 2000. **76**(4): p. 415-417.

291.   Hartlieb, P., et al., *Chemical, electrical, and structural properties of Ni/Au contacts on chemical vapor cleaned p-type GaN.* Journal of applied physics, 2002. **91**(11): p. 9151-9160.

292.   Wenzel, R., G.G. Fischer, and R. Schmid-Fetzer, *Ohmic contacts on p-GaN (Part I):: investigation of different contact metals and their thermal treatment.* Materials Science in Semiconductor Processing, 2001. **4**(4): p. 357-365.

293.   Lee, J.L., et al., *Transparent Pt Ohmic Contact on p-Type GaN with Low Resistivity Using (NH 4) 2 S x Treatment.* Electrochemical and Solid-State Letters, 2000. **3**(1): p. 53-55.

294. Jang, J.-S., S.-J. Park, and T.-Y. Seong, *Formation of low resistance Pt ohmic contacts to p-type GaN using two-step surface treatment.* Journal of Vacuum Science & Technology B: Microelectronics and Nanometer Structures Processing, Measurement, and Phenomena, 1999. **17**(6): p. 2667-2670.

295. Jang, H.W., T. Sands, and J.-L. Lee, *Effects of KrF excimer laser irradiation on metal contacts to n-type and p-type GaN.* Journal of applied physics, 2003. **94**(5): p. 3529-3535.

296. Suzuki, M., et al., *Low-resistance Ta/Ti Ohmic contacts for p-type GaN.* Applied physics letters, 1999. **74**(2): p. 275-277.

297. Perillat-Merceroz, G., et al., *Intrinsic degradation mechanism of nearly lattice-matched InAlN layers grown on GaN substrates.* Journal of Applied Physics, 2013. **113**(6): p. 063506.

298. Li, H., T.C. Sadler, and P.J. Parbrook, *AlN heteroepitaxy on sapphire by metalorganic vapour phase epitaxy using low temperature nucleation layers.* Journal of Crystal Growth, 2013. **383**: p. 72-78.

299. Smith, M.D., et al., *Determination of Ga auto-incorporation in nominal InAlN epilayers grown by MOCVD.* Journal of Materials Chemistry C, 2014. **2**(29): p. 5787-5792.

300. Fan, Z.Y., et al., *Defect annihilation in AlN thin films by ultrahigh temperature processing.* Applied Physics Letters, 2000. **76**(14): p. 1839-1841.

301. S. F. Chichibu, A.U., T. Onuma, S. P. DenBaars, U. K. Mishra, J. S. Speck, S. Nakamura, , *Impact of Point Defects on the Luminescence Properties of (Al,Ga)N,* in *Materials Science Forum*, B. Monemar, M. Kittler, and H. Grimmeiss, Editors. 2008.

302. Chichibu, S.F., et al., *High internal quantum efficiency ultraviolet to green luminescence peaks from pseudomorphic m-plane Al1−xInxN epilayers grown on a low defect density m-plane freestanding GaN substrate.* Journal of Applied Physics, 2014. **116**(21): p. 213501.

303. Roqan, I.S., et al., *Optical and structural properties of Eu-implanted InxAl1−xN.* Journal of Applied Physics, 2009. **106**(8): p. 083508.

304. Feneberg, M., et al., *Synchrotron-based photoluminescence excitation spectroscopy applied to investigate the valence band splittings in AlN and Al0.94Ga0.06N.* Applied Physics Letters, 2011. **99**(2): p. 021903.

305. Schulz, S., et al., *Impact of cation-based localized electronic states on the conduction and valence band structure of Al1−xInxN alloys.* Applied Physics Letters, 2014. **104**(17): p. 172102.

306. Li, J., et al., *200nm deep ultraviolet photodetectors based on AlN.* Applied Physics Letters, 2006. **89**(21): p. 213510.

307. Rossbach, G., et al., *Influence of exciton-phonon coupling and strain on the anisotropic optical response of wurtzite AlN around the band edge.* Physical Review B, 2011. **83**(19): p. 195202.

308. Chichibu, S.F., et al., *Excitonic emission dynamics in homoepitaxial AlN films studied using polarized and spatio-time-resolved cathodoluminescence measurements.* Applied Physics Letters, 2013. **103**(14): p. 142103.

309. Shan, W., et al., *Band Anticrossing in GaInNAs Alloys.* Physical Review Letters, 1999. **82**(6): p. 1221-1224.

310.   Lindsay, A. and E.P. O'Reilly, *Unification of the Band Anticrossing and Cluster-State Models of Dilute Nitride Semiconductor Alloys.* Physical Review Letters, 2004. **93**(19): p. 196402.

311.   Reilly, E.P.O., et al., *Trends in the electronic structure of dilute nitride alloys.* Semiconductor Science and Technology, 2009. **24**(3): p. 033001.

312.   Lindsay, A. and E.P. O'Reilly, *Theory of enhanced bandgap non-parabolicity in GaNxAs1−x and related alloys.* Solid State Communications, 1999. **112**(8): p. 443-447.

313.   Fu, S., T. Chen, and Y. Chen, *Photoluminescent properties of InN epifilms.* Semiconductor science and technology, 2006. **21**(3): p. 244.

314.   Nanishi, Y., Y. Saito, and T. Yamaguchi, *RF-molecular beam epitaxy growth and properties of InN and related alloys.* Japanese journal of applied physics, 2003. **42**(5R): p. 2549.

315.   Gorczyca, S.P.Ł.a.I., *Poisson Ratio and Biaxial Relaxation Coefficient in InxGa1-xN and InxAl1-xN Alloys.* Acta Physica Polonica Series a 2011. **120**(5).

316.   Gorczyca, I., et al., *Anomalous composition dependence of the band gap pressure coefficients in In-containing nitride semiconductors.* Physical Review B, 2010. **81**(23): p. 235206.

317.   Uesugi, K., et al., *Temperature dependence of band gap energies of GaAsN alloys.* Applied Physics Letters, 2000. **76**(10): p. 1285-1287.

318.   Kim, T., et al., *Composition dependence of the band-gap energy of GaAsN alloys.* Journal of the Korean Physical Society, 2003. **43**(2): p. 273-276.

319.   Franssen, G., et al., *Bowing of the band gap pressure coefficient in InxGa1−xN alloys.* Journal of Applied Physics, 2008. **103**(3): p. 033514.

320.   Feneberg, M., et al., *High-excitation and high-resolution photoluminescence spectra of bulk AlN.* Physical Review B, 2010. **82**(7): p. 075208.

321.   Kong, W., et al., *Room temperature photoluminescence from InxAl(1−x)N films deposited by plasma-assisted molecular beam epitaxy.* Applied Physics Letters, 2014. **105**(13): p. 132101.

322.   King, P.D.C., et al., *Valence band offset of InN/AlN heterojunctions measured by x-ray photoelectron spectroscopy.* Applied Physics Letters, 2007. **90**(13): p. 132105.

323.   Westmeyer, A.N., et al., *Determination of energy-band offsets between GaN and AlN using excitonic luminescence transition in AlGaN alloys.* Journal of Applied Physics, 2006. **99**(1): p. 013705.

324.   Carlin, J.-F. and M. Ilegems, *High-quality AlInN for high index contrast Bragg mirrors lattice matched to GaN.* Applied Physics Letters, 2003. **83**(4): p. 668-670.

325.   Butté, R., et al., *Current status of AlInN layers lattice-matched to GaN for photonics and electronics.* Journal of Physics D: Applied Physics, 2007. **40**(20): p. 6328.

326.   Lupu, A., et al., *Lattice-Matched GaN–InAlN Waveguides at $\lambda= 1.55\mu $ m Grown by Metal–Organic Vapor Phase Epitaxy.* IEEE Photonics Technology Letters, 2008. **20**(2): p. 102-104.

327.   Piprek, J., *Semiconductor optoelectronic devices: introduction to physics and simulation.* 2013: Academic press.

328.   Takeuchi, K., S. Adachi, and K. Ohtsuka, *Optical properties of Al x Ga 1− x N alloy.* Journal of Applied Physics, 2010. **107**(2): p. 023306.

329.   Touré, A., et al., *Characterization of low Al content AlxGa1− xN epitaxial films grown by atmospheric‑pressure MOVPE.* physica status solidi (a), 2012. **209**(5): p. 977-983.

330.   Adachi, S., *Refractive indices of III–V compounds: Key properties of InGaAsP relevant to device design.* Journal of Applied Physics, 1982. **53**(8): p. 5863-5869.

331.   Peng, T. and J. Piprek, *Refractive index of AlGaInN alloys.* Electronics letters, 1996. **32**(24): p. 2285-2286.

332.   Brunner, D., et al., *Optical constants of epitaxial AlGaN films and their temperature dependence.* Journal of applied physics, 1997. **82**(10): p. 5090-5096.

333.   Laws, G., et al., *Improved refractive index formulas for the Al x Ga 1− x N and In y Ga 1− y N alloys.* Journal of applied Physics, 2001. **89**(2): p. 1108-1115.

334.   Piprek, J., et al. *Energy gap bowing and refractive index spectrum of AlInN and AlGaInN.* in *Compound Semiconductors, 1997 IEEE International Symposium on*. 1997. IEEE.

335.   Bosund, M., et al., *Properties of AlN grown by plasma enhanced atomic layer deposition.* Applied Surface Science, 2011. **257**(17): p. 7827-7830.

336.   Oliva, R., et al., *Pressure dependence of the refractive index in wurtzite and rocksalt indium nitride.* Applied Physics Letters, 2014. **105**(23): p. 232111.

337.   Rigler, M., et al., *Refractive index of III-metal-polar and N-polar AlGaN waveguides grown by metal organic chemical vapor deposition.* Appl Phys Lett, 2013. **102**.

338.   Sanford, N.A., et al., *Refractive index study of AlxGa1-xN films grown on sapphire substrate.* J Appl Phys, 2003. **94**.

339.   Antoine-Vincent, N., et al., *Determination of the refractive indices of AlN, GaN, and Al x Ga 1− x N grown on (111) Si substrates.* Journal of applied physics, 2003. **93**(9): p. 5222-5226.

340.   Yu, G., et al., *Optical properties of wurtzite structure GaN on sapphire around fundamental absorption edge (0.78–4.77 eV) by spectroscopic ellipsometry and the optical transmission method.* Appl Phys Lett, 1997. **70**.

341.   Kim, S., et al., *Effects of barrier growth temperature on the properties of InGaN/GaN multi-quantum wells.* Journal of Crystal Growth, 2003. **247**(1–2): p. 62-68.

342.   Olaizola, S.M., et al., *Influence of GaN barrier growth temperature on the photoluminescence of InGaN/GaN heterostructures.* Journal of Physics D: Applied Physics, 2002. **35**(7): p. 599.

343.   Costa, P., et al., *Misfit dislocations in In‑rich InGaN/GaN quantum well structures.* physica status solidi (a), 2006. **203**(7): p. 1729-1732.

344.   Shahab Norouzian Alam, V.Z.Z., Pietro Pampili, Peter J. Parbrook, *Excitation Power Dependent Photoluminescence Spectroscopy of InAlN/AlGaN Quantum Wells on Sapphire Substrate*, in *7th Wide Band Gap Semiconductor and Components Workshop* 2014: Frascati (Rome), Italy.

345.   Liou, B.-T. and Y.-K. Kuo, *Effect of biaxial strain on the band gap of wurtzite Al x Ga1−x N.* Applied Physics A, 2012. **106**(4): p. 1013-1016.

346.   Rajanna, G., et al., *Temperature and excitation intensity dependence of photoluminescence in AlGaN quantum wells with mixed two-dimensional and three-dimensional morphology.* Journal of Applied Physics, 2011. **110**(7): p. 073512.

347.   Nam, K.B., et al., *Deep impurity transitions involving cation vacancies and complexes in AlGaN alloys.* Applied Physics Letters, 2005. **86**(22): p. 222108.

348.   Yablonskii, G., et al., *Luminescence and lasing in InGaN/GaN multiple quantum well heterostructures grown at different temperatures.* Applied physics letters, 2004. **85**.

349.   Mauder, C., et al., *Effect of indium incorporation on optical and structural properties of m-plane InGaN/GaN MQW on LiAlO2 substrates.* Journal of Crystal Growth, 2011. **315**(1): p. 246-249.

350.   Mukai, T., D. Morita, and S. Nakamura, *High-power UV InGaN/AlGaN double-heterostructure LEDs.* Journal of Crystal Growth, 1998. **189–190**: p. 778-781.

351.   Takashi, M., Y. Motokazu, and N. Shuji, *Current and Temperature Dependences of Electroluminescence of InGaN-Based UV/Blue/Green Light-Emitting Diodes.* Japanese Journal of Applied Physics, 1998. **37**(11B): p. L1358.

352.   Gurskii, A.L., et al., *Influence of MQW growth temperature and post-epitaxial annealing on luminescence and laser properties of InGaN/GaN MQW heterostructures grown by MOCVD on sapphire substrates.* Journal of Crystal Growth, 2005. **275**(1–2): p. e1047-e1051.

353.   *Origin 9.1 User Guide*. Available from: https://www.originlab.com/doc/User-Guide/.

354.   Lee, Y.-J., et al., *Study of the excitation power dependent internal quantum efficiency in InGaN/GaN LEDs grown on patterned sapphire substrate.* IEEE Journal of selected Topics in Quantum Electronics, 2009. **15**(4): p. 1137-1143.

355.   Zubialevich, V.Z., et al., *Mechanisms for spontaneous and stimulated recombination in multiple quantum wells of InGaN/GaN heterostructures on silicon substrates.* Journal of Applied Spectroscopy, 2008. **75**(1): p. 96-103.

356.   Zubialevich, V.Z., et al., *Varying of content of InAlN/AlGaN multiple quantum wells by in-plane lattice constant of AlGaN buffer.* Submitted to physica status solidi (b), 2016.

357.   Silveira, E., et al., *AlN bandgap temperature dependence from its optical properties.* Journal of Crystal Growth, 2008. **310**(17): p. 4007-4010.

358.   Herrnsdorf, J., et al., *Active-Matrix GaN Micro Light-Emitting Diode Display With Unprecedented Brightness.* IEEE Transactions on Electron Devices, 2015. **62**(6): p. 1918-1925.

359.   Zhang, K., et al., *Investigation of Photon-Generated Leakage Current for High-Performance Active Matrix Micro-LED Displays.* IEEE Transactions on Electron Devices, 2016. **63**(12): p. 4832-4838.

360.   Soltan, A., et al. *High density μLED array for retinal prothesis with a eye-tracking system.* in *2016 IEEE Biomedical Circuits and Systems Conference (BioCAS)*. 2016.

361.   Chen, R., et al., *Nanophotonic integrated circuits from nanoresonators grown on silicon.* Nature communications, 2014. **5**.

362.   Bai, D., et al., *Suspended GaN-based nanostructure for integrated optics.* Applied Physics B, 2016. **122**(1): p. 9.

363.   Yeh, T.-W., et al., *InGaN/GaN Multiple Quantum Wells Grown on Nonpolar Facets of Vertical GaN Nanorod Arrays.* Nano Letters, 2012. **12**(6): p. 3257-3262.

364.   Hong, Y.J., et al., *Visible-Color-Tunable Light-Emitting Diodes.* Advanced Materials, 2011. **23**(29): p. 3284-3288.

365.   Pan, J.-W. and C.-S. Wang, *Light extraction efficiency of GaN-based LED with pyramid texture by using ray path analysis.* Optics Express, 2012. **20**(S5): p. A630-A640.

366.   Hersee, S.D., X. Sun, and X. Wang, *The Controlled Growth of GaN Nanowires.* Nano Letters, 2006. **6**(8): p. 1808-1811.

367.   Kishino, K., H. Sekiguchi, and A. Kikuchi, *Improved Ti-mask selective-area growth (SAG) by rf-plasma-assisted molecular beam epitaxy demonstrating extremely uniform GaN nanocolumn arrays.* Journal of Crystal Growth, 2009. **311**(7): p. 2063-2068.

368.   Kishino, K., et al. *Selective-area growth of GaN nanocolumns on titanium-mask-patterned silicon (111) substrates by RF-plasma-assisted molecular-beam epitaxy.* Electronics Letters, 2008. **44**, 819-821.

369.   Lin, Y.T., et al., *Catalyst-Free GaN Nanorods Synthesized by Selective Area Growth.* Advanced Functional Materials, 2014. **24**(21): p. 3162-3171.

370.   Katsumi, K. and I. Shunsuke, *Selective-area growth of GaN nanocolumns on Si(111) substrates for application to nanocolumn emitters with systematic analysis of dislocation filtering effect of nanocolumns.* Nanotechnology, 2015. **26**(22): p. 225602.

371.   Duan, X. and C.M. Lieber, *Laser-Assisted Catalytic Growth of Single Crystal GaN Nanowires.* Journal of the American Chemical Society, 2000. **122**(1): p. 188-189.

372.   Wu, Y. and P. Yang, *Direct Observation of Vapor−Liquid−Solid Nanowire Growth.* Journal of the American Chemical Society, 2001. **123**(13): p. 3165-3166.

373.   Köster, R., et al., *Self-assembled growth of catalyst-free GaN wires by metal–organic vapour phaseepitaxy.* Nanotechnology, 2009. **21**(1): p. 015602.

374.   Kim, J.-H., et al., *Dislocation-eliminating chemical control method for high-efficiency GaN-based light emitting nanostructures.* Crystal Growth & Design, 2012. **12**(3): p. 1292-1298.

375.   Hahn, Y.B., et al., *High-density plasma-induced etch damage of InGaN/GaN multiple quantum well light-emitting diodes.* Journal of Applied Physics, 2002. **92**(3): p. 1189-1194.

376.   Hennessy, K., et al., *Tuning photonic crystal nanocavity modes by wet chemical digital etching.* Applied Physics Letters, 2005. **87**(2): p. 021108.

377.   Hock, M.N., et al., *Patterning GaN Microstructures by Polarity-Selective Chemical Etching.* Japanese Journal of Applied Physics, 2003. **42**(12A): p. L1405.

378.   Weyher, J.L., et al., *Recent advances in defect-selective etching of GaN.* Journal of Crystal Growth, 2000. **210**(1): p. 151-156.

379.   Zhuang, D. and J.H. Edgar, *Wet etching of GaN, AlN, and SiC: a review.* Materials Science and Engineering: R: Reports, 2005. **48**(1): p. 1-46.

380.   Waag, A., et al., *The nanorod approach: GaN NanoLEDs for solid state lighting.* physica status solidi (c), 2011. **8**(7-8): p. 2296-2301.

381.   Stöber, W., A. Fink, and E. Bohn, *Controlled growth of monodisperse silica spheres in the micron size range.* Journal of Colloid and Interface Science, 1968. **26**(1): p. 62-69.

382.   Oh, J.R., et al., *Fabrication of wafer-scale polystyrene photonic crystal multilayers via the layer-by-layer scooping transfer technique.* Journal of Materials Chemistry, 2011. **21**(37): p. 14167-14172.

383.   Zeniou, A., et al., *Ultra-high aspect ratio Si nanowires fabricated with plasma etching: plasma processing, mechanical stability analysis against adhesion and capillary forces and oleophobicity.* Nanotechnology, 2014. **25**(3): p. 035302.

384.   Le Boulbar, E.D., et al., *Fabrication of high-aspect ratio GaN nanostructures for advanced photonic devices.* Microelectronic Engineering, 2016. **153**: p. 132-136.

385.   Senga, T., Y. Matsumi, and M. Kawasaki, *Chemical dry etching mechanisms of GaAs surface by HCl and Cl2.* Journal of Vacuum Science & Technology B: Microelectronics and Nanometer Structures Processing, Measurement, and Phenomena, 1996. **14**(5): p. 3230-3238.

386.   Shields, P., et al., *Fabrication and properties of etched GaN nanorods.* physica status solidi (c), 2012. **9**(3-4): p. 631-634.

387.   Sun, Q. and J. Han, *Heteroepitaxy of nonpolar and semipolar GaN*, in *GaN and ZnO-based Materials and Devices*. 2012, Springer. p. 1-27.

388.   Krames, M.R., et al., *Status and Future of High-Power Light-Emitting Diodes for Solid-State Lighting.* Journal of Display Technology, 2007. **3**(2): p. 160-175.

389.   Murai, A., et al., *Hexagonal pyramid shaped light-emitting diodes based on ZnO and GaN direct wafer bonding.* Applied Physics Letters, 2006. **89**(17): p. 171116.

390.   Ma, J., et al., *Nitride-based micron-scale hexagonal pyramids array vertical light emitting diodes by N-polar wet etching.* Optics Express, 2013. **21**(3): p. 3547-3556.

391.   Li, T., et al., *Carrier localization and nonradiative recombination in yellow emitting InGaN quantum wells.* Applied Physics Letters, 2010. **96**(3): p. 031906.

392.   Wang, H., et al., *Influence of excitation power and temperature on photoluminescence in InGaN/GaN multiple quantum wells.* Optics express, 2012. **20**(4): p. 3932-3940.

393.   Martínez-Criado, G., et al., *Photoluminescence study of excitons in homoepitaxial GaN.* Journal of Applied Physics, 2001. **90**(11): p. 5627-5631.

394.   Bimberg, D., M. Sondergeld, and E. Grobe, *Thermal Dissociation of Excitons Bounds to Neutral Acceptors in High-Purity GaAs.* Physical Review B, 1971. **4**(10): p. 3451-3455.

395.   Lu, T., et al., *Temperature-dependent photoluminescence in light-emitting diodes.* Scientific reports, 2014. **4**.

396.   Ebaid, M., et al., *Towards highly efficient photoanodes: the role of carrier dynamics on the photoelectrochemical performance of InGaN/GaN multiple quantum well coaxial nanowires.* RSC Advances, 2015. **5**(30): p. 23303-23310.

397.   Grandjean, N., et al., *GaN/AlGaN quantum wells for UV emission: heteroepitaxy versus homoepitaxy.* Semiconductor Science and Technology, 2001. **16**(5): p. 358.

398.   Kaeding, J., et al., *Realization of high hole concentrations in Mg doped semipolar (10 1⁻ 1⁻) GaN.* Applied physics letters, 2006. **89**(20): p. 202104.